

1 LEVERAGING MULTI-MESSENGER ASTROPHYSICS FOR DARK MATTER SEARCHES

By

Daniel Nicholas Salazar-Gallegos

A DISSERTATION

Submitted to  
Michigan State University  
in partial fulfillment of the requirements  
for the degree of

Physics—Doctor of Philosophy  
Computational Mathematics in Science and Engineering—Dual Major

Today

**ABSTRACT**

3 I did Dark Matter with HAWC and IceCube. I also used Graph Neural Networks

## ACKNOWLEDGMENTS

5 I love my friends. Thanks to everyone that helped me figure this out. Amazing thanks to the people  
6 at LANL who supported me. Eames, etc Dinner Parties Jenny and her child Kaydince Kirsten, Pat,  
7 Andrea Family. You're so far but so critical to my formation. Unconditional love. Roommate

## TABLE OF CONTENTS

9	LIST OF TABLES . . . . .	vi
10	LIST OF FIGURES . . . . .	viii
11	CHAPTER 1      DARK MATTER IN THE COSMOS . . . . .	1
12	1.1 Introduction . . . . .	1
13	1.2 Dark Matter Basics . . . . .	2
14	1.3 Evidence for Dark Matter . . . . .	3
15	1.4 Searching for Dark Matter: Particle DM . . . . .	10
16	1.5 Sources for Indirect Dark Matter Searches . . . . .	15
17	1.6 Multi-Messenger Dark Matter . . . . .	17
18	CHAPTER 2      HIGH ALTITUDE WATER CHERENKOV (HAWC) OBSERVATORY . . . . .	20
19	2.1 The Detector . . . . .	20
20	2.2 Event Reconstruction . . . . .	25
21	2.3 Background Estimation: Direct Integration . . . . .	33
22	CHAPTER 3      GLORY DUCK: MULTI-WAVELENGTH SEARCH FOR DARK MATTER ANNIHILATION TOWARDS DWARF SPHEROIDAL GALAXIES . . . . .	35
25	3.1 Introduction . . . . .	35
26	3.2 Dataset and Background . . . . .	37
27	3.3 Analysis . . . . .	39
28	3.4 Likelihood Methods . . . . .	43
29	3.5 HAWC Results . . . . .	50
30	3.6 Glory Duck Combined Results . . . . .	52
31	3.7 HAWC Systematics . . . . .	57
32	3.8 <i>J</i> -factor distributions . . . . .	59
33	3.9 Discussion and Conclusions . . . . .	65
34	CHAPTER 4      MULTITHREADING HAWC ANALYSES FOR DARK MATTER SEARCHES . . . . .	69
36	4.1 Introduction . . . . .	69
37	4.2 Dataset and Background . . . . .	69
38	4.3 Analysis . . . . .	71
39	4.4 Likelihood Methods . . . . .	75
40	4.5 Computational Methods: Multithreading . . . . .	75
41	4.6 Analysis Results . . . . .	81
42	4.7 Systematics . . . . .	86
43	4.8 Conclusion and Discussion . . . . .	86
44	CHAPTER 5      ICECUBE NEUTRINO OBSERVATORY . . . . .	88
45	5.1 The Detector . . . . .	89
46	5.2 Event Reconstruction . . . . .	93

47	5.3 Background . . . . .	99
48	CHAPTER 6 HEAVY DARK MATTER ANNIHILATION SEARCH WITH ICE-	
49	CUBE'S NORTH SKY TRACK DATA . . . . .	101
50	6.1 Introduction . . . . .	101
51	6.2 Dataset and Background . . . . .	101
52	6.3 Analysis . . . . .	103
53	6.4 Likelihood Methods . . . . .	112
54	6.5 Background Simulation . . . . .	112
55	6.6 Signal Recovery . . . . .	130
56	6.7 Systematics . . . . .	133
57	6.8 Conclusions . . . . .	136
58	CHAPTER 7 NU DUCK: CONCLUSIONS AND FUTURE DIRECTIONS . . . . .	138
59	7.1 Conclusions . . . . .	138
60	7.2 Future Directions: Multi-Messenger Dark Matter Search . . . . .	139
61	APPENDIX A MULTI-EXPERIMENT SUPPLEMENTARY FIGURES . . . . .	141
62	APPENDIX B MULTITHREADING DARK MATTER ANALYSES SUPPLEMEN-	
63	TARY MATERIAL . . . . .	142
64	B.1 Remaining Spectral Models . . . . .	142
65	B.2 <code>mpu_analysis.py</code> . . . . .	143
66	B.3 Comparison with Glory Duck . . . . .	152
67	APPENDIX C ICECUBE HEAVY DARK MATTER ANALYSIS SUPPLEMEN-	
68	TARY MATERIAL . . . . .	155
69	C.1 Docker Image for Oscillating Neutrino Spectra . . . . .	155
70	C.2 Spline Fitting Statuses . . . . .	158
71	C.3 Neutrino Composite Spectra . . . . .	159
72	C.4 Segue 1 And Ursa Major II Signal Recovery . . . . .	160
73	C.5 $n_s$ Sensitivities . . . . .	166
74	BIBLIOGRAPHY . . . . .	168

## LIST OF TABLES

<p>76    Table 2.1    Definitions of <math>f_{\text{hit}}</math> energy estimator bins. Bins are defined by the fraction of 77    available PMTs that are triggered during an air shower event. The angular 78    resolution, <math>\Theta_{68}</math>, is the bin containing 68% of events [34]. . . . .</p> <p>79    Table 3.1    Summary of the relevant properties of the dSphs used in the present work. 80    Column 1 lists the dSphs. Columns 2 and 3 present their heliocentric distance 81    and galactic coordinates, respectively. Columns 4 and 5 report the <math>J</math>-factors of 82    each source given from the <math>\mathcal{GS}</math> and <math>\mathcal{B}</math> independent studies and their estimated 83    <math>\pm 1\sigma</math> uncertainties. The values <math>\log_{10} J</math> (<math>\mathcal{GS}</math> set) [59] correspond to the mean 84    <math>J</math>-factor values for a source extension truncated at the outermost observed star. 85    The values <math>\log_{10} J</math> (<math>\mathcal{B}</math> set) [63] are provided for a source extension at the tidal 86    radius of each dSph. <b>Bolded sources are within HAWC's field of view and</b> 87    <b>provided to the Glory Duck analysis.</b> . . . . .</p> <p>88    Table 3.2    Summary of dSph observations by each experiment used in this work. A 89    ‘-’ indicates the experiment did not observe the dSph for this study. For 90    Fermi-LAT, the exposure at 1 GeV is given. For HAWC, <math> \Delta\theta </math> is the absolute 91    difference between the source declination and HAWC latitude. HAWC is more 92    sensitive to sources with smaller <math> \Delta\theta </math>. For IACTs, we show the zenith angle 93    range, the total exposure, the energy range, the angular radius <math>\theta</math> of the signal or 94    ON region, the ratio of exposures between the background-control (OFF) and 95    signal (ON) regions (<math>\tau</math>), and the significance of gamma-ray excess in standard 96    deviations, <math>\sigma</math>. . . . .</p> <p>97    Table 4.1    Summary of the relevant properties of the dSphs used in the present work. 98    Column 1 lists the dSphs. Columns 2 and 3 present their heliocentric distance 99    and galactic coordinates, respectively. Column 4 reports the <math>J</math>-factors of each 100   source given from the <math>\mathcal{LS}</math> studies and estimated <math>\pm 1\sigma</math> uncertainties. The 101   values <math>\log_{10} J</math> (<math>\mathcal{LS}</math> set) [80] correspond to the mean <math>J</math>-factor values for a 102   source extension truncated at <math>0.5^\circ</math>. . . . .</p> <p>103   Table 4.2    Timing summaries for analyses for serial and multithreaded processes. <math>M</math> 104   tasks is the number of functional-parallel tasks ran for the computation. <math>T_{p,c}</math> 105   is a single run time in hours:minutes:seconds for runs utilizing <math>p</math> nodes and 106   <math>c</math> threads. Runs are run interactively on the same computer to maximize 107   consistency. Empty entries are indicated with ‘-’. (·) entries are estimated 108   entries extrapolated from data earlier in the column. . . . .</p> <p>109   Table 4.3    Speed up summaries for analyses for serial and multithreaded processes. <math>M</math> 110   tasks is the number of functional-parallel tasks ran for the computation. <math>S_{p,c}</math> 111   is a single speedup comparison for runs utilizing <math>p</math> nodes and <math>c</math> threads. [·] 112   are the estimated speedups calculated from Tab. 4.2, Eq. (4.7), and Eq. (4.4). 113   Empty entries are indicated with ‘-’. . . . .</p>	<p>29</p> <p>44</p> <p>45</p> <p>75</p> <p>79</p> <p>81</p>
--	---

114	Table 6.1 Spline err tolerances used for input in particle physics component to Eq. (3.1).	
115	Column 1 is the DM annihilation channel being fit. Columns 2, 3, and 4	
116	are the tolerances for "GOOD" (pass), "OK" requires inspection, and "FAIL"	
117	(tune and refit) respectively. Column 5 has the X ranges over which the error	
118	is evaluated. MAX/MIN [.,.] takes the maximum or minimum of the two	
119	enclosed values. . . . .	109

## LIST OF FIGURES

121	Figure 1.1	Rotation curve fit to NGC 6503 from [7]. Dashed line is the contribution from visible matter. Dotted curves are from gas. Dash-dot curves are from dark matter (DM). Solid line is the composite contribution from all matter and DM sources. Data are indicated with bold dots with error bars. Data agree strongly with a matter + DM composite prediction. . . . .	4
126	Figure 1.2	Light from distant galaxy is bent in unique ways depending on the distribution of mass between the galaxy and Earth. Yellow dashed lines indicate where the light would have gone if the matter were not present [8]. . . . .	6
129	Figure 1.3	(left) Optical image of galactic cluster 1E0657-558. (right) X-ray image of the cluster with redder meaning hotter and higher baryon density. (both) Green contours are reconstruction of gravity contours from weak lensing. White rings are the best fit mass maxima at 68.3%, 95.5%, and 99.7% confidence. The matter maxima of the clusters are clearly separated from x-ray maxima. [9]	7
134	Figure 1.4	Plank CMB sky. Sky map features small variations in temperature in primordial light. These anisotropies are used to make inferences about the universe's energy budget and developmental history. [10] . . . . .	8
137	Figure 1.5	Observed Cosmic Microwave Background power spectrum as a function of multipole moment from Plank [10]. Blue line is best fit model from $\Lambda$ CDM. Red points and lines are data and error, respectively. . . . .	9
140	Figure 1.6	Predicted power spectra of CMB for different $\Omega_m h^2$ values for fixed baryon density from [11]. (left) Low $\Omega_m h^2$ increases the prominence of first and second peaks. (middle) $\Omega_m h^2$ is most similar to the observed power spectrum. The second and third peaks are similar in height. (right) $\Omega_m h^2$ is large which suppresses the first peak and raises the prominence of the third peak. . . . .	9
145	Figure 1.7	The Standard Model (SM) of particle physics. Figure taken from <a href="http://www.quantumdiaries.org/2014/03/14/the-standard-model-a-beautiful-but-flawed-theory/">http://www.quantumdiaries.org/2014/03/14/the-standard-model-a-beautiful-but-flawed-theory/</a> . . . . .	11
148	Figure 1.8	Simplified Feynman diagram demonstrating with different ways DM can interact with SM particles. The 'X's refer to the DM particles whereas the SM refer to fundamental particles in the SM. The large circle in the center indicates the vertex of interaction and is purposely left vague. The colored arrows refer to different directions of time as well as their respective labels. The arrows indicate the initial and final state of the DM -SM interaction in time.	12

154	Figure 1.9 A single jet event in ATLAS detector from 2017 [16]. Jet momentum was 155 observed to be 1.9 TeV. Missing transverse momentum was observed to be 156 1.9 TeV compared to the initial transverse momentum of the event was 0. 157 Implied MET is traced by a red dashed line in event display. . . . .	13
158	Figure 1.10 More detailed pseudo-Feynman diagram of particle cascade from dark matter 159 annihilation into 2 quarks. The quarks hadronize and down to stable particles 160 like $\gamma$ or the anti-proton ( $p^-$ ). Diagram pulled from ICRC 2021 presentation 161 on DM annihilation search [17]. . . . .	14
162	Figure 1.11 Dark Matter (DM) decay spectrum for $b\bar{b}$ initial state and $\gamma$ final state. Redder 163 spectra are for larger DM masses. Bluer spectra are light DM masses. $x$ is a 164 unitless factor defined as the ratio of the mass of DM, $m_\chi$ , and the final state 165 particle energy $E_\gamma$ . Figure from [19]. . . . .	16
166	Figure 1.12 Different dark matter density profiles compared. Some models produce ex- 167 ceptionally large densities at small r [20]. . . . .	17
168	Figure 1.13 The Milky Way Galaxy in photons ( $\gamma$ ) and neutrinos ( $\nu$ ) [22]. The Galactic 169 center is at $l=0^\circ$ and is the brightest region in all panels. (top) An Optical 170 color image of the Milky Way galaxy seen from Earth. Clouds of gas and dust 171 obscure some light from stars. (2nd down) Integrated flux of $\gamma$ -rays observed 172 by the Fermi-LAT telescope [23]. (middle) Expected neutrino emission 173 that corresponds with Fermi-LAT observations. (2nd up) Expected neutrino 174 emission profile after considering detector systematics of IceCube. (bottom) 175 Observed neutrino emission from region of the galactic plane. Substantial 176 neutrino emission was detected. . . . .	18
177	Figure 1.14 Dark Matter annihilation spectra for different final state particle and standard 178 model annihilation channels [24]. Photons (red), $e^\pm$ (green), $\bar{p}$ (blue), $\nu$ (black). . . . .	19
179	Figure 2.1 Photo of the HAWC detector that I took on May 17, 2023. Main array is 180 centered in the photo and comprised of the larger tanks. Outriggers are the 181 smaller tanks around the main array. . . . .	20
182	Figure 2.2 A particle physics illustration of high energy particle showers. Left shower is 183 an electromagnetic shower from a high energy gamma-ray. Most particles in 184 the shower will be a combination of photons and charged leptons, in this case 185 electrons (e). Right figure shows a cosmic ray particle shower. The cosmic 186 ray will produce many more types of particles including pions ( $\pi$ ), neutrinos, 187 and charged leptons. Figure pulled from [26]. . . . .	21
188	Figure 2.3 The WCDs. Left image features several WCDs looking from within the main 189 array of HAWC. Right image shows a schematic of a WCD pulled from [25]. . . . .	22

190	Figure 2.4	Overview of HAWC control and data electronics. The LoToT and HiToT threshold signals are discussed in Section 2.1.2. Figure from [27] . . . . .	23
192	Figure 2.5	Schematic of data flow in HAWC data acquisition and online processing system. Pulled from [29]. . . . .	24
194	Figure 2.6	How HAWC FEB intially processes analog PMT signals. Signals are split through an amplifier and discriminator circuit. Each path is designated for ei- ther the HIGH or LOW threshold for the signal. The 2-edge event corresponds to LOW, while the 4 edge corresponds to HIGH. . . . .	24
198	Figure 2.7	An particle shower incident on WCDs. Secondary particles of an air shower travel in a cone centered on primary incident particle. Reconstruction of the initial angle is possible with arrival time of hits in PMTs inside WCDs. Figure from [33]. . . . .	26
202	Figure 2.8	Charge deposition in each PMT for a reconstructed gamma-ray event. WCDs are outlined in black surrounding the 4 smaller circles that represent PMTs. The color scale indicates the charge deposition in each PMT. The best shower core fit from SFCF is noted with a red star in the center of the dashed circle [34].	27
206	Figure 2.9	Simulated normalized energy distribution of each $f_{\text{hit}}$ bin defined in Tab. 2.1. Monte Carlo simulation of gamma-rays with $E^{-2.63}$ spectral shape and sim- ulated source at 20° declination. Figure from [34]. . . . .	29
209	Figure 2.10	Neural Network energy estimator performance compared to true energy. The dotted line is the identity line where the estimator and injection agree. Gam- ma/hadron separation cuts were applied with the energy estimation. Figure pulled from [37] . . . . .	31
213	Figure 2.11	Lateral distribution functions (LDFs) for cosmic ray (left) and a photon can- didate from the Crab Nebula (right). Cosmic ray LDF has clearly isolated hits far from the reconstructed shower core. Gamma-ray shower shows a more cuspy event [34]. . . . .	32

217	Figure 3.1	Sensitivities of five gamma-ray experiments compared to percentages of the Crab nebula's emission and dark matter annihilation. Solid lines present estimated sensitivities to power law spectra [FACT CHECK THIS]for each experiment. Green lines are Fermi-LAT sensitivities where lighter green is the sensitivity to the galactic center and dark green is its sensitivity to higher declinations. Orange, red, and purple solid lines represent the MAGIC, HESS, and VERITAS 50 hour sensitivities respectively. The maroon and brown lines are the HAWC 1 year and 5 year sensitivities. Across four decades of gamma-ray energy, these experiments have similar sensitivities on the order $10^{-12}$ erg cm $^{-2}$ s $^{-1}$ . The dotted lines are estimated dark matter fluxes assuming $m_\chi = 5$ TeV DM annihilating to bottom quarks (red), tau leptons (blue), and W bosons (green). Faded gray lines outline percentage flux of the Crab nebula. Figure is an augmented version of [40] . . . . .	36
230	Figure 3.2	Effect of Electroweak (EW) corrections on expected DM annihilation spectrum for $\chi\chi \rightarrow W^-W^+$ . Solid lines are spectral models that consider EW corrections. Dash-dot lines are spectral models without EW corrections. Red lines are models for $M_\chi = 1$ TeV. Blue lines represent models for $M_\chi = 100$ TeV. All models are sourced from the PPPC4DMID [58]. . . . .	40
235	Figure 3.3	$\frac{dJ}{d\Omega}$ maps for Segue1 (top) and Coma Berenices (bottom). Origin is centered on the specific dwarf spheroidal galaxies (dSph). X and Y axes are the angular separation from the center of the dwarf. Profile is truncated at the scale radius. Plots of the remaining 11 dSph HAWC studied are linked in Fig. A.1. . . . .	42
239	Figure 3.4	Illustration of the combination technique showing a comparison between $-2 \ln \lambda$ provided by four instruments (colored lines) from the observation of the same dSph without any $J$ nuisance and their sum, <i>i.e.</i> the resulting combined likelihood (thin black line). According to the test statistics of Equation (3.7), the intersection of the likelihood profiles with the line $-2 \ln \lambda = 2.71$ indicates the 95% C.L. upper limit on $\langle \sigma v \rangle$ . The combined likelihood (thin black line) shows a smaller value of upper limit on $\langle \sigma v \rangle$ than those derived by individual instruments. We also show how the uncertainties on the $J$ factor effects the combined likelihood and degrade the upper limit on $\langle \sigma v \rangle$ (thick black line). All likelihood profiles are normalized so that the global minimum $\widehat{\langle \sigma v \rangle}$ is 0. We note that each profile depends on the observational conditions in which a target object was observed. The sensitivity of a given instrument can be degraded and the upper limits less constraining if the observations are performed in non-optimal conditions such as a high zenith angle or a short exposure time. . . . .	48
254	Figure 3.5	. . . . .	51

255	Figure 3.6 HAWC TS values for best fit $\langle\sigma v\rangle$ versus $m_\chi$ for seven SM annihilation channels with $J$ factors from $\mathcal{GS}$ . The solid black line shows the combined best fit TS values. The colored, dashed lines are the TS values for each of the 13 sources HAWC studied.	52
259	Figure 3.7 HAWC Brazil bands at 95% confidence level on $\langle\sigma v\rangle$ versus DM mass for seven annihilation channels with $J$ -factors from $\mathcal{GS}$ [69]. The solid line represents the combined limit from 13 dSphs. The dashed line is the expected limit. The green band is the 68% containment. The yellow band is the 95% containment.	53
264	Figure 3.8 Upper limits at 95% confidence level on $\langle\sigma v\rangle$ in function of the DM mass for eight annihilation channels, using the set of $J$ factors from Ref. [69] ( $\mathcal{GS}$ set in Table 3.1). The black solid line represents the observed combined limit, the black dashed line is the median of the null hypothesis corresponding to the expected limit, while the green and yellow bands show the 68% and 95% containment bands. Combined upper limits for each individual detector are also indicated as solid, colored lines. The value of the thermal relic cross-section in function of the DM mass is given as the red dotted-dashed line [70].	54
273	Figure 3.9 Same as Fig. 3.8, using the set of $J$ factors from Ref. [63, 71] ( $\mathcal{B}$ set in Table 3.1).	55
274	Figure 3.10 Comparisons of the combined limits at 95% confidence level for each of the eight annihilation channels when using the $J$ factors from Ref. [69] ( $\mathcal{GS}$ set in Table 3.1), plain lines, and the $J$ factor from Ref. [63, 71] ( $\mathcal{B}$ set in Table 3.1), dashed lines. The cross-section given by the thermal relic is also indicated [70].	57
278	Figure 3.11 Comparisons of the combined limits at 95% confidence level for a point source analysis and extended source using [69] $\mathcal{GS}$ J-factor distributions and PPPC [58] annihilation spectra. Shown are the limits for Segue1 which will have the most significant impact on the combined limit. 6 of the 7 DM annihilation channels are shown. Solid lines are extended source studies. Dashed lines are point source studies. Overall, the extended source analysis improves the limit by a factor of 2.	59
285	Figure 3.12 Same as Fig. 3.11 on Coma Berenices. This dSph also contributes significantly to the limit. The limits are identical in this case.	60
287	Figure 3.13 Comparison of combined limits when correcting for HAWC's pointing systematic. All DM annihilation channels are shown. The solid black line is the ratio between published limit to the declination corrected limit. The blue solid line or "Combined_og" represented the limits computed for Glory Duck. The solid orange line or "Combined_ad" represented the limits computed after correcting for the pointing systematic.	61

293	Figure 3.14 Differential map of $dJ/\Omega$ from model built in Section 3.8.1 and profiles provided directly from authors. (Top) Differential from Segue1. (bottom) Differential from Coma Berenices. Note that their scales are not the same. Segue1 shows the deepest discrepancies which is congruent with its large uncertainties. Both models show anuli where unique models become apparent.	62
298	Figure 3.15 HAWC limits for Coma Berenices (top) and Segue1 (bottom) for two different map sets. Blue lines are limits calculated on maps with poor model representation. Orange lines are limits calculated on spatial profiles provided by the authors of [59]. Black line is the ratio of the poor spatial model limits to the corrected spatial models. The left y-axis measures $\langle\sigma v\rangle$ for the blue and orange lines. The right y-axis measures the ratio and is unitless.	63
304	Figure 3.16 Comparisons between the $J$ -factors versus the angular radius for the computation of $J$ factors from Ref. [69] ( $\mathcal{GS}$ set in Table 3.1) in blue and for the computation from Ref. [63, 71] ( $\mathcal{B}$ set in Tab. 3.1) in orange. The solid lines represent the central value of the $J$ -factors while the shaded regions correspond to the $1\sigma$ standard deviation.	65
309	Figure 3.17 Comparisons between the $J$ -factors versus the angular radius for the computation of $J$ factors from Ref. [69] ( $\mathcal{GS}$ set in Tab. 3.1) in blue and for the computation from Ref. [63, 71] ( $\mathcal{B}$ set in Tab. 3.1) in orange. The solid lines represent the central value of the $J$ -factors while the shaded regions correspond to the $1\sigma$ standard deviation.	66
314	Figure 4.1 Spectral hypotheses from PPPC [58] and HDM [79] for DM annihilation: $\chi\chi \rightarrow W^-W^+$ . Solid lines are spectral models with EW corrections from the PPPC. Dash-dot lines are spectral models from HDM. Red lines are models for $M_\chi = 1$ TeV. Blue lines represent models for $M_\chi = 100$ TeV.	71
318	Figure 4.2 Photon spectra for $\chi\chi \rightarrow \gamma\gamma$ (left) and $\chi\chi \rightarrow ZZ$ (right) after Gaussian convolution of line features. Both spectra have $\delta$ -features at photon energies equal to the DM mass. Bluer lines are annihilation spectra with lower DM mass. Redder lines are spectra from larger DM mass. All spectral models are sourced from the Heavy Dark Matter models [79]. Axes are drawn roughly according to the energy sensitivity of HAWC.	72
324	Figure 4.3 $\frac{dJ}{d\Omega}$ maps for Coma Berenices, Draco, Segue1, and Sextans. Columns are divided for the $\pm 1\sigma$ uncertainties in $dJ/d\Omega$ around the mean value from $\mathcal{LS}$ [80]. Origin is centered on the specific dwarf spheroidal galaxies (dSph). $\theta$ and $\phi$ axes are the angular separation from the center of the dwarf. Profiles are truncated at $1^\circ$ and flattened beyond.	74

329	Figure 4.4	Infographic on how jobs and DM computation was organized in Section 3.3. Jobs were built for each permutation of CHANS and SOURCES shown by the left block in the figure. Each job, which took on the order 2 hrs to compute, had the following work flow: 1. Import HAWC analysis software, 2 min to run. 2. Load HAWC count maps, 5 min to run. 3. Load HAWC energy and spatial resolutions, 4 min. 5. Load DM spatial source templates and spectral models, less than 1 s. 6. Perform likelihood fit on data and model, about 8 min per DM mass. 7. Write results to file, less than 1s. . . . .	76
337	Figure 4.5	Graphic of Gustafson parallel coding pattern. $f_s$ is the fraction of a program, in time, spent on serial computation. $f_p$ is the fraction of computing time that is parallelizable. $T_p$ is the total time for a parallel program to run. $T_1$ is the total time for a parallel program to run if only 1 processor is allocated. $P_N$ is the $N$ -th processor where it's row is the computation the processor performs. The Gustafson pattern is most similar to what is implemented for this analysis. Figure is pulled from [82]. . . . .	77
344	Figure 4.6	Task chart for one multithreaded job developed for this project. Green blocks indicate a shared resource across the threads AND computation performed serially. Red blocks indicate functional parallel processing within each thread. 3 threads are represented here, yet many more can be employed during the full analysis. Jobs are defined by the SOURCE as these require unique maps to be loaded into the likelihood estimator. The $m_\chi$ , CHAN, and $\langle\sigma v\rangle$ variables are entered into the thread pool and allocated as evenly as possible across the threads. . . . .	79
352	Figure 4.7	HAWC upper limits at 95% confidence level on $\langle\sigma v\rangle$ versus $m_\chi$ for $\chi\chi \rightarrow b\bar{b}$ , $t\bar{t}$ , $u\bar{u}$ , $d\bar{d}$ , $s\bar{s}$ , $c\bar{c}$ , $gg$ , $W^+W^-$ , and $hh$ . Limits are with $\mathcal{LS}$ $J$ -factors [80]. The solid line represents the observed combined limit. Dashed lines represent limits from individual dSphs. . . . .	82
356	Figure 4.8	HAWC upper limits at 95% confidence level on $\langle\sigma v\rangle$ versus $m_\chi$ for $\chi\chi \rightarrow \nu_e \bar{\nu}_e$ , $\nu_\mu \bar{\nu}_\mu$ , $\nu_\tau \bar{\nu}_\tau$ , $e\bar{e}$ , $\mu\bar{\mu}$ , $\tau\bar{\tau}$ , $\gamma\gamma$ and $ZZ$ . Limits use $\mathcal{LS}$ $J$ -factors [80]. The solid line represents the observed combined limit. Dashed lines represent limits from individual dSphs. . . . .	83
360	Figure 4.9	HAWC TS values for best fit $\langle\sigma v\rangle$ versus $m_\chi$ for SM annihilation channels: $\chi\chi \rightarrow b\bar{b}$ , $t\bar{t}$ , $u\bar{u}$ , $d\bar{d}$ , $s\bar{s}$ , $c\bar{c}$ , $gg$ , $W^+W^-$ , and $hh$ . Limits use $\mathcal{LS}$ $J$ -factors. The solid black line shows the combined best fit TS values. The colored, dashed lines are the TS values from each dSph. . . . .	84
364	Figure 4.10	HAWC TS values for best fit $\langle\sigma v\rangle$ versus $m_\chi$ for SM annihilation channels: $\chi\chi \rightarrow \nu_e \bar{\nu}_e$ , $\nu_\mu \bar{\nu}_\mu$ , $\nu_\tau \bar{\nu}_\tau$ , $e\bar{e}$ , $\mu\bar{\mu}$ , $\tau\bar{\tau}$ , $\gamma\gamma$ and $ZZ$ . Limits use $\mathcal{LS}$ $J$ -factors. The solid black line shows the combined best fit TS values. The colored, dashed lines are the TS values from each dSph. . . . .	85

368	Figure 4.11 Comparison of HAWC limits from this analysis to Glory Duck (Fig. 3.5) for 3 dSphs and 3 DM annihilation channels: $b\bar{b}$ , $\tau\bar{\tau}$ , and $e\bar{e}$ . Each sector shows the 95% confidence limit from Glory Duck (blue line) and this analysis (orange line) in the top plot. The lower plot features the ratio in log scale of Glory Duck to this analysis in a red solid line. Horizontal dashed lines are for ratios of 1.0 (black) and $\sqrt{2}$ (blue). Ratios larger than 1.0 are for limits smaller, or stricter, than Glory Duck. Ratios larger than $\sqrt{2}$ indicates limits are stricter than a simple doubling of the Glory Duck data. . . . .	87
376	Figure 5.1 IceCube Neutrino observatory and science center at the South Pole. Detector volume is beneath glacial ice. Image from [83]. . . . .	88
378	Figure 5.2 IceCube Laboratory (ICL) that houses the data acquisition systems. Picture from [83]. . . . .	89
380	Figure 5.3 Composition of the Digital Optical Module (DOM). Left image is an illustration of the mechanical layout. Right is a flow chart of functional connections. Figure from [84] . . . . .	90
383	Figure 5.4 Graphic of the full IceCube Neutrino Observatory. In-ice array is made up of 86 strings with a total of 5160 optical sensors. Deepcore is a denser arrangement of optical sensors for sensitivity to lower energy neutrinos. Figure from [83]. . . . .	91
387	Figure 5.5 Data flow chart PMT waveforms from the DOMs. "Hit Records" are sent to the surface DAQ computers in ICL. Full waveform data, represented with dashed arrows, are included when neighboring DOMs are hit in coincidence above the SPE discriminator threshold. . . . .	92
391	Figure 5.6 Feynman diagrams for W (a/b) and Z (c/d) boson mediated interactions between neutrinos and light quarks. Charged current (CC) interactions are shown in panels a and b. Neutral current (NC) interactions are shown in panels c and d. NC interactions occur between neutrinos and quarks within atomic nuclei in the ice. CC interactions will exchange W bosons and produce a lepton corresponding to the neutrino flavor and a hadronic cascade. NC interactions will exchange a Z boson produce a hadronic cascades. Figure from [85]. . . . .	94
399	Figure 5.7 Event topologies for high energy NC and CC neutrino interactions with ice. Signatures can be split as either: hadronic and electromagnetic cascades; Cherenkov radiation from a single long ranging particle. Cascade from the $\tau$ decay will depend on its decay products. For energies below 1 PeV the double bang of the $\nu_\tau$ signature overlap and are indistinguishable. Figure from [86]. . . . .	95

404	Figure 5.8	A simulation of a track-like event in IceCube. Redder bubbles indicate earlier 405 photon arrival times. Greener bubbles occur later. The size of the DOM 406 bubble illustrate the charge deposition in the DOM. For this event, the CC 407 neutrino interaction occurred by the red hits. There is then a long muon track 408 going to the left. Figure taken from [87]. . . . .	96
409	Figure 5.9	Same as Fig. 5.8 but for a cascade-like event. Figure taken from [87]. . . . .	97
410	Figure 5.10	Same as Fig. 5.8 but for a double-bang event. Two distinct cascades are 411 visible if the initial neutrino is very high energy. Figure taken from [87]. . . . .	97
412	Figure 6.1	Neutrino spectra at production (left panels) and after oscillation at Earth 413 (right panels). Blue, orange, and green lines are the $\nu_e$ , $\nu_\mu$ , and $\nu_\tau$ spectra 414 respectively. Top panels show the spectra in $\frac{dN}{dE}$ . Lower panels plot the flavor 415 ratio to $\nu_e + \nu_\mu + \nu_\tau$ . SM annihilation channels $b\bar{b}$ , $\tau\bar{\tau}$ , and $\nu_\mu\bar{\nu}_\mu$ are shown 416 for $M_\chi = 1$ PeV, TeV, and EeV. . . . .	105
417	Figure 6.2	Signal recovery for 100 TeV DM annihilation into $\nu_\mu\bar{\nu}_\mu$ for a source at Dec 418 = $16.06^\circ$ . $n_{\text{inj}}$ is the number of injected signal events in simulation. $n_s$ is the 419 number of reconstructed signal events from the simulation data. Although 420 the uncertainties are small and tight, the reconstructed $n_s$ are systematically 421 underestimated. . . . .	106
422	Figure 6.3	Left panel shows the two kernels overlaying the original spectrum from 423 $\chi$ aronv after propagation to Earth [95]. The vertical red line indicates where 424 the original neutrino line is maximized. Blue line is the output from $\chi$ aronv. 425 Green line is the spectrum after convolution with a flat kernel. Orange line 426 is the spectrum after Gaussian convolution. Right panel shows the signal 427 recovery of the spectral model using the Gaussian kernel with parameters 428 enumerated above. . . . .	107
429	Figure 6.4	Example spline that failed the fit. Failed splined are corrected on a case by 430 case basis unless the SM channel has a systematic problem fitting the splines. 431 In this case, I made a bookkeeping error and loaded the incorrect spectral model	109
432	Figure 6.5	Summary of input spectral models that were smoothed with Gaussian kernels. 433 Spectral models are for $\chi\chi \rightarrow e\bar{e}$ , $\mu\bar{\mu}$ , $\tau\bar{\tau}$ , $\nu_e\bar{\nu}_e$ , $\nu_\mu\bar{\nu}_\mu$ , and $\nu_\tau\bar{\nu}_\tau$ . These spectra 434 are the composite ( $\nu_\mu + \nu_\tau$ ) of neutrino flavors. Every spectral model used 435 for this analysis is featured as a colored solid line. Bluer lines are for low 436 $m_\chi$ models. $m_\chi$ ranges from 681 GeV to 100 PeV. HDM [79], $\chi$ aronv [95], 437 and Photospline [99] are used to generate these spectra. Energy (x-axis) was 438 chosen to roughly represent the energy sensitivity of NST. . . . .	110

439	Figure 6.6 Test statistic (TS) distributions for Segue 1 and $\chi\chi \rightarrow b\bar{b}$ . Each subplot, 440 except the final, is the TS distribution for a specific DM mass listed in the 441 subplot. Orange dashed lines are the traces for a $\chi^2$ distribution with 1 degree 442 of freedom. $\epsilon[\cdot]$ is the fraction of trials smaller than the bracketed value. The 443 final subplot features the all DM spectral models, similar to Fig. 6.5, used as 444 input for the TS distributions. . . . .	113
445	Figure 6.7 Same as Fig. 6.6 for Segue 1 $\chi\chi \rightarrow \tau\bar{\tau}$ . . . . .	114
446	Figure 6.8 Same as Fig. 6.6 for Segue 1 $\chi\chi \rightarrow \nu_\mu\bar{\nu}_\mu$ . . . . .	115
447	Figure 6.9 Same as Fig. 6.6 for Ursa Major II 1 $\chi\chi \rightarrow b\bar{b}$ . . . . .	116
448	Figure 6.10 Same as Fig. 6.6 for Ursa Major II 1 $\chi\chi \rightarrow \tau\bar{\tau}$ . . . . .	117
449	Figure 6.11 Same as Fig. 6.6 for Ursa Major II 1 $\chi\chi \rightarrow \nu_\mu\bar{\nu}_\mu$ . . . . .	118
450	Figure 6.12 Same as Fig. 6.6 for 15, GS $J$ -factor, stacked sources and $\chi\chi \rightarrow b\bar{b}$ . . . . .	119
451	Figure 6.13 Same as Fig. 6.6 for 15, GS $J$ -factor, stacked sources and $\chi\chi \rightarrow t\bar{t}$ . . . . .	120
452	Figure 6.14 Same as Fig. 6.6 for 15, GS $J$ -factor, stacked sources and $\chi\chi \rightarrow u\bar{u}$ . . . . .	121
453	Figure 6.15 Same as Fig. 6.6 for 15, GS $J$ -factor, stacked sources and $\chi\chi \rightarrow d\bar{d}$ . . . . .	122
454	Figure 6.16 Same as Fig. 6.6 for 15, GS $J$ -factor, stacked sources and $\chi\chi \rightarrow e\bar{e}$ . . . . .	123
455	Figure 6.17 Same as Fig. 6.6 for 15, GS $J$ -factor, stacked sources and $\chi\chi \rightarrow \mu\bar{\mu}$ . . . . .	124
456	Figure 6.18 Same as Fig. 6.6 for 15, GS $J$ -factor, stacked sources and $\chi\chi \rightarrow \tau\bar{\tau}$ . . . . .	125
457	Figure 6.19 Same as Fig. 6.6 for 15, GS $J$ -factor, stacked sources and $\chi\chi \rightarrow W^+W^-$ . . . . .	126
458	Figure 6.20 Same as Fig. 6.6 for 15, GS $J$ -factor, stacked sources and $\chi\chi \rightarrow ZZ$ . . . . .	127
459	Figure 6.21 Same as Fig. 6.6 for 15, GS $J$ -factor, stacked sources and $\chi\chi \rightarrow \nu_e\bar{\nu}_e$ . . . . .	128
460	Figure 6.22 Same as Fig. 6.6 for 15, GS $J$ -factor, stacked sources and $\chi\chi \rightarrow \nu_\mu\bar{\nu}_\mu$ . . . . .	129

461	Figure 6.23 Signal Recovery study for an analysis with 15 stacked sources using the $\mathcal{GS}$	131
462	$J$ -factors [59]. Above shows 14 studies for DM mass ranging between 1	
463	TeV and 20 PeV for $\chi\chi \rightarrow \mu_\mu\overline{\mu_\mu}$ . The bottom right subplot features every	
464	spectral model used as input for the remaining subplots. The remaining	
465	subplots show $n_{\text{inj}}$ as the number of signal events injected into background	
466	simulation. Whereas, $n_s$ is the number of signal events recovered from	
467	analyzing the injected simulation. Blue line represents the median values of	
468	100 simulations. Light blue bands show the $1\sigma$ statistical uncertainty around	
469	the median. . . . .	
470	Figure 6.24 Same as Fig. 6.23 but for $\chi\chi \rightarrow t\bar{t}$ (top) and $b\bar{b}$ (bottom). . . . .	132
471	Figure 6.25 IceCube North Sky Track Sensitivities. Each panel shows sensitivity curves	
472	for various DM annihilation channels. Sensitivities are for the velocity-	
473	weighted cross-section $\langle\sigma v\rangle$ versus $m_\chi$ . Dotted, colored lines are sensitivities	
474	for individual sources. Solid white lines are for the combined sensitivity of	
475	all 15 $\mathcal{GS}$ sources used in this study. . . . .	134
476	Figure 6.26 Same as Fig. 6.25 for three additional DM annihilation channels. . . . .	135
477	Figure 6.27 Panel A: Neutrino's from the Northern sky and incident on the IceCube	
478	detector will travel through the Earth. How much of the Earth these neutrinos	
479	travels is a function of zenith from the vertical axis. Panel B: SM prediction of	
480	neutrino transmission probabilities for neutrinos arriving at $90^\circ - 180^\circ$ zenith	
481	and with 100 GeV to 100 PeV energies. High-energy neutrinos traversing	
482	the whole Earth are completely absorbed, whereas low-energy neutrinos pass	
483	through unimpeded. Neutrinos coming from above the horizon will arrive	
484	unimpeded for all neutrino energies. Figure pulled from [102]. . . . .	136
485	Figure 6.28 $\langle\sigma v\rangle$ sensitivities for 5 imaginary sources with $\log_{10} J = 19.42 \log_{10}(\text{GeV}^2\text{cm}^{-5})$ .	
486	Each imaginary source shares a declination with a source in Tab. 3.1 . . . . .	137
487	Figure 7.1 The prompt electron neutrino and photon spectrum resulting from the decay	
488	of a 2EeV DM particle to $\nu_e\overline{\nu}_e$ , as currently being searched for at IceCube	
489	[5]. Solid curves represent the results of this work, and predict orders of	
490	magnitude more flux at certain energies than the dashed results of Pythia 8.2,	
491	one of the only existing methods to generate spectra at these masses. In both	
492	cases energy conservation is satisfied: there is a considerable contribution to	
493	a $\delta$ -function at $x = 1$ , associated with events where an initial W or Z was never	
494	emitted and thus no subsequent shower developed. Large disagreements are	
495	generically observed at these masses for electroweak dominated channels,	
496	while the agreement is better for colored initial SM states. . . . .	139
497	Figure 7.2 TODO: neutrino and bb plot with nu Sensitivities[NEEDS A SOURCE][FACT	
498	CHECK THIS] . . . . .	140

499	Figure A.1	Sister figure to Figure 3.3. Sources in the first row from left to right: Bootes I, Canes Venatici I, II. In second row: Draco, Hercules, Leo I. In the first row: Leo II, Leo IV, Sextans. In the final row: Ursa Major I, Ursa Major II. . . . .	141
502	Figure B.1	Sister figure to Figure 4.2 for remaining SM primary annihilation channels studied for this thesis. These did not require any post generation smoothing and so are directly pulled from [79] with a binning scheme most helpful for a HAWC analysis. . . . .	142
506	Figure B.2	Comparison of HAWC limits from this analysis to Glory Duck (Fig. 3.5) for Coma Berenices and 7 DM annihilation channels. . . . .	152
508	Figure B.3	Same as Fig. B.2 but for Segue 1. . . . .	153
509	Figure B.4	Same as Fig. B.2 but for Sextans. . . . .	154
510	Figure C.1	Current status of spline tables according to constraints defined by Tab. 6.1. Green splines are splines that passed under the GOOD tolerance. Yellow are splines that are OK. Red are splines that FAIL. All yellow splines were inspected individually before running the analysis. Splines were made for the $\mu$ (PID 14; top panel) flavor and $\tau$ (PID 16; bottom panel) neutrino flavors. . . . .	158
515	Figure C.2	Sister figure to Fig. 6.5 for annihilation channels that did not require kernel smoothing. These spectra are the composite ( $\nu_\mu + \nu_\tau$ ) of neutrino flavors. Every spectral model used for this analysis is featured as a colored solid line. Bluer lines are for lower DM mass spectral models. DM masses range from 681 GeV to 100 PeV. . . . .	159
520	Figure C.3	Same as Fig. 6.23 but for Segue 1 and $\chi\chi \rightarrow b\bar{b}$ . . . . .	160
521	Figure C.4	Same as Fig. 6.23 but for Segue 1 and $\chi\chi \rightarrow t\bar{t}$ . . . . .	161
522	Figure C.5	Same as Fig. 6.23 but for Segue 1 and $\chi\chi \rightarrow \nu_\mu\bar{\nu}_\mu$ . . . . .	162
523	Figure C.6	Same as Fig. 6.23 but for Ursa Major II and $\chi\chi \rightarrow b\bar{b}$ . . . . .	163
524	Figure C.7	Same as Fig. 6.23 but for Ursa Major II and $\chi\chi \rightarrow t\bar{t}$ . . . . .	164
525	Figure C.8	Same as Fig. 6.23 but for Ursa Major II and $\chi\chi \rightarrow \nu_\mu\bar{\nu}_\mu$ . . . . .	165
526	Figure C.9	IceCube North Sky Track Sensitivities for $n_s/\langle N \rangle$ . $n_s$ values are the counts fed into Eq. (6.8) to produce Fig. 6.26 and Fig. 6.25. . . . .	166
528	Figure C.10	Same as Fig. C.9 for three additional DM annihilation channels. . . . .	167

# CHAPTER 1

529

## DARK MATTER IN THE COSMOS

### 530 1.1 Introduction

531 The dark matter problem can be summarized in part by the following thought experiment.

532 Let us say you are the teacher for an elementary school classroom. You take them on a field  
533 trip to your local science museum and among the exhibits is one for mass and weight. The exhibit  
534 has a gigantic scale, and you come up with a fun problem for your class.

535 You ask your class, "What is the total weight of the classroom? Give your best estimation to  
536 me in 30 minutes, and then we'll check your guess on the scale. If your guess is within 10% of the  
537 right answer, we will stop for ice cream on the way back."

538 The students are ecstatic to hear this, and they get to work. The solution is some variation of  
539 the following strategy. The students should give each other their weight or best guess if they do  
540 not know. Then, all they must do is add each student's weight and get a grand total for the class.  
541 The measurement on the giant scale should show the true weight of the class. When comparing  
542 the measured weight to your estimation, multiply the measurement by  $1.0 \pm 0.1$  to get the  $\pm 10\%$   
543 tolerances for your estimation.

544 Two of your students, Sandra and Mario, return to you with a solution.

545 They say, "We weren't sure of everyone's weight. We used 65 lbs. for the people we didn't  
546 know and added everyone who does know. There are 30 of us, and we got 2,000 lbs.! That's a ton!"

547 You estimated 1,900 lbs. assuming the average weight of a student in your class was 60 lbs.  
548 So, you are pleased with Sandra's and Mario's answer. You instruct your students to all gather on  
549 the giant scale and read off the weight together. To all your surprise, the scale reads *10,000 lbs.*!  
550 10,000 is significantly more than a 10% error from 2,000. In fact, it is approximately 5 times more  
551 massive than either your or your students' estimates. You think to yourself and conclude there  
552 must be something wrong with the scale. You ask an employee to check the scale and verify it is  
553 well calibrated. They confirm that the scale is in working order. You weigh a couple of students  
554 individually to assess that the scale is well calibrated. Sandra weighs 59 lbs., and Mario weighs

555 62 lbs., typical weights for their age. You then weigh each student individually and see that their  
556 weights individually do not deviate greatly from 60 lbs. So, where does all the extra weight come  
557 from?

558 This thought experiment serves as an analogy to the Dark Matter problem. The important  
559 substitution to make however is to replace the students with stars and the classroom with a galaxy,  
560 say the Milky Way. Individually the mass of stars is well measured and defined with the Sun as our  
561 nearest test case. However, when we set out to measure the mass of a collection of stars as large as  
562 galaxies, our well-motivated estimation is wildly incorrect. There simply is no way to account for  
563 this discrepancy except without some unseen, or dark, contribution to mass and matter in galaxies.  
564 I set out in my thesis to narrow the possibilities of what this Dark Matter could be.

565 This chapter is organized like the following... **TODO: Text should look like ... Chapter x has**  
566 **blah blah blah.**

## 567 1.2 Dark Matter Basics

568 Presently, a more compelling theory of cosmology that includes Dark Matter (DM) in order  
569 to explain a variety of observations is  $\Lambda$  Cold Dark Matter, or  $\Lambda$ CDM. I present the evidence  
570 supporting  $\Lambda$ CDM in Section 1.3 yet discuss the conclusions of the  $\Lambda$ CDM model here. According  
571 to  $\Lambda$ CDM fit to observations on the Cosmic Microwave Background (CMB), DM is 26.8% of the  
572 universe's current energy budget. Baryonic matter, stuff like atoms, gas, and stars, contributes to  
573 4.9% of the universe's current energy budget [1, 2, 3].

574 DM is dark; it does not interact readily with light at any wavelength. DM also does not interact  
575 noticeably with the other standard model forces (Strong and Weak) at a rate that is readily observed  
576 [3]. DM is cold, which is to say that the average velocity of DM is below relativistic speeds [1].  
577 'Hot' DM would not likely manifest the dense structures we observe like galaxies, and instead  
578 would produce much more diffuse galaxies than what is observed [3, 1]. DM is old; it played a  
579 critical role in the formation of the universe and the structures within it [1, 2].

580 Observations of DM have so far been only gravitational. The parameter space available to what  
581 DM could be therefore is extremely broad. The broad DM parameter space is iteratively tested in

582 DM searches by supposing a hypothesis that has not yet been ruled out and performing observations  
583 to test them. When the observations yield a null result, the parameter space is constrained further.  
584 I present some approaches for DM searches in Section 1.4.

585 **1.3 Evidence for Dark Matter**

586 Dark Matter (DM) has been a looming problem in physics for almost 100 years. Anomalies  
587 have been observed by astrophysicists in galactic dynamics as early as 1933 when Fritz Zwicky  
588 noticed unusually large velocity dispersion in the Coma cluster. Zwicky's measurement was the  
589 first recorded to use the Virial theorem to measure the mass fraction of visible and invisible matter  
590 in celestial bodies [4]. From Zwicky in [5], "*If this would be confirmed, we would get the surprising*  
591 *result that dark matter is present in much greater amount than luminous matter.*" Zwicky's and  
592 others' observation did not instigate a crisis in astrophysics because the measurements did not  
593 entirely conflict with their understanding of galaxies [4]. In 1978, Rubin, Ford, and Norbert  
594 measured rotation curves for ten spiral galaxies [6]. Rubin et al.'s 1978 publication presented a  
595 major challenge to the conventional understanding of galaxies that could no longer be dismissed by  
596 measurement uncertainties. Evidence has been mounting ever since for this exotic form of matter.  
597 The following subsections provide three compelling pieces of evidence in support of the existence  
598 of DM.

599 **1.3.1 First Clues: Stellar Velocities**

600 Zwicky, and later Rubin, measured the stellar velocities of various galaxies to estimate their  
601 virial mass. The Virial Theorem upon which these observations are interpreted is written as

$$2T + V = 0. \quad (1.1)$$

602 Where  $T$  is the kinetic energy and  $V$  is the potential energy in a self-gravitating system. The  
603 classical Newton's law of gravity from stars and gas was used for gravitational potential modeled in  
604 the observed galaxies:

$$V = -\frac{1}{2} \sum_i \sum_{j \neq i} \frac{m_i m_j}{r_{ij}}. \quad (1.2)$$

605 Zwicky et al. measured just the velocities of stars apparent in optical wavelengths [5]. Rubin et al.  
 606 added by measuring the velocity of the hydrogen gas via the 21 cm emission line of Hydrogen [6].  
 607 The velocities of the stars and gas are used to infer the total mass of galaxies and galaxy clusters  
 608 via Equation (1.1). An inferred mass is obtained from the luminosity of the selected sources. The  
 609 two inferences are compared to each other as a luminosity to mass ratio which typically yielded [1]

$$\frac{M}{L} \sim 400 \frac{M_{\odot}}{L_{\odot}} \quad (1.3)$$

610  $M_{\odot}$  and  $L_{\odot}$  referring to stellar mass and stellar luminosity, respectively. These ratios clearly indicate  
 611 a discrepancy in apparent light and mass from stars and gas and their velocities.

612 Rubin et al. [6] demonstrated that the discrepancy was unlikely to be an underestimation of  
 613 the mass of the stars and gas. The inferred "dark" mass was up to 5 times more than the luminous  
 614 mass. This dark mass also needed to extend well beyond the extent of the luminous matter.

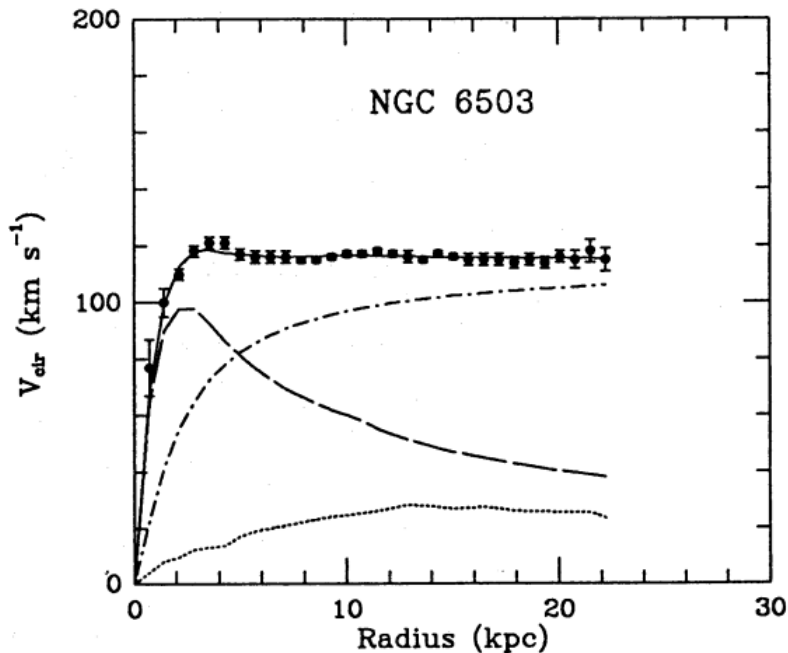


Figure 1.1 Rotation curve fit to NGC 6503 from [7]. Dashed line is the contribution from visible matter. Dotted curves are from gas. Dash-dot curves are from dark matter (DM). Solid line is the composite contribution from all matter and DM sources. Data are indicated with bold dots with error bars. Data agree strongly with a matter + DM composite prediction.

615 Figure 1.1 features one of many rotation curves plotted from the stellar velocities within galaxies.

616 The measured rotation curves mostly feature a flattening of velocities at higher radius which is not  
617 expected if the gravity was only coming from gas and luminous matter. The extension of the  
618 flat velocity region also indicates that the DM is distributed far from the center of the galaxy.  
619 Modern velocity measurements include significantly larger objects, galactic clusters, and smaller  
620 objects, dwarf galaxies. Yet, measurements along this regime are leveraging the Virial theorem  
621 with Newtonian potential energies. We know Newtonian gravity is not a comprehensive description  
622 of gravity. New observational techniques have been developed since 1978, and those are discussed  
623 in the following sections.

624 **1.3.2 Evidence for Dark Matter: Gravitational Lensing**

625 Modern evidence for dark matter comes from new avenues beyond stellar velocities. Grav-  
626 itational lensing from DM is a new channel from general relativity. General relativity predicts  
627 aberrations in light caused by massive objects. In recent decades we have been able to measure the  
628 lensing effects from compact objects and DM halos. Figure 1.2 shows how different massive ob-  
629 jects change the final image of a faraway galaxy resulting from gravitational lensing. Gravitational  
630 lensing developed our understanding of dark matter in two important ways.

631 Gravitational lensing provides additional compelling evidence for DM. The observation of two  
632 merging galactic clusters in 2006, shown in Figure 1.3, provided a compelling argument for DM  
633 outside the Standard Model. These clusters merged recently in astrophysical time scales. Galaxies  
634 and star cluster have mostly passed by each other as the likelihood of their collision is low. Therefore,  
635 these massive objects will mostly track the highest mass, dark and/or baryonic, density. Yet, the  
636 intergalactic gas is responsible for the majority of the baryonic mass in the systems [4]. These gas  
637 bodies will not phase through and will heat up as they collide together. The hot gas is located via  
638 x-ray emission from the cluster. Two observations of the clusters were performed independently of  
639 each other.

640 The first was the lensing of light around the galaxies due to their gravitational influences.  
641 When celestial bodies are large enough, the gravity they exert bends space and time itself. The  
642 warped space-time lenses light and will deflect in an analogous way to how glass lenses will bend

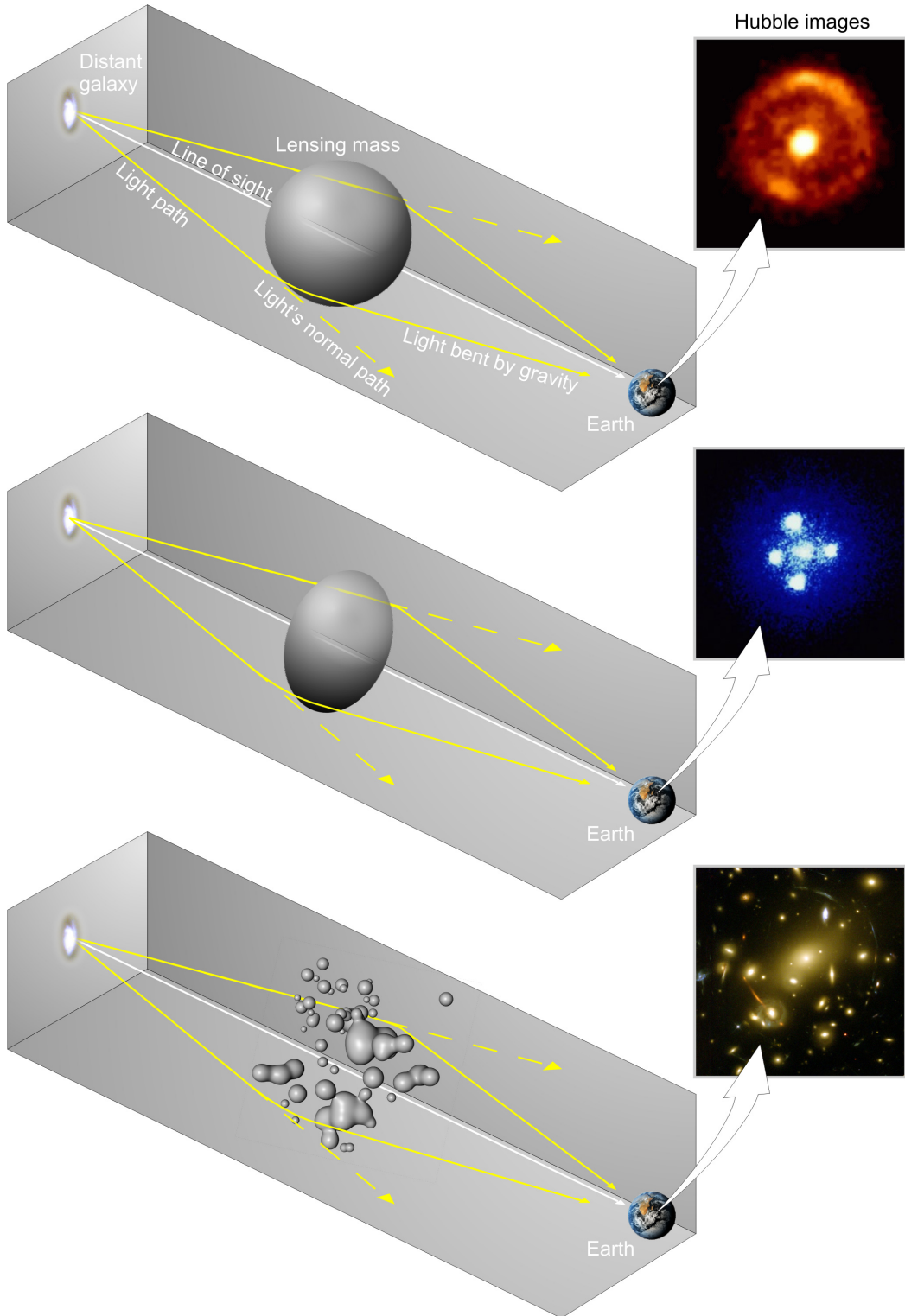


Figure 1.2 Light from distant galaxy is bent in unique ways depending on the distribution of mass between the galaxy and Earth. Yellow dashed lines indicate where the light would have gone if the matter were not present [8].

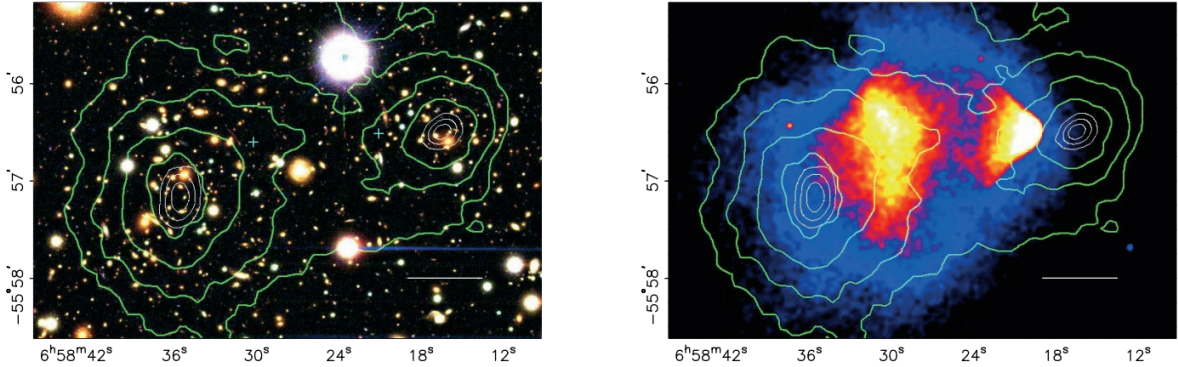


Figure 1.3 (left) Optical image of galactic cluster 1E0657-558. (right) X-ray image of the cluster with redder meaning hotter and higher baryon density. (both) Green contours are reconstruction of gravity contours from weak lensing. White rings are the best fit mass maxima at 68.3%, 95.5%, and 99.7% confidence. The matter maxima of the clusters are clearly separated from x-ray maxima. [9]

643 light, see Figure 1.2. With a sufficient understanding of light sources behind a massive object, we  
 644 can reconstruct the contours of the gravitational lenses. The gradient of the contours shown in  
 645 Figure 1.3 then indicates how dense the matter is and where it is.

646 The x-ray emission can then be observed from the clusters. Since these galaxies are mostly gas  
 647 and are merging, then the gas should be getting hotter. If they are merging, the x-ray emissions  
 648 should be the strongest where the gas is mostly moving through each other. Hence, X-ray emission  
 649 maps out where the gas is in the merging galaxy cluster.

650 The lensing and x-ray observations were done on the Bullet cluster featured on Figure 1.3.  
 651 The x-ray emissions do not align with the gravitational contours from lensing. The incongruence  
 652 in mass density and baryon density suggests that there is a lot of matter somewhere that does  
 653 not interact with light. Moreover, this dark matter cannot be baryonic [9]. The Bullet Cluster  
 654 measurement did not really tell us what DM is exactly, but it did give the clue that DM also does  
 655 not interact with itself very strongly. If DM did interact strongly with itself, then it would have been  
 656 more aligned with the x-ray emission [9]. There have been follow-up studies of galaxy clusters with  
 657 similar results. The Bullet Cluster and others like it provide a persuasive case against something  
 658 possibly amiss in our gravitational theories.

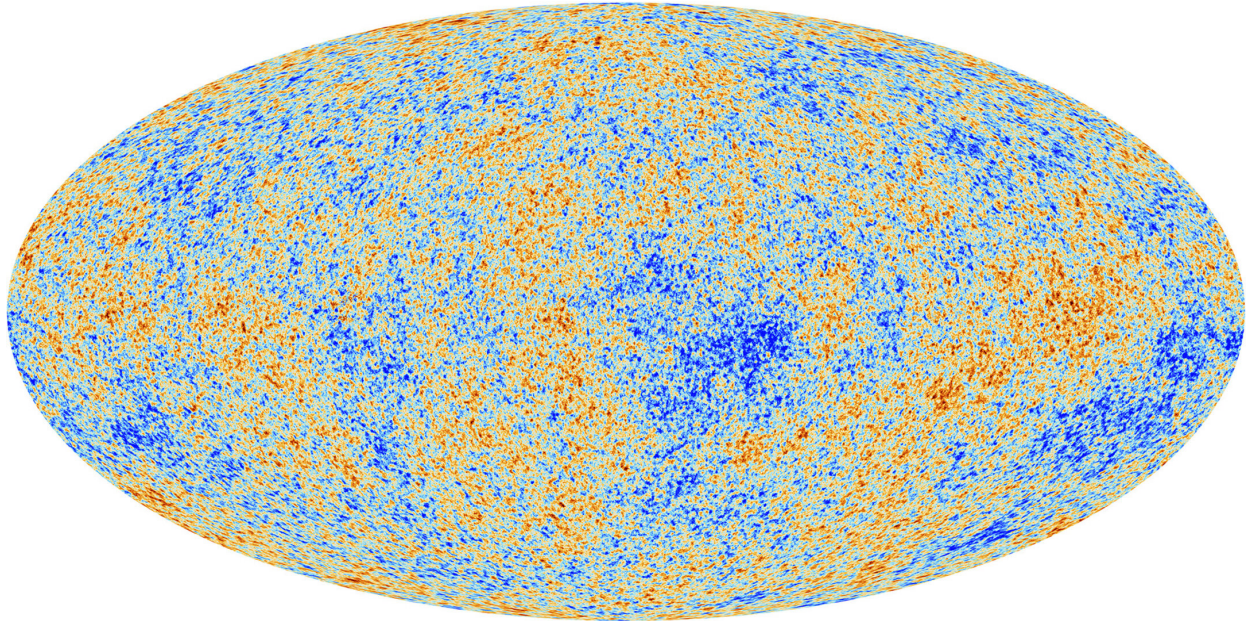


Figure 1.4 Plank CMB sky. Sky map features small variations in temperature in primordial light. These anisotropies are used to make inferences about the universe's energy budget and developmental history. [10]

659 **1.3.3 Evidence for Dark Matter: Cosmic Microwave Background**

660 The Cosmic Microwave Background (CMB) is the primordial light from the early universe  
661 when Hydrogen atoms formed from the free electron and proton soup in the early universe. The  
662 CMB is the earliest light we can observe; released when the universe was about 380,000 years old.  
663 Then we look at how the simulated universes look like compared to what we see. Figure 1.4 is the  
664 most recent CMB image from the Plank satellite after subtracting the average value and masking the  
665 galactic plane [10]. Redder regions indicate a slightly hotter region in the CMB, and blue indicates  
666 colder. The intensity variations are on the order of 1 in 1000 with respect to the average value.

667 The Cosmic Microwave Background shows that the universe had DM in it from an incredibly  
668 early stage. To measure the DM, Dark Energy, and matter fractions of the universe from the CMB,  
669 the image is analyzed into a power spectrum, which shows the amplitude of the fluctuations as  
670 a function of spherical multipole moments.  $\Lambda$ CDM provides the best fit to the power spectra of  
671 the CMB as shown in Figure 1.5. The CMB power spectrum is quite sensitive to the fraction  
672 of each energy contribution in the early universe. Low  $l$  modes are dominated by variations  
673 in gravitational potential. Intermediate  $l$  emerge from oscillations in photon-baryon fluid from

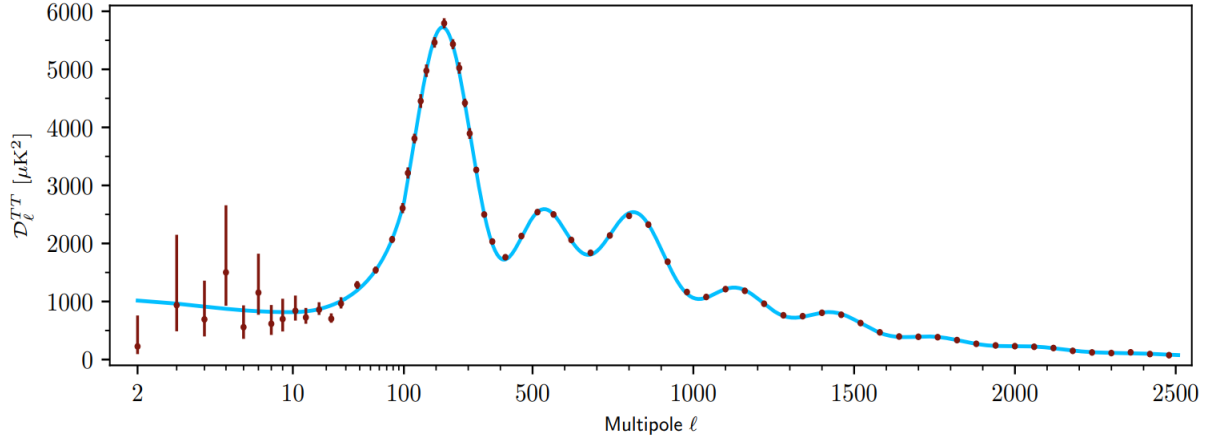


Figure 1.5 Observed Cosmic Microwave Background power spectrum as a function of multipole moment from Plank [10]. Blue line is best fit model from  $\Lambda$ CDM. Red points and lines are data and error, respectively.

674 competing baryon pressures and gravity. High  $l$  is a damped region from the diffusion of photons  
 675 during electron-proton recombination. [1]

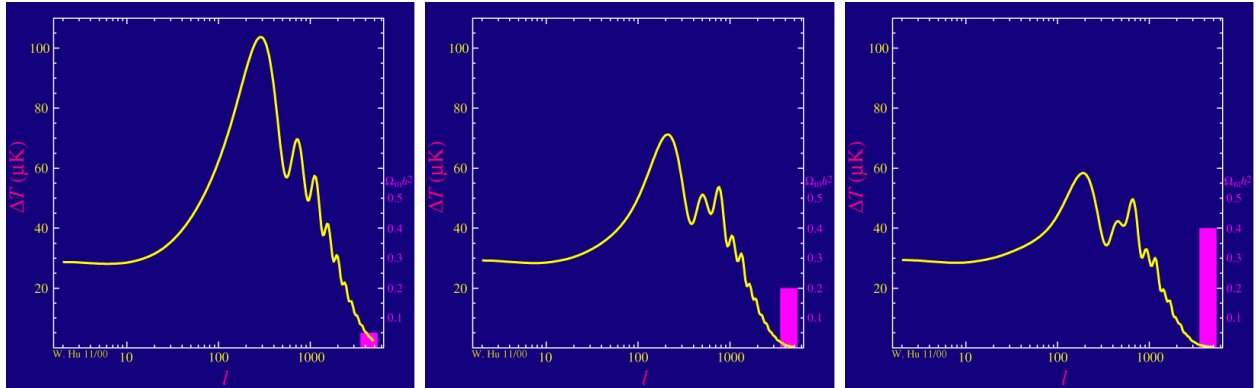


Figure 1.6 Predicted power spectra of CMB for different  $\Omega_m h^2$  values for fixed baryon density from [11]. (left) Low  $\Omega_m h^2$  increases the prominence of first and second peaks. (middle)  $\Omega_m h^2$  is most similar to the observed power spectrum. The second and third peaks are similar in height. (right)  $\Omega_m h^2$  is large which suppresses the first peak and raises the prominence of the third peak.

676 The harmonics would look quite different for a universe with less DM. Figure 1.6 demonstrates  
 677 the effect  $\Omega_m h^2$  has on the expected power spectrum for fixed baryon matter density. [11] Sweeping  
 678  $\Omega_m h^2$  in this way clearly shows the effect dark matter has on the CMB power spectrum. The  
 679 observations fit well with the  $\Lambda$ CDM model, and the derived fractions are as follows. The matter  
 680 fraction:  $\Omega_m = 0.3153$ ; and the baryon fraction:  $\Omega_b = 0.04936$  [10]. Plank's observations also  
 681 provide a measure of the Hubble constant,  $H_0$ .  $H_0$  especially has seen a growing tension in the

682 past decade that continues to deepened with observations from instruments like the James Webb  
683 Telescope [12, 13]. As Hubble tensions deepen, we may find that perhaps  $\Lambda$ **CDM**, despite its  
684 successes, is missing some critical physics.

685 Overall, the Newtonian motion of stars in galaxies, weak lensing from galactic clusters, and  
686 power spectra from primordial light form a compelling body of research in favor of dark matter.  
687 It takes another leap of theory and experimentation to make observations of DM that are non-  
688 gravitational in nature. In Section 1.3, the evidence for DM implies strongly that the DM is matter  
689 and not a lost parameter in the gravitational fields between massive objects. Finally, if we take one  
690 axiom: that this matter has quantum behavior, such as being described by some Bohr wavelength  
691 and abiding by some fermion or boson statistics; then we arrive at particle dark matter. One particle  
692 DM hypothesis is the Weakly Interacting Massive Particle (WIMP). This DM candidate theory is  
693 discussed further in the next section and is the focus of this thesis.

#### 694 1.4 Searching for Dark Matter: Particle DM

695 Section 1.4 shows the Standard Model of particle physics and is currently the most accurate  
696 model for the dynamics of fundamental particles like electrons and photons. The current status  
697 of the SM does not have a viable DM candidate. When looking at the standard model, we can  
698 immediately exclude any charged particle because charged particles interact strongly with light.  
699 Specifically, this will rule out the following charged, fundamental particles:  $e, \mu, \tau, W, u, d, s, c, t, b$   
700 and their corresponding antiparticles. Recalling from Section 1.2 that DM must be long-lived and  
701 stable over the age of the universe which excludes all SM particles with decay half-lives at or shorter  
702 than the age of the universe. The lifetime constraint additionally eliminates the  $Z$  and  $H$  bosons.  
703 Finally, the candidate DM needs to be somewhat massive. Recall from Section 1.2 that DM is cold  
704 or not relativistic through the universe. This eliminates the remaining SM particles:  $\nu_{e,\mu,\tau}, g, \gamma$  as  
705 DM candidates. Because there are no DM candidates within the SM, the DM problem strongly  
706 hints to physics beyond the SM (BSM).

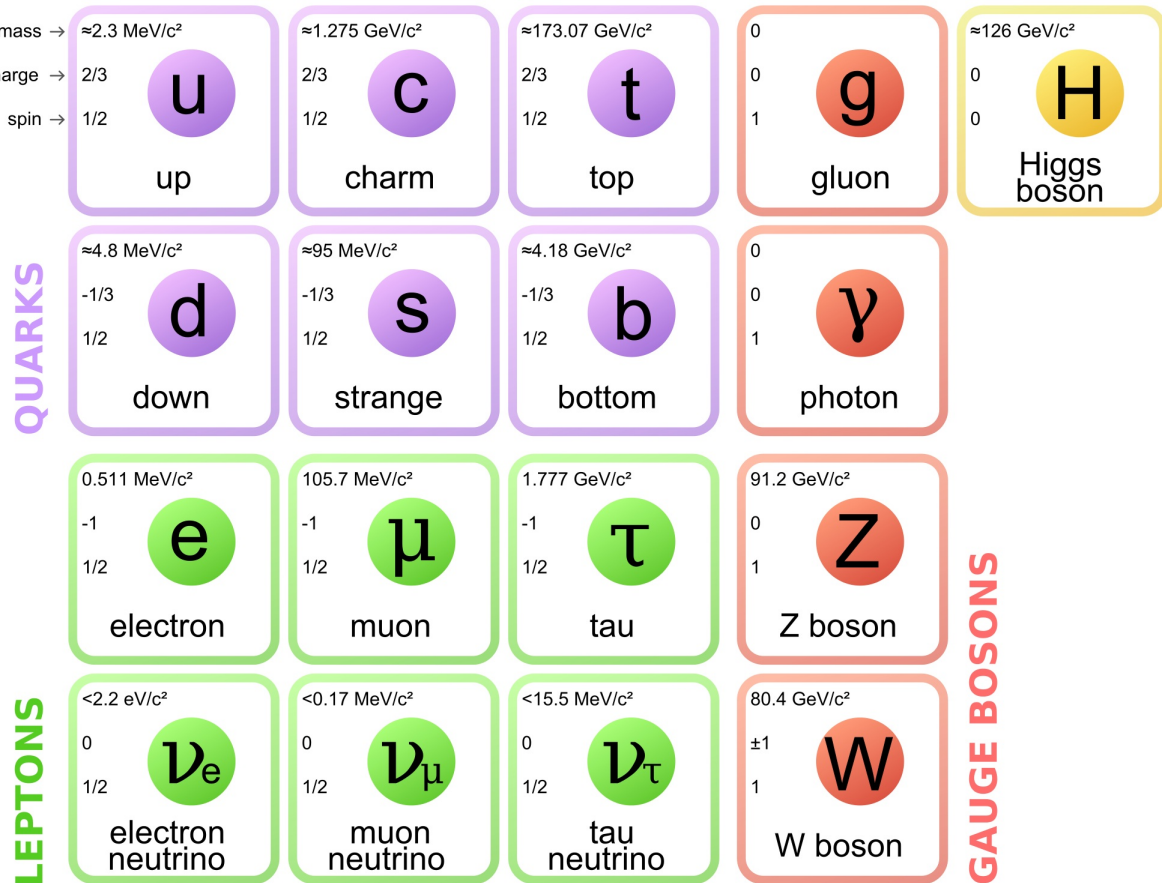


Figure 1.7 The Standard Model (SM) of particle physics. Figure taken from <http://www.quantumdiaries.org/2014/03/14/the-standard-model-a-beautiful-but-flawed-theory/>

### 707 1.4.1 Shake it, Break it, Make it

708 When considering DM that couples in some way with the SM, the interactions are roughly  
 709 demonstrated by interaction demonstrated in Figure 1.8. The figure is a simplified Feynman  
 710 diagram where the arrow of time represents the interaction modes of: **Shake it, Break it, Make it.**

711 **Shake it** refers to the direct detection of dark matter. Direct detection interactions start with  
 712 a free DM particle and an SM particle. The DM and SM interact via elastic or inelastic collision  
 713 and recoil away from each other. The DM remains in the dark sector and imparts some momentum  
 714 onto the SM particle. The hope is that the momentum imparted onto the SM particle is sufficiently  
 715 high enough to pick up with extremely sensitive instruments. Because we cannot create the DM in  
 716 the lab, a direct detection experiment must wait until DM is incident on the detector. Most direct  
 717 detection experiments are therefore placed in low-background environments with inert detection

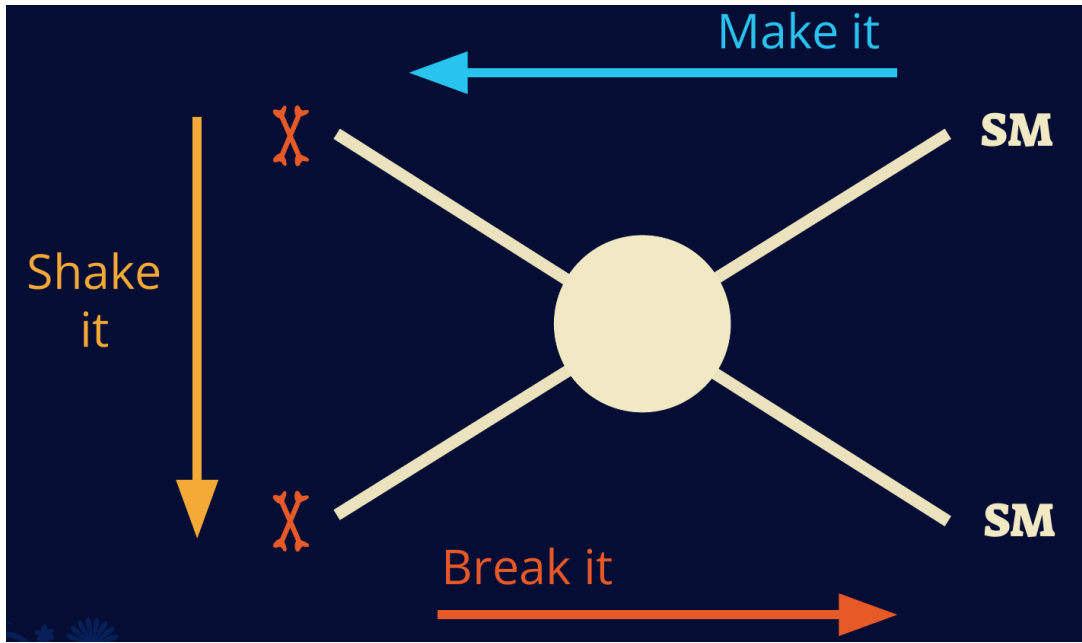


Figure 1.8 Simplified Feynman diagram demonstrating different ways DM can interact with SM particles. The 'X's refer to the DM particles whereas the SM refer to fundamental particles in the SM. The large circle in the center indicates the vertex of interaction and is purposely left vague. The colored arrows refer to different directions of time as well as their respective labels. The arrows indicate the initial and final state of the DM -SM interaction in time.

<sup>718</sup> media like the noble gas Xenon. [14]

<sup>719</sup> **Make it** refers to the production of DM from SM initial states. The experiment starts with  
<sup>720</sup> particles in the SM. These SM particles are accelerated to incredibly high energies and then collide  
<sup>721</sup> with each other. In the confluence of energy, DM hopefully emerges as a byproduct of the SM  
<sup>722</sup> annihilation. Often it is the collider experiments that are energetic enough to hypothetically produce  
<sup>723</sup> DM. These experiments include the world-wide collaborations ATLAS and CMS at CERN where  
<sup>724</sup> proton collide together at extreme energies. The DM searches, however, are complex. DM likely  
<sup>725</sup> does not interact with the detectors and lives long enough to escape the detection apparatus of  
<sup>726</sup> CERN's colliders. This means any DM production experiment searches for an excess of events  
<sup>727</sup> with missing momentum or energy in the events. An example event with missing transverse  
<sup>728</sup> momentum is shown in Figure 1.9. The missing momentum with no particle tracks implies a  
<sup>729</sup> neutral particle carried the energy out of the detector. However, there are other neutral particles  
<sup>730</sup> in the SM, like neutrons or neutrinos, so any analysis has to account for SM signatures of missing

731 momentum. [15]

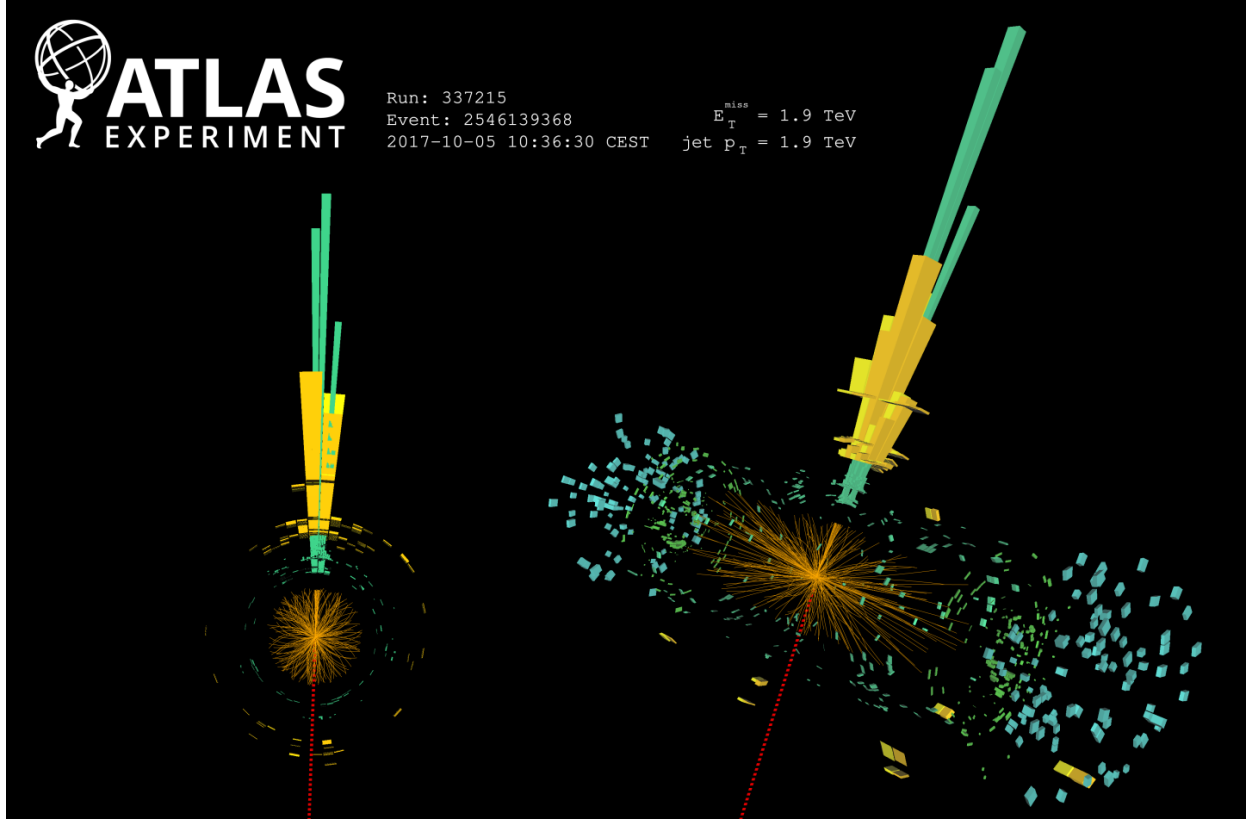


Figure 1.9 A single jet event in ATLAS detector from 2017 [16]. Jet momentum was observed to be 1.9 TeV. Missing transverse momentum was observed to be 1.9 TeV compared to the initial transverse momentum of the event was 0. Implied MET is traced by a red dashed line in event display.

### 732 1.4.2 Break it: Standard Model Signatures of Dark Matter through Indirect Searches

733 **Break it** refers to the creation of SM particles from the dark sector, and it is the primary focus  
734 of this thesis. The interaction begins with DM or in the dark sector. The hypothesis is that this  
735 DM will either annihilate with itself or decay and produce an SM byproduct. This method is  
736 often referred to as the Indirect Detection of DM because we have no lab to directly control or  
737 manipulate the DM. Therefore, most indirect DM searches are performed using observations of  
738 known DM densities among the astrophysical sources. The strength is that we have the whole of the  
739 universe and its 13.6-billion-year lifespan to use as a detector and particle accelerator. Additionally,  
740 locations of dark matter are well cataloged since it was astrophysical observations that presented

741 the problem of DM in the first place.

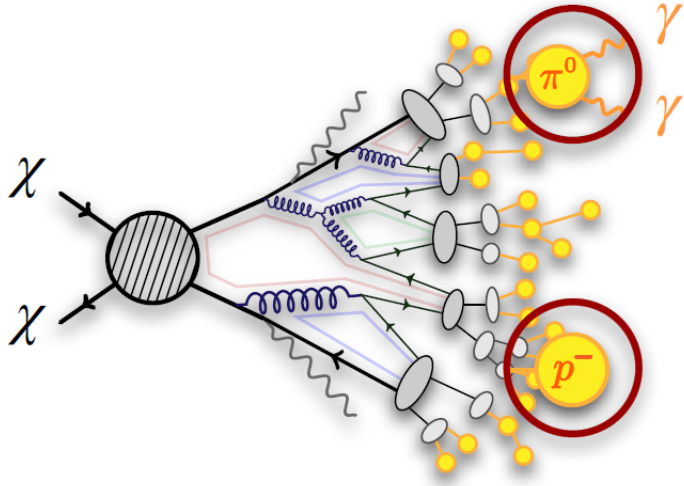


Figure 1.10 More detailed pseudo-Feynman diagram of particle cascade from dark matter annihilation into 2 quarks. The quarks hadronize and down to stable particles like  $\gamma$  or the anti-proton ( $p^-$ ). Diagram pulled from ICRC 2021 presentation on DM annihilation search [17].

742 However, anything can happen in the universe. There are many difficult to deconvolve back-  
743 grounds when searching for DM. One prominent example is the galactic center. We know the  
744 galactic center has a large DM content because of stellar kinematics in our Milky Way and DM halo  
745 simulations. Yet, any signal from the galactic center is challenging to parse apart from the extreme  
746 environment of our supermassive black hole, unresolved sources, and diffuse emission from the  
747 interstellar medium [18]. Despite the challenges, any DM model that yields evidence in the other  
748 two observation methods, **Shake it or Make it** must be corroborated with indirect observations of  
749 the known DM sources. Without corroborating evidence, DM observation in the lab is hard-pressed  
750 to demonstrate that it is the model contributing to the DM seen at the universal scale.

751 In the case of WIMP DM, signals are described in terms of primary SM particles produced  
752 from DM decay or annihilation. The SM initial state particles are then simulated down to stable  
753 final states such as the  $\gamma$ ,  $\nu$ ,  $p$ , or  $e$  which can traverse galactic lengths to reach Earth.

754 Figure 1.10 shows the quagmire of SM particles that emerges from SM initial states that are not  
755 stable [17]. There are many SM particles with varying energies that can be produced in such an

756 interaction. For any arbitrary DM source and stable SM particle, the SM flux from DM annihilating  
 757 to a neutral particle in the SM,  $\phi$ , from a region in the sky is described by the following.

$$\frac{d\Phi_\gamma}{dE_\gamma} = \frac{\langle\sigma v\rangle}{8\pi m_\chi^2} \frac{dN_\gamma}{dE_\gamma} \times \int_{\text{source}} d\Omega \int_{l.o.s} \rho_\chi^2 dl(r, \theta') \quad (1.4)$$

758 In Equation (3.1),  $\langle\sigma v\rangle$  is the velocity-weighted annihilation cross-section of DM to the SM.  $m_\chi$   
 759 refers to the mass of DM, noted with Greek letter  $\chi$ .  $\frac{dN_\phi}{dE_\phi}$  is the N particle flux weighted by the  
 760 particle energy. An example is provided in Figure 1.11 for the  $\gamma$  final state. The integrated terms  
 761 are performed over the solid angle,  $d\Omega$ , and line of sight, l.o.s.  $\rho$  is the density of DM for a  
 762 location  $(r, \theta')$  in the sky. The terms left of the '×' are often referred to as the particle physics  
 763 component. The terms on the right are referred to as the astrophysical component. For decaying  
 764 DM, the equation changes to...

$$\frac{d\Phi_\phi}{dE_\phi} = \frac{1}{4\pi\tau m_\chi} \frac{dN_\phi}{dE_\phi} \times \int_{\text{source}} d\Omega \int_{l.o.s} \rho_\chi dl(r, \theta') \quad (1.5)$$

765 In Equation (1.5),  $\tau$  is the decay lifetime of the DM. Just as in Equation (3.1), the left and right  
 766 terms are the particle physics and the astrophysical components respectively. The integrated  
 767 astrophysical component of Equation (3.1) is often called the J-Factor. Whereas the integrated  
 768 astrophysical component of Equation (1.5) is often called the D-Factor.

769     Exact DM  $\text{DM} \rightarrow \text{SM SM}$  branching ratios are not known, so it is usually assumed to go 100%  
 770 into an SM particle/anti-particle. Additionally, when a DM annihilation or decay produces one of  
 771 the neutral, long-lived SM particles ( $\nu$  or  $\gamma$ ), the particle is traced back to a DM source. For DM  
 772 above GeV energies, there are very few SM processes that can produce particles with such a high  
 773 energy. Seeing such a signal would almost certainly be an indication of the presence of dark matter.  
 774 Fortunately, the universe provides us with the largest volume and lifetime ever for a particle physics  
 775 experiment.

## 776 1.5 Sources for Indirect Dark Matter Searches

777     The first detection of DM relied on optical observations. Since then, we have developed new  
 778 techniques to find DM dense regions. As described in Section 1.3.1, many DM dense regions were  
 779 through observing galactic rotation curves. Our Milky Way galaxy is among DM dense regions

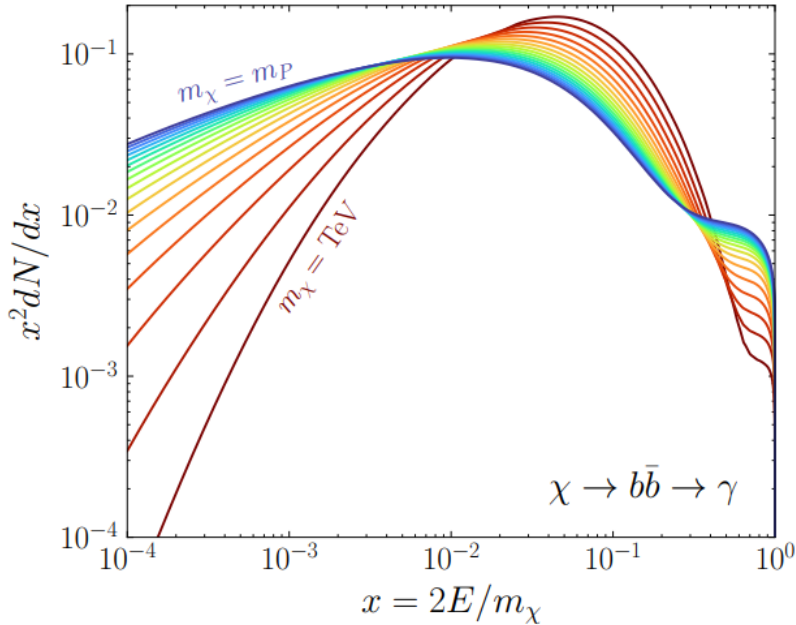


Figure 1.11 Dark Matter (DM) decay spectrum for  $b\bar{b}$  initial state and  $\gamma$  final state. Redder spectra are for larger DM masses. Bluer spectra are light DM masses.  $x$  is a unitless factor defined as the ratio of the mass of DM,  $m_\chi$ , and the final state particle energy  $E_\gamma$ . Figure from [19].

discovered, and it is the largest nearby DM dense region to look at. Additionally, the DM halo surrounding the Milky Way is clumpy [18]. There are regions in the DM halo of the Milky Way that have more DM than others that have captured gas over time. These sub-halos were dense enough to collapse gas and form stars. These apparent sub galaxies are known as dwarf spheroidal galaxies and are the main sources studied in this thesis. Each source type comes with different trade-offs. Galactic Center studies will be very sensitive to the assumed distribution of DM. The central DM density can vary substantially as demonstrated in Figure 1.12. At distances close to the center of the galaxy, or small  $r$ , the differences in DM densities can be 3-4 orders of magnitude. Searches toward the galactic center will therefore be quite sensitive to the assumed DM distribution.

Searches toward Dwarf Spheroidal Galaxies (dSph's) suffer from uncertainties in the DM density less than the galactic center studies. This is mostly from their diminutive size being smaller than the angular resolution of most  $\gamma$ -ray observatories [18]. The DM content dSph's are typically determined with the Virial theorem, Equation (1.1), and are usually majority DM [18] in mass. DSph's tend to be ideal sources to look at for DM searches. Their environments are quiet with little

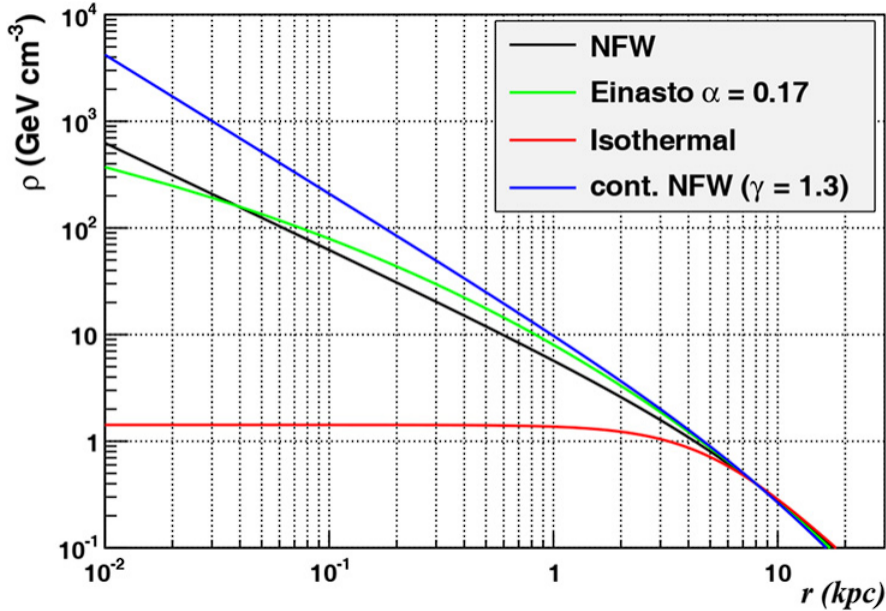


Figure 1.12 Different dark matter density profiles compared. Some models produce exceptionally large densities at small  $r$  [20].

794 astrophysical background. Unlike the galactic center, the most active components of dSph's are the  
 795 stars within them versus a violent accretion disc around a black hole. All this together means that  
 796 dSph's are among the best sources to look at for indirect DM searches. dSph's are the targets of  
 797 focus for this thesis.

## 798 1.6 Multi-Messenger Dark Matter

799 Astrophysics entered a new phase in the past few decades that leverages our increasing sensitivity  
 800 to SM channels and general relativity (GR). Up until the 21st century, astrophysical observations  
 801 were performed with photons ( $\gamma$ ) only. Astrophysics with this 'messenger' is fairly mature now.  
 802 Novel observations of the universe have since only adjusted the sensitivity of the wavelength of  
 803 light that is observed except at MeV energies. Gems like the CMB [10], and more have ultimately  
 804 been observations of different wavelengths of light. Multi-messenger astrophysics proposes using  
 805 other SM particles such the  $p^{+-}$ , or  $\nu$  or gravitation waves predicted by general relativity.

806 The experiment LIGO had a revolutionary discovery in 2016 with the first detection of a binary  
 807 black hole merger [21]. This opened the collective imagination to observing the universe through  
 808 gravitational waves. There has also been a surge of interest in the neutrino ( $\nu$ ) sector. IceCube

809 demonstrated that we are sensitive to neutrinos in regions that correlate with significant photon  
 810 emission like the galactic plane [22]. Neutrinos, like gravitational waves and light, travel mostly  
 811 unimpeded from their source to our observatories. This makes pointing to the originating source  
 812 of these messengers much easier than it is for cosmic rays which are deflected from their source by  
 813 magnetic fields.

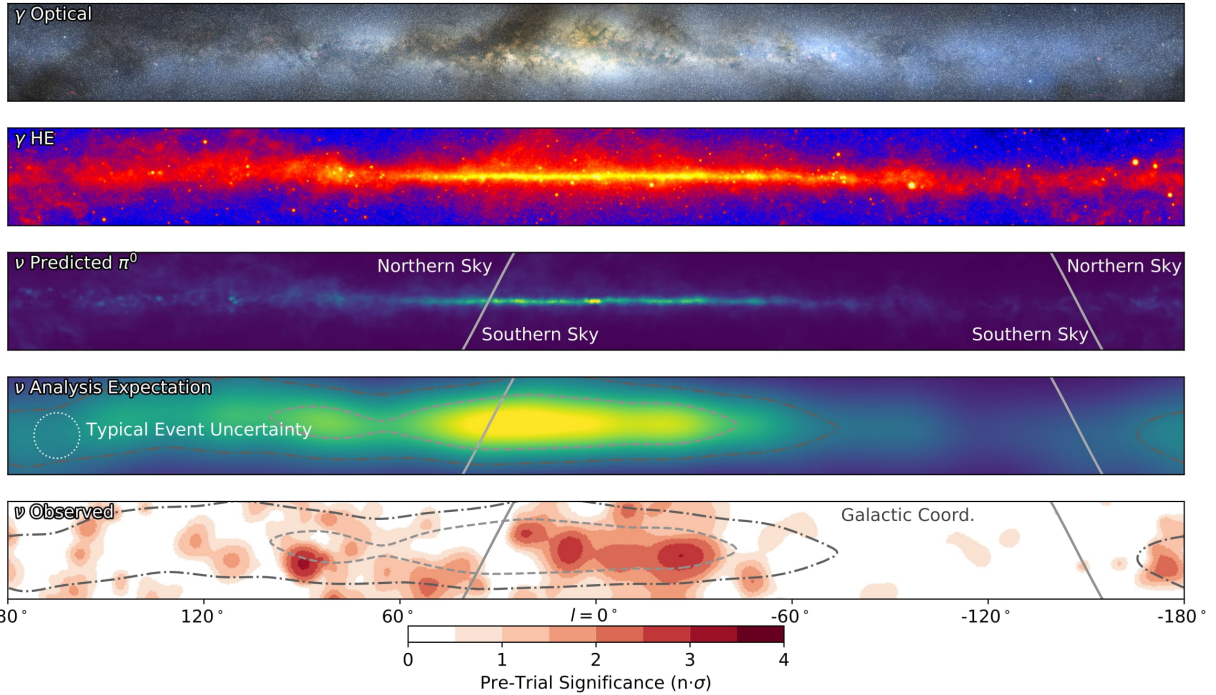


Figure 1.13 The Milky Way Galaxy in photons ( $\gamma$ ) and neutrinos ( $\nu$ ) [22]. The Galactic center is at  $l=0^\circ$  and is the brightest region in all panels. (top) An Optical color image of the Milky Way galaxy seen from Earth. Clouds of gas and dust obscure some light from stars. (2nd down) Integrated flux of  $\gamma$ -rays observed by the Fermi-LAT telescope [23]. (middle) Expected neutrino emission that corresponds with Fermi-LAT observations. (2nd up) Expected neutrino emission profile after considering detector systematics of IceCube. (bottom) Observed neutrino emission from region of the galactic plane. Substantial neutrino emission was detected.

814 The IceCube collaboration recently published a groundbreaking result of the Milky Way in  
 815 neutrinos. The recent result from IceCube, shown in Figure 1.13, proves that we can make  
 816 observations under different messenger regimes. The top two panels show the appearance of the  
 817 galactic plane to different wavelengths of light. Some sources are more apparent in some panels,  
 818 while others are not. This new channel is powerful because neutrinos are readily able to penetrate  
 819 through gas and dust in the Milky Way. This new image also refines our understanding of how high

820 energy particles are produced. For example, the fit to IceCube data prefers neutrino production  
 821 from the decay of  $\pi^0$  [22].

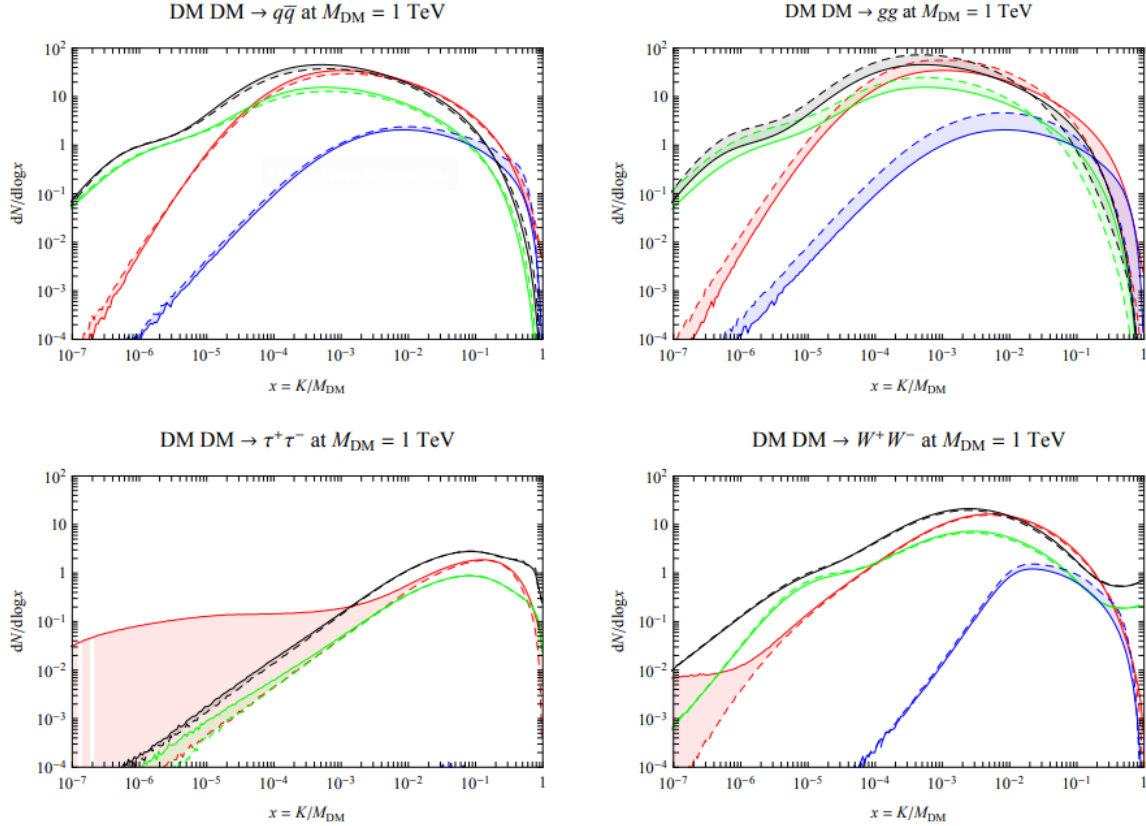


Figure 1.14 Dark Matter annihilation spectra for different final state particle and standard model annihilation channels [24]. Photons (red),  $e^\pm$  (green),  $\bar{p}$  (blue),  $\nu$  (black).

822 Exposing our observations to more cosmic messengers greatly increases our sensitivity to  
 823 rare processes. In the case of DM, Figure 1.14, there are many SM particles produced in DM  
 824 annihilation. Among the final state fluxes are gammas and neutrinos. Charged particles are also  
 825 produced however they would not likely make it to Earth since they will be deflected by magnetic  
 826 fields between the source and Earth. This means observatories that can see the neutral messengers  
 827 are especially good for DM searches and for combining data for a multi-messenger DM search.

## CHAPTER 2

828

### HIGH ALTITUDE WATER CHERENKOV (HAWC) OBSERVATORY

829



Figure 2.1 Photo of the HAWC detector that I took on May 17, 2023. Main array is centered in the photo and comprised of the larger tanks. Outriggers are the smaller tanks around the main array.

830

The High Altitude Water Cherenkov (HAWC) Observatory is a specialized instrument designed

831

for the observation of high energy gamma-rays and cosmic rays [25]. Located on the Sierra

832

Negra volcano in Mexico, HAWC observes gamma rays and cosmic rays in the energy range of

833

approximately 100 GeV to 100's of TeV. HAWC is strategically situated to maximize observational

834

efficiency due to its high altitude. At an elevation of 4,100 meters, it monitors about two-thirds of

835

the sky every day with an uptime above 90%. This capability is essential for studying high-energy

836

astrophysical phenomena.

837

HAWC consists of 300 water Cherenkov detectors (WCDs) spread over  $22,000 \text{ m}^2$ . Each main

838

array detector is filled with purified water and equipped with four, upward-facing photomultiplier

839

tubes (PMTs). See Fig. 2.3 for schematic of WCDs. These PMTs detect Cherenkov radiation from

840

charged particles passing through the tanks. These charged particles are generated when a high

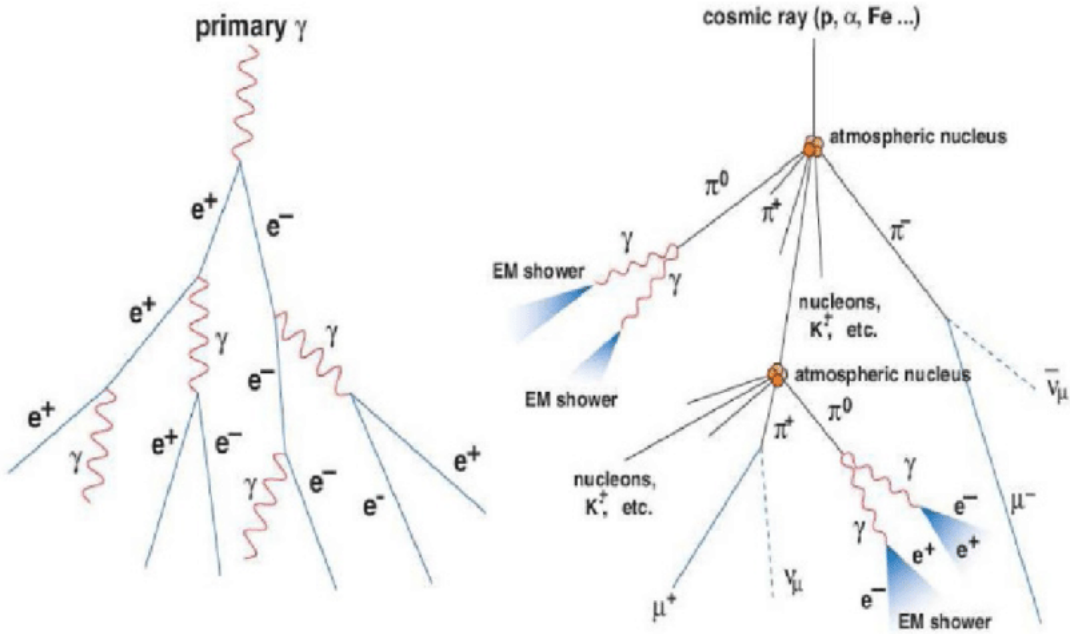


Figure 2.2 A particle physics illustration of high energy particle showers. Left shower is an electromagnetic shower from a high energy gamma-ray. Most particles in the shower will be a combination of photons and charged leptons, in this case electrons ( $e$ ). Right figure shows a cosmic ray particle shower. The cosmic ray will produce many more types of particles including pions ( $\pi$ ), neutrinos, and charged leptons. Figured pulled from [26].

841 energy gamma or cosmic ray collides with gas in the atmosphere to create a charged particle shower,  
 842 see Fig. 2.2. The observatory includes a separate tank configuration which are referred to as the  
 843 outriggers. They are a secondary array of 345 smaller WCD's. Surrounding the main array, each  
 844 outrigger tank measures 1.55 meters in diameter and height and contain a single upward-facing  
 845 eight-inch PMT. This add-on increases the instrumented footprint fourfold. The outriggers are  
 846 meant to improve the reconstruction of showers extending beyond the main array, especially for  
 847 events above 10 TeV. However, at the time of writing this thesis, the outriggers have not been fully  
 848 integrated into HAWC's reconstruction software.

#### 849 2.1.1 Construction and Hardware

850 Each main array WCD, see Fig. 2.3, is a cylindrical tank with dimensions of 7.3 m in diameter  
 851 and 5.4 m in height and filled with 180,000 L of water [25]. The metal shell of these tanks is made  
 852 from bolted together, corrugated, galvanized steel panels. The tanks are placed into 0.6 m deep

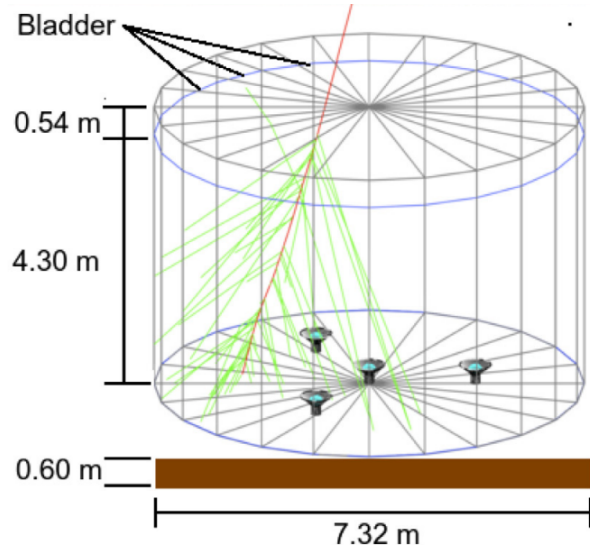


Figure 2.3 The WCDs. Left image features several WCDs looking from within the main array of HAWC. Right image shows a schematic of a WCD pulled from [25].

853 trenches filled with rammed earth to secure it against seismic activity [27]. The interior of each  
 854 tank is lined with a black, low-density polyethylene bladder, designed to be impermeable to external  
 855 light and to prevent reflection of Cherenkov light within the tank. This bladder is approximately 0.4  
 856 mm thick and composed of two layers of three-substrate film. To further minimize light penetration,  
 857 a black agricultural foil covers the bladder. The ground and walls inside the tank are protected  
 858 with felt and sand to safeguard against punctures. The tanks are filled 4.5 m deep of purified water,  
 859 achieving a photon attenuation length for Cherenkov photons that exceeds the tank's dimensions  
 860 [27]. This purification level ensures the optimal detection environment for the photons generated  
 861 by traversing charged particles.

862 At the base of each tank, four photomultiplier tubes (PMTs) are installed to detect the Cherenkov  
 863 radiation emitted by charged particles in water. Three 8-inch diameter PMTs surround a larger  
 864 10 inch PMT from Hamamatsu [28]. The variation in PMT response is carefully accounted for  
 865 in event reconstruction algorithms. Signals from the PMTs traverse 610 ft cables to the counting  
 866 house, where they are processed by Front-End Boards (FEBs), see Figs. 2.4 and 2.5. These FEBs,  
 867 along with Time to Digital Converters (TDCs), digitize the signals and manage the high voltage  
 868 supply to the PMTs.

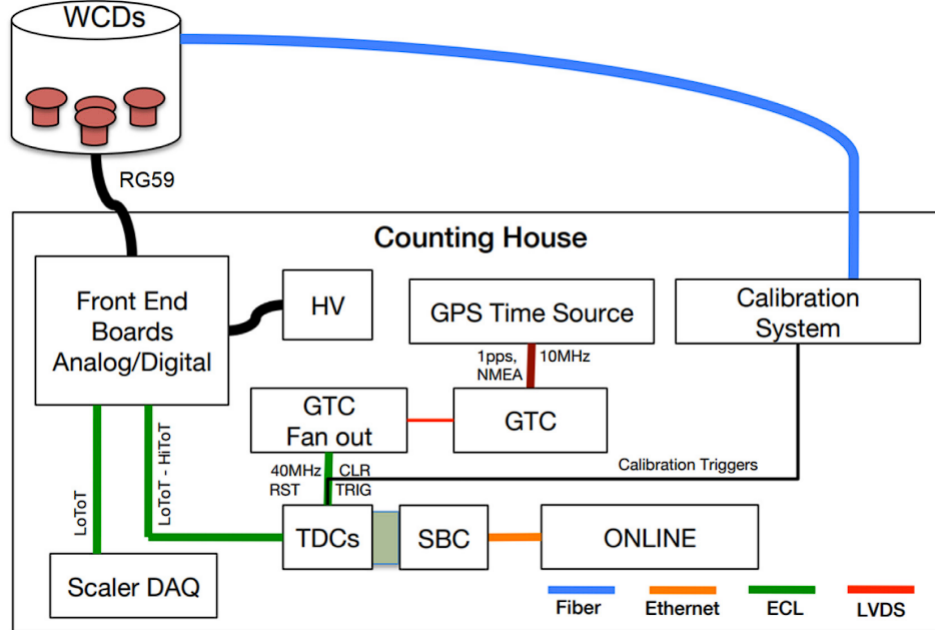


Figure 2.4 Overview of HAWC control and data electronics. The LoToT and HiToT threshold signals are discussed in Section 2.1.2. Figure from [27]

### 869 2.1.2 Data Acquisition and Signal Processing

870 The HAWC data acquisition (DAQ) and signal processing systems convert the physical detection  
 871 of particles into analyzable data. This process involves a series of steps from initial signal detection  
 872 by PMTs to digital conversion and preliminary analysis, see Figs. 2.5 and 2.6.

873 Once the signal from the PMTs arrive at the counting house, they enter the Front-End Boards  
 874 (FEBs). The FEBs are responsible for the initial processing of these signals, which includes  
 875 amplification and integration [30]. Each PMT signal is compared against preset LOW/HIGH  
 876 voltage thresholds in the FEBs, see Fig. 2.6, identifying signals that correspond to about 1/4 and  
 877 4 photoelectrons, respectively. This differentiation allows the system to gauge the strength of  
 878 the detected Cherenkov radiation. The processed signals are then digitized by Time to Digital  
 879 Converters (TDCs). These converters measure the time over threshold (ToT) for each signal, a  
 880 parameter that reflects both the duration and amplitude of the signal. This digitization facilitates  
 881 reconstruction of the original event for translating the physical interactions within the detectors into  
 882 data [27, 29, 30].

883 Synchronization across the HAWC observatory is maintained by a central GPS Timing and

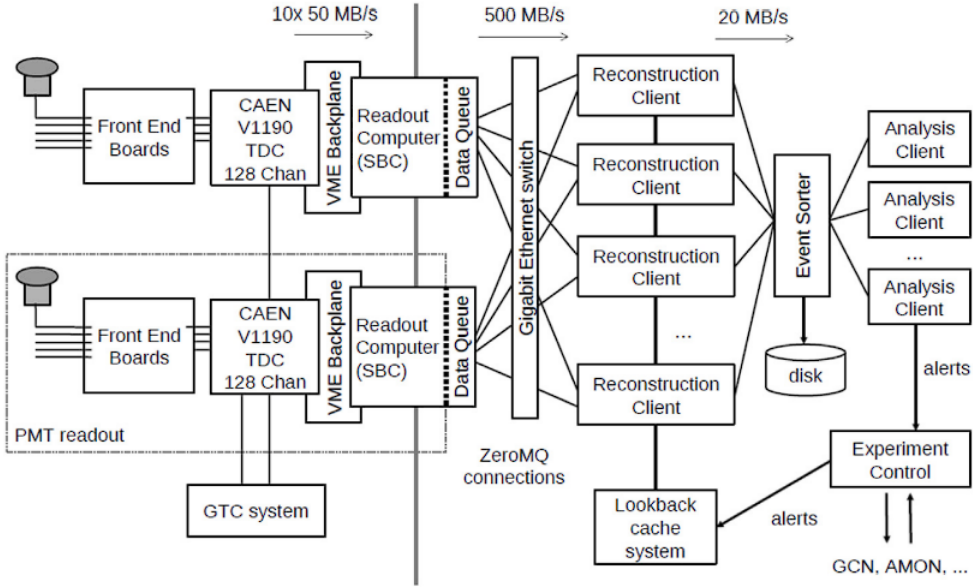


Figure 2.5 Schematic of data flow in HAWC data acquisition and online processing system. Pulled from [29].

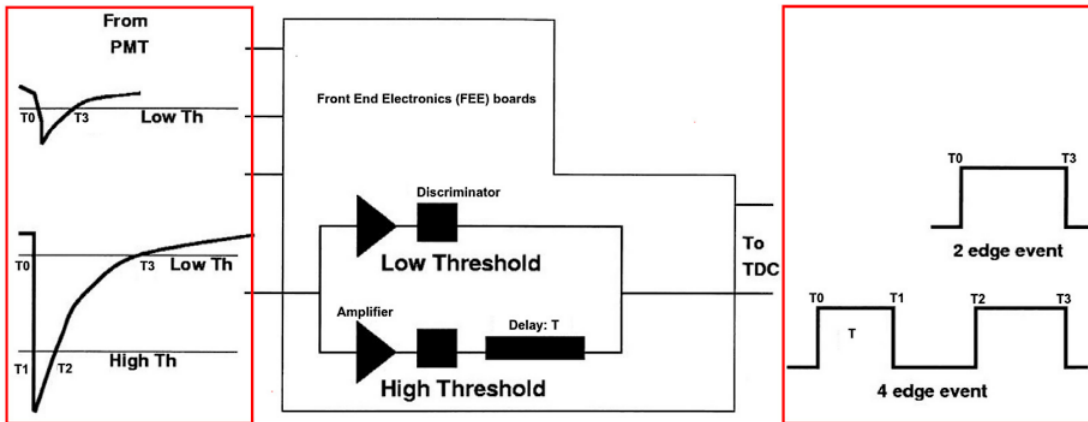


Figure 2.6 How HAWC FEB intially processes analog PMT signals. Signals are split through an amplifier and discriminator circuit. Each path is designated for either the HIGH or LOW threshold for the signal. The 2-edge event corresponds to LOW, while the 4 edge corresponds to HIGH.

884 Control (GTC) system, which achieves a timing resolution of 98 ps. This high-resolution timing  
885 is vital for accurately reconstructing the timing and location of air showers initiated by cosmic  
886 and gamma rays. The GTC system ensures that all components of the DAQ operate in unison to  
887 preserve the temporal integrity of the detected events [27, 31].

888 Once digitized, the data are transferred to an online event reconstruction system. This system  
889 runs the Reconstruction Client, which utilizes the raw PMT data to reconstruct the characteristics  
890 of the air showers, such as their direction and energy [29]. The capacity for real-time analysis  
891 allows HAWC to promptly respond to astrophysical phenomena like Gamma Ray Bursts (GRBs)  
892 and to participate in multi-messenger astronomy by following up on alerts from other observatories.  
893 This real-time processing system is designed to handle high data throughput, using ZeroMQ [32]  
894 for efficient data transfer between software components. Analysis Clients perform specific online  
895 analyses that require immediate data, including monitoring for GRBs, solar flare activity, and  
896 participation in global efforts to track gravitational waves and neutrinos [27].

897 The DAQ system is overseen by an Experiment Control system and crew that manage the  
898 operational aspects of data collection. This includes initiating and terminating data collection  
899 runs and monitoring the experiment for errors. In the event of a system crash, often caused by  
900 environmental factors such as lightning, the Experiment Control system is designed to automatically  
901 restart the experiment and minimize downtime [27, 29].

## 902 **2.2 Event Reconstruction**

903 Event reconstruction at the HAWC Observatory is a critical procedure that converts the raw data  
904 from the observatory’s WCDs into a coherent framework for understanding cosmic and gamma-  
905 ray events. This process includes several distinct steps. Core Fitting determines the geometric  
906 center of the air shower on the detector plane. Angle Reconstruction assesses the trajectory of the  
907 incoming particle, revealing its origin in the sky. Energy Estimation is performed using both  $f$ -hit  
908 and Neural Network (NN) methods to quantify the energy of the detected events. Gamma/Hadron  
909 discrimination differentiates between gamma-ray and hadronic cosmic ray initiated showers, a vital  
910 step for astrophysical interpretations. Each of these steps is integral to the observatory’s objective

911 of investigating the high-energy universe and enable the transformation of signals into detailed  
 912 insights about high energy cosmic phenomena.

913 **2.2.1 Core Fitting**

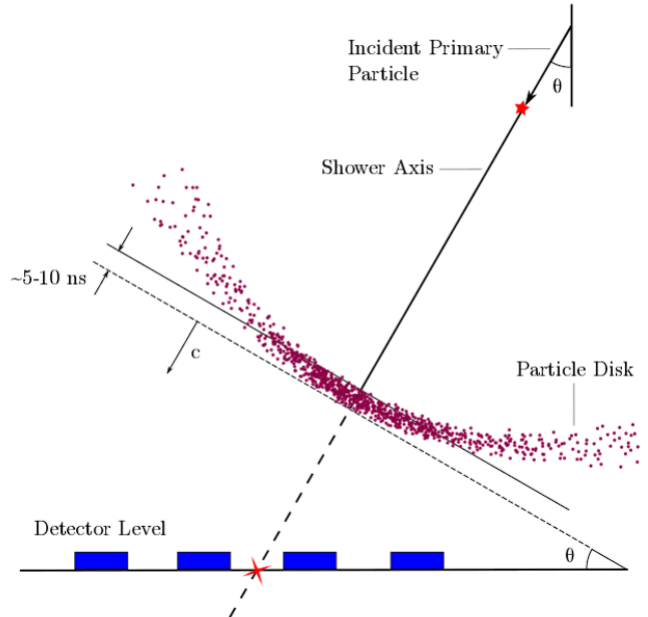


Figure 2.7 An air shower incident on WCDs. Secondary particles of an air shower travel in a cone centered on primary incident particle. Reconstruction of the initial angle is possible with arrival time of hits in PMTs inside WCDs. Figure from [33].

914 In the study of air showers, accurately determining the location of the air shower core on the  
 915 ground is crucial for reconstructing the direction of the originating primary particle. An illustration  
 916 of this can be seen in a HAWC event plot, Figs. 2.2 and 2.11, where the lateral charge distribution  
 917 across the array is displayed. The core is identified and marked with a red star, reconstructed using  
 918 a predetermined functional form, Eq. (2.1).

919 We model signal  $S_i$  from the  $i$ th PMT is given by the following equation:

$$S_i = S(A, \tilde{x}, \tilde{x}_i) = A \left( \frac{1}{2\pi\sigma^2} e^{-\frac{|\vec{x}_i - \vec{x}|^2}{2\sigma^2}} + \frac{N}{(0.5 + |\vec{x}_i - \vec{x}|/R_m)^3} \right) \quad (2.1)$$

920 In this model,  $\tilde{x}$  represents the core location and  $\tilde{x}_i$  is the position of the  $i$ th PMT.  $R_m$  stands for  
 921 the Molière radius, which is approximately 120 meters at the altitude of HAWC.  $\sigma$  is the standard  
 922 deviation of the Gaussian distribution.  $N$  is the normalization factor for the tail of the distribution.

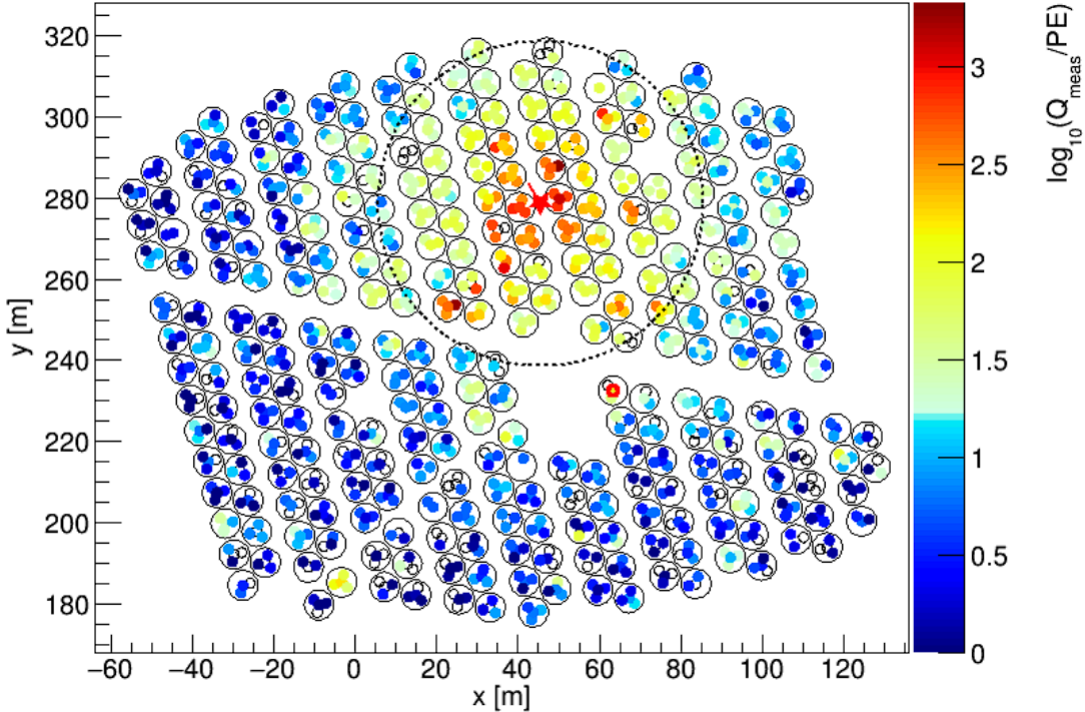


Figure 2.8 Charge deposition in each PMT for a reconstructed gamma-ray event. WCDs are outlined in black surrounding the 4 smaller circles that represent PMTs. The color scale indicates the charge deposition in each PMT. The best shower core fit from SFCF is noted with a red star in the center of the dashed circle [34].

923 The equation incorporates fixed values of  $\sigma = 10$  m and  $N = 5 \cdot 10^{-5}$ . This leaves the core location  
 924 and overall amplitude  $A$  as the free parameters to be determined during fitting.

925 The chosen functional form for the Super Fast Core Fit (SFCF) algorithm is a simplified version  
 926 of a modified Nishimura-Kamata-Greisen (NKG) function [35], selected for its computational  
 927 efficiency which is essential for rapid fitting of air shower cores. The SFCF form allows numerical  
 928 minimization to converge more quickly due to the function's simplicity, the analytical computation  
 929 of its derivatives, and the absence of a pole at the core location [34]. Figure 2.8 provides a  
 930 visualization of a recorded event, with the plot depicting the charge recorded by each PMT as a  
 931 function of the distance to the reconstructed shower core. Through the application of the SFCF,  
 932 core locations can be identified with a median error of approximately 2 m for large events and about  
 933 4 m for smaller ones, assuming the gamma-ray event core impacts directly upon the HAWC detector  
 934 array [34]. It is noted that as the core's distance from the main array increases, the precision in

935 locating the core diminishes [34], highlighting the importance of proximity in the accuracy of core  
936 reconstruction.

937 **2.2.2 Angle Reconstruction**

938 After establishing the core position, the next step is angle reconstruction. This process deter-  
939 mines the primary particle's trajectory. The angle of arrival is indicative of the originating gamma  
940 ray's direction. It correlates to the cosmic source of the gamma-ray. We deduce this angle using  
941 the timing of PMT hits [34].

942 The air shower's front is conically shaped, not flat. This shape arises from the travel patterns  
943 of secondary particles. An event example is illustrated in Fig. 2.7. Far from the core, secondary  
944 particles undergo multiple scattering. They also travel longer distances [36]. Particle sampling  
945 decreases with distance from the core. This decrease results in measurable delays in arrival times  
946 [36, 34]. Simulations provide a corrective measure for these effects. The correction is a function of  
947 shower parameters [34]. It adjusts both curvature and sampling. The distance from the shower core  
948 and the charge recorded by PMTs are crucial to this correction. A function based on simulation  
949 and Crab Nebula observations is used for this purpose [34]. This curvature correction allows us to  
950 fit the particle front as a plane wave.

951 Corrections lead to the  $\chi^2$  minimization step. This technique fits a plane to the timing data of  
952 the PMTs. It then calculates the shower's angle of arrival. The zenith and azimuth angles are the  
953 results of this fit [36]. The local angles are converted to celestial coordinates. These coordinates  
954 allow correlation with gamma-ray sources. Right ascension (RA) and declination (Dec) are used  
955 for this purpose. RA is akin to longitude, and Dec to latitude.

956 The reconstructed angle's resolution ranges from  $0.1^\circ$  to  $1^\circ$ . This range depends on the incoming  
957 particle's energy and zenith angle [36]. The analysis uses a curvature/sampling correction. This  
958 correction applies a quadratic function based on distance from the core [34]. The adjustment  
959 improves angular resolution. However, discrepancies between simulation and observation persist.  
960 These discrepancies introduce systematic errors into HAWC analyses [34].

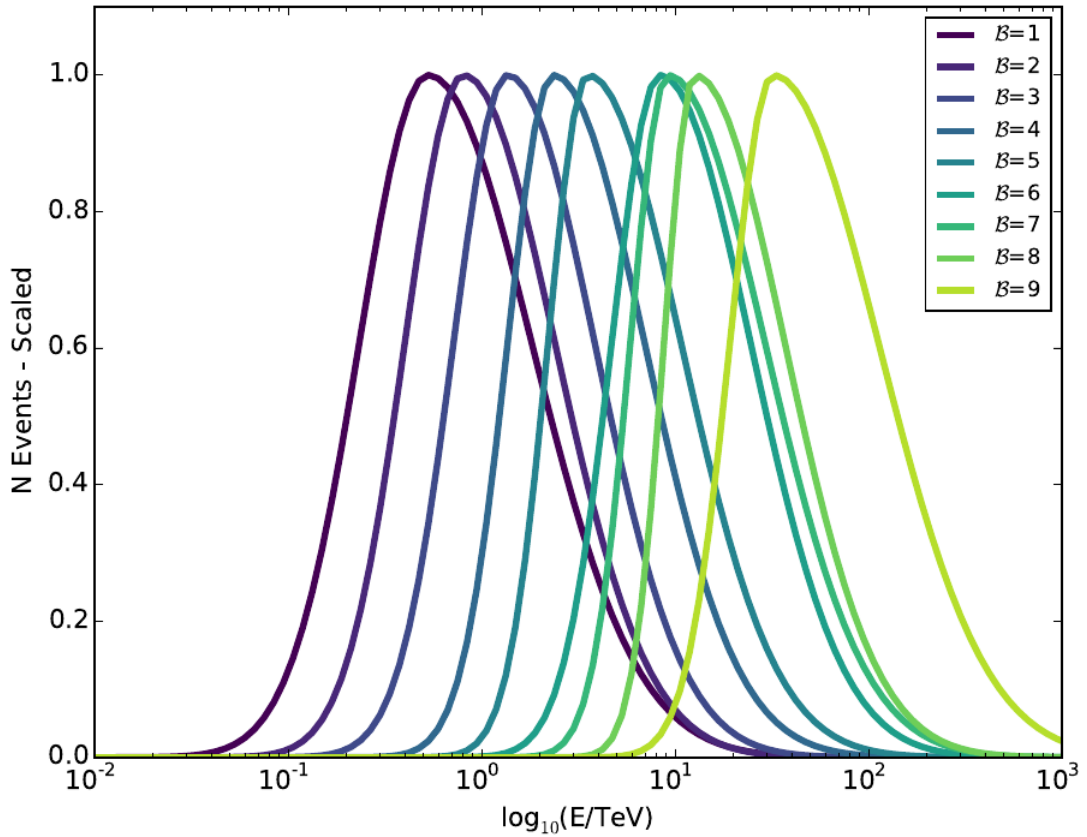


Figure 2.9 Simulated normalized energy distribution of each  $f_{\text{hit}}$  bin defined in Tab. 2.1. Monte Carlo simulation of gamma-rays with  $E^{-2.63}$  spectral shape and simulated source at  $20^\circ$  declination. Figure from [34].

Bin	Lower Edge %	Upper Edge %	$\Theta_{68}$ ( $^\circ$ )
1	6.7	10.5	1.05
2	10.5	16.2	0.69
3	16.2	24.7	0.50
4	24.7	35.6	0.39
5	35.6	48.5	0.30
6	48.5	61.8	0.28
7	61.8	74.0	0.22
8	74.0	84.0	0.20
9	84.0	100	0.17

Table 2.1 Definitions of  $f_{\text{hit}}$  energy estimator bins. Bins are defined by the fraction of available PMTs that are triggered during an air shower event. The angular resolution,  $\Theta_{68}$ , is the bin containing 68% of events [34].

961    **2.2.3  $f_{\text{hit}}$  Energy Estimation**

962    The HAWC Observatory quantifies the primary particle energy of air showers using a metric  
963    known as  $f_{\text{hit}}$ . This ratio compares the count of PMTs involved in the event reconstruction to the  
964    total number of functional PMTs at the time [34]. The main array consists of about 1200 PMTs,  
965    but the count may vary due to maintenance or other operational factors.

966    Events are stratified into several  $f_{\text{hit}}$  bins. Each bin corresponds to a specific range of angular  
967    resolutions, enabling a structured approach to event analysis based on the extent of the shower  
968    footprint, see Tab. 2.1. The  $f_{\text{hit}}$  metric, while effective, has several limitations. It is dependent on  
969    the zenith angle and the spectral characteristics presumed for the observed source. The variable  
970    also reaches a saturation point around 10 TeV, after which the detector's ability to discriminate  
971    between higher energy levels diminishes [34]. Furthermore, the energy distribution for each  $f_{\text{hit}}$   
972    bin is notably broad, see Fig. 2.9. In response to these limitations, HAWC has developed more  
973    intricate algorithms for energy estimation. These algorithms incorporate the zenith angle and  
974    the distribution of charge around the shower core for a more accurate assessment of the primary  
975    particle's energy, particularly at energies surpassing 10 TeV [36].

976    The relationship between  $f_{\text{hit}}$  and primary energy is complex. Atmospheric attenuation can  
977    cause high-energy showers to present a smaller footprint, misrepresenting their energy in the  $f_{\text{hit}}$   
978    metric. This effect is captured in simulations that chart the actual energy distribution across  $f_{\text{hit}}$   
979    categories [36]. Such distributions vary with the declination of the source and the theoretical  
980    energy spectrum used in the model.

981    **2.2.4 Neural Network Energy Estimation**

982    The energy estimation for photon events at the HAWC Observatory is refined through an  
983    artificial neural network (NN) algorithm. This method, based on the Toolkit for Multivariate  
984    Analysis NN, adopts a multilayer-perceptron model with logistic activation functions across its  
985    layers. The structure includes two hidden layers, the first with 15 nodes and the second with 14,  
986    designed to process input variables through a neural network optimized to estimate primary particle  
987    energies [38].

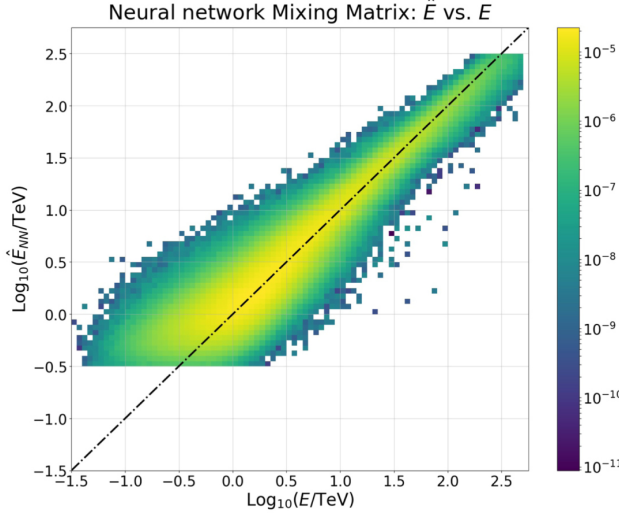


Figure 2.10 Neural Network energy estimator performance compared to true energy. The dotted line is the identity line where the estimator and injection agree. Gamma/hadron separation cuts were applied with the energy estimation. Figure pulled from [37]

988     The NN is trained to minimize a specific error function that measures discrepancies between the  
 989    NN's energy predictions and the actual energies from Monte Carlo simulations. This minimization  
 990    targets an error function that incorporates the relative importance of each event, weighting more  
 991    the importance to mimic an  $E^{-2}$  power law spectrum. This approach helps achieve a uniform  
 992    error rate across energies ranging from 1 to 100 TeV. The optimization process leverages the  
 993    Broyden-Fletcher-Goldfarb-Shanno algorithm that calibrates the NN's 479 weights [37].

994     The spectral analysis employs a binned likelihood method, using a forward-folding technique  
 995    to accommodate the energy estimate's bias and resolution [37]. This establishes a 2D binning  
 996    scheme that categorizes events by both their  $f_{\text{hit}}$  value and estimated energy. The decision to use  
 997    this scheme over a simple energy-based binning lies in the correlation between gamma/hadron  
 998    separation parameters and the angular resolution with both the size and energy of the event. The  
 999    spectrum of interest is partitioned into nine  $f_{\text{hit}}$  bins, each further divided into 12 energy bins,  
 1000    spanning from 0.316 TeV to 316 TeV, encompassing a total of 108 bins [37]. However, not all  
 1001    bins contribute to the final estimate. Bins with low event populations or insufficient Monte Carlo  
 1002    simulation are excluded. This approach focuses on the central 99% of events by estimated energy  
 1003    within each  $f_{\text{hit}}$  bin, effectively removing outliers [37].

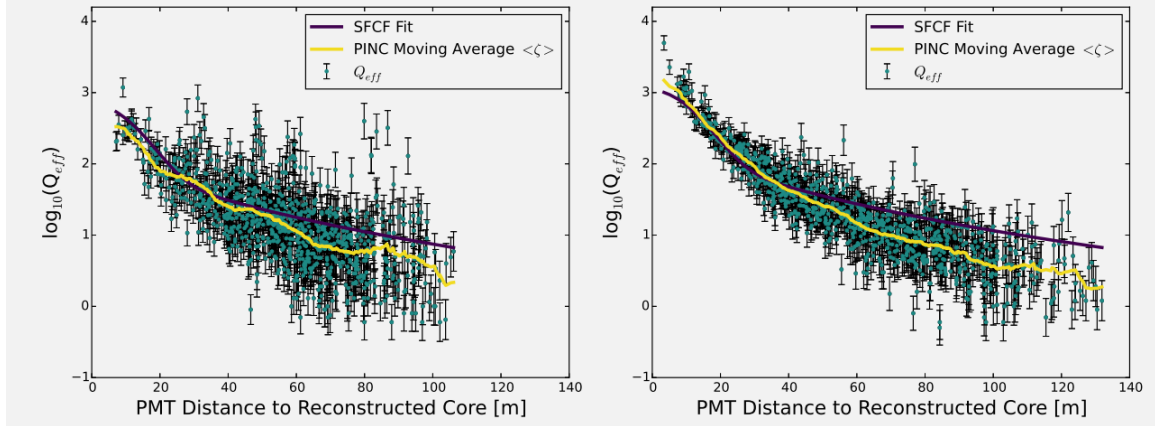


Figure 2.11 Lateral distribution functions (LDFs) for cosmic ray (left) and a photon candidate from the Crab Nebula (right). Cosmic ray LDF has clearly isolated hits far from the reconstructed shower core. Gamma-ray shower shows a more cuspy event [34].

1004 Input variables for the NN are selected to capture key characteristics of the air shower: energy  
 1005 deposition, containment, and atmospheric attenuation. The algorithm calculates energy deposition  
 1006 using the fraction of PMTs and tanks activated, alongside the logarithm of the normalization from  
 1007 the lateral distribution fit. Containment is inferred from the distance between the shower core and  
 1008 the array's center, while atmospheric attenuation is evaluated using the reconstructed zenith angle  
 1009 and a detailed analysis of the shower's lateral charge distribution [38, 37].

1010 This refined NN energy estimation methodology is an integral component of HAWC's toolkit,  
 1011 enabling precise analysis of high-energy gamma-ray events. It represents a significant advancement  
 1012 in the field by more accurately mapping observed shower characteristics to primary particle energies.

### 1013 2.2.5 G/H Discrimination

1014 At the HAWC Observatory, distinguishing between air showers initiated by gamma rays and  
 1015 those by hadronic cosmic rays is fundamental for astrophysical data purity. The separation process  
 1016 leverages differences in shower characteristics: electromagnetic showers from gamma rays typically  
 1017 display fewer muons and a smoother lateral distribution, whereas hadronic showers are more chaotic  
 1018 due to the abundance of muons and hadronic sub-showers.

1019 Two primary parameters facilitate the identification of cosmic-ray events [34]:

1020 Compactness (C): This parameter evaluates the charge captured by PMTs, particularly focusing  
 1021 on the PMT with the highest effective charge beyond a 40-meter radius from the shower core.

1022 Compactness is inversely proportional to this effective charge, as higher charges at extended  
1023 distances from the core are indicative of hadronic showers. It is mathematically expressed as:

$$C = \frac{N_{\text{hit}}}{CxPE_{40}} \quad (2.2)$$

1024 where  $N_{\text{hit}}$  is the number of PMTs hit and  $CxPE_{40}$  is the effective charge measured outside a 40 m  
1025 radius from the shower cores [34].

1026 PINCness (P): PINCness quantifies the "clumpiness" of a shower using the charges recorded  
1027 by PMTs and is short for Parameter for Identifying Nuclear Cosmic Rays. It is computed from the  
1028 logarithm of the effective charge,  $Q_{\text{eff},i}$ , of each PMT hit,  $i$ , compared to an expected average for  
1029 that annular region. A higher PINCness suggests a less smooth distribution, typical of hadronic  
1030 showers. The formula is:

$$P = \frac{1}{N} \sum_{i=0}^N \frac{(\zeta_i - \langle \zeta \rangle)^2}{\sigma_{\zeta_i}^2} \quad (2.3)$$

1031 where  $\zeta_i = \log_{10}(Q_{\text{eff},i})$ . The average,  $\langle \zeta \rangle$  is the average over an annular region surrounding the  
1032 shower core. The errors,  $\sigma_{\zeta_i}$ , are computed and allocated from gamma-ray candidates close to the  
1033 Crab.

1034 These parameters are tested and modeled in simulations and with observational data near the  
1035 Crab Nebula. Figure 2.11 illustrating the lateral distributions for representative cosmic-ray and  
1036 photon candidate showers, as well as the distribution of these discrimination parameters, affirm  
1037 their efficacy [34].

1038 The discrimination technique has remained consistent, but cut values have been reoptimized  
1039 for the 2D bins based on  $f_{\text{hit}}$  and NN estimated energy. This refinement enhances the selection  
1040 of high-energy events. Each bin ensures at least 50% efficiency for gamma-ray detection, with  
1041 efficiencies extending up to nearly 100% in certain bins [34, 37].

## 1042 2.3 Background Estimation: Direct Integration

1043 The ratio of cosmic rays to gamma rays can be as high as 10,000 to 1, depending on the energy.  
1044 At HAWC, we confront a significant challenge even after gamma/hadron cuts: our gamma-ray data  
1045 is still inundated with cosmic-ray events. To tackle this, we rely on the direct integration method

1046 developed by Milagro [39]. This method capitalizes on the cosmic rays' isotropic nature resulting  
1047 from their deflection by interstellar magnetic fields.

1048 The direct integration method estimates background events by integrating over a stable two-  
1049 hour period of detector operation. The expected number of background events at a particular sky  
1050 coordinate  $(\phi, \theta)$  is determined by integrating the normalized detector's efficiency with the all-sky  
1051 event rate:

$$N_{\text{exp}}(\phi, \theta) = \int \int E(\text{ha}, \theta) \cdot R(t) dt \quad (2.4)$$

1052 Here,  $E(\text{ha}, \theta)$ , represents the detector's efficiency, which varies with local coordinates (hour angle  
1053 and declination).  $R(t)$  is the event rate as a function of time [39].

1054 Our background estimation is expected to falter in high-energy ranges where cosmic-ray events  
1055 are less frequent due to enhanced gamma/hadron discrimination. Sparsity in our background and  
1056 data also arise at the limits of HAWC's sensitivity and during short-term analyses of transient events.  
1057 HAWC addresses these issues by using a pixel size of  $0.5^\circ$  in our direct integration to maintain  
1058 robustness in our estimation [34, 36]. In constructing the background model, it's crucial to exclude  
1059 areas of the sky with known gamma-ray sources. Regions containing the Crab Nebula, Mrk 421,  
1060 Mrk 501, and the Galactic Plane are masked to prevent their significant gamma-ray signals from  
1061 biasing our background estimate [34].

## CHAPTER 3

### GLORY DUCK: MULTI-WAVELENGTH SEARCH FOR DARK MATTER ANNIHILATION TOWARDS DWARF SPHEROIDAL GALAXIES

#### 3.1 Introduction

The field of astrophysics now has several instruments and observatories sensitive to high energy gamma-rays. The energy sensitivity for the modern gamma-ray program spans many orders of magnitude. Figure 3.1 demonstrates these comparable sensitivities across energies for the five experiments: Fermi-LAT, HAWC, HESS, MAGIC, and VERITAS.

Each of the five experiments featured in Figure 3.1 have independently searched for DM annihilation from dwarf spheroidal galaxies (dSph) and set limits on annihilation cross-section of WIMPs. Intriguingly, there are regions of substantial overlap in their energy sensitivities. This clearly motivates an analysis that combines data from these five. Each experiment has unique gamma-ray detection methods and their weaknesses and strengths can be leveraged with each other. The HAWC gamma-ray observatory is extensively introduced in chapter 2, so it is not introduced here. A brief description of the remaining experiments are in the following paragraphs.

The Large Area Telescope (LAT) is a pair conversion telescope mounted on the NASA Fermi satellite in orbit  $\sim$ 550 km above the Earth [41]. LAT's field of view covers about 20% of the whole sky, and it sweeps the whole sky approximately every 3 hours. LAT's gamma-ray energy sensitivity ranges from 20 MeV up to 1 TeV. Previous DM searches towards dSphs using Fermi-LAT are published in [42] and [43].

The High Energy Spectroscopic System (HESS), Major Atmospheric Gamma Imaging Cherenkov (MAGIC), and Very Energetic Radiation Imaging Telescope Array System (VERITAS) are arrays of Imaging Atmospheric Cherenkov Telescopes (IACT). These telescopes observe the Cherenkov light emitted from gamma-ray showers in the Earth's atmosphere. The field of view for these telescopes is no larger than  $5^\circ$  with energy sensitivities ranging from 30 GeV up to 100 TeV [44, 45, 46]. IACTs are able to make precise observations in selected regions of the sky, however can only be operated in ideal dark conditions. HESS's observations of the dwarves

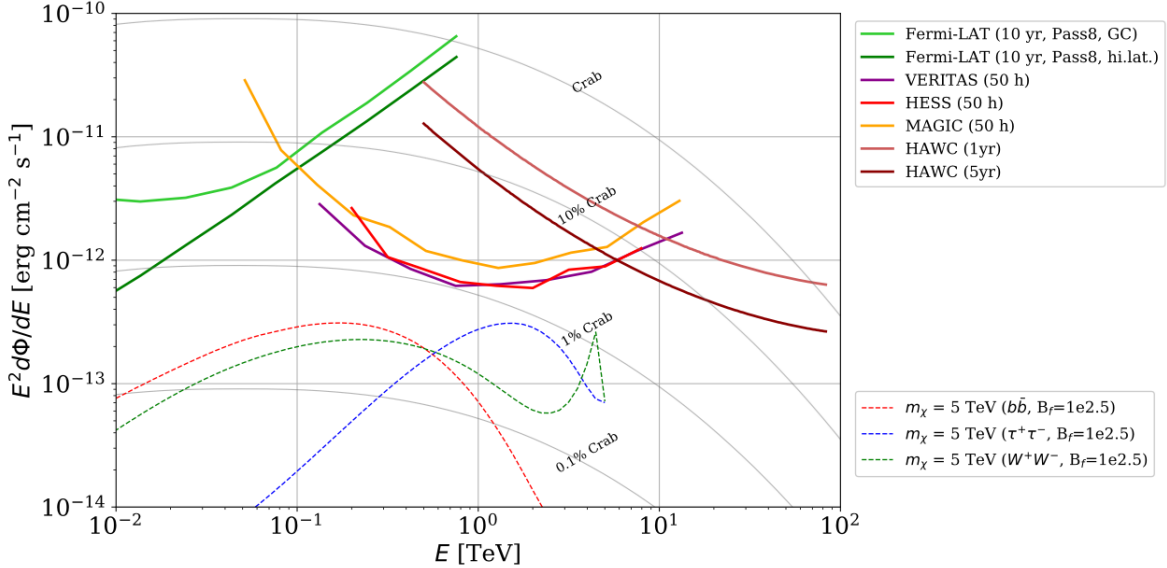


Figure 3.1 Sensitivities of five gamma-ray experiments compared to percentages of the Crab nebula's emission and dark matter annihilation. Solid lines present estimated sensitivities to power law spectra [FACT CHECK THIS] for each experiment. Green lines are Fermi-LAT sensitivities where lighter green is the sensitivity to the galactic center and dark green is its sensitivity to higher declinations. Orange, red, and purple solid lines represent the MAGIC, HESS, and VERITAS 50 hour sensitivities respectively. The maroon and brown lines are the HAWC 1 year and 5 year sensitivities. Across four decades of gamma-ray energy, these experiments have similar sensitivities on the order  $10^{-12}$  erg  $\text{cm}^{-2}\text{s}^{-1}$ . The dotted lines are estimated dark matter fluxes assuming  $m_\chi = 5$  TeV DM annihilating to bottom quarks (red), tau leptons (blue), and W bosons (green). Faded gray lines outline percentage flux of the Crab nebula. Figure is an augmented version of [40]

1088 Sculptor and Carina were between January 2008 and December 2009. HESS's observations of  
 1089 Coma Berenices were taken from 2010 to 2013, and Fornax was observed in 2010 [47, 48, 49].  
 1090 MAGIC provided deep observations of Segue1 between 2011 and 2013 [50]. MAGIC also provides  
 1091 data for three additional dwarves: Coma Berenices, Draco, and Ursa Major II where observations  
 1092 were made in: January - June 2019 [51], March - September 2018 [51], and 2014 - 2016 [52]  
 1093 respectively. VERITAS provided data for Boötes I, Draco, Segue 1, and Ursa Minor from 2009 to  
 1094 2016 [53].

1095 This chapter presents the Glory Duck analysis, the name given for the search for dark matter  
 1096 annihilation from dSph by combining data from the five gamma-ray observatories: Fermi-LAT,  
 1097 HAWC, HESS, MAGIC, and VERITAS. Specifically, the methods in analysis and modeling are  
 1098 presented for the HAWC gamma-ray observatory. This work will be published in the Journal of

1099 Cosmology and Astroparticle Physics and presented at the International Cosmic Ray Conference  
1100 in 2019, 2021, and 2023 [54, 55, 56] and others.

1101 **3.2 Dataset and Background**

1102 This section enumerates the data analysis and background estimation methods used for HAWC's  
1103 study of dSphs. Section 3.2.1 and Section 3.2.2 are most useful for fellow HAWC collaborators  
1104 looking to replicate the Glory Duck analysis.

1105 **3.2.1 Itemized HAWC files**

1106 These files are only available withing HAWC's internal documentation and collaborators. They  
1107 are not meant for public access, and are presented here so that HAWC collaborators can reproduce  
1108 results accurately.

- 1109 • Detector Response: `response_aerie_svn_27754_systematics_best_mc_test_noBr`  
1110       `oadpulse\10pctlogchargesmearing_0.63qe_25kHzNoise_run5481_curvature`  
1111       `0_index3.root`
- 1112 • Data Map: `maps-20180119/liff/maptree_1024.root`
- 1113 • Spectral Dictionary: `DM_CirrelliSpectrum_dict_gammas.npy`
- 1114 • Analysis wiki: [https://private.hawc-observatory.org/wiki/index.php/Glory\\_Duck\\_Multi-Experiment\\_Dark\\_Matter\\_Search](https://private.hawc-observatory.org/wiki/index.php/Glory_Duck_Multi-Experiment_Dark_Matter_Search)

1116 **3.2.2 Software Tools and Development**

1117 This analysis was performed using HAL and 3ML [34, 57] in Python version 2. I built software  
1118 to implement the *A Poor Particle Physicist Cookbook for Dark Matter Indirect Detection* (PPPC)  
1119 [58] DM spectral model and dSphs spatial model from [59] for HAWC analysis. A NumPy version  
1120 of this dictionary was made for both Py2 and Py3. The code base for creating this dictionary is  
1121 linked on my GitLab sandbox:

- 1122 • Py2: [Dictionary Generator \(Deprecated\)](#)

- 1123 • Py3: [PPPC2Dict](#)

1124 The analysis was performed using the  $f_{hit}$  framework as used and described in the HAWC Crab  
1125 paper [34]. The Python2 NumPy dictionary file for gamma-ray final states is `dmCirSpecDict.npy`.  
1126 The corresponding Python3 file is `DM_CirrelliSpectrum_dict_gammas.npy`. These files can  
1127 also be used for decay channels and the PPPC describes how [58]. All other software used for data  
1128 analysis, DM profile generation, and job submission to SLURM are also kept in my sandbox for  
1129 [the Glory Duck](#) project.

1130 **3.2.3 Data Set and Background Description**

1131 The HAWC data maps used for this analysis contain 1017 days of data between runs 2104  
1132 (2014-11-26) and 7476 (2017-12-20). They were generated from pass 4.0 reconstruction. The  
1133 analysis is performed using the  $f_{hit}$  energy binning scheme with bins (1-9) similar to what was done  
1134 for the Crab and previous HAWC dSph analysis [34, 60]. Bin 0 was excluded as it has substantial  
1135 hadronic contamination and poor angular resolution.

1136 This analysis was done on dSphs because of their large DM mass content relative to baryonic  
1137 mass. We consider the following to estimate the background to this study.

- 1138 • The dSphs' angular extent are small relative to HAWC's spatial resolution, so the analysis is  
1139 not sensitive to large or small scale anisotropies.
- 1140 • The dSphs used in this analysis are off the galactic plane and therefore not contaminated by  
1141 diffuse emission from the galaxy.
- 1142 • The dSphs are baryonically faint relative to their expected dark matter content and are not  
1143 expected to contain high energy gamma-ray sources.

1144 Therefor we make no additional assumptions on the background from our sources and use  
1145 HAWC's standard direct integration method for background estimation [34]. The largest background  
1146 under this consideration is from an isotropic flux of cosmic rays. The contamination of this hadronic  
1147 flux is worse at lower energies where HAWC's gamma/hadron discrimination worse. It is possible

1148 for gamma rays from DM annihilation to scatter in transit to HAWC via Inverse Compton Scattering  
1149 (ICS). This was investigated and its impact on the flux is negligible. Supporting information on  
1150 this is in Section 3.7.1

1151 **3.3 Analysis**

1152 The expected differential photon flux from DM-DM annihilation to standard model particles,  
1153  $d\Phi_\gamma/dE_\gamma$ , over solid angle,  $\Omega$ , is described by the familiar equation.

$$\frac{d\Phi_\gamma}{dE_\gamma} = \frac{\langle\sigma v\rangle}{8\pi m_\chi^2} \frac{dN_\gamma}{dE_\gamma} \times \int_{\text{source}} d\Omega \int_{l.o.s} dl \rho_\chi^2 J(r, \theta') \quad (3.1)$$

1154 Where  $\langle\sigma v\rangle$  is the velocity weighted annihilation cross-section.  $\frac{dN}{dE}$  is the expected differential  
1155 number of photons produced at each energy per annihilation.  $m_\chi$  is the rest mass of the supposed  
1156 DM particle.  $\rho_\chi$  is the DM density.  $J$  is the astrophysical J-factor and is defined as

$$J = \int d\Omega \int_{l.o.s} dl \rho_\chi^2(r, \theta') \quad (3.2)$$

1157  $l$  is the distance to the source from Earth.  $r$  is the radial distance from the center of the source.  $\theta'$  is  
1158 the half angle defining a cone containing the DM source. How each component is synthesized and  
1159 considered for HAWC's analysis is presented in the following sections. Section 3.3.1 presents the  
1160 particle physics model for DM annihilation. Section 3.3.2 presents the spatial distributions built  
1161 for each dSph.

1162 **3.3.1  $\frac{dN_\gamma}{dE_\gamma}$  - Particle Physics Component**

1163 For these spectra, we import the PPPC with Electroweak (EW) corrections [58]. Public versions  
1164 of the imported tables are provided by the [authors online](#). The spectrum is implemented as a model  
1165 script in astromodels for 3ML. The EW corrections were previously not considered for HAWC and  
1166 are significant for DM annihilating to EW coupled SM particles such as all leptons, and the  $\gamma$ ,  
1167  $Z$ , and  $W$  bosons [60]. Figure 3.2 demonstrates the significance of EW corrections for W boson  
1168 annihilation. Across EW SM channels, the gamma-ray spectra become harder than spectra without  
1169 EW corrections. Tables from the PPPC were reformatted into Python NumPy dictionaries for  
1170 collaboration-wide use. A class in astromodels was developed to include the EW correction from  
1171 the PPPC and is aptly named `PPPCSpectra` within `DM_models.py`.

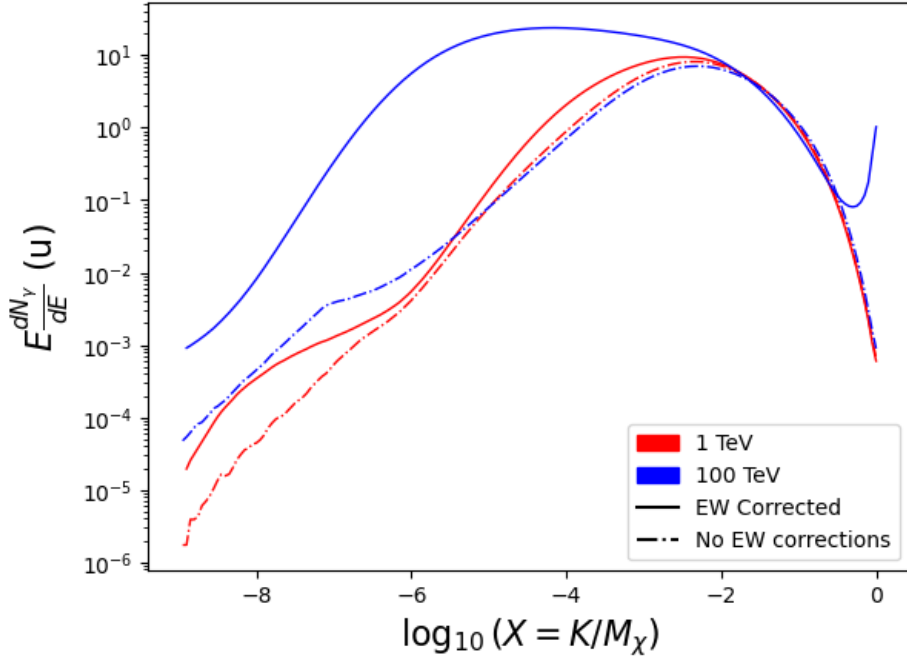


Figure 3.2 Effect of Electroweak (EW) corrections on expected DM annihilation spectrum for  $\chi\chi \rightarrow W^-W^+$ . Solid lines are spectral models that consider EW corrections. Dash-dot lines are spectral models without EW corrections. Red lines are models for  $M_\chi = 1$  TeV. Blue lines represent models for  $M_\chi = 100$  TeV. All models are sourced from the PPPC4DMID [58].

### 1172 3.3.2 J- Astrophysical Component

1173 The J-factor profiles for each source are imported from Geringer-Sameth (referred to with  $\mathcal{GS}$ )

1174 [59].  $\mathcal{GS}$  fits the Zhao DM profile to the dSphs which has a DM density described as [61]

$$\rho(r) = \frac{\rho_0}{(r/R_s)^\gamma (1 + (r/R_s)^\alpha)^{(\beta-\gamma)}}. \quad (3.3)$$

1175  $R_s$  is the scale radius and free parameter in the model.  $\gamma$  is the logarithmic slope in the region

1176  $r \ll R_s$ .  $\beta$  is the logarithmic slope in the region  $r \gg R_s$ .  $\alpha$  is known as the sharpness of transition

1177 where  $r \approx R_s$ . The classic Navarro-Frenk-White [62] (NFW) can be retrieved from Zhao by fixing

1178  $(\alpha, \beta, \gamma) = (1, 3, 1)$ .

1179  $\mathcal{GS}$  best fits were pulled from the publication as  $J(\theta)$ , where  $\theta$  is the angular separation from

1180 the center of the source. HAWC requires maps in terms of  $\frac{dJ}{d\Omega}$ , so the conversion from the maps

1181 was done in the following way...

1182 First, convert the angular distances to solid angles

$$\Omega = 2 \cdot \pi(1 - \cos(\theta)) \quad (3.4)$$

1183 which reduces with a small angle approximation to  $\pi\theta^2$ . Next, the central difference for both the  
1184  $\Delta J$  and  $\Delta\Omega$  value were calculated from the discretized  $J(\theta)$  with the central difference stencil:

$$\Delta\phi_i = \phi_{i+1} - \phi_{i-1} \quad (3.5)$$

1185 Where  $\phi$  is either  $\Omega$  or  $J$ . These were done separately in case the grid spacing in  $\theta$  was not uniform.  
1186 Finally, these lists are divided so that we are left with an approximation of the  $dJ/d\Omega$  profile that  
1187 is a function of  $\theta$ . Admittedly, this is an approximation method for the map which introduces small  
1188 errors compared to the true profile estimate. This was checked as a systematic against the author's  
1189 profiling of the spatial distribution and is documented in Section 3.8.1.

1190 With  $\frac{dJ}{d\Omega}(\theta)$ , a map is generated, first by filling in the north-east quadrant of the map. This  
1191 quadrant is then reflected twice, vertically then horizontally, to fill the full map. Maps are then  
1192 normalized by dividing the discrete 2D integral of the map. The 2D integral was a simple height  
1193 of bins, Newton's integral:

$$p^2 \cdot \sum_{i,j=0}^{N,M} \frac{dJ}{d\Omega}(\theta_{i,j}, \phi_{i,j}) \quad (3.6)$$

1194 These maps are HEALpix maps with NSIDE 16384 and saved in the .fits format. The hyper fine  
1195 resolution was selected to better preserve the total expected counts after integrating Eq. (3.1) with  
1196 the detector response.

1197 Another DM spatial distribution model from Bonnivard ( $\mathcal{B}$ ) [63] was used for the Glory Duck  
1198 study. However, to save computational time, limits from  $\mathcal{GS}$  were scaled to  $\mathcal{B}$  instead of each  
1199 experiment performing a full study a second time. How these models compare is demonstrated  
1200 for each dSph in Figure 3.16 and Figure 3.17 Plots of these maps are provided for each source  
1201 in chapter A Examples of the two most impactful dSphs derived from  $\mathcal{GS}$ , Segue1 and Coma  
1202 Berenices are featured in Figure 3.3

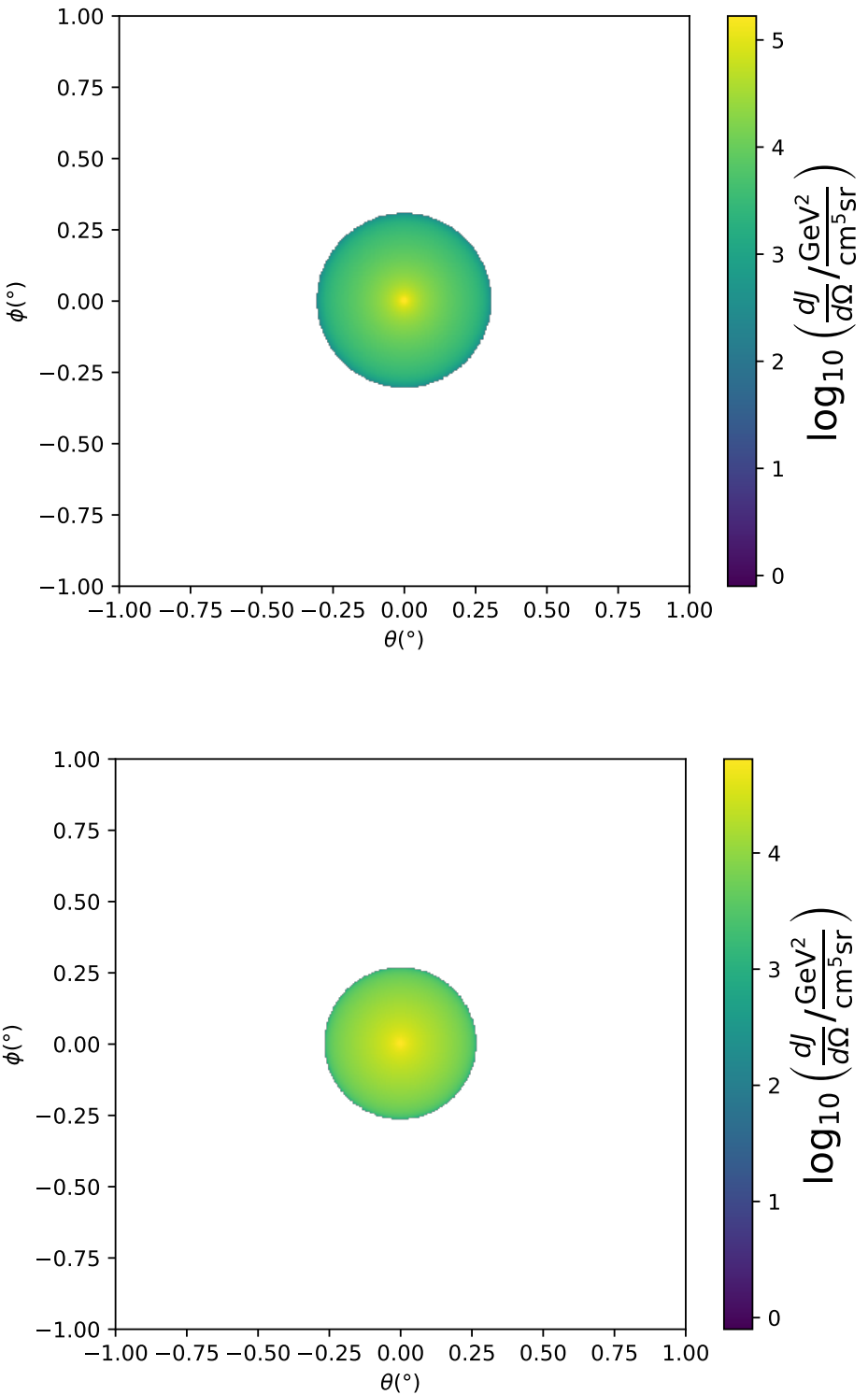


Figure 3.3  $\frac{dJ}{d\Omega}$  maps for Segue1 (top) and Coma Berenices (bottom). Origin is centered on the specific dwarf spheroidal galaxies (dSph). X and Y axes are the angular separation from the center of the dwarf. Profile is truncated at the scale radius. Plots of the remaining 11 dSph HAWC studied are linked in Fig. A.1.

1203 **3.3.3 Source Selection and Annihilation Channels**

1204 We use many of the dSphs presented in HAWC’s previous dSph DM search [60]. HAWC’s  
1205 sources for Glory Duck include Boötes I, Coma Berenices, Canes Venatici I + II, Draco, Hercules,  
1206 Leo I, II, + IV, Segue 1, Sextans, and Ursa Major I + II. A full description of all sources used  
1207 in Glory Duck is found in Table 3.1. Triangulum II was excluded from the Glory Duck analysis  
1208 because of large uncertainties in its  $J$  factor. Ursa Minor was excluded from HAWC’s contribution  
1209 to the combination because the source extension model extended Ursa Minor beyond HAWC’s field  
1210 of view. Ursa Minor was not expected to contribute significantly to the combined limit, so work  
1211 was not invested in a solution to include Ursa Minor.

1212 This analysis improves on the previous HAWC dSph paper [60] in the following ways. Pre-  
1213 viously, the dSphs were treated and implemented as point sources. For this analysis, dSphs are  
1214 modeled and treated as extended source. The impact of this change with respect to the upper limit  
1215 is source dependent and is explored in Section 3.7.2. Previously, the particle physics model used for  
1216 gamma-ray spectra from DM annihilation did not have EW corrections where the PPPC includes  
1217 them. Finally, the gamma-ray ray dataset is much larger. The study performed here analyzes over  
1218 1000 days of data compared to 507.

1219 The SM annihilation channels probed for the Glory Duck combination include  $b\bar{b}$ ,  $e\bar{e}$ ,  $\mu\bar{\mu}$ ,  $\tau\bar{\tau}$ ,  
1220  $t\bar{t}$ ,  $W^+W^-$ , and  $ZZ$ . A summary of all sources, with a description of each experiments’ sensitivity  
1221 to the source, is provided in Table 3.2.

1222 **3.4 Likelihood Methods**

1223 **3.4.1 HAWC Likelihood**

1224 For every analysis bin in energy,  $f_{hit}$  bins (1-9), and location, we can expect  $N$  signal events and  
1225  $B$  background events. The expected number of excess signal events from dark matter annihilation,  
1226  $S$ , is estimated by convolving Equation (3.1) with HAWC’s energy response and pixel point spread  
1227 functions. I then compute the test statistic (TS) with the log-likelihood ratio test,

$$TS_{\max} = -2 \ln \left( \frac{\mathcal{L}_0}{\mathcal{L}_{\max}} \right) \quad (3.7)$$

Table 3.1 Summary of the relevant properties of the dSphs used in the present work. Column 1 lists the dSphs. Columns 2 and 3 present their heliocentric distance and galactic coordinates, respectively. Columns 4 and 5 report the  $J$ -factors of each source given from the  $\mathcal{GS}$  and  $\mathcal{B}$  independent studies and their estimated  $\pm 1\sigma$  uncertainties. The values  $\log_{10} J$  ( $\mathcal{GS}$  set) [59] correspond to the mean  $J$ -factor values for a source extension truncated at the outermost observed star. The values  $\log_{10} J$  ( $\mathcal{B}$  set) [63] are provided for a source extension at the tidal radius of each dSph. **Bolded sources are within HAWC’s field of view and provided to the Glory Duck analysis.**

Name	Distance (kpc)	$l, b$ ( $^{\circ}$ )	$\log_{10} J$ ( $\mathcal{GS}$ set) $\log_{10}(\text{GeV}^2\text{cm}^{-5}\text{sr})$	$\log_{10} J$ ( $\mathcal{B}$ set) $\log_{10}(\text{GeV}^2\text{cm}^{-5}\text{sr})$
<b>Boötes I</b>	66	358.08, 69.62	$18.24^{+0.40}_{-0.37}$	$18.85^{+1.10}_{-0.61}$
<b>Canes Venatici I</b>	218	74.31, 79.82	$17.44^{+0.37}_{-0.28}$	$17.63^{+0.50}_{-0.20}$
<b>Canes Venatici II</b>	160	113.58, 82.70	$17.65^{+0.45}_{-0.43}$	$18.67^{+1.54}_{-0.97}$
Carina	105	260.11, -22.22	$17.92^{+0.19}_{-0.11}$	$18.02^{+0.36}_{-0.15}$
<b>Coma Berenices</b>	44	241.89, 83.61	$19.02^{+0.37}_{-0.41}$	$20.13^{+1.56}_{-1.08}$
<b>Draco</b>	76	86.37, 34.72	$19.05^{+0.22}_{-0.21}$	$19.42^{+0.92}_{-0.47}$
Fornax	147	237.10, -65.65	$17.84^{+0.11}_{-0.06}$	$17.85^{+0.11}_{-0.08}$
<b>Hercules</b>	132	28.73, 36.87	$16.86^{+0.74}_{-0.68}$	$17.70^{+1.08}_{-0.73}$
<b>Leo I</b>	254	225.99, 49.11	$17.84^{+0.20}_{-0.16}$	$17.93^{+0.65}_{-0.25}$
<b>Leo II</b>	233	220.17, 67.23	$17.97^{+0.20}_{-0.18}$	$18.11^{+0.71}_{-0.25}$
<b>Leo IV</b>	154	265.44, 56.51	$16.32^{+1.06}_{-1.70}$	$16.36^{+1.44}_{-1.65}$
Leo V	178	261.86, 58.54	$16.37^{+0.94}_{-0.87}$	$16.30^{+1.33}_{-1.16}$
Leo T	417	214.85, 43.66	$17.11^{+0.44}_{-0.39}$	$17.67^{+1.01}_{-0.56}$
Sculptor	86	287.53, -83.16	$18.57^{+0.07}_{-0.05}$	$18.63^{+0.14}_{-0.08}$
<b>Segue I</b>	23	220.48, 50.43	$19.36^{+0.32}_{-0.35}$	$17.52^{+2.54}_{-2.65}$
Segue II	35	149.43, -38.14	$16.21^{+1.06}_{-0.98}$	$19.50^{+1.82}_{-1.48}$
<b>Sextans</b>	86	243.50, 42.27	$17.92^{+0.35}_{-0.29}$	$18.04^{+0.50}_{-0.28}$
<b>Ursa Major I</b>	97	159.43, 54.41	$17.87^{+0.56}_{-0.33}$	$18.84^{+0.97}_{-0.43}$
<b>Ursa Major II</b>	32	152.46, 37.44	$19.42^{+0.44}_{-0.42}$	$20.60^{+1.46}_{-0.95}$
Ursa Minor	76	104.97, 44.80	$18.95^{+0.26}_{-0.18}$	$19.08^{+0.21}_{-0.13}$

Table 3.2 Summary of dSph observations by each experiment used in this work. A ‘-’ indicates the experiment did not observe the dSph for this study. For Fermi-LAT, the exposure at 1 GeV is given. For HAWC,  $|\Delta\theta|$  is the absolute difference between the source declination and HAWC latitude. HAWC is more sensitive to sources with smaller  $|\Delta\theta|$ . For IACTs, we show the zenith angle range, the total exposure, the energy range, the angular radius  $\theta$  of the signal or ON region, the ratio of exposures between the background-control (OFF) and signal (ON) regions ( $\tau$ ), and the significance of gamma-ray excess in standard deviations,  $\sigma$ .

Source name	Fermi-LAT	HAWC	H.E.S.S, MAGIC, VERITAS						
	Exposure ( $10^{11}$ s m $^2$ )	$ \Delta\theta $ ( $^\circ$ )	IACT	Zenith ( $^\circ$ )	Exposure (h)	Energy range (GeV)	$\theta$ ( $^\circ$ )	$\tau$	$S$ ( $\sigma$ )
Boötes I	2.6	4.5	VERITAS	15 – 30	14.0	100–41000	0.10	8.6	-1.0
Canes Venatici I	2.9	14.6	–	–	–	–	–	–	–
Canes Venatici II	2.9	15.3	–	–	–	–	–	–	–
Carina	3.1	–	H.E.S.S.	27 – 46	23.7	310 – 70000	0.10	18.0	-0.3
Coma Berenices	2.7	4.9	H.E.S.S.	47 – 49	11.4	550 – 70000	0.10	14.4	-0.4
Draco	3.8	38.1	MAGIC	5 – 37	49.5	60 – 10000	0.17	1.0	–
			MAGIC	29 – 45	52.1	70 – 10000	0.22	1.0	–
			VERITAS	25 – 40	49.8	120 – 70000	0.10	9.0	-1.0
Fornax	2.7	–	H.E.S.S.	11 – 25	6.8	230 – 70000	0.10	45.5	-1.5
Hercules	2.8	6.3	–	–	–	–	–	–	–
Leo I	2.5	6.7	–	–	–	–	–	–	–
Leo II	2.6	3.1	–	–	–	–	–	–	–
Leo IV	2.4	19.5	–	–	–	–	–	–	–
Leo V	2.4	–	–	–	–	–	–	–	–
Leo T	2.6	–	–	–	–	–	–	–	–
Sculptor	2.7	–	H.E.S.S.	10 – 46	11.8	200 – 70000	0.10	19.8	-2.2
Segue I	2.5	2.9	MAGIC	13 – 37	158.0	60 – 10000	0.12	1.0	-0.5
			VERITAS	15 – 35	92.0	80 – 50000	0.10	7.6	0.7
Segue II	2.7	–	–	–	–	–	–	–	–
Sextans	2.4	20.6	–	–	–	–	–	–	–
Ursa Major I	3.4	32.9	–	–	–	–	–	–	–
Ursa Major II	4.0	44.1	MAGIC	35 – 45	94.8	120 – 10000	0.30	1.0	-2.1
Ursa Minor	4.1	–	VERITAS	35 – 45	60.4	160 – 93000	0.10	8.4	-0.1

1228 where  $\mathcal{L}_0$  is the null hypothesis, or no DM emission, likelihood.  $\mathcal{L}^{\max}$  is the best fit signal  
 1229 hypothesis where  $\langle\sigma v\rangle$  maximizes the likelihood. We calculate the likelihood of each source and  
 1230 model, assuming events are Poisson distributed, with

$$\mathcal{L} = \prod_i \frac{(B_i + S_i)^{N_i} e^{-(B_i + S_i)}}{N_i!} \quad (3.8)$$

1232 where  $S_i$  is the sum of expected number of signal counts.  $B_i$  is the number of background counts  
 1233 observed.  $N_i$  is the total number of counts.

1234 I also calculate an upper limit on  $\langle\sigma v\rangle$  by calculating the 95% confidence level (CL). For the  
 1235 CL, we define a parameter,  $TS_{95}$ , as

$$TS_{95} \equiv \sum_{\text{bins}} \left[ 2N \ln \left( 1 + \frac{\epsilon S_{\text{ref}}}{B} \right) - 2\epsilon S_{\text{ref}} \right] \quad (3.9)$$

1236 where the expected signal counts from a dSph is scaled by  $\epsilon$ .  $S_{\text{ref}}$  is the expected number of excess  
 1237 counts in a bin from DM emission from a dSph with a corresponding annihilation cross-section,  
 1238  $\langle\sigma v\rangle$ . We scan  $\epsilon$  such that

$$2.71 = TS_{\max} - TS_{95} \quad (3.10)$$

1239 HAWC's exclusive results are provided in Section 3.5.

### 1240 3.4.2 Glory Duck Joint Likelihood

1241 The joint likelihood for the 5-experiment combination was done similarly as Section 3.4.1. We  
 1242 calculate upper limits on  $\langle\sigma v\rangle$  from the TS, Eq. (3.7), and define the likelihood ratio more generally

$$\lambda(\langle\sigma v\rangle | \mathcal{D}_{\text{dSphs}}) = \frac{\mathcal{L}(\langle\sigma v\rangle; \hat{\nu} | \mathcal{D}_{\text{dSphs}})}{\mathcal{L}(\widehat{\langle\sigma v\rangle}; \hat{\nu} | \mathcal{D}_{\text{dSphs}})} \quad (3.11)$$

1243  $\mathcal{D}_{\text{dSphs}}$  is the totality of observations across experiments and dSphs.  $\nu$  are the nuisance parameters  
 1244 which are the  $J$  factors in this study.  $\widehat{\langle\sigma v\rangle}$  and  $\hat{\nu}$  are the respective estimate that maximize  $\mathcal{L}$   
 1245 globally. Finally,  $\hat{\nu}$  is the set of nuisance parameters that maximize  $\mathcal{L}$  for a fixed value of  $\langle\sigma v\rangle$ .

1246 The *complete* joint likelihood,  $\mathcal{L}$  that encompasses all observations from all instruments and  
 1247 dSphs can be factorized into *partial* functions for each dSph  $l$  (with  $\mathcal{L}_{\text{dSph},l}$ ) and its  $J$  factor ( $\mathcal{J}_l$ ):

$$\mathcal{L}(\langle\sigma v\rangle; \nu | \mathcal{D}_{\text{dSphs}}) = \prod_{l=1}^{N_{\text{dSphs}}} \mathcal{L}_{\text{dSph},l}(\langle\sigma v\rangle; J_l, \nu_l | \mathcal{D}_l) \times \mathcal{J}_l(J_l | J_{l,\text{obs}}, \sigma_{\log J_l}). \quad (3.12)$$

1248 For this study,  $N_{\text{dSphs}} = 20$  is the number of dSphs studied.  $\mathcal{D}_l$  are the gamma-ray observations  
 1249 of dSph,  $l$ .  $\nu_l$  are the nuisance parameters modifying the gamma-ray observations of dSph,  $l$ ,  
 1250 but excludes  $\mathcal{J}_l$ .  $\mathcal{J}_l$  is the  $J$  factor for dSph,  $l$ , as defined in Equation (3.2), and it is a nuisance  
 1251 parameter whose value is unknown.  $\log_{10} J_{l,\text{obs}}$  and  $\sigma_{\log J_l}$  are obtained by fitting a log-normal  
 1252 function of  $J_{l,\text{obs}}$  to the posterior distribution of  $J_l$  [64].  $\log_{10} J_{l,\text{obs}}$  and  $\sigma_{\log J_l}$  values are provided  
 1253 in Table 3.1. The term  $\mathcal{J}_l$  constraining  $J_l$  is written as:

$$\mathcal{J}_l(J_l | J_{l,\text{obs}}, \sigma_{\log J_l}) = \frac{1}{\ln(10)J_{l,\text{obs}}\sqrt{2\pi}\sigma_{\log J_l}} \exp\left(-\frac{(\log_{10} J_l - \log_{10} J_{l,\text{obs}})^2}{2\sigma_{\log J_l}^2}\right). \quad (3.13)$$

1254 Both the  $\mathcal{GS}$  and  $\mathcal{B}$ , displayed in Table 3.1, sets of  $J$  factors are used in this analysis. Equation (3.13)  
 1255 is also normalized, so it can also be interpreted as a probability density function (PDF) for  $J_{l,\text{obs}}$ .  
 1256 From Equation (3.1), we can also see that  $\langle\sigma v\rangle$  and  $J_l$  are degenerate when computing  $\mathcal{L}_{\text{dSph},l}$ .  
 1257 Therefore, as noted in [65], it is sufficient to compute  $\mathcal{L}_{\text{dSph},l}$  versus  $\langle\sigma v\rangle$  for a fixed value of  $J_l$ .  
 1258 We used  $J_{l,\text{obs}}(\mathcal{GS})$  reported in Tab. 3.1, in order to perform the profile of  $\mathcal{L}$  with respect to  $J_l$ .  
 1259 The degeneracy implies that for any  $J'_l \neq J_{l,\text{obs}}$  (in practice in our case we used  $J'_l = J_{l,\text{obs}}(\mathcal{B})$  to  
 1260 compute results from a different set of  $J$  factors):

$$\mathcal{L}_{\text{dSph},l}(\langle\sigma v\rangle; J'_l, \nu_l | \mathcal{D}_l) = \mathcal{L}_{\text{dSph},l}\left(\frac{J'_l}{J_{l,\text{obs}}} \langle\sigma v\rangle; J_{l,\text{obs}}, \nu_l | \mathcal{D}_l\right), \quad (3.14)$$

1261 which is a straightforward rescaling operation that reduces the computational needs of the profiling  
 1262 operation since:

$$\mathcal{L}(\langle\sigma v\rangle; \hat{\nu} | \mathcal{D}_{\text{dSphs}}) = \prod_{l=1}^{N_{\text{dSphs}}} \max_{J_l} \left[ \mathcal{L}_{\text{dSph},l}(\langle\sigma v\rangle; J_l, \hat{\nu}_l | \mathcal{D}_l) \times \mathcal{J}_l(J_l | J_{l,\text{obs}}, \sigma_{\log J_l}) \right]. \quad (3.15)$$

1263 In addition, Eq. (3.14) enables the combination of data from different gamma-ray instruments and  
 1264 observed dSphs via tabulated values of  $\mathcal{L}_{\text{dSph},l}$ , or equivalently of  $\lambda$  from Eq. (3.11) as was done in  
 1265 this work, versus  $\langle\sigma v\rangle$ .  $\mathcal{L}_{\text{dSph},l}$  is computed for a fixed value of  $J_l$  and profiled with respect to all  
 1266 instrumental nuisance parameters  $\nu_l$ , these nuisance parameters are discussed in more detail below.  
 1267 These values are produced by each detector independently and therefore there is no need to share  
 1268 sensitive low-level information used to produce them, such as event lists. Figure 3.4 illustrates the  
 1269 multi-instrument combination technique used in this study with a comparison of the upper limit

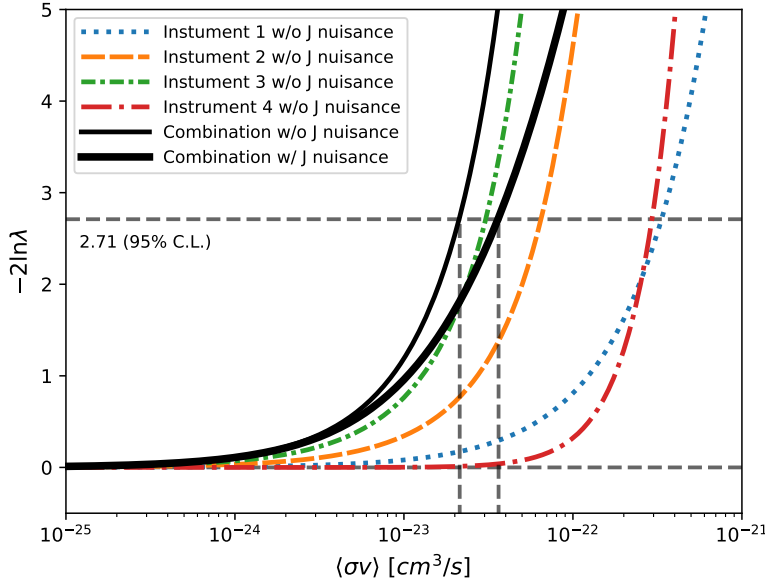


Figure 3.4 Illustration of the combination technique showing a comparison between  $-2 \ln \lambda$  provided by four instruments (colored lines) from the observation of the same dSph without any  $J$  nuisance and their sum, *i.e.* the resulting combined likelihood (thin black line). According to the test statistics of Equation (3.7), the intersection of the likelihood profiles with the line  $-2 \ln \lambda = 2.71$  indicates the 95% C.L. upper limit on  $\langle\sigma v\rangle$ . The combined likelihood (thin black line) shows a smaller value of upper limit on  $\langle\sigma v\rangle$  than those derived by individual instruments. We also show how the uncertainties on the  $J$  factor effects the combined likelihood and degrade the upper limit on  $\langle\sigma v\rangle$  (thick black line). All likelihood profiles are normalized so that the global minimum  $\widehat{\langle\sigma v\rangle}$  is 0. We note that each profile depends on the observational conditions in which a target object was observed. The sensitivity of a given instrument can be degraded and the upper limits less constraining if the observations are performed in non-optimal conditions such as a high zenith angle or a short exposure time.

1270 on  $\langle\sigma v\rangle$  obtained from the combination of the observations of four experiments towards one dSph  
 1271 versus the upper limit from individual instruments. It also shows graphically the effect of the  
 1272  $J$ -factor uncertainty on the combined observations.

1273 The *partial* joint likelihood function for gamma-ray observations of each dSph ( $\mathcal{L}_{\text{dSph},l}$ ) is  
 1274 written as the product of the likelihood terms describing the  $N_{\text{exp},l}$  observations performed with  
 1275 any of our observatories:

$$\mathcal{L}_{\text{dSph},l} (\langle\sigma v\rangle; J_l, \nu_l | \mathcal{D}_l) = \prod_{k=1}^{N_{\text{exp},l}} \mathcal{L}_{lk} (\langle\sigma v\rangle; J_l, \nu_{lk} | \mathcal{D}_{lk}), \quad (3.16)$$

1276 where each  $\mathcal{L}_{lk}$  term refers to an observation of the  $l$ -th dSph with associated  $k$ -th instrument

1277 responses.  $N_{\text{exp},l}$  varies from dSph to dSph and can be inferred from Table 3.2.

1278     Each collaboration separately analyzes their data for  $\mathcal{D}_{lk}$  corresponding to dSph  $l$  and gamma-  
 1279     ray detector  $k$ , using as many common assumptions as possible in the analysis. HAWC's treatment  
 1280     was described earlier in Section 3.4.1 whereas the specifics of the remaining experiments is left to  
 1281     the publication. We compute the values for the likelihood functions  $\mathcal{L}_{lk}$  (see Eq. (3.16)) for a fixed  
 1282     value of  $J_l$  and profile over the rest of the nuisance parameters  $\nu_{lk}$ . Then, values of  $\lambda$  from Eq. (3.11)  
 1283     are computed as a function of  $\langle\sigma v\rangle$ , and shared using a common format. Results are computed for  
 1284     seven annihilation channels,  $W^+W^-$ ,  $ZZ$ ,  $b\bar{b}$ ,  $t\bar{t}$ ,  $e^+e^-$ ,  $\mu^+\mu^-$ , and  $\tau^+\tau^-$  over 62  $m_\chi$  values between  
 1285     5 GeV and 100 TeV provided in [58]. The  $\langle\sigma v\rangle$  range is defined between  $10^{-28}$  and  $10^{-18}\text{cm}^3 \cdot \text{s}^{-1}$ ,  
 1286     with 1001 logarithmically spaced values. The likelihood combination, i.e. Equation (3.12), and  
 1287     profile over the  $J$ -factor to compute the profile likelihood ratio  $\lambda$ , Equation (3.11), are carried out  
 1288     with two different public analysis software packages, namely `gLike` [66] and `LklCom` [67], that  
 1289     provide the same results [68].

1290     As mentioned previously, each experiment computes the  $\mathcal{L}_{lk}$  from Equation (3.11) differently.  
 1291     The remainder of this section highlights the differences in this calculation across the experiments.  
 1292     Four experiments, namely *Fermi*-LAT, H.E.S.S., HAWC and MAGIC, use a binned likelihood to  
 1293     compute the  $\mathcal{L}_{lk}$ . For these experiments, for each observation  $\mathcal{D}_{lk}$  of a given dSph  $l$  carried out  
 1294     using a given gamma-ray detector  $k$ , the binned likelihood function is:

$$\mathcal{L}_{lk} (\langle\sigma v\rangle; J_l, \nu_{lk} | \mathcal{D}_{lk}) = \prod_{i=1}^{N_E} \prod_{j=1}^{N_P} \left[ \mathcal{P}(s_{lk,ij}(\langle\sigma v\rangle, J_l, \nu_{lk}) + b_{lk,ij}(\nu_{lk}) | N_{lk,ij}) \right] \times \mathcal{L}_{lk,\nu} (\nu_{lk} | \mathcal{D}_{\nu_{lk}}) \quad (3.17)$$

1295     where  $N_E$  and  $N_P$  are the number of considered bins in reconstructed energy and arrival direction,  
 1296     respectively;  $\mathcal{P}$  represents a Poisson PDF for the number of gamma-ray candidate events  $N_{lk,ij}$   
 1297     observed in the  $i$ -th bin in energy and  $j$ -th bin in arrival direction, when the expected number is  
 1298     the sum of the expected mean number of signal events  $s_{ij}$  (produced by DM annihilation) and of  
 1299     background events  $b_{ij}$ ;  $\mathcal{L}_{lk,\nu}$  is the likelihood term for the extra  $\nu_{lk}$  nuisance parameters that vary  
 1300     from one instrument  $k$  to another. The expected counts for signal events  $s_{ij}$  for a given dSph  $l$  and

1301 detector  $k$  is given by:

$$s_{ij}(\langle\sigma\nu\rangle, J) = \int_{E'_{\min,i}}^{E'_{\max,i}} dE' \int_{P'_{\min,j}}^{P'_{\max,j}} d\Omega' \int_0^\infty dE \int_{\Delta\Omega_{tot}} d\Omega \int_0^{T_{\text{obs}}} dt \frac{d^2\Phi(\langle\sigma\nu\rangle, J)}{dEd\Omega} \text{IRF}(E', P' | E, P, t) \quad (3.18)$$

1302 where  $E'$  and  $E$  are the reconstructed and true energies,  $P'$  and  $P$  the reconstructed and true  
1303 arrival directions;  $E'_{\min,i}$ ,  $P'_{\min,j}$ ,  $E'_{\max,i}$ , and  $P'_{\max,j}$  are their lower and upper limits of the  $i$ -th  
1304 energy bin and the  $j$ -th arrival direction bin;  $T_{\text{obs}}$  is the (dead-time corrected) total observation  
1305 time;  $t$  is the time along the observations;  $d^2\Phi/dEd\Omega$  is the DM flux in the source region (see  
1306 Equation (3.1)); and  $\text{IRF}(E', P' | E, P, t)$  is the IRF, which can be factorized as the product of the  
1307 effective collection area of the detector  $A_{\text{eff}}(E, P, t)$ , the PDFs for the energy estimator  $f_E(E' | E, t)$ ,  
1308 and arrival direction  $f_P(P' | E, P, t)$  estimators. Note that for Fermi-LAT, HAWC, MAGIC, and  
1309 VERITAS the effect of the finite angular resolution is taken into account through the convolution  
1310 of  $d\Phi/dEd\Omega$  with  $f_P$  in Equation (3.18), whereas in the cases of H.E.S.S.  $f_P$  is approximated by a  
1311 delta function. This approximation has been made in order to maintain compatibility of the result  
1312 with what has been previously published. The difference introduced by this approximation is  $< 5\%$   
1313 for all considered dSphs. A more comprehensive review of the differences between the analyses of  
1314 different instruments can be found in [40].

### 1315 3.5 HAWC Results

1316 13 of the 20 dSphs considered for the Glory Duck analysis are within HAWC's field of view.  
1317 These dSph are analyzed for emission from DM annihilation according to the likelihood method  
1318 described in Section 3.4. The 13 likelihood profiles are then stacked to synthesize a combined  
1319 limit on the dark matter cross-section,  $\langle\sigma\nu\rangle$ . This combination is done for the 7 SM annihilation  
1320 channels used in the Glory Duck analysis. Figure 3.5 shows the combined limit for all annihilation  
1321 channels with HAWC only observations. We also perform 300 studies of Poisson trials on the  
1322 background. These trials are used to produce HAWC sensitivities with  $\pm 1\sigma$  and  $\pm 2\sigma$  uncertainty  
1323 bands which were shared with the other collaborators for combination. The results on fitting to  
1324 HAWC's Poisson trials of the DM hypothesis is shown in Figure 3.7 for all the DM annihilation  
1325 channels studied for Glory Duck.

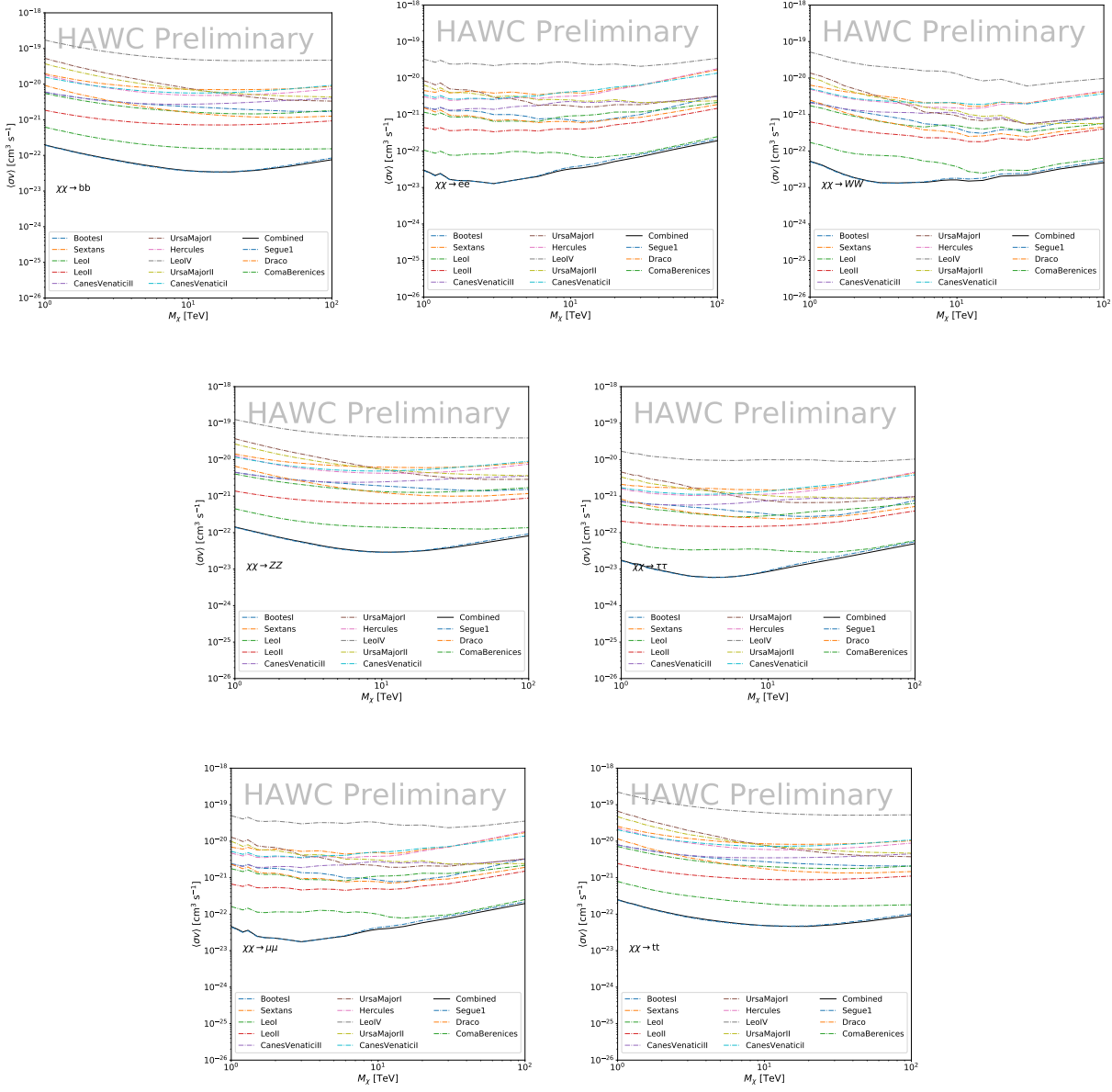


Figure 3.5

1326     No DM was found in HAWC observations. HAWC's limits are dominated by the dSphs Segue1  
 1327     and Coma Berenices. The remaining 11 dSphs do not contribute significantly to the limit because  
 1328     they are at high zenith and/or have much smaller  $J$  factors. Even though some remaining dSphs  
 1329     have large  $J$  factors, they are towards the edge of HAWC's field of view where HAWC analysis is  
 1330     less sensitive.

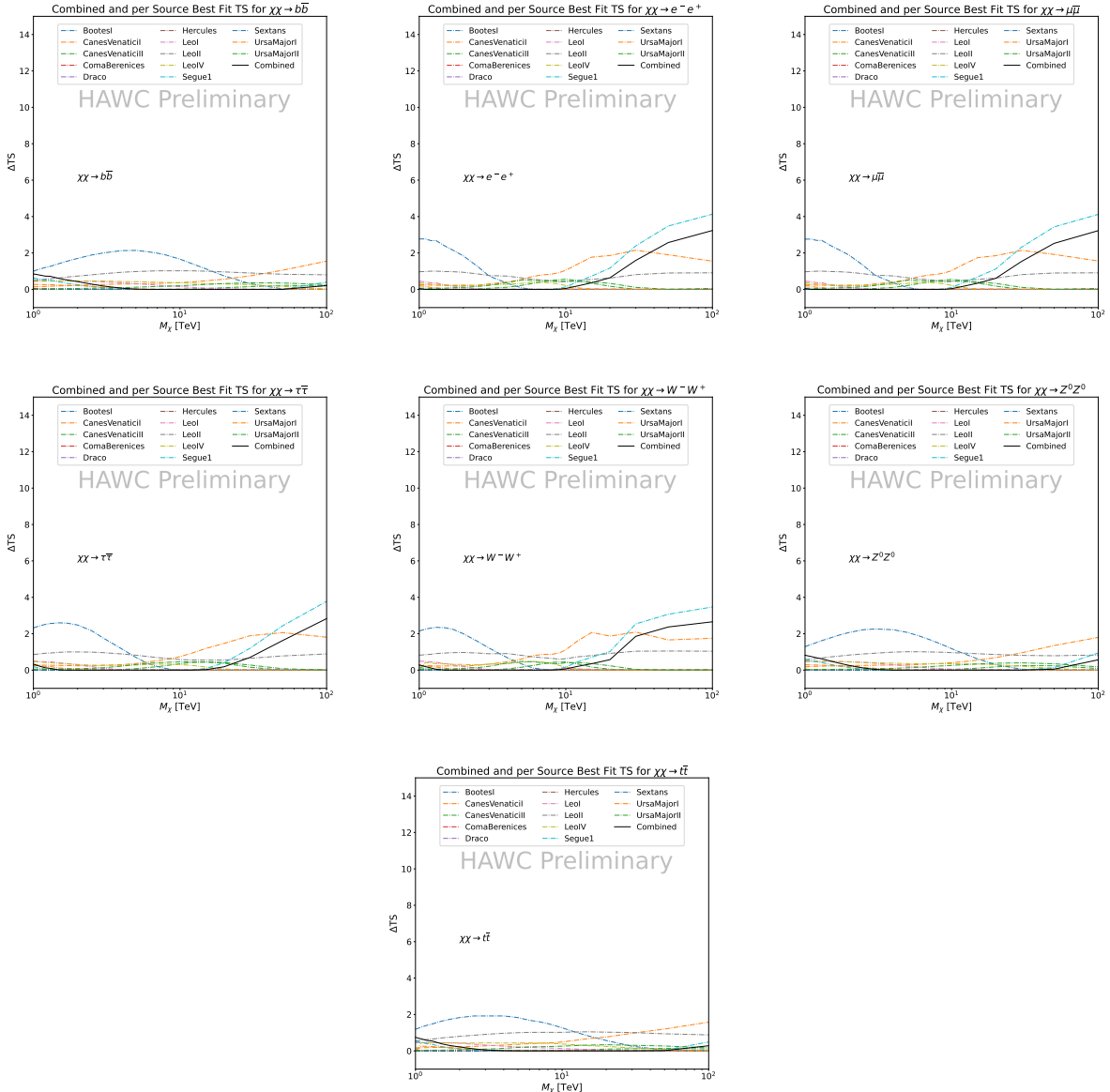


Figure 3.6 HAWC TS values for best fit  $\langle\sigma v\rangle$  versus  $m_\chi$  for seven SM annihilation channels with  $J$  factors from  $\mathcal{GS}$ . The solid black line shows the combined best fit TS values. The colored, dashed lines are the TS values for each of the 13 sources HAWC studied.

### 1331 3.6 Glory Duck Combined Results

1332 The crux of this analysis is that HAWC's results are combined with 4 other gamma-ray observa-  
 1333 tories: Fermi-LAT, H.E.S.S., MAGIC, and VERITAS. No significant DM emission was observed  
 1334 by any of the five instruments. We present the upper limits on  $\langle\sigma v\rangle$  assuming seven independent  
 1335 DM self annihilation channels, namely  $W^+W^-$ ,  $Z^+Z^-$ ,  $b\bar{b}$ ,  $t\bar{t}$ ,  $e^+e^-$ ,  $\mu^+\mu^-$ , and  $\tau^+\tau^-$ . The 68%

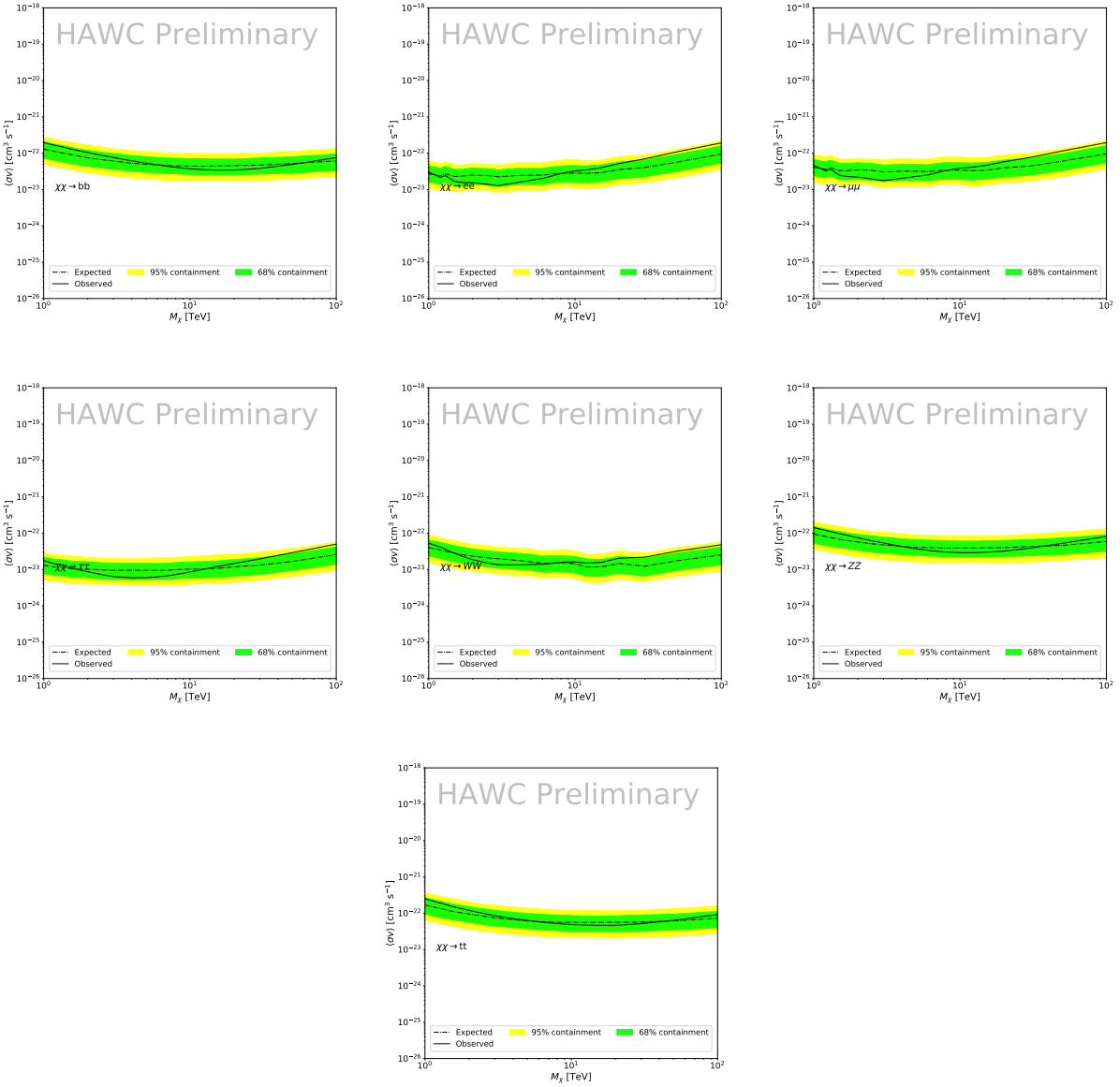


Figure 3.7 HAWC Brazil bands at 95% confidence level on  $\langle\sigma v\rangle$  versus DM mass for seven annihilation channels with  $J$ -factors from  $\mathcal{GS}$  [69]. The solid line represents the combined limit from 13 dSphs. The dashed line is the expected limit. The green band is the 68% containment. The yellow band is the 95% containment.

1336 and 95% containment bands are produced from 300 Poisson realizations of the null hypothesis  
 1337 corresponding to each of the combined datasets. These 300 realizations are combined identically  
 1338 to dSph observations. The containment bands and the median are extracted from the distribution  
 1339 of resulting limits on the null hypothesis. These 300 realizations are obtained either by fast simu-  
 1340 lations of the OFF observations, for H.E.S.S., MAGIC, VERITAS, and HAWC, or taken from real

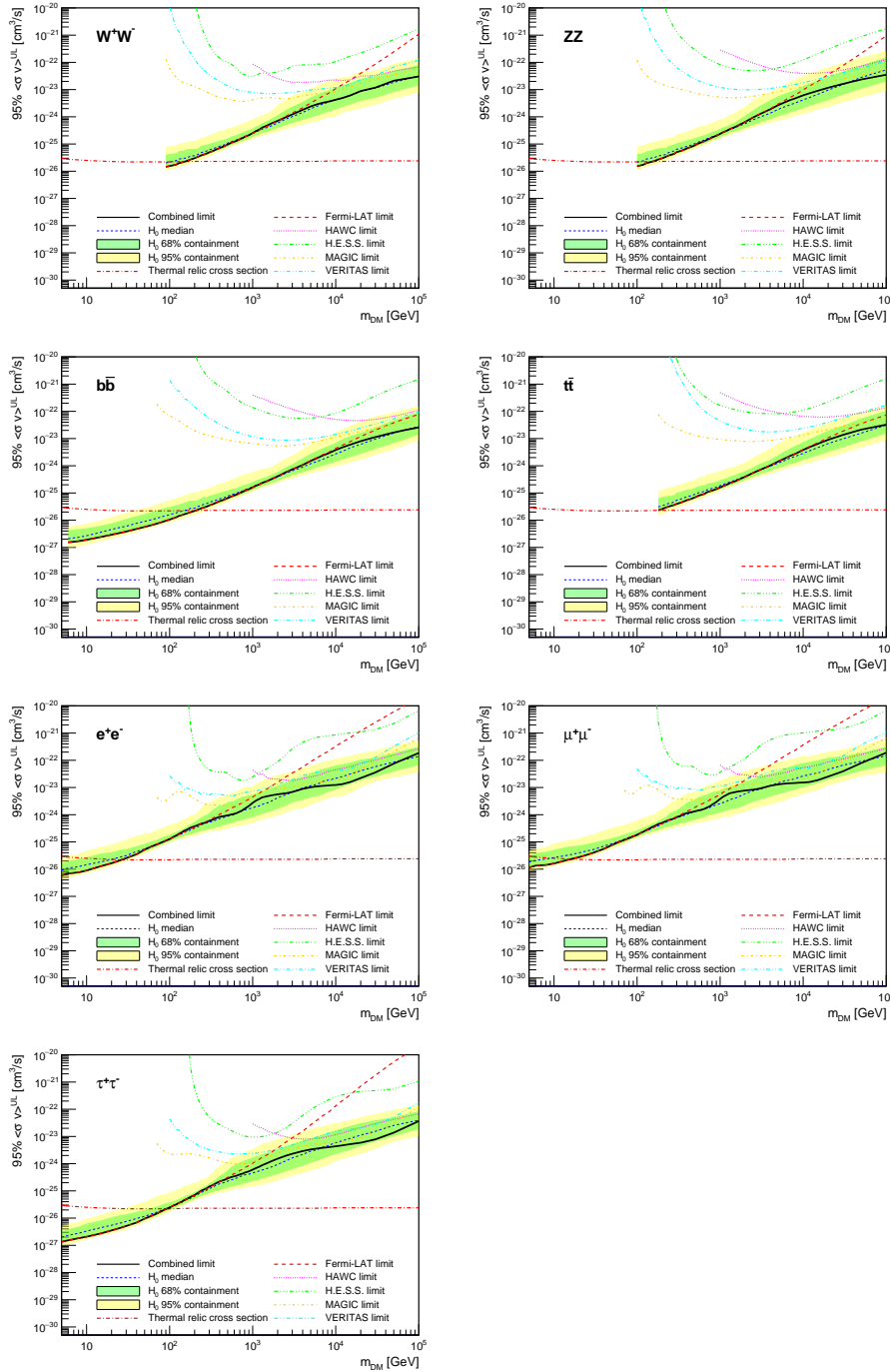


Figure 3.8 Upper limits at 95% confidence level on  $\langle\sigma v\rangle$  in function of the DM mass for eight annihilation channels, using the set of  $J$  factors from Ref. [69] ( $\mathcal{GS}$  set in Table 3.1). The black solid line represents the observed combined limit, the black dashed line is the median of the null hypothesis corresponding to the expected limit, while the green and yellow bands show the 68% and 95% containment bands. Combined upper limits for each individual detector are also indicated as solid, colored lines. The value of the thermal relic cross-section in function of the DM mass is given as the red dotted-dashed line [70].

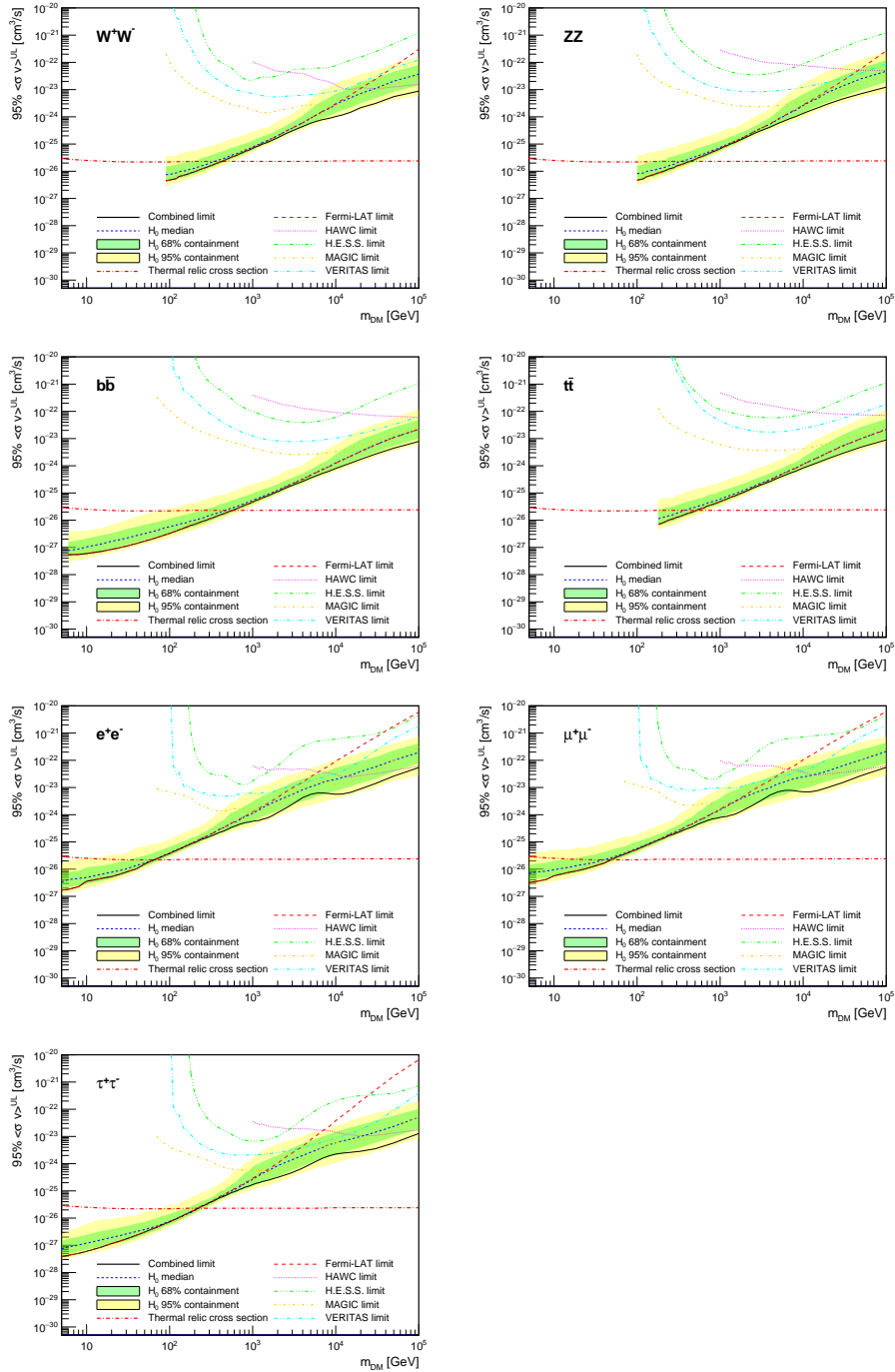


Figure 3.9 Same as Fig. 3.8, using the set of  $J$  factors from Ref. [63, 71] ( $\mathcal{B}$  set in Table 3.1).

1341 observations of empty fields of view in the case of Fermi-LAT [64, 72, 73].

1342 The obtained limits are shown in Figure 3.8 for the  $\mathcal{GS}$  set of  $J$ -factors [69] and in Figure 3.9  
1343 for the  $\mathcal{B}$  set of  $J$ -factors [63, 71]. The combined limits are presented with their 68% and 95%  
1344 containment bands, and are expected to be close to the median limit when no signal is present.

1345 We observe agreement with the null hypothesis for all channels, within  $2\sigma$  standard deviations,  
1346 between the observed limits and the expectations given by the median limits. Limits obtained from  
1347 each detector are also indicated in the figures, where limits for all dSphs observed by the specific  
1348 instrument have been combined.

1349 Below  $\sim 300$  GeV, the *Fermi*-LAT dominates the DM limits for all annihilation channels. From  
1350  $\sim 300$  GeV to  $\sim 2$  TeV, *Fermi*-LAT continues to dominate for the hadronic and bosonic DM channels,  
1351 yet the IACTs (H.E.S.S., MAGIC, and VERITAS) and *Fermi*-LAT all contribute to the limit for  
1352 leptonic DM channels. For DM masses between  $\sim 2$  TeV to  $\sim 10$  TeV, the IACTs dominate leptonic  
1353 DM annihilation channels, whereas both the *Fermi*-LAT and the IACTs dominate bosonic and  
1354 hadronic DM annihilation channels. From  $\sim 10$  TeV to  $\sim 100$  TeV, both the IACTs and HAWC  
1355 contribute significantly to the leptonic DM limit. For hadronic and bosonic DM, the IACTs and  
1356 *Fermi*-LAT both contribute strongly.

1357 We notice that the limits computed using the  $\mathcal{B}$  set of  $J$ -factor are always better compared to the  
1358 ones calculated with the  $\mathcal{GS}$  set. For the  $W^+W^-$ ,  $Z^+Z^-$ ,  $b\bar{b}$ , and  $t\bar{t}$  channels, the ratio between the  
1359 limits computed with the two sets of  $J$ -factor is varying between a factor of  $\sim 3$  and  $\sim 5$  depending  
1360 on the energy, with the largest ratio around 10 TeV. For the channels  $e^+e^-$ ,  $\mu^+\mu^-$ , and  $\tau^+\tau^-$ , the  
1361 ratio lies between  $\sim 2$  to  $\sim 6$ , being maximum around 1 TeV. Examining Figure 3.16 and Figure 3.17  
1362 in Section 3.8, these differences are explained by the fact that the  $\mathcal{B}$  set provides higher  $J$ -factors  
1363 for the majority of the studied dSphs, with the notable exception of Segue I. The variation on the  
1364 ratio of the limits for the two sets is due to different dSph dominating the limits depending on the  
1365 energy. One set,  $\mathcal{B}$ , pushes the range of which thermal cross-section which can be excluded to  
1366 higher mass. This comparison demonstrates the magnitude of systematic uncertainties associated  
1367 with the choice of the  $J$ -factor calculation. The  $\mathcal{GS}$  and  $\mathcal{B}$  sets present a difference in the limits for  
1368 all channels of about This difference is explained, see Figure 3.16 and Figure 3.17, by the fact that  
1369 the  $\mathcal{B}$  set provides higher  $J$ -factors for all dSph except for Segue I.

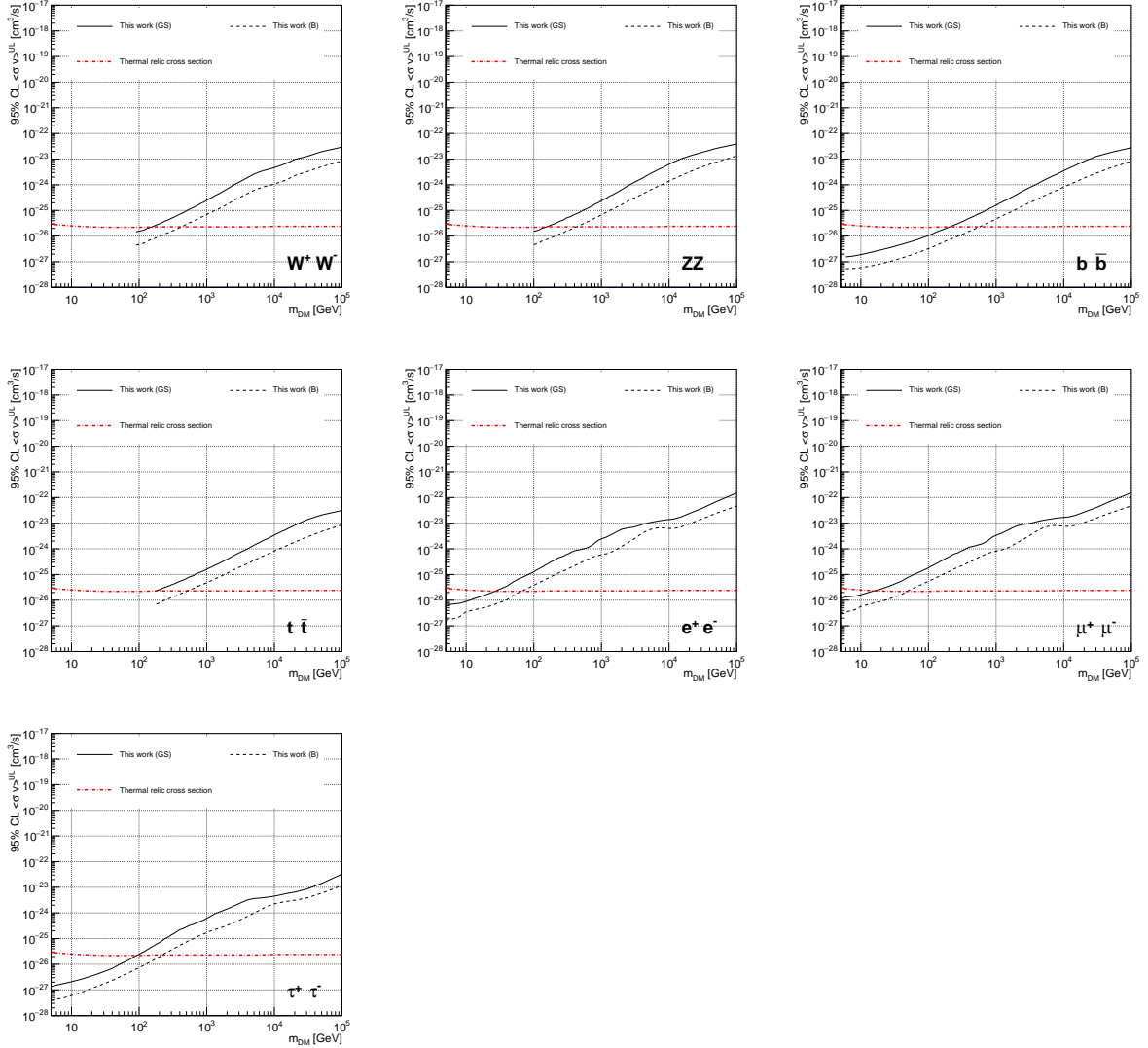


Figure 3.10 Comparisons of the combined limits at 95% confidence level for each of the eight annihilation channels when using the  $J$  factors from Ref. [69] ( $\mathcal{GS}$  set in Table 3.1), plain lines, and the  $J$  factor from Ref. [63, 71] ( $\mathcal{B}$  set in Table 3.1), dashed lines. The cross-section given by the thermal relic is also indicated [70].

### 1370 3.7 HAWC Systematics

#### 1371 3.7.1 Inverse Compton Scattering

1372 The DM-DM annihilation channels produce many high energy electrons regardless of the  
 1373 primary annihilation channel. These high energy electrons can produce high energy gamma-rays  
 1374 through Inverse Compton Scattering (ICS). If this effect is strong, it would change the morphology  
 1375 of the source and increase the total expected gamma-ray counts from any source. The PPPC [58]

1376 provides tools in Mathematica for calculating the impact of ICS for an arbitrary location in the  
1377 sky for a specified annihilation channel. We calculated the change in gamma-ray counts for DM  
1378 annihilation to primary  $e\bar{e}$  for RA and Dec corresponding to Segue1 and Coma Berenices. These  
1379 dSphs were chosen because they are the strongest contributors to the limit.  $e\bar{e}$  was selected because  
1380 it would have the largest number of high energy electrons. The effect was found to be on the order  
1381 of  $10^{-7}$  on the gamma-ray spectrum. As a result, this systematic is not considered in our analysis.

### 1382 **3.7.2 Point Source Versus Extended Source Limits**

1383 The previous DM search toward dSph approximated the dSphs as point sources [60]. In  
1384 this analysis, the dSphs are implemented as extended with J-factor distributions following those  
1385 produced by [69]. The resolution of the cited map is much finer than HAWC’s angular resolution.  
1386 The vast majority of the J-factor distribution is represented on the central HAWC pixel of the dSph  
1387 spatial map. However, the neighboring 8 pixels are not negligible and contribute to our limit.

1388 Figure 3.11 shows a substantial improvement to the limit for Segue1. Fig. 3.12 however showed  
1389 identical limits. These disparities are best explained by the relative difference in their J-Factors.  
1390 Both dSphs pass almost overhead the HAWC detector, however Segue1 has the larger J-Factor  
1391 between the two. Adjacent pixels to the central pixel will therefore contribute to the limits. This is  
1392 the case for other dSph that are closer to the zenith of the HAWC detector.

1393 Comparison plots for all sources and the combined limit can be found in the sandbox for the  
1394 Glory Duck project.

### 1395 **3.7.3 Impact of Pointing Systematic**

1396 During the analysis it was discovered that directional reconstruction of gamma-rays had a  
1397 systematic bias at large zenith angles. Slides describing this systematic can be found [here](#). Shown  
1398 on the presentation is dependence on the pointing systematic on declination. New spatial profiles  
1399 were generated for every dSph and limits were computed for the adjusted declination.

1400 Section 3.7.3 demonstrates the impact of this systematic for all DM annihilation channels  
1401 studied by HAWC. The impact is a tiny improvement, yet mostly identical, to the combined limits.

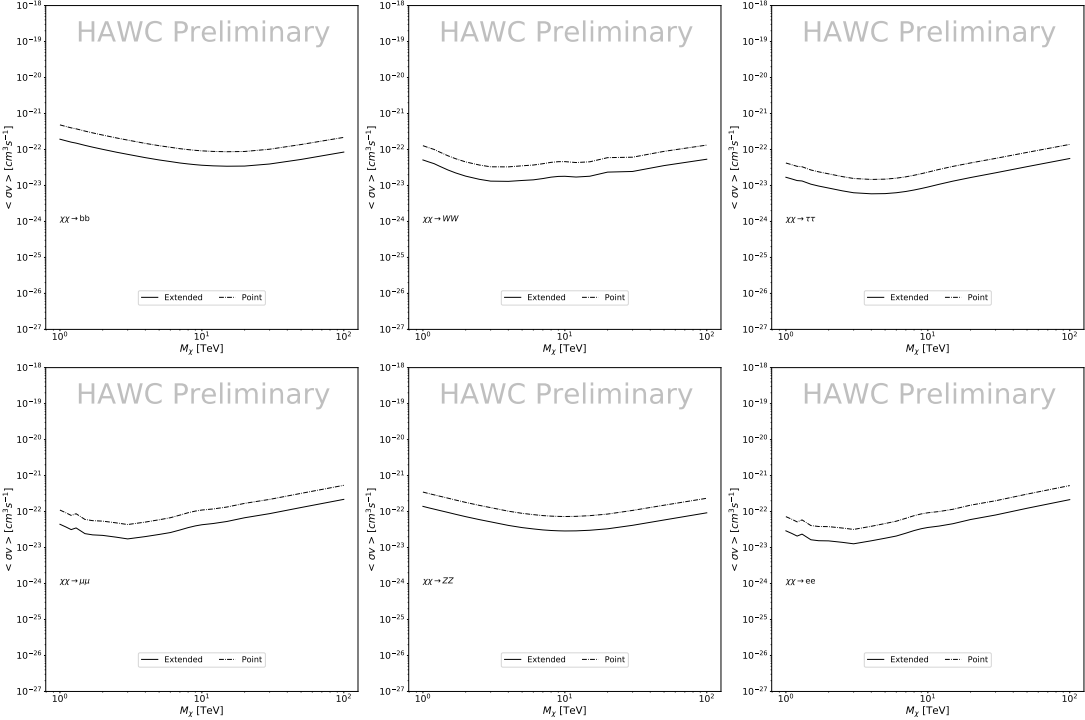


Figure 3.11 Comparisons of the combined limits at 95% confidence level for a point source analysis and extended source using [69]  $\mathcal{GS}$  J-factor distributions and PPPC [58] annihilation spectra. Shown are the limits for Segue1 which will have the most significant impact on the combined limit. 6 of the 7 DM annihilation channels are shown. Solid lines are extended source studies. Dashed lines are point source studies. Overall, the extended source analysis improves the limit by a factor of 2.

## 1402 3.8 J-factor distributions

### 1403 3.8.1 Numerical integration of $\mathcal{GS}$ maps

1404 It was discovered well after the HAWC analysis was completed that the published tables from  
 1405  $\mathcal{GS}$  [59] quoted median  $J$ -factors were computed in a non-trivial manner. The assumption myself  
 1406 and collaborators had been that the published tables represented the  $J$ -factor as a function of  $\theta$  for  
 1407 the best global fit model on a per-source basis. However, this is not the case. Instead, what is  
 1408 published are the best fit model for each dwarf that only considers stars up to the angular separation  
 1409  $\theta$ . Therefore, the model is changing for each value of  $\theta$  for each dwarf. Yet, the introduced features  
 1410 from unique models at each  $\theta$  are much smaller than the angular resolution of HAWC. It is not  
 1411 expected for these effects to impact the limits and TS greatly as a result.

1412 Median  $J$ -factor model profiles were provided by the authors. New maps were generated

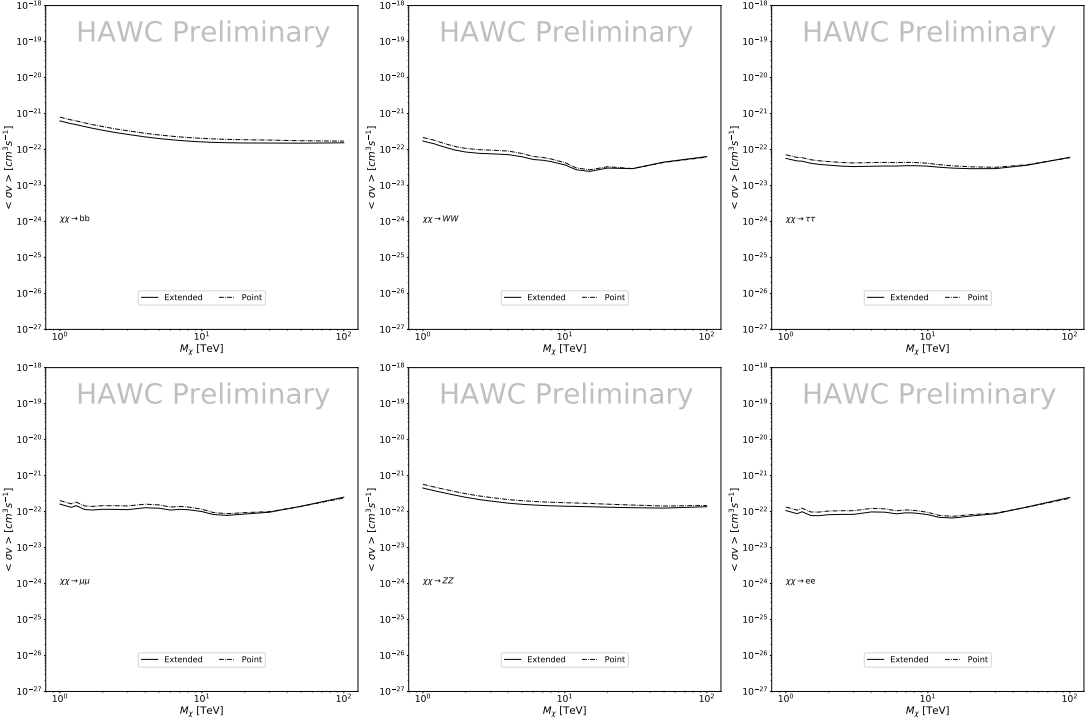


Figure 3.12 Same as Fig. 3.11 on Coma Berenices. This dSph also contributes significantly to the limit. The limits are identical in this case.

and analyzed for Segue1 and Coma Berenices. Figure 3.14 shows the differential between maps generated with the method from Section 3.8.1 and from the authors of [59]. These maps were reanalyzed for all SM DM annihilation channels. Upper limits for these channels are shown in Figure 3.15

From Figure 3.15, we can see that the impact of these model difference was no substantial. The observed impact was a fractional effect which is much smaller than the impact from selecting another DM spatial distribution model as was shown in Figure 3.10.

### 3.8.2 $\mathcal{GS}$ Versus $\mathcal{B}$ spatial models

We show in this appendix a comparison between the  $J$ -factors computed by Geringer-Sameth *et al.* [69] (the  $\mathcal{GS}$  set) and the ones computed by Bonnivard *et al.* [63, 71] (the  $\mathcal{B}$  set). The  $\mathcal{GS}$   $J$ -factors are computed through a Jeans analysis of the kinematic stellar data of the selected dSphs, assuming a dynamic equilibrium and a spherical symmetry for the dSphs. They adopted the generalized DM density distribution, known as Zhao-Hernquist, introduced by [61], carrying

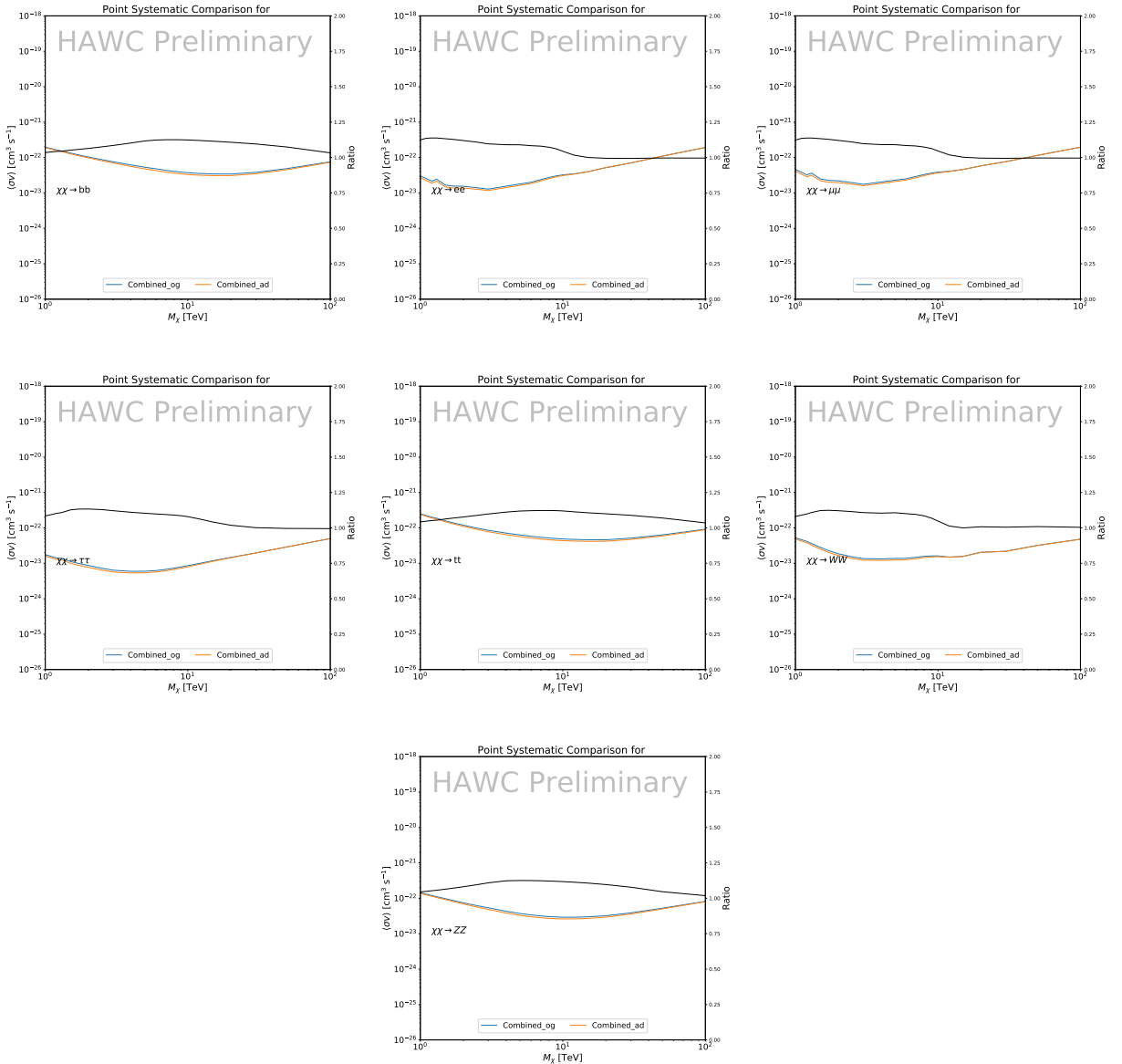


Figure 3.13 Comparison of combined limits when correcting for HAWC's pointing systematic. All DM annihilation channels are shown. The solid black line is the ratio between published limit to the declination corrected limit. The blue solid line or "Combined\_og" represented the limits computed for Glory Duck. The solid orange line or "Combined\_ad" represented the limits computed after correcting for the pointing systematic.

1426 three additional index parameters to describe the inner and outer slopes, and the break of the  
 1427 density profile. Such a profile parametrization allows the reduction of the theoretical bias from  
 1428 the choice of a specific radial dependency on the kinematic data. In other words, the increase of  
 1429 free parameters with the use of the Zhao-Hernquist profile allows a better description of the mass

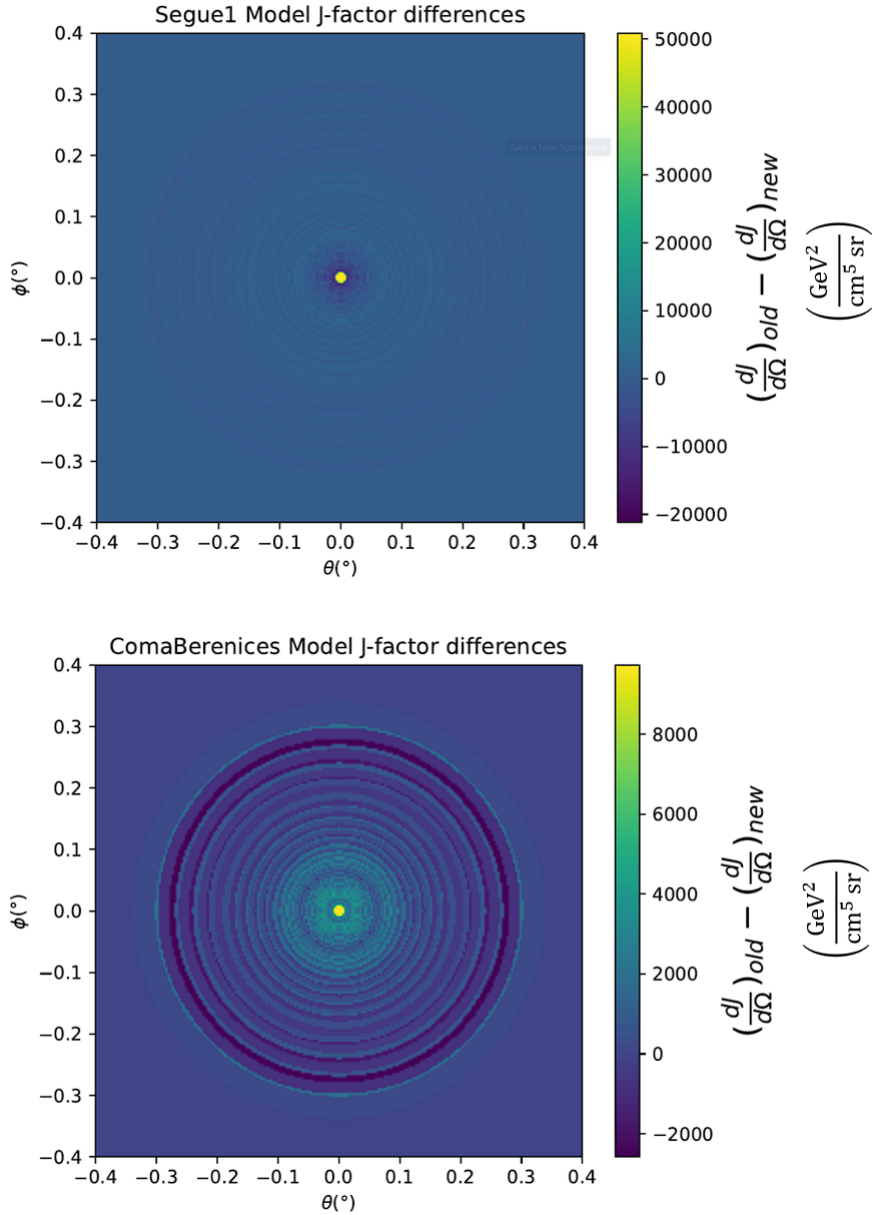


Figure 3.14 Differential map of  $dJ/\Omega$  from model built in Section 3.8.1 and profiles provided directly from authors. (Top) Differential from Segue1. (bottom) Differential from Coma Berenices. Note that their scales are not the same. Segue1 shows the deepest discrepancies which is congruent with its large uncertainties. Both models show anuli where unique models become apparent.

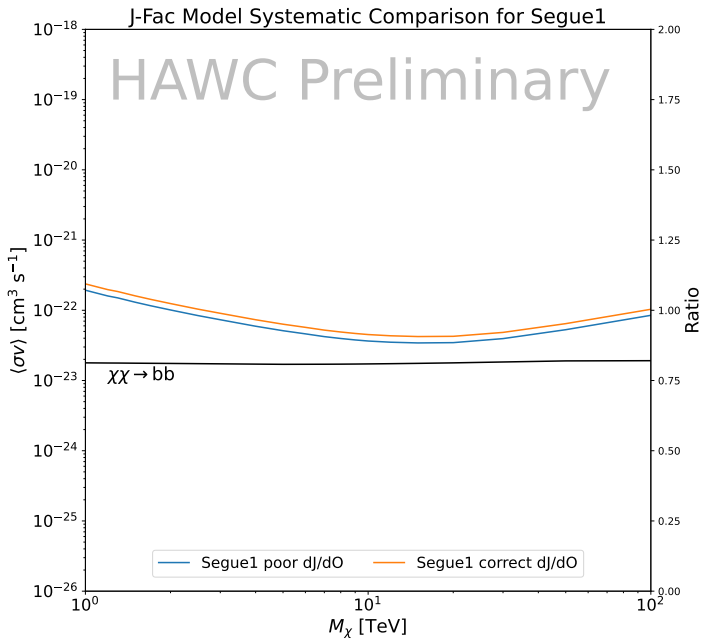
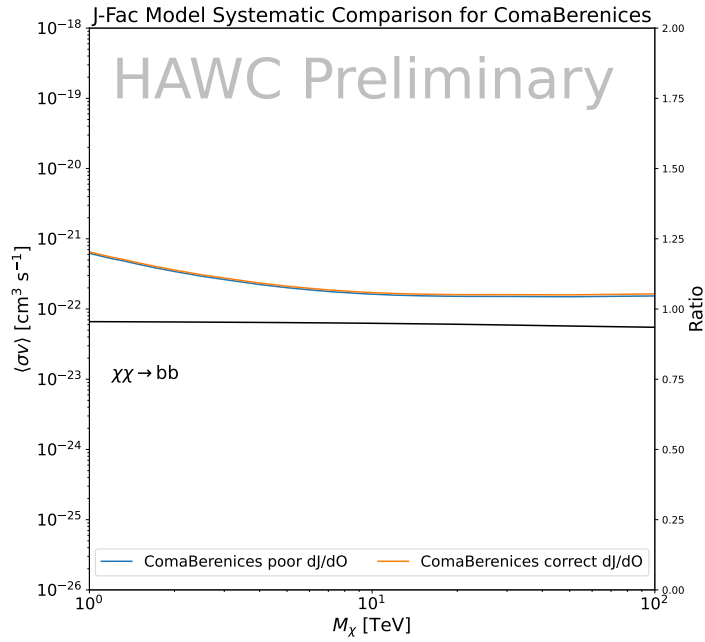


Figure 3.15 HAWC limits for Coma Berenices (top) and Segue1 (bottom) for two different map sets. Blue lines are limits calculated on maps with poor model representation. Orange lines are limits calculated on spatial profiles provided by the authors of [59]. Black line is the ratio of the poor spatial model limits to the corrected spatial models. The left y-axis measures  $\langle\sigma v\rangle$  for the blue and orange lines. The right y-axis measures the ratio and is unitless.

1430 density distribution of dark matter.

1431 In addition, a constant velocity anisotropy profile and a Plummer light profile [74] for the stellar  
1432 distribution were assumed. The velocity anisotropy profile depends on the radial and tangential  
1433 velocity dispersion. However, its determination remains challenging since only the line-of-sight  
1434 velocity dispersion can be derived from velocity measurements. Therefore, the parametrization of  
1435 the anisotropy profile is obtained from simulated halos (see [75] for more details). They provide the  
1436 values of the  $J$ -factors of regions extending to various angular radius up to the outermost member  
1437 star.

1438 The  $\mathcal{B}$   $J$ -factors were computed through a Jeans analysis taking into account the systematic  
1439 uncertainties induced by the DM profile parametrization, the radial velocity anisotropy profile, and  
1440 the triaxiality of the halo of the dwarf galaxies. They performed a more complete study of the dSph  
1441 kinematics and dynamics than  $\mathcal{GS}$  for the determination of the  $J$ -factor. Conservative values of the  
1442  $J$ -factors where obtained using an Einasto DM density profile [76], a realistic anisotropy profile  
1443 known as the Baes & Van Hese profile [77] which takes into account that the inner regions can be  
1444 significantly non-isotropic, and a Zhao-Hernquist light profile [61].

1445 For both sets,  $J$ -factor values are provided for all dSphs as a function of the radius of the  
1446 integration region [69, 63, 71]. Table 3.1 shows the heliocentric distance and Galactic coordinates  
1447 of the twenty dSphs, together with the two sets of  $J$ -factor values integrated up to the outermost  
1448 observed star for  $\mathcal{GS}$  and the tidal radius for  $\mathcal{B}$ . Both  $J$ -factor sets were derived through a Jeans  
1449 analysis based on the same kinematic data, except for Draco where the measurements of [78] have  
1450 been adopted in the computation of the  $\mathcal{B}$  value. The computations for producing the  $\mathcal{GS}$  and  $\mathcal{B}$   
1451 samples differ in the choice of the DM density, velocity anisotropy, and light profiles, for which the  
1452 set  $\mathcal{B}$  takes into account some sources of systematic uncertainties.

1453 Figure 3.16 and Figure 3.17 show the comparisons for the  $J$ -factor versus the angular radius  
1454 for each of the 20 dSphs used in this study. The uncertainties provided by the authors are also  
1455 indicated in the figures. For the  $\mathcal{GS}$  set, the computation stops at the angular radius corresponding  
1456 to the outermost observed star, while for the  $\mathcal{B}$  set, the computation stops at the angular radius

1457 corresponding to the tidal radius.

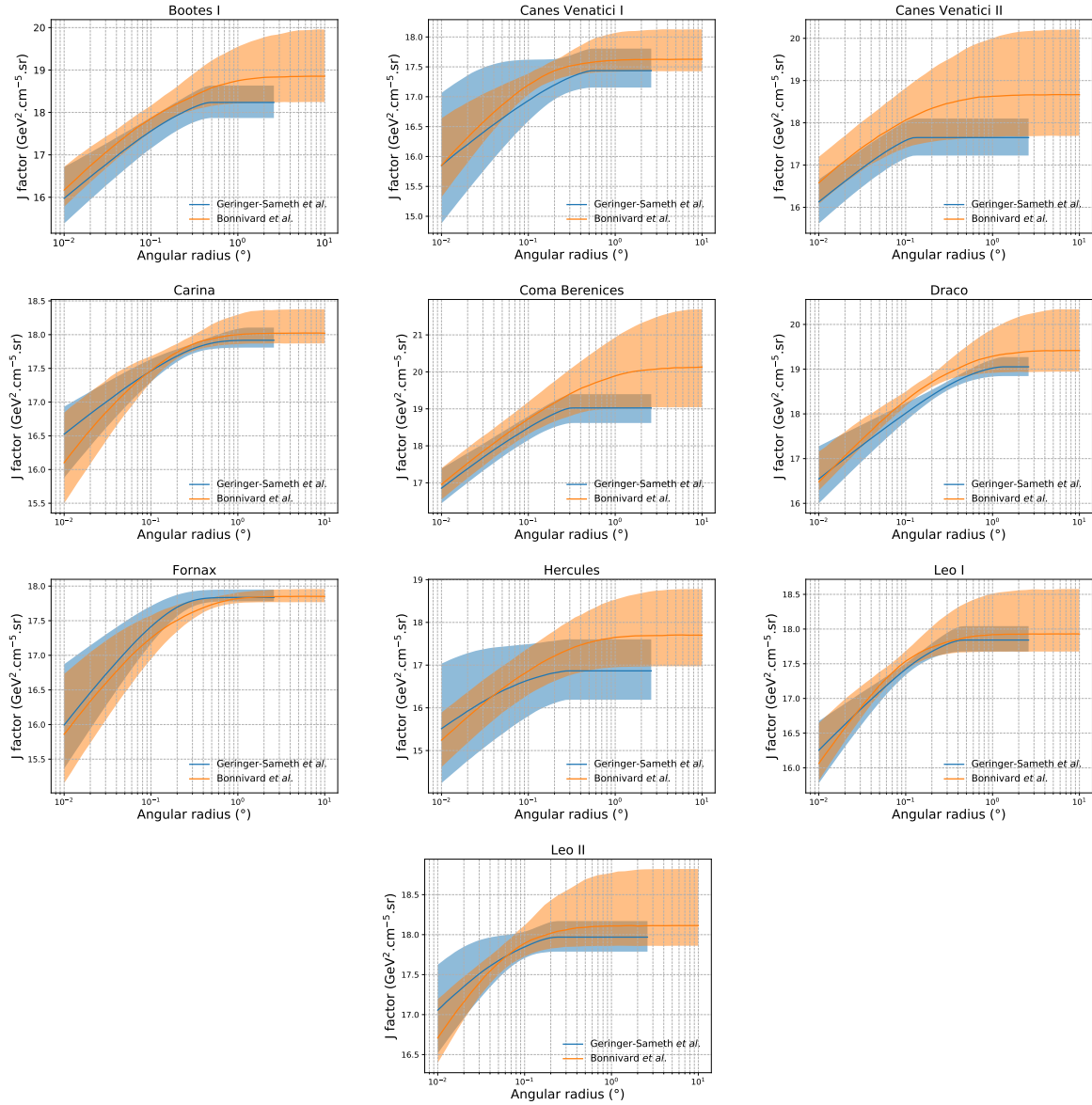


Figure 3.16 Comparisons between the  $J$ -factors versus the angular radius for the computation of  $J$  factors from Ref. [69] ( $\mathcal{GS}$  set in Table 3.1) in blue and for the computation from Ref. [63, 71] ( $\mathcal{B}$  set in Tab. 3.1) in orange. The solid lines represent the central value of the  $J$ -factors while the shaded regions correspond to the  $1\sigma$  standard deviation.

### 1458 3.9 Discussion and Conclusions

1459 In this multi-instrument analysis, we have used observations of 20 dSphs from the gamma-ray  
 1460 telescopes Fermi-LAT, H.E.S.S., MAGIC, VERITAS, and HAWC to perform a collective DM  
 1461 search annihilation signals. The data were combined across sources and detectors to significantly

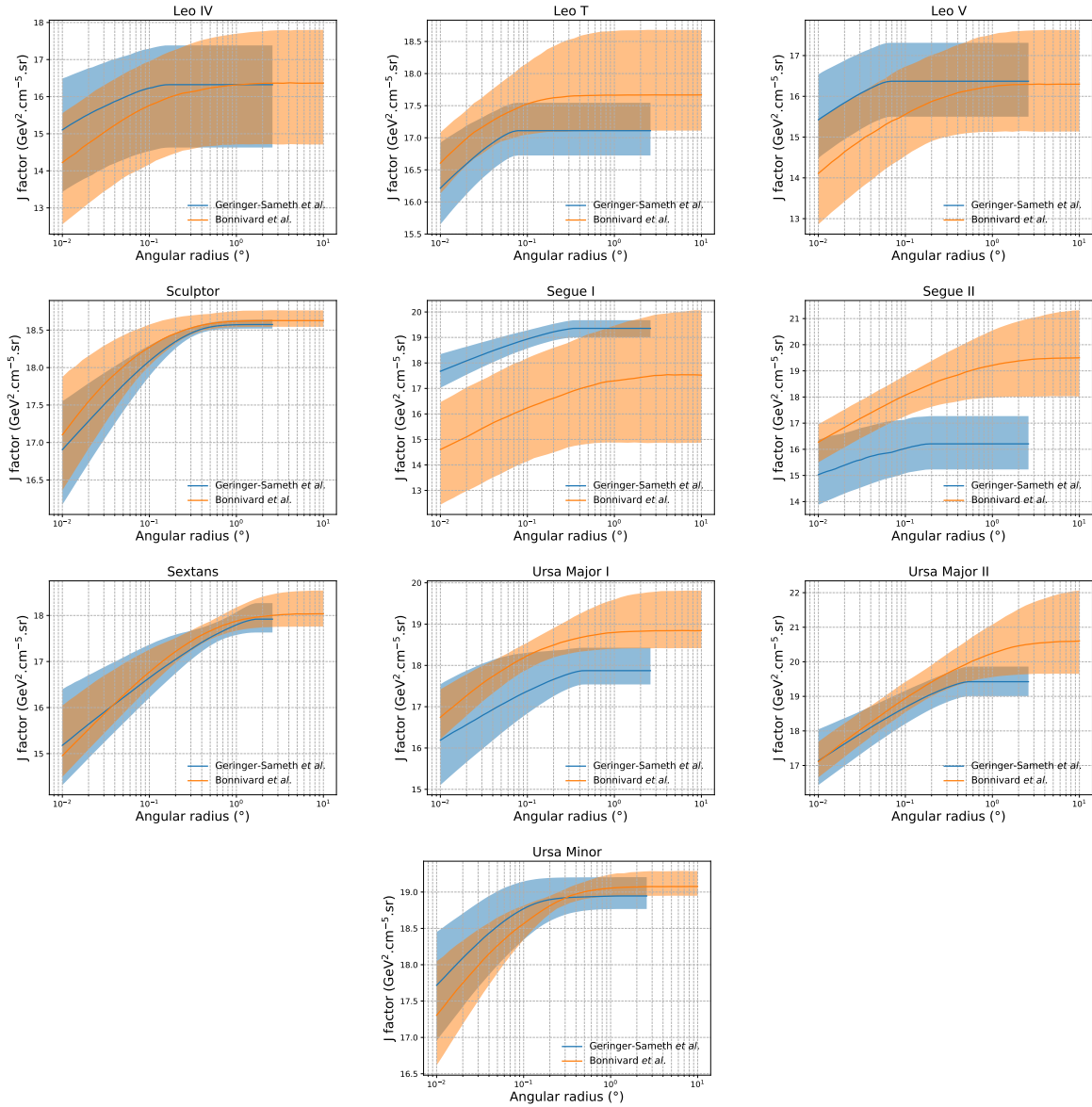


Figure 3.17 Comparisons between the  $J$ -factors versus the angular radius for the computation of  $J$  factors from Ref. [69] ( $\mathcal{GS}$  set in Tab. 3.1) in blue and for the computation from Ref. [63, 71] ( $\mathcal{B}$  set in Tab. 3.1) in orange. The solid lines represent the central value of the  $J$ -factors while the shaded regions correspond to the  $1\sigma$  standard deviation.

increase the sensitivity of the search. We have observed no significant deviation from the null, no DM hypothesis, and so present our results in terms of upper limits on the annihilation cross-section for seven potential DM annihilation channels.

Fermi-LAT brings the most stringent constraints for continuum channels below approximately 1 TeV. The remaining detectors dominate at higher energies. Overall, for multi-TeV DM mass,

1467 the combined DM constraints from all five telescopes are 2-3 times stronger than any individual  
1468 telescope for multi-TeV DM.

1469     Derived from observations of many dSphs, our results produce robust limits given the DM  
1470 content of the dSphs is relatively well constrained. The obtained limits span the largest mass  
1471 range of any WIMP DM search. Our combined analysis improves the sensitivity over previously  
1472 published results from each detector which produces the most stringent limits on DM annihilation  
1473 from dSphs. These results are based on deep exposures of the most promising known dSphs with  
1474 the currently most sensitive gamma-ray instruments. Therefore, our results constitute a legacy of  
1475 a generation of gamma-ray instruments on WIMP DM searches towards dSphs. Our results will  
1476 remain the reference in the field until a new generation of more sensitive gamma-ray instruments  
1477 begin operations, or until new dSphs with higher  $J$ -factors are discovered.

1478     This analysis serves as a proof of concept for future multi-instrument and multi-messenger  
1479 combination analyses. With this collaborative effort, we have managed to sample over four orders  
1480 in magnitude in gamma-ray energies with distinct observational techniques. Determining the nature  
1481 of DM continues to be an elusive and difficult problem. Larger datasets with diverse measurement  
1482 techniques could be essential to tackling the DM problem. A future collaboration using similar  
1483 techniques as the ones described in this paper could grow even beyond gamma rays. The models we  
1484 used for this study include annihilation channels with neutrinos in the final state. Advanced studies  
1485 could aim to merge our results with those from neutrino observatories with large data sets. Efforts  
1486 are already underway to add data from the IceCube, ANTARES, and KM3NeT observatories to  
1487 these gamma-ray results.

1488     From this work, a selection of the best candidates for observations, according to the latest  
1489 knowledge on stellar dynamics and modelling techniques for the derivation of the  $J$ -factors on  
1490 the potential dSphs targets, is highly desirable at the time that new experiments are starting their  
1491 dark matter programs using dSphs. Given the systematic uncertainty inherent to the derivation of  
1492 the  $J$ -factors, an informed observational strategy would be to select both objects with the highest  
1493  $J$ -factors that could lead to DM signal detection, and objects with robust  $J$ -factor predictions, i.e.

1494 with kinematic measurements on many bright stars, which would strengthen the DM interpretation  
1495 reliability of the observation outcome.

1496 This analysis combines data from multiple telescopes to produce strong constraints on astro-  
1497 physical objects. From this perspective, these methods can be applied beyond just DM searches.  
1498 Almost every astrophysical study can benefit from multi-telescope, multi-wavelength gamma-ray  
1499 studies. We have enabled these telescopes to study the cosmos with greater precision and detail.  
1500 Many astrophysical searches can benefit from multi-instrument gamma-ray studies, for which our  
1501 analysis lays the foundation.

## CHAPTER 4

### 1502 MULTITHREADING HAWC ANALYSES FOR DARK MATTER SEARCHES

#### 1503 4.1 Introduction

1504 HAWC’s current software suite, plugins to 3ML and HAL [68, 34], do not fully utilize compu-  
1505 tational advancements of recent decades. Said advancements include the proliferation of Graphical  
1506 Processing Units (GPUs), and multithreading on multicore processors. The analysis described in  
1507 chapter 3 took up to 3 months of wall time waiting for the full gambit of data analysis and simulation  
1508 of background to compute. Additionally, with the updated 2D energy binning scheme,  $f_{\text{hit}}$  and  
1509 Neural Network (NN), the time needed to compute expected to grow. Although excessive comput-  
1510 ing time was, in part, from an intense use of a shared computing cluster, it was evident that there  
1511 was room for improvement. In HAWC’s next generation dSph DM search, I decided to develop  
1512 codes that would utilize the multicore processors on modern high performance computing clusters.  
1513 The results of this work are featured in this chapter and brought a human timing improvement to  
1514 computation that scales approximately as  $1/N$  where  $N$  is the number of threads.

#### 1515 4.2 Dataset and Background

1516 This section enumerates the data and background methods used for HAWC’s multithreaded  
1517 study of dSphs. Section 4.2.1 and Section 4.2.2 are most useful for fellow HAWC collaborators  
1518 looking to replicate a multithreaded dSph DM search.

##### 1519 4.2.1 Itemized HAWC files

1520 These files are only available withing HAWC’s internal documentation and collaborators. They  
1521 are not meant for public access, and are presented here so that HAWC collaborators can reproduce  
1522 results accurately.

- 1523 • Detector Resolution: `refit-Pass5-Final-NN-detRes-zenith-dependent.root`
- 1524 • Data Map: `Pass5-Final-NN-maptree-ch103-ch1349-zenith-dependent.root`
- 1525 • Spectral Dictionary: `HDMspectra_dict_gamma.npy`

1526 **4.2.2 Software Tools and Development**

1527 This analysis was performed using HAL and 3ML [34, 57] in Python3. I built software  
1528 in collaboration with Michael Martin and Letrell Harris to implement the *Dark Matter Spectra*  
1529 *from the Electroweak to the Planck Scale* (HDM) [79] and dSphs spatial model from [80] for  
1530 HAWC analysis. A NumPy dictionary of HDM, `HDMspectra_dict_gamma.npy`, was made for  
1531 portability within the collaboration. These dictionaries were generated from the [git repository](#) [79].  
1532 The analysis was performed using the Neural Network energy estimator for Pass 5.F. A description  
1533 of this estimator was provided in chapter 2. [TODO: Define a subsection when it's written](#), and its  
1534 key, relevant improvements are an improved energy estimation and improved sensitivities at higher  
1535 zenith angles. All other software used for data analysis, DM profile generation, and job submission  
1536 to SLURM are also kept in my sandbox in the [Dark Matter HAWC](#) project. The above repository  
1537 also incorporates the model inputs used previously in Glory Duck, described in chapter 3, so Glory  
1538 Duck remains compatible with modern software.

1539 **4.2.3 Data Set and Background Description**

1540 The HAWC data maps used for this analysis contain 2565 days of data between runs 2104 and  
1541 7476. They were generated from pass 5.f reconstruction. The analysis is performed using the NN  
1542 energy estimator with bin list:

1543 `B1C0Ea, B1C0Eb, B1C0Ec, B1C0Ed, B1C0Ee, B2C0Ea, B2C0Eb, B2C0Ec, B2C0Ed, B2C0Ee,`  
1544 `B3C0Ea, B3C0Eb, B3C0Ec, B3C0Ed, B3C0Ee, B3C0Ef, B4C0Eb, B4C0Ec, B4C0Ed, B4C0Ee,`  
1545 `B4C0Ef, B5C0Ec, B5C0Ed, B5C0Ee, B5C0Ef, B5C0Eg, B6C0Ed, B6C0Ee, B6C0Ef, B6C0Eg,`  
1546 `B6C0Eh, B7C0Ee, B7C0Ef, B7C0Eg, B7C0Eh, B7C0Ei, B8C0Ee, B8C0Ef, B8C0Eg, B8C0Eh,`  
1547 `B8C0Ei, B8C0Ej, B9C0Ef, B9C0Eg, B9C0Eh, B9C0Ei, B9C0Ej, B10C0Eg, B10C0Eh,`  
1548 `B10C0Ei, B10C0Ej, B10C0Ek, B10C0El`

1549 Bin 0 was excluded as it has substantial hadronic contamination and poor angular resolution.

1550 Background considerations and source selection was identical to Section 3.2.3, and no additional  
1551 arguments are provided here. Many of the HAWC systematics explored in Section 3.7 also apply

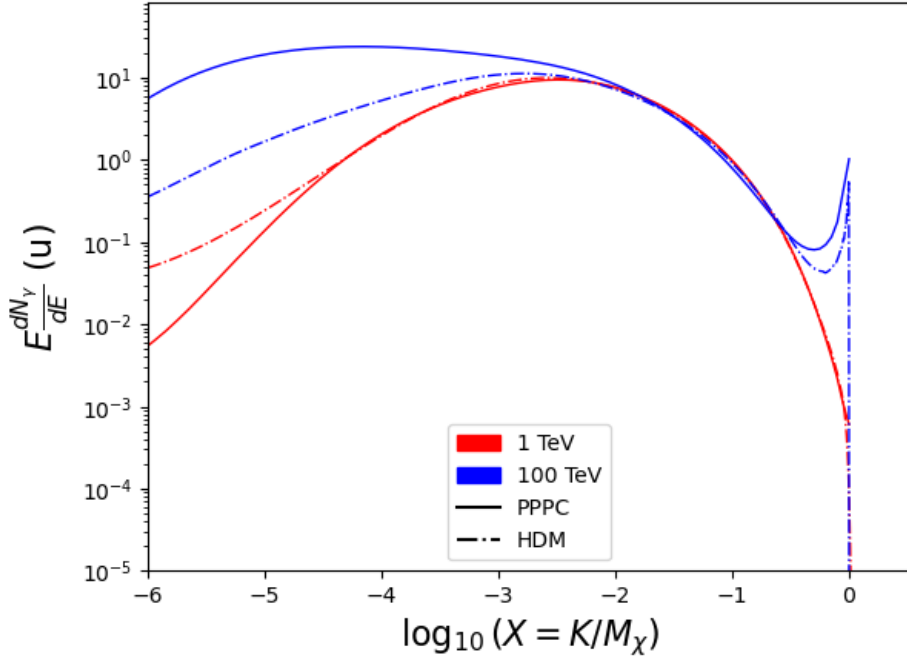


Figure 4.1 Spectral hypotheses from PPPC [58] and HDM [79] for DM annihilation:  $\chi\chi \rightarrow W^-W^+$ . Solid lines are spectral models with EW corrections from the PPPC. Dash-dot lines are spectral models from HDM. Red lines are models for  $M_\chi = 1$  TeV. Blue lines represent models for  $M_\chi = 100$  TeV.

1552 for this DM search and are not added upon here.

1553 **4.3 Analysis**

1554 The analysis and its systematics are almost identical to Section 3.3. Importantly, we use the  
 1555 same **TODO: fix this ref** Equation (3.1) and Equation (3.2) for estimating the gamma-ray flux at  
 1556 HAWC from our sources.

1557 **4.3.1  $\frac{dN_\gamma}{dE_\gamma}$  - Particle Physics Component**

1558 For these spectra, we import HDM with Electroweak (EW) corrections and additional correc-  
 1559 tions for neutrinos above the EW scale [79]. The spectra are implemented as a model script in  
 1560 astromodels for 3ML. A comprehensive description of EW corrections and neutrino considerations  
 1561 are provided later in Sec. 7.

1562 Figure 4.1 demonstrates the impact of changes implemented in HDM on DM annihilation to W  
 1563 bosons. A class in astromodels was developed to include HDM and is aptly named **HDMspectra**  
 1564 within `DM_models.py`. The SM DM annihilation channels studied here are  $\chi\chi \rightarrow$ :

1565         $e^+e^-$ ,  $\mu^+\mu^-$ ,  $\tau^+\tau^-$ ,  $b\bar{b}$ ,  $t\bar{t}$ ,  $gg$ ,  $W^+W^-$ ,  $ZZ$ ,  $c\bar{c}$ ,  $u\bar{u}$ ,  $d\bar{d}$ ,  $s\bar{s}$ ,  $\nu_e\bar{\nu}_e$ ,  $\nu_\mu\bar{\nu}_\mu$ ,  $\nu_\tau\bar{\nu}_\tau$ ,  $\gamma\gamma$ ,  $hh$ .

1566 For  $\gamma\gamma$  and  $ZZ$ , a substantial fraction of the signal photons are expected to have  $E_\gamma = m_\chi$  [79].  
 1567 This introduces  $\delta$ -function that is much narrower than the energy resolution of the HAWC detector.  
 1568 To ensure that this feature is not lost in the likelihood fits, the 'line' feature is convolved with a  
 1569 Gaussian kernel with a  $1\sigma$  width of  $0.05 \cdot m_\chi$  and total kernel window of  $\pm 4\sigma$ . This differs from  
 1570 HAWC's previous line study where 30% of HAWC's energy resolution was used for the kernel [81].  
 1571 The NN energy estimator's strength compared to  $f_{\text{hit}}$  at low gamma-ray energy enables narrower  
 1572 kernels [79].  $\chi\chi \rightarrow \gamma\gamma$  and  $ZZ$  spectral hypotheses are shown in Figure 4.2. We did not explore  
 1573 how well we reconstruct injected signal events for various kernels widths. This is a systematic  
 1574 that should be tested before publication to journal. Spectral models for the remaining annihilation  
 1575 channels are plotted for each  $m_\chi$  in Figure B.1.

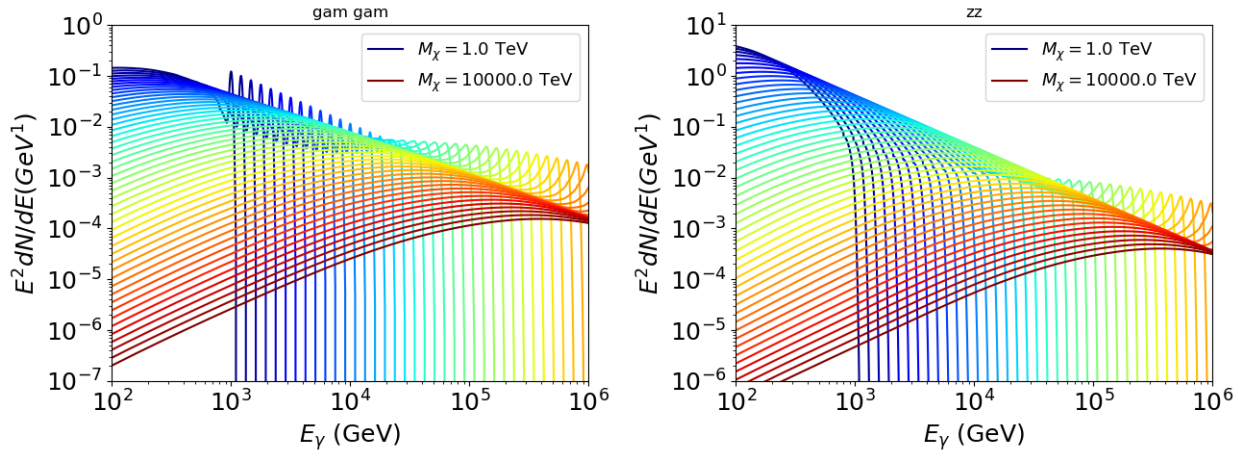


Figure 4.2 Photon spectra for  $\chi\chi \rightarrow \gamma\gamma$  (left) and  $\chi\chi \rightarrow ZZ$  (right) after Gaussian convolution of line features. Both spectra have  $\delta$ -features at photon energies equal to the DM mass. Bluer lines are annihilation spectra with lower DM mass. Redder lines are spectra from larger DM mass. All spectral models are sourced from the Heavy Dark Matter models [79]. Axes are drawn roughly according to the energy sensitivity of HAWC.

1576 **4.3.2 J Astrophysical Components**

1577 The J-factor profiles for each source are imported from Louis Strigari et al. (referred to with  
 1578  $\mathcal{LS}$ ) [80]. The  $\mathcal{LS}$  catalog fits a Navarro–Frenk–White (NFW) [62] spatial DM distributions to

1579 the dSphs which has a DM density of

$$\rho(r) = \frac{\rho_0}{\frac{r}{R_s} \left(1 + \frac{r}{R_s}\right)^2}. \quad (4.1)$$

1580  $\rho_0$  and the scale radius,  $R_s$  are free parameters fit for each dSph.  $r$  is the distance from the center  
1581 of the dSph.

1582 Profiles in  $\frac{dJ}{d\Omega}(\theta)$  up to an angular separation  $\theta = 0.5^\circ$  were provided directly from the authors.

1583 Map generation from these profiles were almost identical to Section 3.3.2 except that a higher order  
1584 trapezoidal integral was used for the normalization of the square, uniformly-spaced map:

$$p^2 \cdot \sum_{i=0}^N \sum_{j=0}^M w_{i,j} \frac{dJ}{d\Omega}(\theta_{i,j}, \phi_{i,j}) \quad (4.2)$$

1585  $p$  is the angular side of one pixel in the map.  $w_{i,j}$  is a weight assigned the following ways:

1586  $w_{i,j} = 1$  if  $(\theta_{i,j}, \phi_{i,j})$  is fully within the region of integration

1587  $w_{i,j} = 1/2$  if  $(\theta_{i,j}, \phi_{i,j})$  is on an edge of the region of integration

1588  $w_{i,j} = 1/4$  if  $(\theta_{i,j}, \phi_{i,j})$  is on a corner of the region of integration

1589 Figure 4.3 shows the median and  $\pm 1\sigma$  maps used as input for this DM annihilation study.

### 1590 4.3.3 Source Selection and Annihilation Channels

1591 HAWC's sources for this multithreaded analysis include Coma Berenices, Draco, Segue 1, and  
1592 Sextans.  $\mathcal{LS}$  observed up to 43 sources in its publication, however only 4 of the best fit profiles  
1593 were provided at the time this thesis was written. A full description of each source used in this  
1594 analysis is found in Table 4.1.

1595 This analysis improves on chapter 3 in the following ways. Previously, the particle physics  
1596 model used for gamma-ray spectra from DM annihilation was from the PPPC [58] which missed  
1597 important considerations relevant for the neutrino sector. HDM is used to account for this shortfall  
1598 [79]. HDM also models DM to the Planck scale which permits HAWC to probe PeV scale DM. For  
1599 this study, we sample DM masses: 1 TeV - 10 PeV with 6 mass bins per decade in DM mass. In

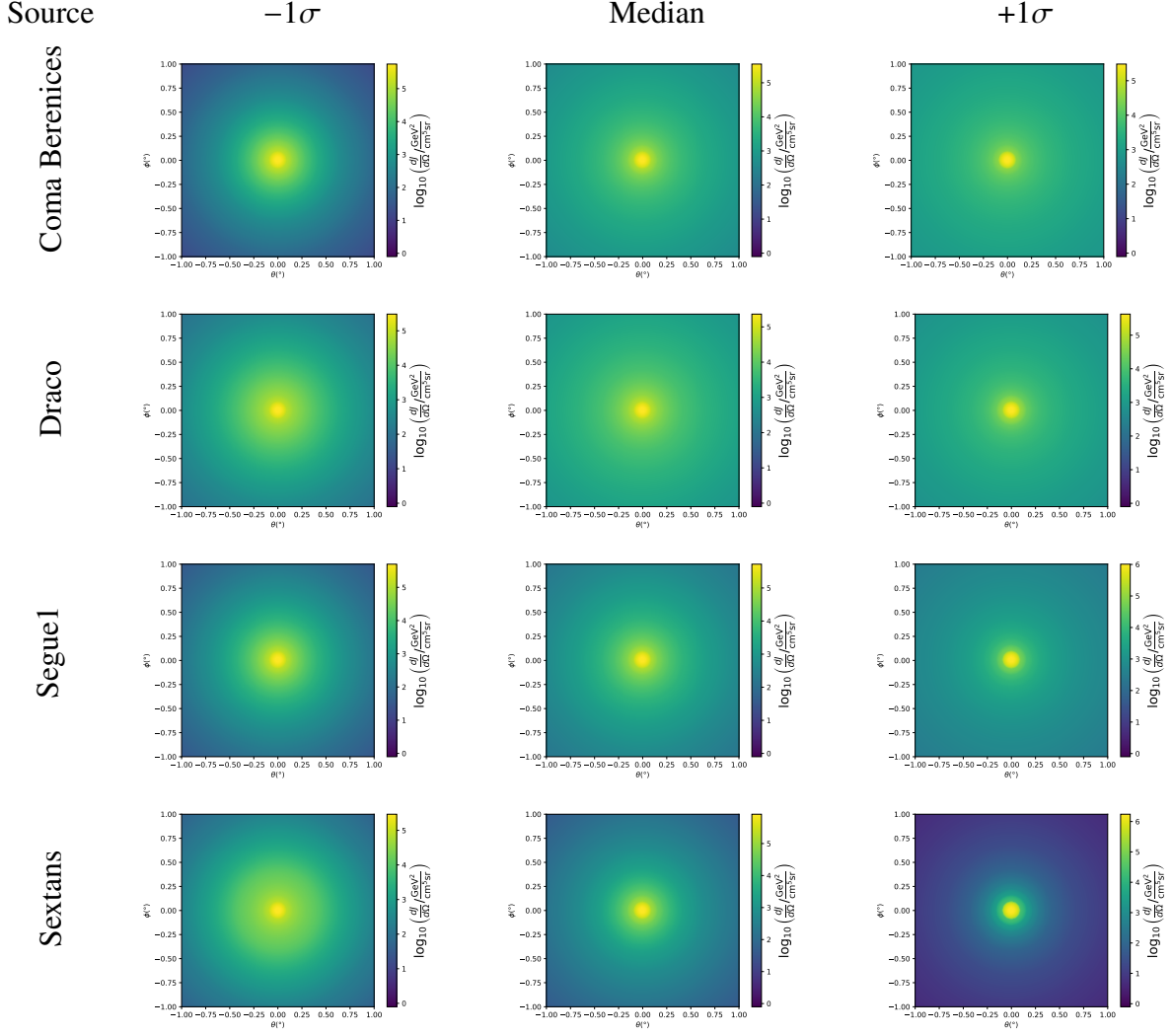


Figure 4.3  $\frac{dJ}{d\Omega}$  maps for Coma Berenices, Draco, Segue1, and Sextans. Columns are divided for the  $\pm 1\sigma$  uncertainties in  $dJ/d\Omega$  around the mean value from  $\mathcal{LS}$  [80]. Origin is centered on the specific dwarf spheroidal galaxies (dSph).  $\theta$  and  $\phi$  axes are the angular separation from the center of the dwarf. Profiles are truncated at  $1^\circ$  and flattened beyond.

the case of line spectra ( $\chi\chi \rightarrow \gamma\gamma$ , or  $ZZ$ ), we double the mass binning to 12 DM mass bins per decade in DM mass.

$\mathcal{LS}$  provides 25 sources within HAWC's field of view. Additionally, NFW [62] DM distributions have fewer parameters than Zhao [61], so  $\mathcal{LS}$  fits ultra-faint dwarves which expands the number of sources. However, all sources were not provided by the authors in time for the completion of this dissertation. Finally, the gamma-ray ray dataset is much larger. The study performed here analyzes 2565 days of data compared to 1017 days analyzed in chapter 3.

1607 **4.4 Likelihood Methods**

1608 These are identical to Section 3.4.1 and no additional changes are made to the likelihood. Bins  
 1609 in this analysis are expanded to include HAWC’s NN energy estimator.

1610 **4.5 Computational Methods: Multithreading**

1611 Previously, as in Section 3.3, the likelihood was minimized for one model at a time. One model  
 1612 in this case representing a DM annihilation channel (CHAN), DM mass ( $m_\chi$ ), and dSph ((SOURCE)).  
 1613 In an effort to conserve human and CPU time, jobs submitted for high performance computing  
 1614 contained a list of  $m_\chi$  to iterate over for likelihood fitting. Jobs were then trivially parallelized  
 1615 for each permutation of the two lists: CHANS and SOURCES. The lists for CHANS and SOURCES are  
 1616 found in Section 4.3.1 and Table 4.1, respectively. Initially, 11  $m_\chi$  were serially sampled for one  
 1617 job defined by a [CHAN, SOURCE] tuple. Computing the likelihoods would take between 1.5 to 2 hrs,  
 1618 stochastically, for a job. We expect to compute likelihoods for data and 300 Poisson background  
 1619 trials. The estimated CPU time based on the above for all CHAN (N = 17) and SOURCE (M = 25)  
 1620 was estimated to 127,925 jobs. In total, 1,407,175 likelihood fits and profiles would be computed  
 1621 for the 11 mass bins we wished to study. The estimated CPU time ranged between 8k CPU days  
 1622 to 10k CPU days. Human time is more challenging to estimate as job allocation is stochastic and  
 1623 highly dependent on what other users are submitting. Yet, it is unlikely that all jobs would run  
 1624 simultaneously. Therefore, we can expect human time to be about as long as was seen in chapter 3

Name	Distance (kpc)	$l, b$ ( $^\circ$ )	$\log_{10} J$ ( $\mathcal{LS}$ set) $\log_{10}(\text{GeV}^2\text{cm}^{-5}\text{sr})$
Coma Berenices	44	241.89, 83.61	$19.00^{+0.36}_{-0.35}$
Draco	76	86.37, 34.72	$18.83^{+0.12}_{-0.12}$
Segue I	23	220.48, 50.43	$19.12^{+0.49}_{-0.58}$
Sextans	86	243.50, 42.27	$17.73^{+0.13}_{-0.12}$

Table 4.1 Summary of the relevant properties of the dSphs used in the present work. Column 1 lists the dSphs. Columns 2 and 3 present their heliocentric distance and galactic coordinates, respectively. Column 4 reports the  $J$ -factors of each source given from the  $\mathcal{LS}$  studies and estimated  $\pm 1\sigma$  uncertainties. The values  $\log_{10} J$  ( $\mathcal{LS}$  set) [80] correspond to the mean  $J$ -factor values for a source extension truncated at  $0.5^\circ$ .

1625 which was on the order of months to fully compute on a smaller analysis. A visual aid to describe  
 1626 how jobs were organized is provided in Figure 4.4.

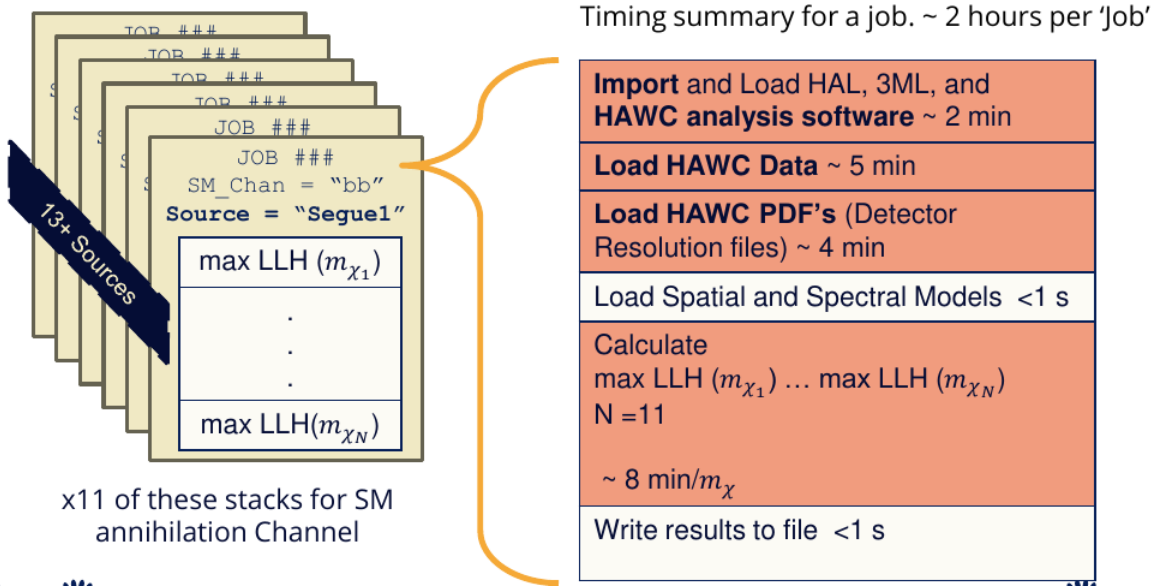


Figure 4.4 Infographic on how jobs and DM computation was organized in Section 3.3. Jobs were built for each permutation of CHANS and SOURCES shown by the left block in the figure. Each job, which took on the order 2 hrs to compute, had the following work flow: 1. Import HAWC analysis software, 2 min to run. 2. Load HAWC count maps, 5 min to run. 3. Load HAWC energy and spatial resolutions, 4 min. 5. Load DM spatial source templates and spectral models, less than 1 s. 6. Perform likelihood fit on data and model, about 8 min per DM mass. 7. Write results to file, less than 1s.

1627 The computational needs for this next generation DM analysis are extreme and is unlike other  
 1628 analyses performed on HAWC. It became clear that there was a lot to gain from optimizing how  
 1629 the likelihoods are computed. This section discusses how multi-threading was applied to solve and  
 1630 reduce HAWC's computing of likelihoods for large parameter spaces like in DM searches.

### 1631 4.5.1 Relevant Foundational Information

1632 The profiling of the likelihood for HAWC is done via gradient descent where the normalization  
 1633 of Equation (3.1) (linearly correlated with  $\langle \sigma v \rangle$ ) is rescaled in the descent. Additionally, we sample  
 1634 the likelihood space for a defined list of  $\langle \sigma v \rangle$ 's described in Section 3.4.2. The time to compute  
 1635 these values is not predictable or consistent because many variables can change across the full  
 1636 model-space. Comprehensively, these variables are:

1637       •  $m_\chi$  : DM rest mass  
 1638       • CHAN : DM annihilation channel in SM.  
 1639       • SOURCE : dSph. Involves a spatial template AND coordinate in HAWC data.  
 1640       •  $\langle\sigma v\rangle$ : Effectively the flux normalization and free parameter in the likelihood fit.  
 1641      Therefore, we develop an asynchronous, functional-parallel coding pattern. Asynchronous meaning  
 1642      the instructions within a function are independent and permitted to be out of sync with sibling  
 1643      computations. Functional-parallel meaning that instructions are the subject of parallelization  
 1644      rather than threading the likelihood computation. This is close to trivial parallelization seen in  
 1645      Figure 4.4 except that we seek to consolidate the loading stages (software, data, and detector  
 1646      resolution loading). Multiple asynchronous threads are expected to reduce total serial processing  
 1647      time and total overhead across the entire project in addition to saving human time.

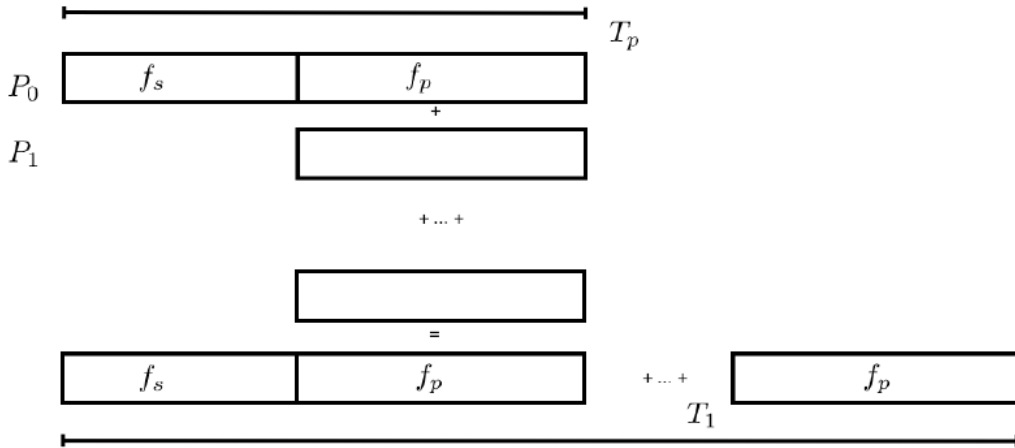


Figure 4.5 Graphic of Gustafson parallel coding pattern.  $f_s$  is the fraction of a program, in time, spent on serial computation.  $f_p$  is the fraction of computing time that is parallelizable.  $T_p$  is the total time for a parallel program to run.  $T_1$  is the total time for a parallel program to run if only 1 processor is allocated.  $P_N$  is the  $N$ -th processor where it's row is the computation the processor performs. The Gustafson pattern is most similar to what is implemented for this analysis. Figure is pulled from [82].

1648      We need a way to measure and compare the expected speedup and efficiency gain for this  
 1649      asynchronous coding pattern. I pull inspiration for timing measurement from [82] and use *Amdahl's*

1650 law with hybrid programming. Hybrid programming meaning that the computation is a mix of  
 1651 distributed and shared memory programming. If we assume the code is fully parallelizable over  $p$   
 1652 processors and  $c$  threads, the ideal speedup is simply  $pc$ , and ideal run-time is  $T_1/(pc)$ .  $T_1$  is the  
 1653 total time for a parallel program to run if only 1 processor is allocated. However, the coding pattern  
 1654 contains some amount of unavoidable serial computation, as shown in Figure 4.5. In our case, the  
 1655 run time,  $T_{p,c}$ , is estimated to be

$$T_{p,c} = \frac{T_1}{pc} (1 + F_s(c - 1)). \quad (4.3)$$

1656  $F_s$  is the fraction of CPU time dedicated to serial computation. The expected speedup,  $S_{p,c}$ , is

$$S_{p,c} \equiv \frac{T_1}{T_{p,c}} = \frac{pc}{1 + F_s(c - 1)}. \quad (4.4)$$

1657 From Equation (4.4), we can see that the speed-up scales with  $p/F_s$ . We are free to minimize  $F_s$   
 1658 asymptotically by enlarging the total models that are submitted to the thread pool, thereby shrinking  
 1659 the CPU fraction dedicated to serial operation. We are also free to define exactly how many threads  
 1660 and processors we utilize, yet eventually hit a hard cap at the hardware available on our computing  
 1661 cluster. HAWC uses Intel Xeon™processors with 48 cores and 96 threads. We see that a successful  
 1662 code will scale well as the expected speedup is inversely correlated with  $F_s$ . As the total number  
 1663 of models sampled grows, the speedup will also.

#### 1664 4.5.2 Implementation

1665 The multithreaded code was written in Python3 and is documented in the `dark_matter_hawc`  
 1666 [repository](#) within the script named `mpu_analysis.py`. A version of the script as of April 25  
 1667 **TODO: make sure to update on this date** is also provided in Section B.2. It has many dependencies  
 1668 including the HAWC analysis software. Figure 4.6 displays the workflow of a job with 3 threads.  
 1669 Within a job, SOURCE is kept fixed and CHANS remains 17 elements long. More  $m_\chi$  are sampled  
 1670 from 11 bins up to 49 (for  $\gamma\gamma$  and ZZ) and 25 (for remaining CHANS) which amounts to 12 or 6  
 1671 mass bins per decade.  $m_\chi$  and CHANS are permuted into a 473 element list which is split evenly  
 1672 across N threads where N is [2, 8, 16]. For each  $m_\chi$ -CHAN tuple, 1001  $\langle\sigma v\rangle$  values are sampled in

Timing summary for a multi-threaded job.

Import and Load HAL, 3ML, and <b>HAWC analysis software</b> ~ 2 min		
Load HAWC Data ~ 5 min		
Load HAWC PDF's (Detector Resolution files) ~ 4 min		
Load Spatial Model < 1s		
Load Spectra Models <1 s	Load Spectra Models <1 s	Load Spectra Models <1 s
Calculate max LLH (Chan_0, $m_{\chi_1}$ ) ... max LLH (Chan_?, $m_{\chi_N}$ ) N = TOTAL/N_THREADS  ~ 8 min/Spec_model	Calculate max LLH (Chan_?, $m_{\chi_1}$ ) ... max LLH (Chan_?, $m_{\chi_N}$ ) N = TOTAL/N_THREADS  ~ 8 min/Spec_model	Calculate max LLH (Chan_?, $m_{\chi_1}$ ) ... max LLH (Chan_?, $m_{\chi_N}$ ) N = TOTAL/N_THREADS  ~ 8 min/Spec_model
Write results to file <1 s	Write results to file <1 s	Write results to file <1 s
Join Threads and terminate < 1s		

Figure 4.6 Task chart for one multithreaded job developed for this project. Green blocks indicate a shared resource across the threads AND computation performed serially. Red blocks indicate functional parallel processing within each thread. 3 threads are represented here, yet many more can be employed during the full analysis. Jobs are defined by the SOURCE as these require unique maps to be loaded into the likelihood estimator. The  $m_{\chi}$ , CHAN, and  $\langle \sigma v \rangle$  variables are entered into the thread pool and allocated as evenly as possible across the threads.

1673 the likelihood, and the value of  $\langle \sigma v \rangle$  that maximizes the likelihood is found. Although rare, fits  
1674 that failed are handled on a case by case basis.

### 1675 4.5.3 Performance

M Tasks	$T_{p,c}$ (hr:min:s)			
	$T_{1,1}$	$T_{1,2}$	$T_{1,8}$	$T_{1,16}$
50	1:40:37.5	0:52:43.7	0:19:13.8	0:13:44.0
74	2:22:30.0	1:15:00.6	0:25:21.3	0:15:49.8
100	(3:07:51.9)	1:40:10.5	0:30:44.4	0:20:01.4
200	(6:02:20.6)	-	1:00:32.0	0:30:35.0
473	(13:58:40.3)	-	2:01:41.4	1:07:53.2

Table 4.2 Timing summaries for analyses for serial and multithreaded processes. M tasks is the number of functional-parallel tasks ran for the computation.  $T_{p,c}$  is a single run time in hours:minutes:seconds for runs utilizing  $p$  nodes and  $c$  threads. Runs are run interactively on the same computer to maximize consistency. Empty entries are indicated with '-'. (·) entries are estimated entries extrapolated from data earlier in the column.

1676 We see a significant reduction to wall time needed for our dSph analyses to run. Table 4.2

shows the timing summaries for analyses of different sizes and thread counts. Additionally, the efficiency gained when consolidating the serial loading of data is also apparent in our ability to study many more tasks in about the same amount of wall time as a smaller serial computation. Trials represented in the table were run on an AMD Opteron® processor 6344 with 48 cores, 2 threads per core; 2.6 GHz clock. This is not the same architecture used for analysis on the HAWC computing cluster however they are similar enough that results shown here are reasonably representative of computing on the HAWC computing cluster. I use Tab. 4.2 for the inferences and conclusions in the following paragraphs.

First, we want to find  $T_s$ , the time of serial computation. From Fig. 4.5, the timing for our coding pattern can be written as

$$T_s + Mt_p = T_{1,1}^M. \quad (4.5)$$

$M$  is the number of functional-parallel tasks (represented as column 1 of Tab. 4.2), and  $t_p$  is the average time to complete a single parallel task.  $T_{1,1}^M$  is the total time for a parallel program to run if only 1 processor is allocated for  $M$  parallel task. With two runs of different  $M$  ( $M_1$  and  $M_2$ ), we can use a system of equations to compute

$$T_s = 803.1\text{s} \text{ and } t_p = 104.6\text{s} \quad (4.6)$$

Now, we have specific estimation for the fraction of serial computing time,  $F_s$ :

$$F_s = \frac{803.1}{803.1 + 104.6 \cdot M}. \quad (4.7)$$

The maximum  $M$  for this study is 473 which evaluates to:  $F_s = 0.016$  or 1.6% of computing time. Table 4.3 shows the resulting speedups.

We see a speedup that generally exceeds expectations from Eq. (4.4) for real trail runs. We also see that there are diminishing returns as the number of threads increases. For small jobs with large  $c$ , both the expected and observed speedup are significantly smaller than  $c$ . One thing not considered in Eq. (4.4) is the time incurred via communication latency. Communication latency increases with the number of threads and contributes to diminishing returns. Additionally, these values are

M Tasks	$F_s$	$S_{1,2}$	$S_{1,8}$	$S_{1,16}$
50	1.33 E-1	1.90 [1.76]	5.23 [4.14]	6.35 [5.34]
74	9.40 E-2	1.90 [1.83]	5.62 [4.82]	9.00 [6.64]
100	7.13 E-2	1.88 [1.87]	6.11 [5.34]	9.38 [7.73]
200	3.70 E-2	- [1.93]	5.98 [6.36]	11.85 [10.29]
473	1.60 E-2	- [1.97]	6.89 [7.20]	12.35 [12.91]

Table 4.3 Speed up summaries for analyses for serial and multithreaded processes. M tasks is the number of functional-parallel tasks ran for the computation.  $S_{p,c}$  is a single speedup comparison for runs utilizing  $p$  nodes and  $c$  threads. [·] are the estimated speedups calculated from Tab. 4.2, Eq. (4.7), and Eq. (4.4). Empty entries are indicated with '-'.

1699 for single runs and do not consider the stochastic variation expected in a shared high performance  
 1700 computing resource. Therefor, these results are not strictly conclusive, yet demonstrate the merits  
 1701 of multi-threading. We see very clearly that there is a lot to gain, and this new coding pattern will  
 1702 expand HAWC's analysis capabilities.

## 1703 4.6 Analysis Results

1704 3 of the 43  $\mathcal{L}\mathcal{S}$  dSphs considered for the multithreaded analysis. These dSph are analyzed  
 1705 for emission from DM annihilation according to the likelihood method described in Section 3.4.  
 1706 The three likelihood profiles are then stacked to synthesize a combined limit on the dark matter  
 1707 annihilation cross-section,  $\langle\sigma v\rangle$ . This combination is done each of the 17 SM annihilation channels.  
 1708 Figure 4.7 and Fig. 4.8 show the combined limits for all annihilation channels with HAWC's  
 1709 observations. Test statistics of the best fit  $\langle\sigma v\rangle$  values for each  $m_\chi$  and CHAN are shown in Fig. 4.9  
 1710 and Fig. 4.10. We also compare these limits to HAWC's Glory Duck limits shown in Section 3.5.  
 1711 The comparison to Glory Duck are featured in Fig. 4.11 for all the DM annihilation channels studied  
 1712 for Glory Duck. A full comparison is provided in the appendix in Fig. B.2, Fig. B.3, and Fig. B.4.  
 1713 Here, we show updated limits for  $\chi\chi \rightarrow b\bar{b}, e\bar{e}, \mu\bar{\mu}, \tau\bar{\tau}, t\bar{t}, W^+W^-$ ,  $\gamma\gamma$  and  $ZZ$ . For the first time  
 1714 ever, we show limits for  $\chi\chi \rightarrow c\bar{c}, s\bar{s}, u\bar{u}, d\bar{d}, \nu_e\bar{\nu}_e, \nu_\mu\bar{\nu}_\mu, \nu_\tau\bar{\nu}_\tau, gg$ , and  $hh$ .

1715 No DM was found in HAWC observations. The largest excess found in HAWC data was for DM  
 1716 annihilating to  $W$ -bosons or  $\nu_e\bar{\nu}_e$  for  $m_\chi = 10$  TeV at significance  $2.11\sigma$  and  $2.14\sigma$  respectively.  
 1717 HAWC's limits and excesses are dominated by Segue1. Coma Berenices shows excesses at higher  
 1718 DM mass, yet no similar excesses were observed in Segue1 or Sextans. Sextans did not contribute

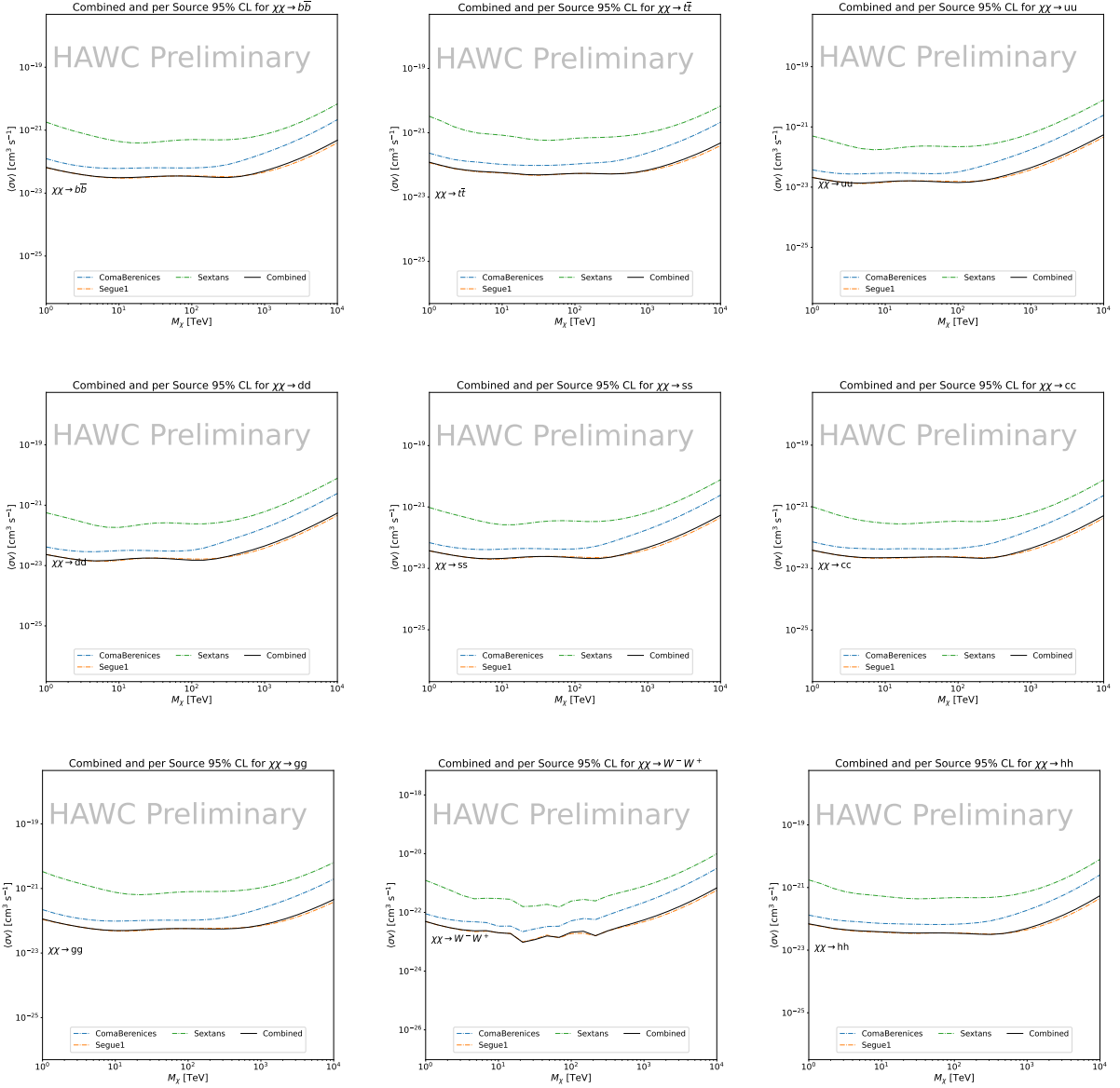


Figure 4.7 HAWC upper limits at 95% confidence level on  $\langle\sigma v\rangle$  versus  $m_\chi$  for  $\chi\chi \rightarrow b\bar{b}$ ,  $t\bar{t}$ ,  $u\bar{u}$ ,  $d\bar{d}$ ,  $s\bar{s}$ ,  $c\bar{c}$ ,  $gg$ ,  $W^+W^-$ , and  $hh$ . Limits are with  $\mathcal{L}\mathcal{S}$   $J$ -factors [80]. The solid line represents the observed combined limit. Dashed lines represent limits from individual dSphs.

1719 significantly to signal excesses or the combined limit as it is at high zenith. Draco was not included  
 1720 as the PDF of some of our analysis bins were wider than what is reasonable for a point source  
 1721 analysis. Draco is at a high zenith for HAWC, so the effort required to include it was not justified  
 1722 by the benefits.

1723 We did not generate background trials in time of writing this thesis. These are not shown and

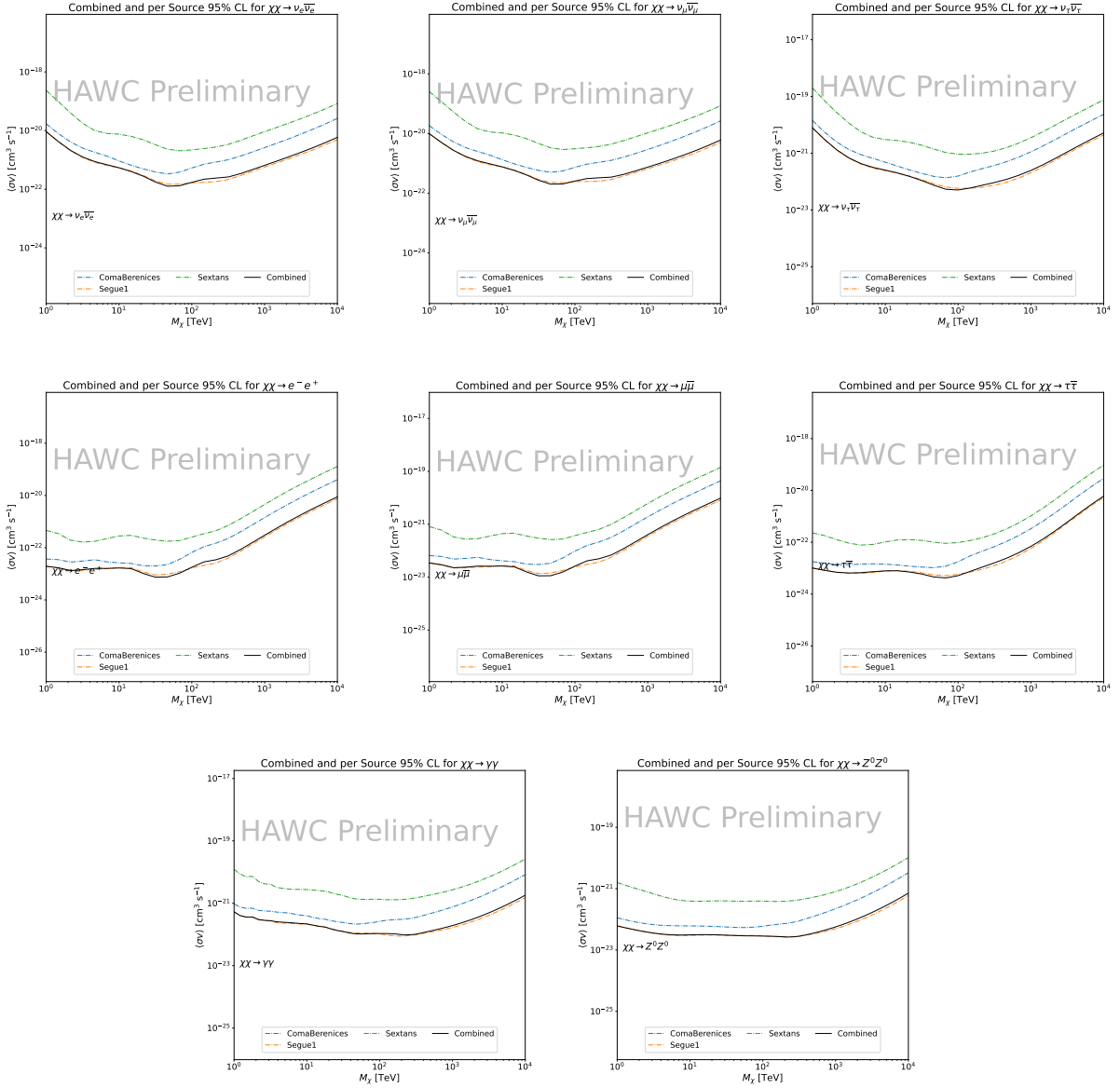


Figure 4.8 HAWC upper limits at 95% confidence level on  $\langle\sigma v\rangle$  versus  $m_\chi$  for  $\chi\chi \rightarrow \nu_e \bar{\nu}_e$ ,  $\nu_\mu \bar{\nu}_\mu$ ,  $\nu_\tau \bar{\nu}_\tau$ ,  $e \bar{e}$ ,  $\mu \bar{\mu}$ ,  $\tau \bar{\tau}$ ,  $\gamma\gamma$  and  $ZZ$ . Limits use  $\mathcal{L}S$   $J$ -factors [80]. The solid line represents the observed combined limit. Dashed lines represent limits from individual dSphs.

1724 are an immediate next step for this analysis before publication.

1725 When comparing these results to Section 3.5, we see an overall decrease to the confidence limit  
 1726 therefore improvement to HAWC's expected sensitivity. This improvement is generally stronger  
 1727 than a doubling of data, or a factor  $\sqrt{2}$  decrease. The comparison is somewhat complex and  
 1728 dependent on the dSph and SM annihilation channel. Figure 4.11 shows the comparisons of limits

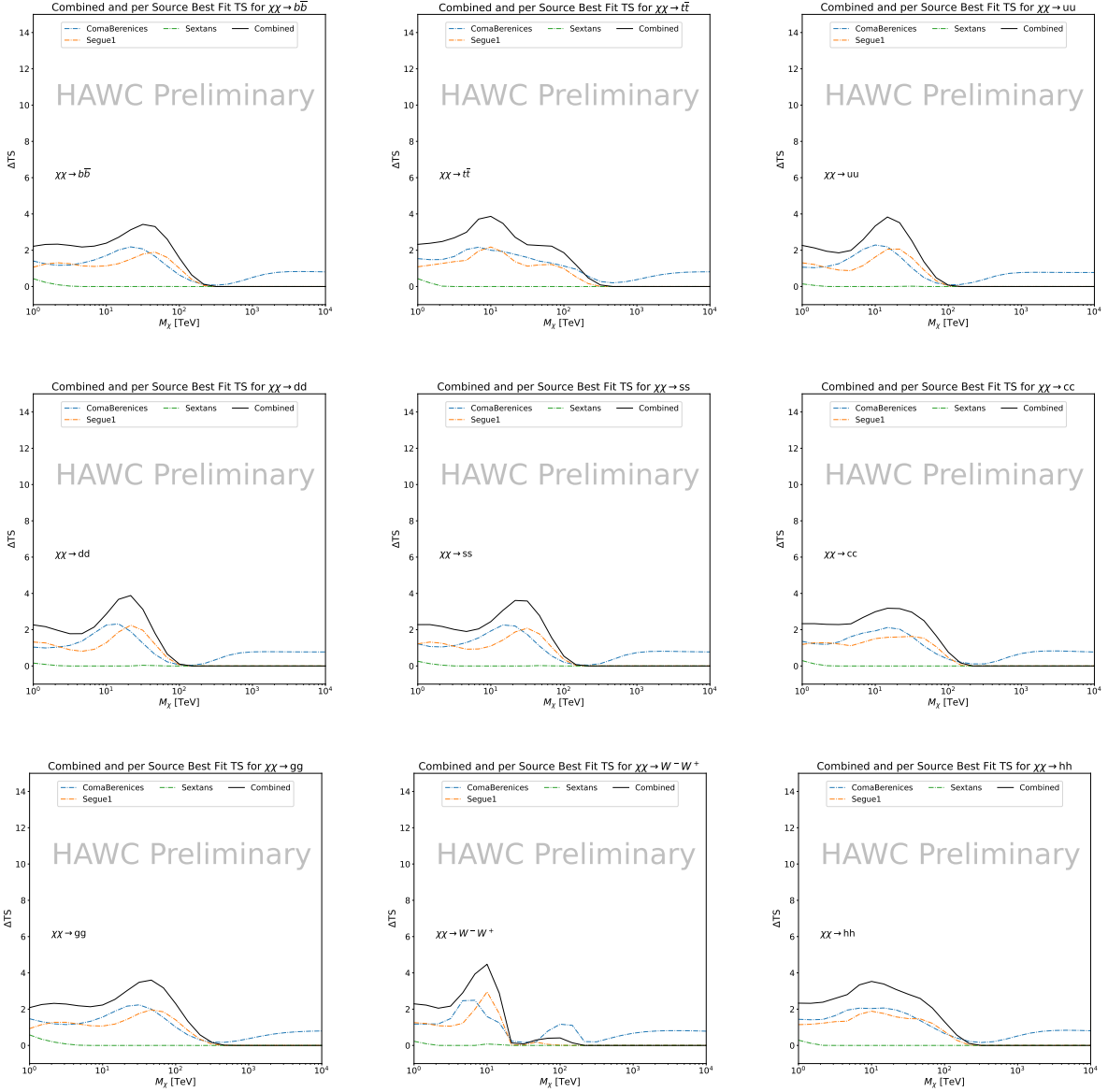


Figure 4.9 HAWC TS values for best fit  $\langle\sigma v\rangle$  versus  $m_\chi$  for SM annihilation channels:  $\chi\chi \rightarrow b\bar{b}$ ,  $t\bar{t}$ ,  $u\bar{u}$ ,  $d\bar{d}$ ,  $s\bar{s}$ ,  $c\bar{c}$ ,  $gg$ ,  $W^-W^+$ , and  $hh$ . Limits use  $\mathcal{LS}$   $J$ -factors. The solid black line shows the combined best fit TS values. The colored, dashed lines are the TS values from each dSph.

1729 calculated for this analysis and Glory Duck (Section 3.5). Segue 1 and Coma Berenices are low  
 1730 zenith where improvements to HAWC's analysis come only from energy estimation. Differences  
 1731 between these two are dominantly from their differences in  $J$ -factor, half-light radii of the dSphs,  
 1732 and the particle physics inputs. Substantial gains in HAWC's analysis methods (pass 5.F) were  
 1733 made at high zenith which is important for sources like Sextans. The HDM particle physics model

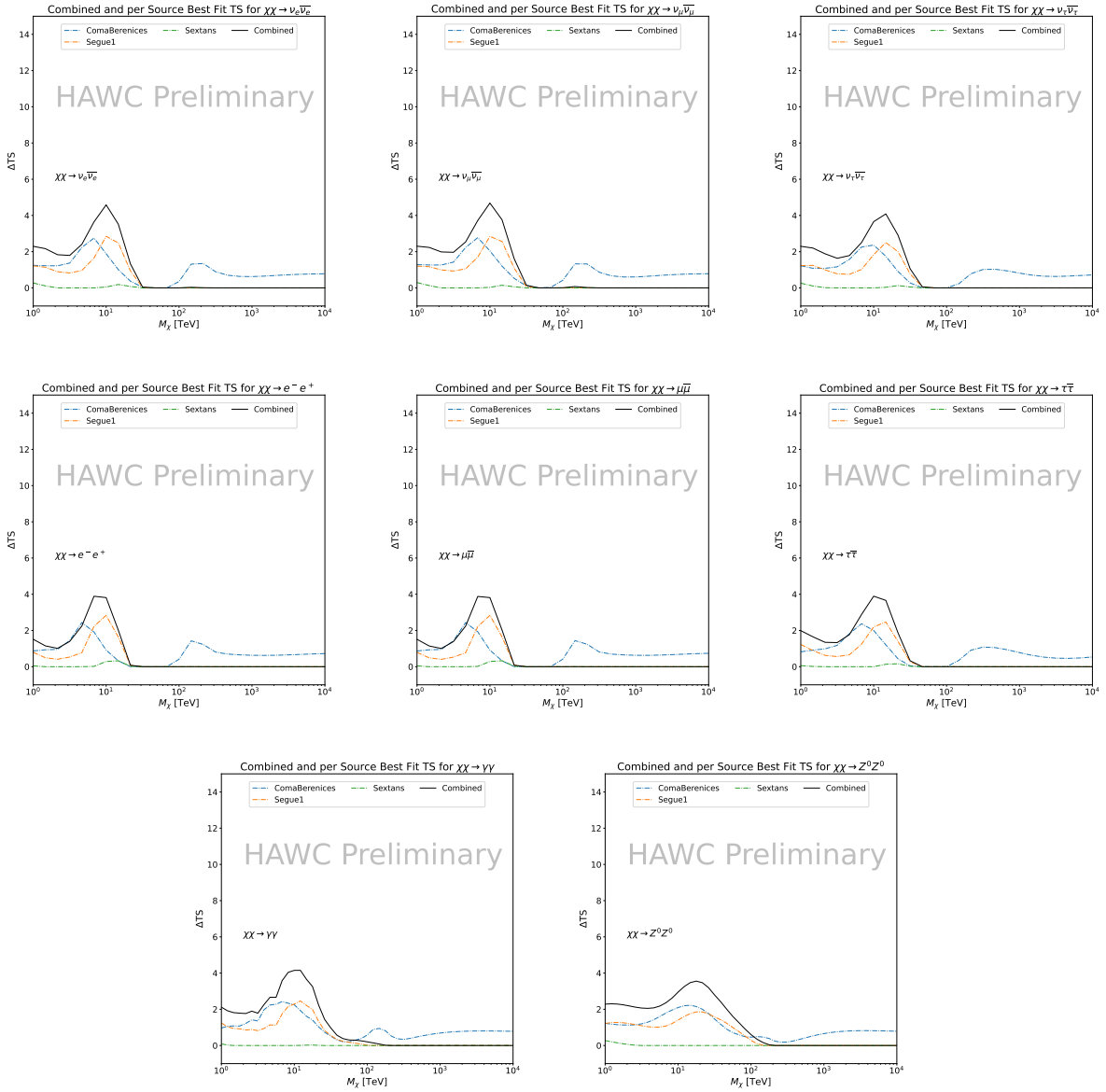


Figure 4.10 HAWC TS values for best fit  $\langle\sigma v\rangle$  versus  $m_\chi$  for SM annihilation channels:  $\chi\chi \rightarrow \nu_e \bar{\nu}_e$ ,  $\nu_\mu \bar{\nu}_\mu$ ,  $\nu_\tau \bar{\nu}_\tau$ ,  $e^- e^+$ ,  $\mu \bar{\mu}$ ,  $\tau \bar{\tau}$ ,  $\gamma\gamma$  and  $ZZ$ . Limits use  $\mathcal{LS}$   $J$ -factors. The solid black line shows the combined best fit TS values. The colored, dashed lines are the TS values from each dSph.

1734 produces almost identical spectra to the PPPC for  $\chi\chi \rightarrow e^- e^+$ . This channel can be used to  
 1735 compare limits between dSph spatial models. Overhead sources see minimal improvement to the  
 1736 limits, while high zenith sources see an order of magnitude improvement for all DM masses. Softer  
 1737 SM annihilation channels see broad improvements to the limit compared to harder channels.

1738 **4.7 Systematics**

1739     Systematics to this analysis are identical to what was performed earlier in Glory Duck, Sec-  
1740     tion 3.7. We are also sensitive to the choice in spatial template, and this was explored in Section 3.7.2  
1741     and Section 3.8.2.

1742 **4.8 Conclusion and Discussion**

1743     In this multithreaded analysis, we have used observations of 3 dSphs from HAWC to perform  
1744     a collective DM annihilation search towards dSphs. The data were combined across sources  
1745     to significantly increase the sensitivity of the search. Advanced computational techniques were  
1746     deployed to accelerate wall-time spent analyzing by an order of magnitude. We have observed  
1747     no significant deviation from the null, no DM hypothesis, and so present our results in terms of  
1748     upper limits on the velocity-weighted cross-section,  $\langle\sigma v\rangle$ , for seventeen potential DM annihilation  
1749     channels across four decades of DM mass.

1750     This analysis serves as a proof of concept for multithreaded HAWC analyses with large parameter  
1751     spaces. Larger datasets with fast techniques will be essential to tackling the DM problem. The  
1752     models we used for this study include annihilation channels with neutrinos in the final state.  
1753     Advanced studies could aim to merge our results with those from neutrino observatories with large  
1754     data sets.

1755     A full HAWC analysis will include systematic studies of the  $J$ -factor distributions. Additionally,  
1756     because of the timing reduction, the study can be doubled in size to include DM decay. We have not  
1757     yet received the remaining spatial profiles to the  $\mathcal{LS}$  catalog, and limits can be quickly computed  
1758     once these are received. Finally, statistical studies with Poisson variation of HAWC's background  
1759     are essential to a comprehensive understanding of our observed excesses.

Segue1

Coma Berenices

Sextans

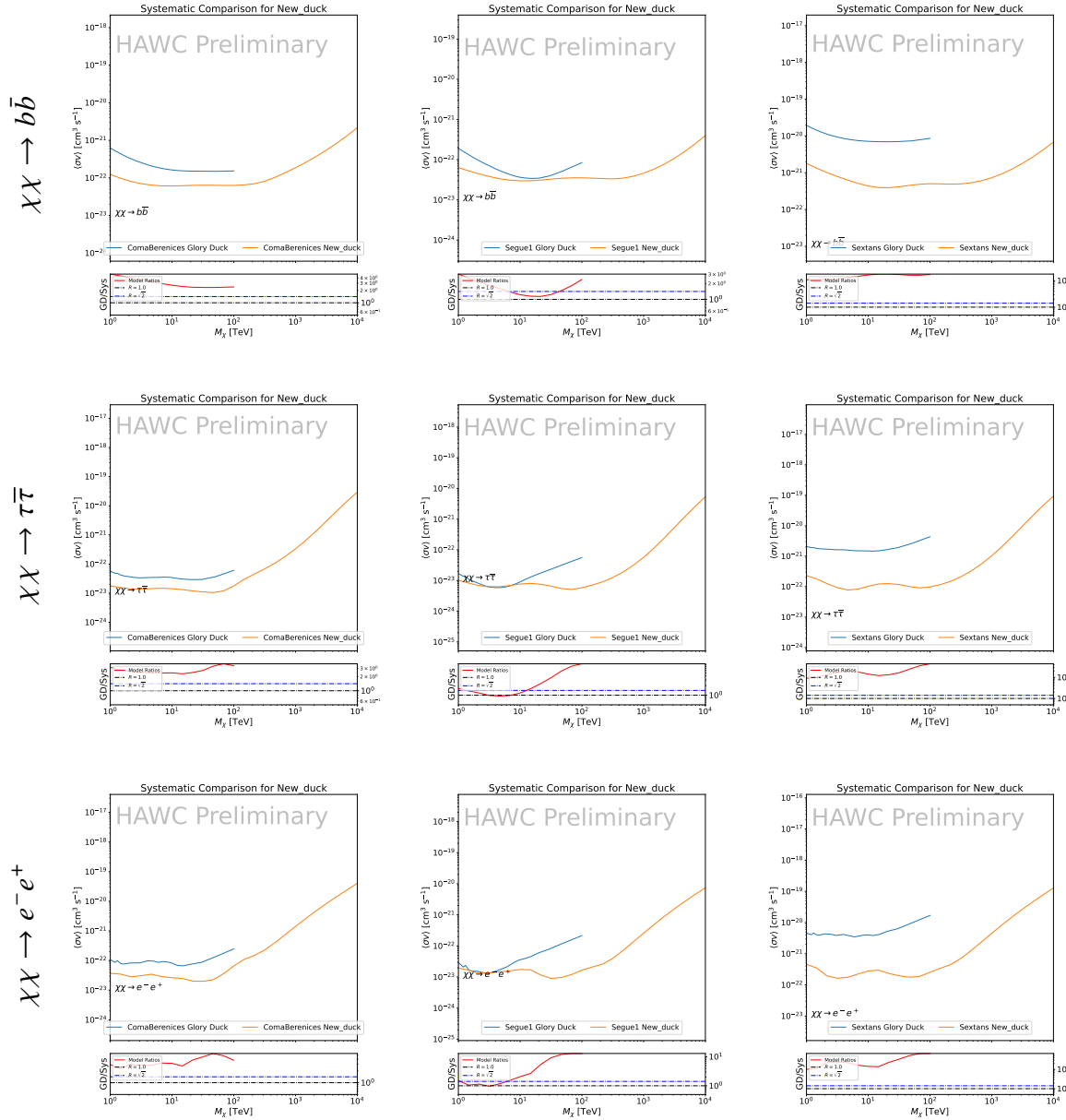


Figure 4.11 Comparison of HAWC limits from this analysis to Glory Duck (Fig. 3.5) for 3 dSphs and 3 DM annihilation channels:  $b\bar{b}$ ,  $\tau\bar{\tau}$ , and  $e\bar{e}$ . Each sector shows the 95% confidence limit from Glory Duck (blue line) and this analysis (orange line) in the top plot. The lower plot features the ratio in log scale of Glory Duck to this analysis in a red solid line. Horizontal dashed lines are for ratios of 1.0 (black) and  $\sqrt{2}$  (blue). Ratios larger than 1.0 are for limits smaller, or stricter, than Glory Duck. Ratios larger than  $\sqrt{2}$  indicates limits are stricter than a simple doubling of the Glory Duck data.

## CHAPTER 5

### ICECUBE NEUTRINO OBSERVATORY



Figure 5.1 IceCube Neutrino observatory and science center at the South Pole. Detector volume is beneath glacial ice. Image from [83].

1761 Located at the South Pole, the IceCube Neutrino Observatory is a pivotal instrument for  
1762 neutrino astronomy. IceCube's primary function is the detection and analysis of elusive, high-  
1763 energy neutrinos. These neutrinos carry information from the most energetic and distant cosmic  
1764 phenomena. The observatory uses thousands of digital optical modules embedded in a cubic  
1765 kilometer of Antarctic ice to detect Cherenkov radiation. This radiation occurs when neutrinos  
1766 interact with the ice, revealing their origin and energy.

1767 IceCube is a critical component in the multi-messenger astrophysics toolkit, especially in the  
1768 search for dark matter and beyond standard model (BSM) astrophysical processes. The observa-  
1769 tory's analysis of neutrino signals enhances our understanding of the universe by correlating these  
1770 signals with other cosmic messengers, including electromagnetic, gravitational waves, and cosmic



Figure 5.2 IceCube Laboratory (ICL) that houses the data acquisition systems. Picture from [83].

1771 rays.

1772 The following sections will discuss the observatory’s design, data acquisition, event recon-

1773 struction methodologies, and its significance in observing the Northern Sky. These details will

1774 underscore IceCube’s role in advancing our understanding of the cosmos through data-driven

1775 insights.

## 1776 **5.1 The Detector**

1777 The IceCube Neutrino Observatory is embedded within a cubic kilometer of Antarctic ice at

1778 the South Pole. IceCube’s modules are designed to detect neutrinos through Cherenkov radiation

1779 emitted during neutrino interactions with the ice. It comprises 5160 Digital Optical Modules

1780 (DOMs), arranged across 86 strings that span depths of 1450 m to 2450 m beneath the surface. This

1781 arrangement allows IceCube to capture high-energy neutrinos across a broad neutrino spectrum.

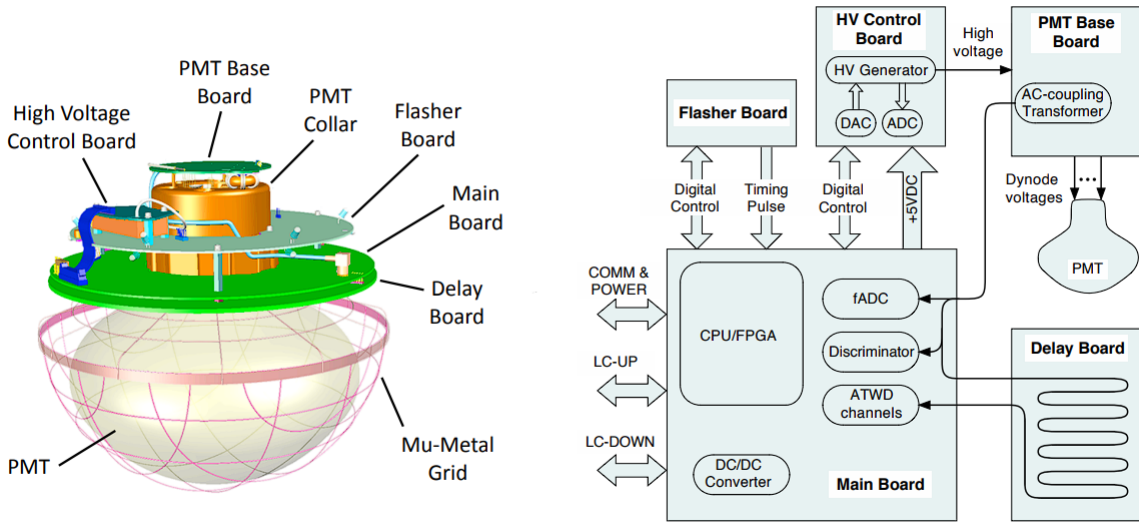


Figure 5.3 Composition of the Digital Optical Module (DOM). Left image is an illustration of the mechanical layout. Right is a flow chart of functional connections. Figure from [84]

### 1782 5.1.1 Hardware and Construction

1783     Digital Optical Modules (DOMs) are at the core of IceCube's detection technology, each encased  
 1784    in a glass sphere to withstand deep-ice pressures. A DOM features a 10-inch photomultiplier tube  
 1785    (PMT) for Cherenkov light detection, a high-voltage power supply for the PMT, and a Main  
 1786    Board for signal digitization and timestamping. An LED Flasher Board is included for calibration  
 1787    purposes, assisting in verifying DOM responses and measuring ice optical properties. The DOMs  
 1788    are deployed along cables on strings in a hexagonal grid pattern, which spans a cubic kilometer.  
 1789    Strings are placed with 125 meters of horizontal spacing, and DOMs are vertically separated  
 1790    by 17 meters on each string, chosen to optimize detection capability for neutrinos within the  
 1791    teraelectronvolt (TeV) to petaelectronvolt (PeV) energy range.

1792     DeepCore and IceTop, additional components of IceCube, extend its research capabilities.  
 1793    DeepCore, with its denser array of DOMs, targets lower energy neutrinos for studies such as  
 1794    neutrino oscillations and dark matter. IceTop, situated at the ice surface, measures cosmic rays,  
 1795    contributing data that complement the neutrino observations from below the ice.

1796     The central hub for IceCube's operations is the IceCube Laboratory (ICL), situated at the  
 1797    surface at the center of the array. This facility houses the servers and computers responsible for

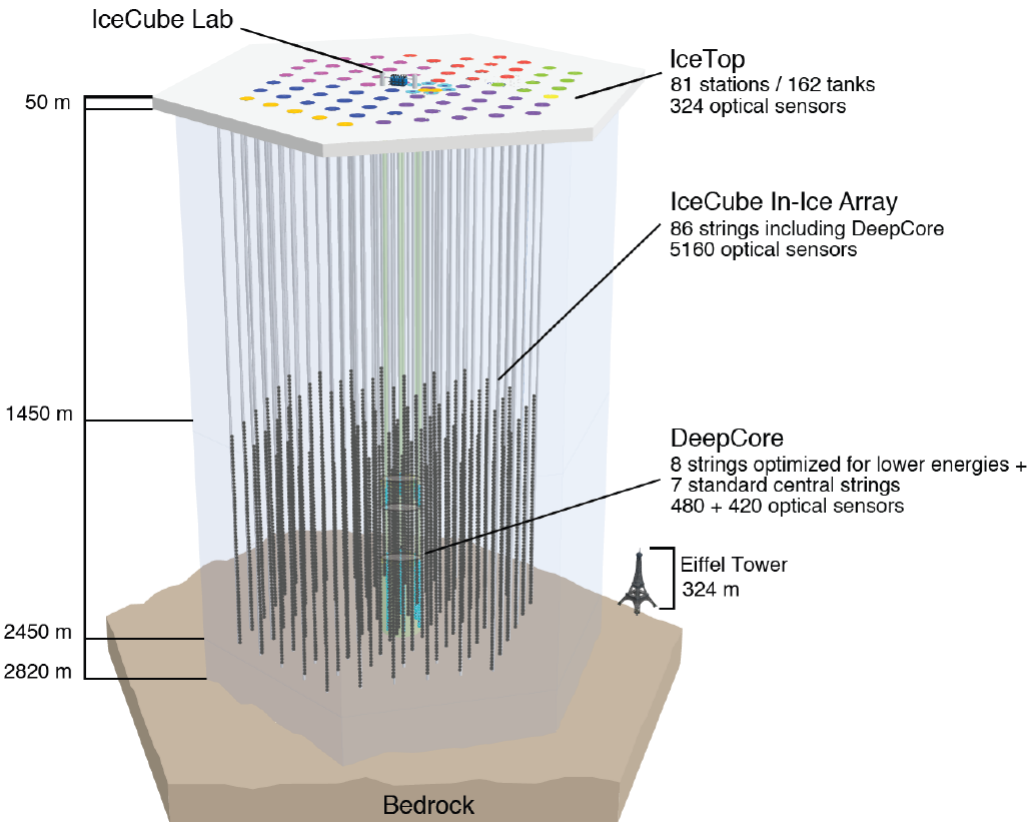


Figure 5.4 Graphic of the full IceCube Neutrino Observatory. In-ice array is made up of 86 strings with a total of 5160 optical sensors. Deepcore is a denser arrangement of optical sensors for sensitivity to lower energy neutrinos. Figure from [83].

1798 data acquisition and online filtering, connected to the DOMs via cables routed up from beneath the  
 1799 ice [84]. The ICL plays a crucial role in managing the data flow from the ice, ensuring continuous  
 1800 operation and data integrity. It is designed to maintain optimal conditions for its electronic  
 1801 equipment, including temperature control and protection against electromagnetic interference,  
 1802 which is vital for the accurate processing and analysis of the collected data [84].

### 1803 **5.1.2 Data Acquisition**

1804 The data acquisition process in the IceCube Neutrino Observatory starts when a photomultiplier  
 1805 tube (PMT) within a Digital Optical Module (DOM), distributed between 1450 m and 2450 m  
 1806 beneath the ice, detects light surpassing a threshold of 0.25 photoelectrons. The importance of the  
 1807 information transmitted to the surface computers depends on the detection of signals by neighboring

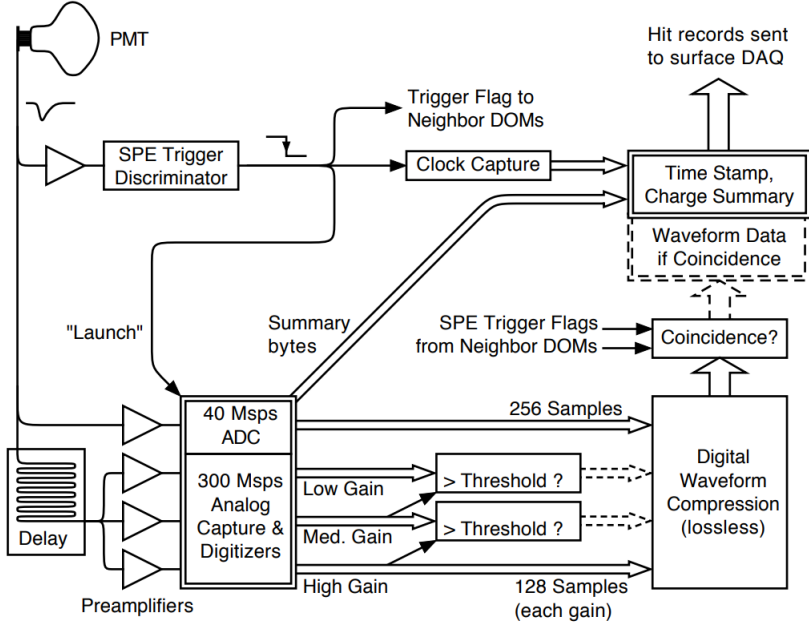


Figure 5.5 Data flow chart PMT waveforms from the DOMs. “Hit Records” are sent to the surface DAQ computers in ICL. Full waveform data, represented with dashed arrows, are included when neighboring DOMs are hit in coincidence above the SPE discriminator threshold.

1808 DOMs within a microsecond window. Isolated signals prompt a Soft Local Coincidence (SLC)  
 1809 response, transmitting only a timestamp and a charge summary. In contrast, signals detected by  
 1810 neighboring DOMs initiate a Hard Local Coincidence (HLC), resulting in the full waveform being  
 1811 compressed and sent along with the timestamp and charge summary to the IceCube Laboratory  
 1812 (ICL), located at the surface at the center of the array [84].

1813 Achieving uniform timing across DOMs is essential for accurate event reconstruction. Each  
 1814 DOM’s independent clock undergoes a rigorous calibration process to synchronize with the ICL’s  
 1815 clocks, with the times further translated to Universal Coordinated Time (UTC). This calibration is  
 1816 critical, involving continuous pulses sent between the DOMs and the ICL to adjust the waveforms  
 1817 by subtracting the common baseline and applying the gain. This step is vital for the precise  
 1818 interpretation of the collected data [84].

1819 Within the ICL, the Data Acquisition (DAQ) system employs various trigger algorithms to  
 1820 discern neutrino events from the vast majority of DOM hits caused by dark noise. One such  
 1821 mechanism, the Simple Multiplicity Trigger (SMT), requires a specific number of HLC hits within

1822 a brief timeframe to recognize a series of hits as an event. This approach is pivotal for identifying  
1823 sequences of detections likely resulting from neutrino interactions [84].

1824 Further refining the observatory's data, the Processing and Filtering (PnF) system, also housed  
1825 within the ICL, applies around 25 different filters after initial event detection. Each filter is  
1826 designed for specific physics analyses, significantly managing the observatory's data throughput  
1827 by focusing on scientifically valuable information. The system employs filters like the Muon Track  
1828 Filter to isolate high-quality track events crucial for neutrino source identification, the Shower  
1829 Event Filter to select events with large energy deposits indicative of neutrino interactions, and the  
1830 High-Charge Filter to highlight events with extensive photoelectron deposits, pointing to high-  
1831 energy astrophysical neutrinos. These filters ensure that the data prepared for further analysis and  
1832 transmission to researchers in the Northern Hemisphere contains the most significant scientific  
1833 insights [84].

1834 The operational control of the observatory, maintained by the LiveControl system within the  
1835 ICL, oversees the DAQ and PnF systems. It handles the initiation and conclusion of data-taking  
1836 runs and maintains a database of operational parameters. Alerting operators to any deviations  
1837 from expected conditions, this system is crucial for ensuring the observatory operates within its  
1838 optimal parameters, highlighting the integrated effort required to manage and analyze the vast data  
1839 generated by the IceCube Neutrino Observatory [84].

1840 **5.2 Event Reconstruction**

1841 Event Reconstruction within the IceCube Neutrino Observatory transforms signals captured by  
1842 Digital Optical Modules into quantifiable scientific insights. The goal of event reconstruction is  
1843 to ascertain the origin, trajectory, and strength of interacting neutrinos. This process is pivotal for  
1844 interpreting signals as either originating from celestial neutrino sources or other phenomena. I will  
1845 focus mostly one how IceCube reconstructs track-like events as these are the most relevant for this  
1846 dissertation.

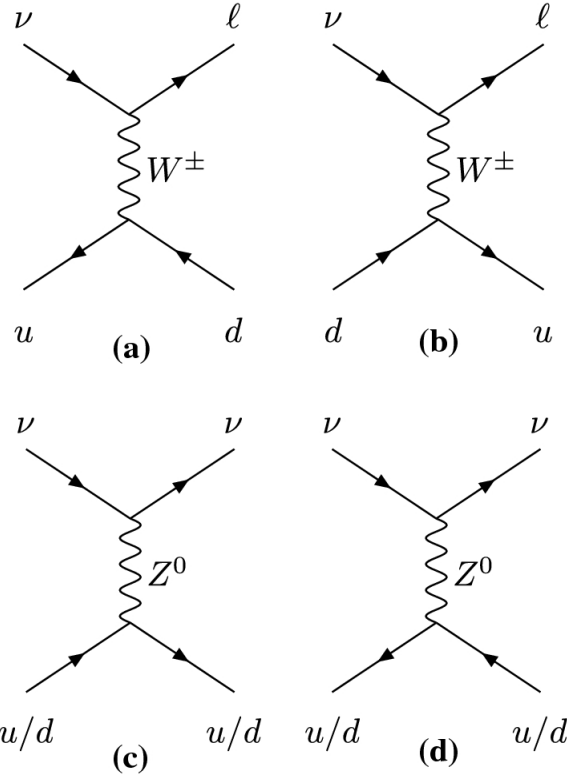


Figure 5.6 Feynman diagrams for W (a/b) and Z (c/d) boson mediated interactions between neutrinos and light quarks. Charged current (CC) interactions are shown in panels a and b. Neutral current (NC) interactions are shown in panels c and d. NC interactions occur between neutrinos and quarks withing atomic nucluei in the ice. CC interactions will exchange W bosons and produce a lepton corresponding to the neutrino flavor and a hadronic cascade. NC interactions will exchange a Z boson produce a hadronic cascades. Figure from [85].

### 1847 5.2.1 Tracks and Cascades

1848 Events in IceCube’s detector volume manifest primarily as either tracks or cascades. The  
 1849 primary cause of the event topology are both the neutrino flavor and the nature of the primary  
 1850 neutrino’s interaction with the ice.

1851 Tracks emerge from charged-current (CC) interactions involving muon neutrinos ( $\nu_\mu$ ). These  
 1852 events are characterized by the production of a high-energy muon ( $\mu$ ). These muons, due to its  
 1853 relatively large mass compared to electrons, can traverse substantial distances through the ice,  
 1854 exceeding kilometers. These long trajectories are obvious from continuous, distinct, and elongated  
 1855 track of Cherenkov light in the ice. See Fig. 5.8 for a simulated track event. The angular deviation  
 1856 between the incoming  $\nu_\mu$  and the secondary muon is notably slight, tapering to near  $0.3^\circ$  above  
 1857 TeV energies. Therefore, muon tracks closely approximate the primary neutrino’s path [85, 88].

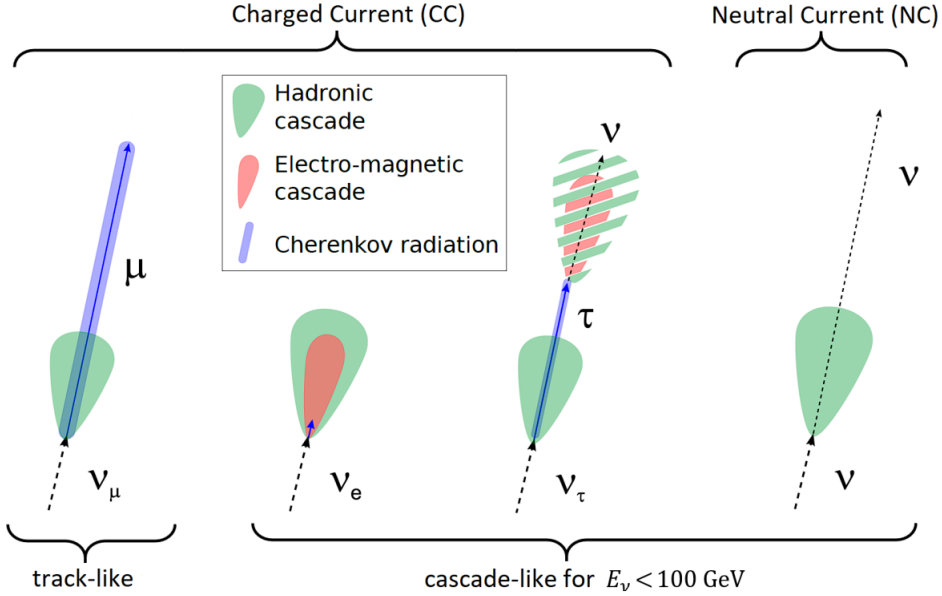


Figure 5.7 Event topologies for high energy NC and CC neutrino interactions with ice. Signatures can be split as either: hadronic and electromagnetic cascades; Cherenkov radiation from a single long ranging particle. Cascade from the  $\tau$  decay will depend on its decay products. For energies below 1 PeV the double bang of the  $\nu_\tau$  signature overlap and are indistinguishable. Figure from [86].

1858 Such precision affords angular resolutions finer than  $1^\circ$  for TeV neutrinos which facilitates the  
 1859 determination of their cosmic origins [85].

1860 Cascades are products of both neutral-current (NC) interactions across all neutrino flavors and  
 1861 CC interactions involving electron or tau neutrinos,  $\nu_e$  and  $\nu_\tau$  respectively. Unlike tracks, cascades  
 1862 result in a more localized burst of Cherenkov radiation. The burst imprints as a nearly spherical  
 1863 light pattern from the rapid dissipation of energy by the produced particles. This diffusion creates  
 1864 a distinct event signature with good energy estimation, but worse directional clarity compared to  
 1865 track events. The isotropic nature of cascades leads to larger angular uncertainties, typically around  
 1866  $15^\circ$ . Yet, cascades excel in providing energy measurements, with resolutions reaching as tight as  
 1867 15% from the contained nature of the energy deposition [85, 88].

1868 A rarely observed event type, the double-bang event, posited for  $\nu_\tau$  interacting via CC at energies  
 1869 above 1 PeV, would display as two distinct cascades within the detector. These events start from an  
 1870 initial interaction and subsequent decay of the  $\tau$  lepton over a discernible distance. The double bang  
 1871 offers a unique marker for high-energy  $\nu_\tau$  detection [85]. Preliminary whispers of double-bang

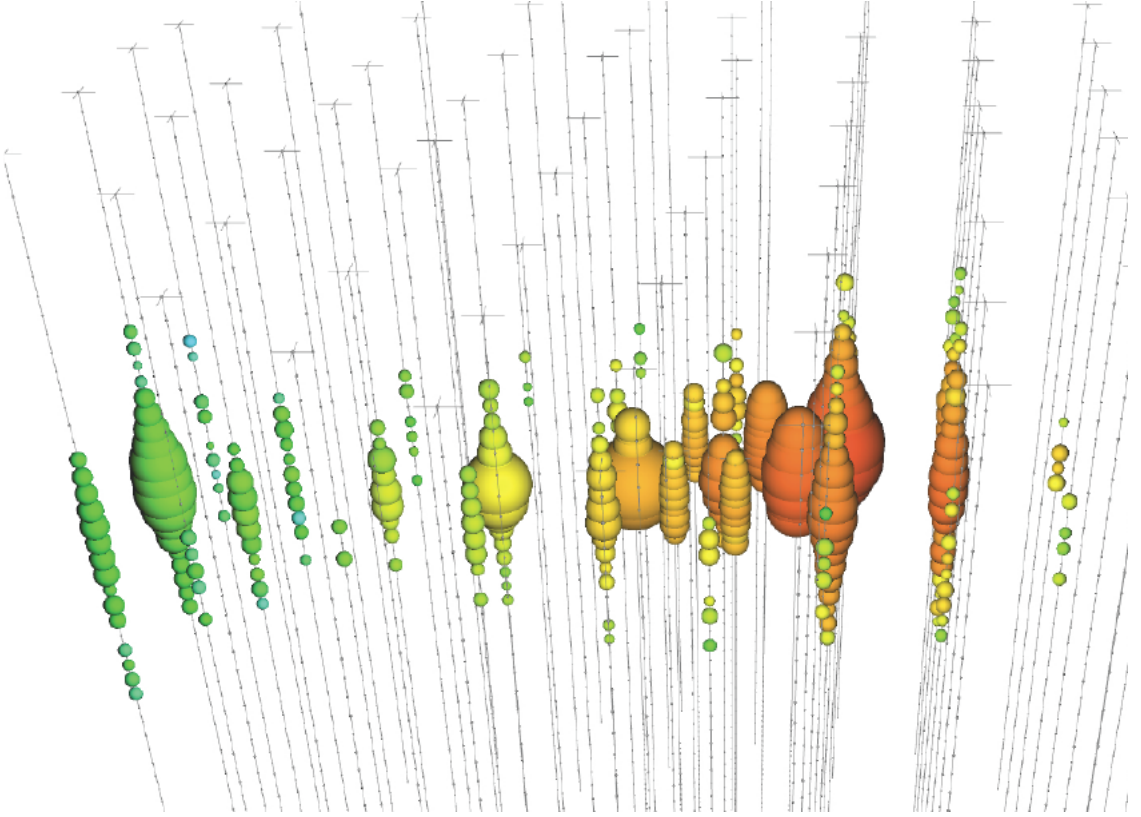


Figure 5.8 A simulation of a track-like event in IceCube. Redder bubbles indicate earlier photon arrival times. Greener bubbles occur later. The size of the DOM bubble illustrate the charge deposition in the DOM. For this event, the CC neutrino interaction occurred by the red hits. There is then a long muon track going to the left. Figure taken from [87].

1872 events IceCube have been observed [89]. Yet, efforts are ongoing to isolate such an event.

### 1873 5.2.2 Reconstruction of Track Direction

1874 Angular reconstruction for  $\nu_\mu$  induced tracks in the IceCube detector volume starts with the  
 1875 LineFit algorithm [90]. LineFit estimates the muon's trajectory through a least squares fit to the  
 1876 Cherenkov light hits on the DOMs. LineFit assumes the muon propagates with constant velocity  
 1877 and treats its path as linear in order to simplify the emission patterns of Cherenkov radiation. To  
 1878 improve this approximation, the Huber penalty function [91] is applied which distinguishes between  
 1879 signal and noise by considering the spatial distribution of hits relative to the track [92].

1880 The reconstruction process is refined further by the Single Photoelectron (SPE) likelihood  
 1881 method, which calculates the probability of photon arrival times at the DOMs [91]. It does so by

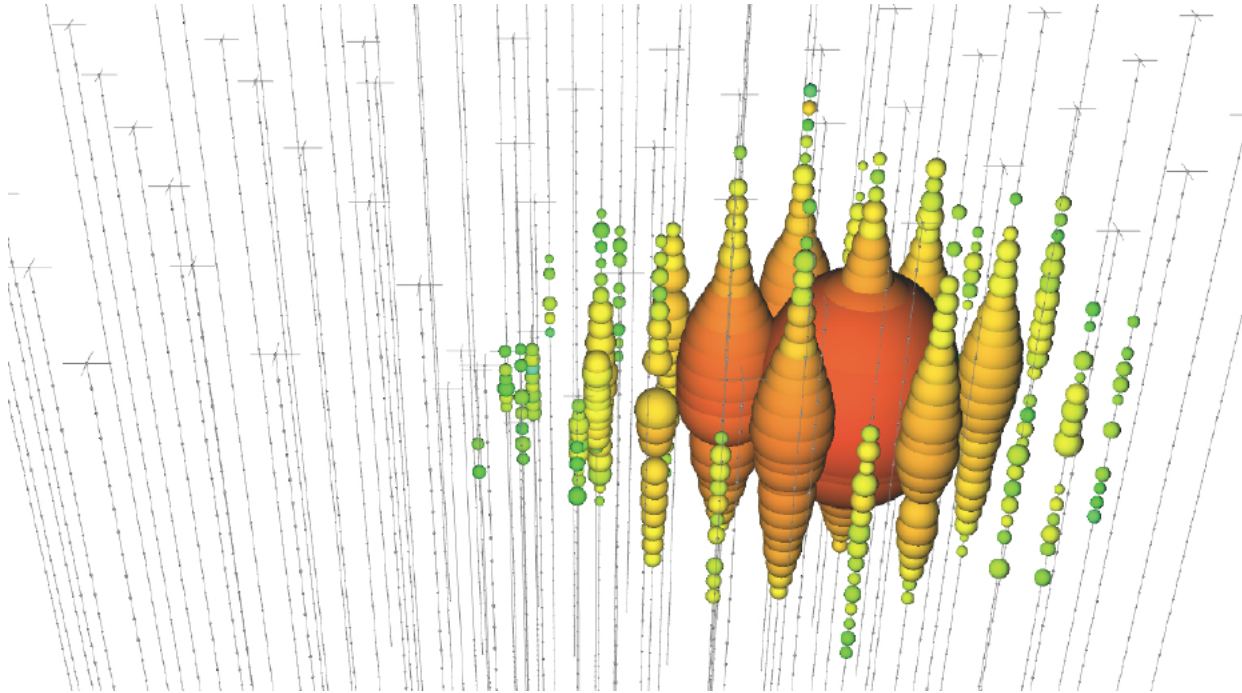


Figure 5.9 Same as Fig. 5.8 but for a cascade-like event. Figure taken from [87].

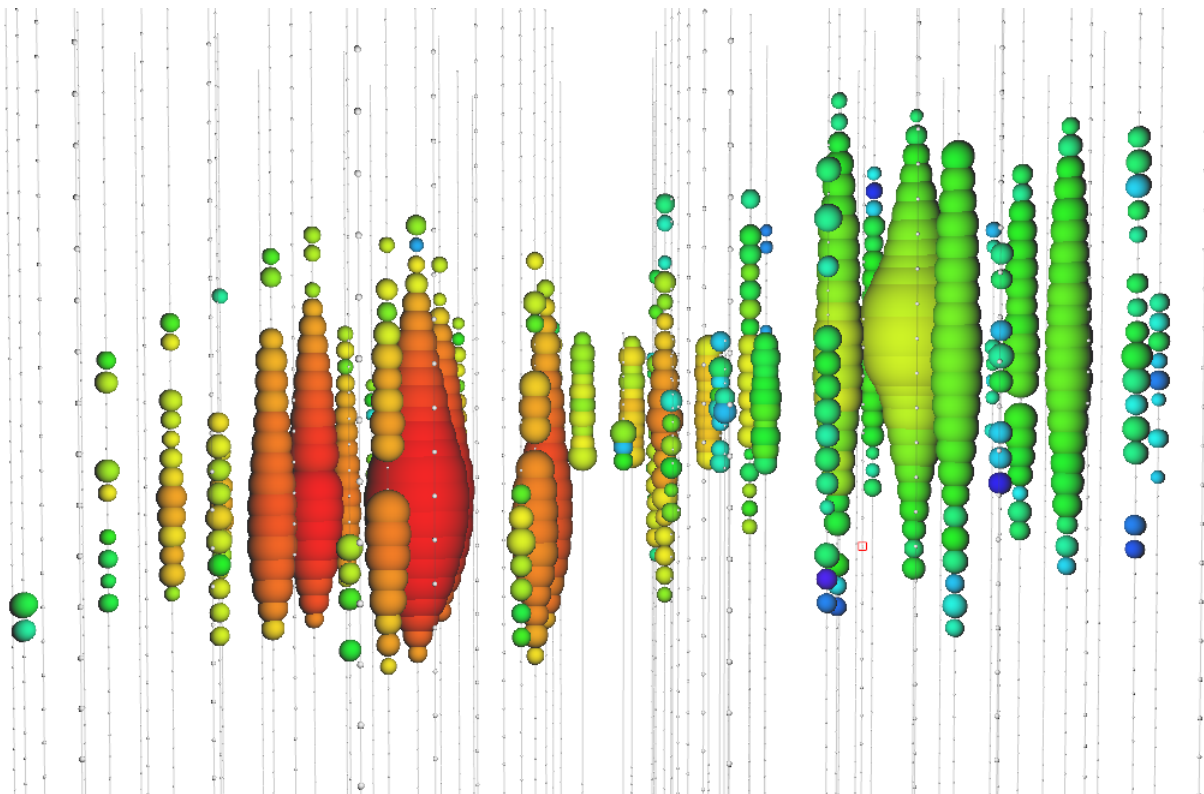


Figure 5.10 Same as Fig. 5.8 but for a double-bang event. Two distinct cascades are visible if the initial neutrino is very high energy. Figure taken from [87].

1882 taking into account the earliest detected photons as they are least likely to have been scattered:

$$L(\Theta) = \prod_{j=1}^{N_{\text{DOM}}} \prod_{i=1}^{N_{\text{hit}}} p_j(t_i)^{q_i} \quad (5.1)$$

1883 where  $N_{\text{DOM}}$  is the number of Digital Optical Modules involved in the event.  $N_{\text{hit}}$  is the number of  
1884 hits registered [90]. The charge detected by each DOM,  $q_i$ , factors into the probability calculation,  
1885 assuming that earlier photons provide more reliable directional information.

1886 An alternative to SPE, the Multi-Photoelectron (MPE) likelihood method accounts for all  
1887 detected photons. MPE uses the total observed charge to weight the significance of each hit:

$$L(\Theta) = \prod_{j=1}^{N_{\text{DOM}}} \left[ p_j(t_1)^{q_1} \cdot (1 - P_j(t_1))^{Q_j - q_1} \right], \quad (5.2)$$

1888 where  $Q_j$  is the sum of charges observed by the j-th DOM, providing a more detailed picture of the  
1889 muon's path [90].

1890 SplineMPE, is the final step and employs a spline-based parameterization of the photon arrival  
1891 times. These spline fits encode a detailed understanding of the ice's optical properties derived from  
1892 calibration data [90]. This approach yields the following likelihood function for improved angular  
1893 resolution:

$$L(\vec{r}_0, t_0, \theta, \phi) = \prod_k L_{\text{DOM}_k}(\vec{r}_0, t_0, \theta, \phi), \quad (5.3)$$

1894 where the parameters  $\vec{r}_0$ ,  $t_0$ ,  $\theta$ , and  $\phi$  describe the reconstructed track within IceCube's voluminous  
1895 array [90].

1896 From the light weight LineFit to the complex SplineMPE, each step incorporates more detailed  
1897 physics to enhance the reconstruction's accuracy. Each hones in on the muon track and revealing  
1898 the muon's origin from cosmic distances. This nuanced tracking is crucial for IceCube's mission  
1899 to map the universe through the lens of high-energy neutrino interactions.

### 1900 5.2.3 Energy

1901 After pinpointing the muon track's direction, IceCube employs the MuEX algorithm to estimate  
1902 the energy deposited by the muon inside the detector. The MuEX algorithm uses a Poisson  
1903 likelihood model, comparing the observed photoelectrons  $k$  to the expected light output,  $\Lambda$ , which

1904 is directly related to the deposited energy  $E$ :

$$\ln \mathcal{L} = k \ln(\Lambda E + \rho) - (\Lambda E + \rho) - \ln(k!) \quad (5.4)$$

1905 where  $\rho$  is the number of expected noise photons, and  $\Lambda$  reflects the light yield per unit energy,  
1906 taking into account the optical properties of the ice and the detector response. The logarithm of the  
1907 likelihood is minimized with respect to the energy, resulting in the best-fit estimate [88].

1908 For a more detailed energy reconstruction, the Millipede algorithm unfolds the muon's energy  
1909 loss along its path by adapting the Poisson likelihood. This approach accounts for the stochas-  
1910 tic energy losses due to Bremsstrahlung and pair production, treating the muon as a series of  
1911 electromagnetic cascades:

$$\vec{k} - \vec{\rho} = \Lambda \cdot \vec{E} \quad (5.5)$$

$$\mathcal{L} = \prod_j \int_0^\infty d\lambda_j G(\lambda_i, \lambda_j) \frac{\lambda_j^{k_i} e^{-\lambda_i}}{k_i!}, \quad (5.6)$$

1913 where  $k$  denotes the observed photons,  $\rho$  the noise,  $E$  the energy losses, and  $\Lambda$  the matrix of  
1914 predicted light yields throughout the detector. By fitting the muon's position, direction, and the  
1915 vector of energy losses, Millipede achieves a resolution on total deposited energy along the muon  
1916 track of approximately 10-15% [88].

1917 IceCube's energy reconstruction techniques, from the direct approach of MuEX to the com-  
1918 prehensive unfolding by Millipede, illustrate the observatory's robust analytical framework for  
1919 interpreting the intricate signals of neutrino interactions [88].

## 1920 5.3 Background

1921 In IceCube, the primary challenge in detecting astrophysical neutrinos is the background noise  
1922 from atmospheric neutrinos. These are produced from cosmic rays hitting the Earth's atmosphere,  
1923 leading to a cascade that includes both neutrinos and muons (see Fig. 2.2). These particles  
1924 sometimes generate detector signals similar to those from astrophysical sources.

1925 IceCube employs selective criteria to reduce this background. For instance, downward-moving  
1926 tracks are scrutinized more heavily, as these are more likely to be related to atmospheric events.

1927 Upward-moving neutrinos, however, are less likely to be confused with this background because  
1928 the Earth filters out most other particles, including muons.

1929 The detector uses the Earth itself as a filter to increase the purity of potential astrophysical  
1930 neutrino signals. This differentiation between upgoing and downgoing events helps IceCube focus  
1931 on the neutrinos that are of most interest for astronomical observations.

## CHAPTER 6

### HEAVY DARK MATTER ANNIHILATION SEARCH WITH ICECUBE'S NORTH SKY TRACK DATA

#### 6.1 Introduction

Neutrinos are another astrophysical messenger than can travel long distances without significant attenuation or deflection. Additionally, Neutrinos come in three flavors which triples the multiplicity of the particles we are searching for. Uniquely, they interact less readily than photons especially above PeV energies. Neutrinos therefore provide another window through which we can perform dark matter searches.

The previous IceCube DM annihilation analysis towards dwarf galaxies was performed in 2013 [93] which, in technical terms, is more than a minute ago. This is in spite of IceCube's crucial sensitivity afforded from neutrino spectral lines [94]. A lot has changed in IceCube since its previous DM annihilation search such as, additional strings, more sophisticated analysis methods, and more accurate theory modeling. It has come time for IceCube to make a DM dSph contribution.

IceCube is sensitive to annihilating DM for DM masses above 1 TeV. Additionally, IceCube's sensitivity is comparable gamma-ray observatories in spectral models that produce hard neutrino features. The goal of this analysis is to perform a DM annihilation search using the Northern Sky Tracks datasets. The search will only be towards dwarf spheroidal galaxies (dSph) for the strengths mentioned in Section 3.3.3. These sources are treated as point sources for IceCube with little loss to sensitivity or model dependence on how the DM is distributed. DM masses from 500 GeV to 100 PeV are considered for this analysis. Several DM annihilation channels available from the HDMspectra [79] are studied in this analysis. This chapter presents the analysis work for IceCube to update our DM searches toward dSphs.

#### 6.2 Dataset and Background

This section enumerates the data and background methods used for IceCube's study of dSphs. Section 6.2.1 and Section 6.2.2 are most useful for fellow IceCube collaborators looking to replicate this analysis.

1958 **6.2.1 Itemized IceCube files**

1959 These files are only available within IceCube’s internal documentation and wikis. They are not  
1960 meant for public access, and are presented here so that IceCube collaborators can reproduce results  
1961 accurately.

1962 • Software Environment: CVMFS Py3-v4.1.1

1963 • Data Sample: Northern Tracks NY86v5p1

1964 • Analysis Software: csky ([nu\\_dark\\_matter](#))

1965 • Analysis wiki: [https://wiki.icecube.wisc.edu/index.php/Dark\\_Matter\\_Annihilation\\_Search\\_towards\\_dwarf\\_spheroidals\\_with\\_NST\\_and\\_DNN\\_Cascades](https://wiki.icecube.wisc.edu/index.php/Dark_Matter_Annihilation_Search_towards_dwarf_spheroidals_with_NST_and_DNN_Cascades)

1967 • Project repository

1968 **6.2.2 Software Tools and Development**

1969 This analysis was performed inside IceCube’s CVMFS (3.4.1.1) software environment using  
1970 csky for likelihood calculations. Csky at first did not come with dark matter spectral models nor  
1971 could accommodate custom flux models. We developed these capacities for single source and  
1972 stacked source studies for this analysis. The analysis code is held in a separate repository from  
1973 csky. The [nu\\_dark\\_matter branch of csky](#) manages the input of custom dark matter spectra and  
1974 accompanied DM astrophysical source. Csky also enables the use of multithreading which was  
1975 shown to be crucial for DM searches (see Sec. 4). Csky then calculates likelihoods with a selected  
1976 data sample. The [IceCube Dark Matter dSph repository](#) manages the generation of spectral models  
1977 for neutrinos, physics parameter extraction from  $n_{\text{sig}}$ ,  $J$ -factor per source inputs, and bookkeeping  
1978 for the large parameter space. The project repository required a secondary software environment  
1979 for neutrino oscillations. How to launch and run those calculations are documented in the project  
1980 repository and the Docker image is additionally saved in Section C.1.

1981 **6.2.3 Data Set and Background Description**

1982 For this analysis, I use the Northern Sky Tracks (NST) Sample (Version V005-P01). The sample  
1983 contains up-going track-like events, usually from  $\nu_\mu$  and  $\nu_\tau$ , with a superior angular resolution  
1984 compared to the cascade dataset. This sample covers 10.4 years of data (IC86\_2011-2021). The  
1985 accepted neutrino energy range used for the analysis is unique from most other IceCube searches  
1986 because DM spectra are hard with large contributions close to  $E_\nu = m_\chi$ . Therefore, the sampled  
1987 energy range is  $1 < \log(E_\nu/\text{GeV}) < 9.51$  with step size 0.125.

1988 The strengths of a dwarf analysis is that there are no additional background considerations  
1989 beyond nominal, baseline background estimations (see Section 3.2.3). For NST, the nominal  
1990 contributions come from atmospheric neutrinos and isotropic astrophysical neutrinos. We estimate  
1991 the background by scrambling NST data along Right Ascension.

1992 **6.3 Analysis**

1993 The expected differential neutrino flux from DM-DM annihilation to standard model particles,  
1994  $d\Phi_\nu/dE_\nu$ , over solid angle,  $\Omega$  is described by the familiar equation.

$$\frac{d\Phi_\nu}{dE_\nu} = \frac{\langle\sigma\nu\rangle}{8\pi m_\chi^2} \frac{dN_\nu}{dE_\nu} \times \int_{\text{source}} d\Omega \int_{l.o.s} \rho_\chi^2 dl(r, \theta') \quad (6.1)$$

1995 This is identical to Eq. (3.1) except that there are 3 neutrino flavors, so there are a corresponding  
1996 3 flux equations. Section 3.3 has a complete description of each term in Eq. (6.1). Additionally,  
1997 neutrinos oscillate between flavors which needs to be considered for the expected neutrino flux  
1998 at Earth. Section 6.3.1 presents the particle physics model and processing for DM annihilation.  
1999 Section 6.3.2 presents the spatial distributions built for each dSph.

2000 **6.3.1  $\frac{dN_\nu}{dE_\nu}$  - Particle Physics Component**

2001 Neutrino spectra from heavy DM annihilation were generated using HDMspectra [79] and  
2002  $\chi$ arov [95]. HDMspectra has tables for the decay and annihilation of heavy DM for different  
2003 dark DM and SM primary annihilation channels. The simulation includes electroweak or gluon  
2004 radiative corrections and higher order loop corrections from the  $W$  and  $Z$  bosons ( $WWZ$  and  $WW\gamma$ ).  
2005 These corrections are especially important for accurately estimating the prompt neutrino flux. This

2006 publication also pushes the simulated DM mass to the Plank scale (1 EeV), however this study will  
2007 not explore that high.

2008 An important feature in the spectra is that neutrino line channels will be accompanied by a low  
2009 energy tail [79], see Fig. 6.1. Thus, the Earth will not fully attenuate a heavy neutrino line-like  
2010 signal from high declination sources where the neutrino flux must first traverse through the Earth.  
2011 The DM annihilation channels that feature lines include all leptonic channels:  $\nu_{e,\mu,\tau}$ ,  $e$ ,  $\mu$ , and  $\tau$ . We  
2012 use the `xarov` software to propagate and oscillate the neutrinos from the source to Earth. Because  
2013 these sources are quite large in absolute terms, and also far (order 10 kpc or more), the resulting  
2014 flavor spectra are the averages of the transition probabilities [95]:

$$P(\nu_\alpha \rightarrow \nu_\beta) \approx \begin{bmatrix} 0.55 & 0.18 & 0.27 \\ 0.18 & 0.44 & 0.38 \\ 0.27 & 0.38 & 0.35 \end{bmatrix} \quad (6.2)$$

2015 Examples of the spectra before and after propagation are shown in Fig. 6.1.

2016 When calculating the expected contribution to  $n_s$ , only  $\nu_\mu$  and  $\nu_\tau$  are considered as NST's  
2017 effective area to  $\nu_e$  is negligible [96]. Therefore, the expected composite neutrino spectrum is the  
2018 sum of the two flavors:  $\frac{dN\nu_\mu}{dE\nu_\mu} + \frac{dN\nu_\tau}{dE\nu_\tau}$ . The spectral tables are then converted to splines to condense  
2019 information, enable random sampling of the spectra, and reduce computing times. The spectral  
2020 splines are finally implemented as a DM class in csky.

### 2021 6.3.1.1 Treatment of Neutrino Line Features

2022 All DM annihilation channels into leptons  $\chi\chi \rightarrow [\nu_{e,\mu,\tau}, e, \mu, \tau]$  develop a prominent and  
2023 narrow spectral line feature. For all neutrino flavors, this line is visible and prominent in all  $m_\chi$   
2024 studied in this analysis. For charged leptons, the feature typically manifests at  $m_{ch} > 10$  TeV, yet  
2025 its prominence varies slightly between the flavors. Examples for lines in the annihilation spectra  
2026 with neutrinos or charged leptons are provided in Fig. 6.1.

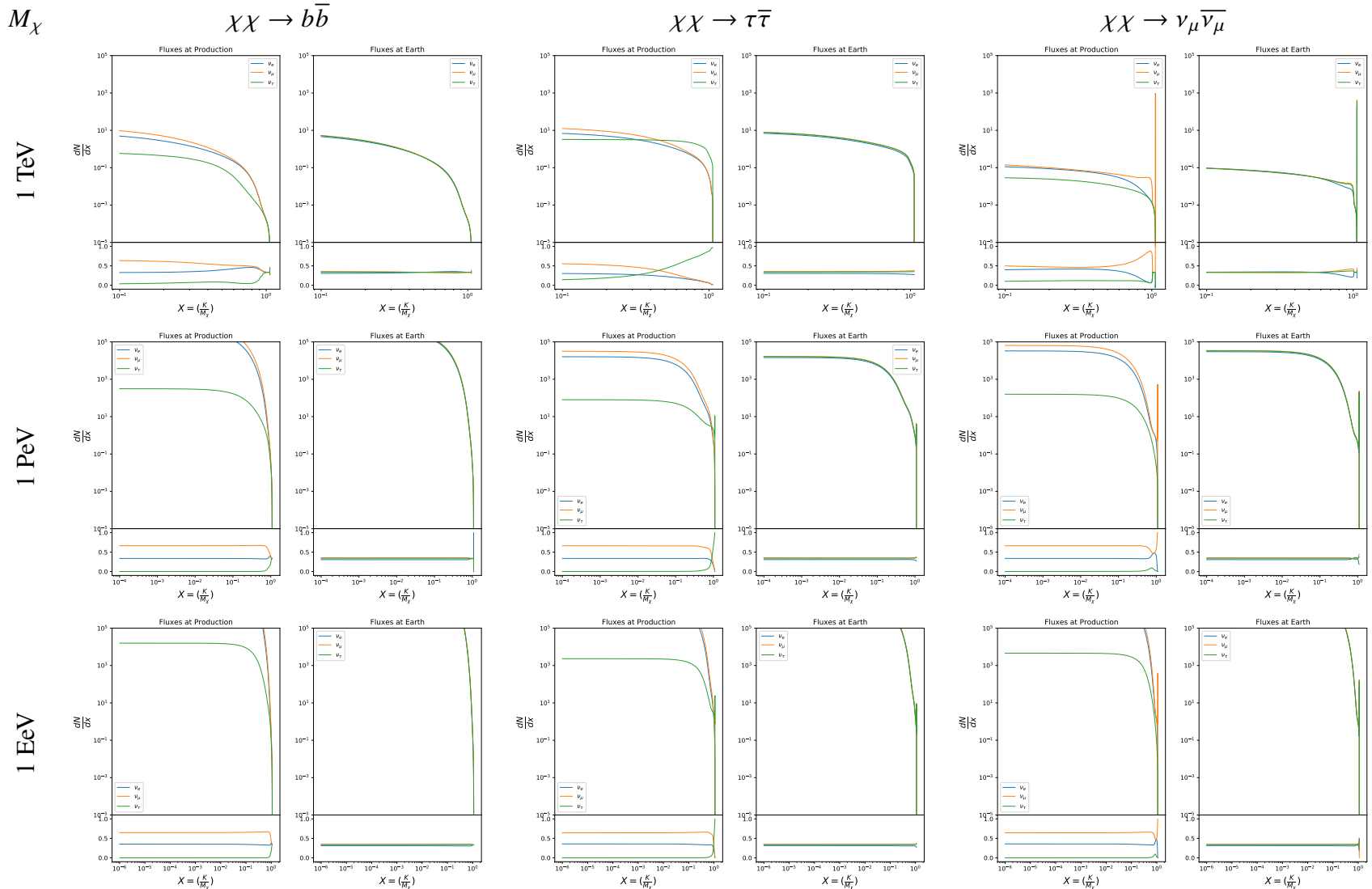


Figure 6.1 Neutrino spectra at production (left panels) and after oscillation at Earth (right panels). Blue, orange, and green lines are the  $\nu_e$ ,  $\nu_\mu$ , and  $\nu_\tau$  spectra respectively. Top panels show the spectra in  $\frac{dN}{dE}$ . Lower panels plot the flavor ratio to  $\nu_e + \nu_\mu + \nu_\tau$ . SM annihilation channels  $b\bar{b}$ ,  $\tau\bar{\tau}$ , and  $\nu_\mu\bar{\nu}_\mu$  are shown for  $M_\chi = 1 \text{ PeV}$ ,  $\text{TeV}$ , and  $\text{EeV}$ .

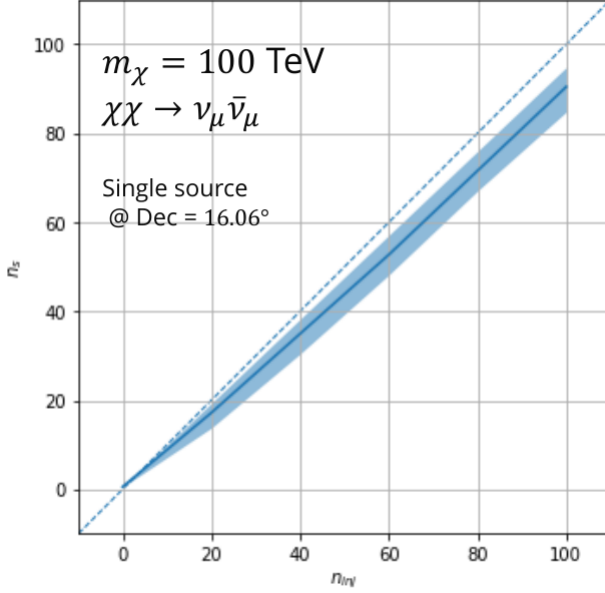


Figure 6.2 Signal recovery for 100 TeV DM annihilation into  $\nu_\mu \bar{\nu}_\mu$  for a source at Dec = 16.06°.  $n_{\text{inj}}$  is the number of injected signal events in simulation.  $n_s$  is the number of reconstructed signal events from the simulation data. Although the uncertainties are small and tight, the reconstructed  $n_s$  are systematically underestimated.

2027     The neutrino line feature is so narrow relative the sampled energy range that the random  
 2028   sampling of the spectra and likelihood fitting rarely capture the line in computation. As a result,  
 2029   often the best fit to simulation of background will always floor to TS = 0 and the signal recovery  
 2030   systematically underestimates the signal (see Fig. 6.2).

2031     To remedy this, we take a similar approach to the IceCube’s decay analysis [97] and the previous  
 2032   gamma-ray study in Section 4.3.1. Two smoothing kernels were tested (Gaussian and uniform)  
 2033   to widen the line feature. The widths were tuned such that the signal recovery approached unity  
 2034   for DM mass 100 TeV to 1 PeV for a source at Segue 1’s declination, 16.06°. Near horizon  
 2035   was chosen in order to isolate loss in signal recovery away from Earth’s attenuation of very high  
 2036   energy neutrinos and atmospheric backgrounds. The kernel convolution needed closely preserve  
 2037   the integrated counts of neutrinos. The optimized kernel parameters for all lines are summarized  
 2038   as:

- 2039     • Gaussian kernel with  $1\sigma$  width =  $1.75\text{E-}3 \cdot m_\chi$
- 2040     • Minimum energy included in convolution =  $\text{MIN}[0.995 \cdot m_\chi, E(\nu_{\text{line}}) - 4\sigma]$

- 2041 • Maximum energy included in convolution =  $\text{MAX}[1.005 \cdot m_\chi, E(\nu_{\text{line}}) + 4\sigma]$

2042 where  $E(\nu_{\text{line}})$  is the neutrino energy where the neutrino line is at the maximum.

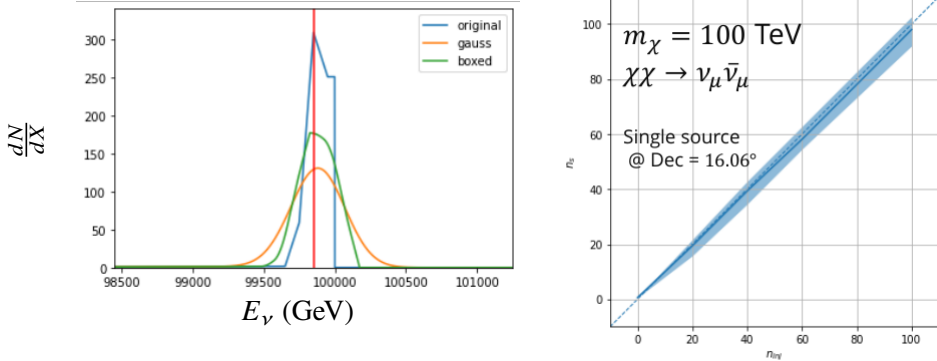


Figure 6.3 Left panel shows the two kernels overlaying the original spectrum from  $\chi\text{aron}\nu$  after propagation to Earth [95]. The vertical red line indicates where the original neutrino line is maximized. Blue line is the output from  $\chi\text{aron}\nu$ . Green line is the spectrum after convolution with a flat kernel. Orange line is the spectrum after Gaussian convolution. Right panel shows the signal recovery of the spectral model using the Gaussian kernel with parameters enumerated above.

2043 These parameters broadly improved the signal recovery of the line spectra. An example is in  
2044 Fig. 6.3. Analysis level signal recovery studies are expanded upon in Section 6.6.

### 2045 6.3.1.2 Spline Fitting

2046 In an effort to reduce computational work, memory burden, and align with point source methods  
2047 used for NGC1068 [98], spectral splines were created and adopted for estimating the neutrino flux  
2048 for the different spectral models. Software was written to generate, book keep, and calculate values  
2049 on the splines.

2050 When using splines, one has to be careful of the goodness to fit. The spline software used here,  
2051 Photospline [99], uses the penalized spline technique [100]. Through the penalized technique,  
2052 poor fits are penalized according to the accuracy of the nominal value, and the smoothness of the  
2053 first and second derivatives. However, this construction does not penalize on the integral of the  
2054 fit distribution which is critical in low signal studies, such as DM searches. There are additional  
2055 caveats when testing the goodness to fit to the MC generated above for all DM annihilation channels.

- 2056 • The splines must be Log10(\*) in Energy and dN/dX to account for the exponential nature of  
 2057 the flux.
- 2058 • The fidelity of the fit matters more at  $E_\nu \approx m_\chi$  where the model uncertainties are minimal  
 2059 and physical considerations (like the cut-off) are most important.
- 2060 • The fidelity of the fit matters less at low  $E_\nu$  as the model uncertainties are large AND  
 2061 IceCube's sensitivity diminishes significantly below 500 GeV.
- 2062 • Total integrated counts should be well-preserved.

2063 The resulting cost function was built to evaluate the goodness of spline fits to account for the above  
 2064 considerations.

$$e_i = x_i \cdot \left( \frac{dN_i}{dX_i} - 10^{\hat{e}_i} \right) \quad (6.3)$$

2065 Where  $\hat{e}_i$  is the spline estimator's value for  $x_i$ .  $x_i = E_{\nu_i}/m_\chi$ .  $\frac{dN_i}{dX_i}$  is the flux value from MC. I then  
 2066 take the RMS of the error distribution and the resulting value, err, is used to evaluate the fidelity of  
 2067 the spectral spline.

$$\text{err} = \sqrt{\frac{1}{x_{\max} - x_{\min}} \int_{x_{\min}}^{x_{\max}} e^2 dx} \quad (6.4)$$

2068  $x_{\min}$  and  $x_{\max}$  are the scope of the error evaluation and are provided in Tab. 6.1.

2069 Each SM channel had unique tolerances for 'err'. Channels with very hard cut-offs had looser  
 2070 tolerance for err because a significant error would be generated from single counts over/underes-  
 2071 timated at the cut-off. Soft channels do not share this issue, so the tolerance is much stricter. All  
 2072 annihilation channels from HDM are modeled well below IceCube's NST sensitivity which falls  
 2073 off substantially below 100 GeV [96]. We do not think it is necessary to evaluate the spline fits  
 2074 below 100 GeV and use this value as the default lower cut-off. Yet, HDM's model uncertainties  
 2075 at  $E_\nu < 10^{-6} \cdot m_\chi$  span an order of magnitude [79]. We also choose not to evaluate the splines  
 2076 below this critical value if it is within IceCube's sensitivity. Finally, the smoothing of the spectral  
 2077 lines in leptonic annihilation channels are ignored for evaluating the fit. We used the lower limit of

$\chi\chi \rightarrow$	GOOD	OK	FAIL	Limits of err calc [ $X_{min}, X_{max}$ ]
$Z^0 Z^0, W^+ W^-$	1.0E-3	1.0E-3, 1.0E-2	1.0E-2	MAX[100GeV/ $m_\chi$ , $10^{-6}$ ], 1.0
$t\bar{t}, hh$	1.0E-5	1.0E-5, 1.0E-4	1.0E-4	MAX[100GeV/ $m_\chi$ , $10^{-6}$ ], 1.0
$b\bar{b}, d\bar{d}, u\bar{u}$	9.0E-7	9.0E-7, 9.0E-6	9.0E-6	MAX[100GeV/ $m_\chi$ , $10^{-6}$ ], 1.0
$\nu\bar{\nu}_{e,\mu,\tau}$	1.0E-3	1.0E-3, 1.0E-2	1.0E-2	MAX[100GeV/ $m_\chi$ , $10^{-6}$ ], MIN[0.995, ( $E_n(\nu_{line}) - 4\sigma$ )/ $M_\chi$ ]
$e\bar{e}, \mu\bar{\mu}, \tau\bar{\tau}$	1.0E-3	1.0E-3, 1.0E-2	1.0E-2	MAX[100GeV/ $m_\chi$ , $10^{-6}$ ], MIN[0.995, ( $E_n(\nu_{line}) - 4\sigma$ )/ $M_\chi$ ]

Table 6.1 Spline err tolerances used for input in particle physics component to Eq. (3.1). Column 1 is the DM annihilation channel being fit. Columns 2, 3, and 4 are the tolerances for "GOOD" (pass), "OK" requires inspection, and "FAIL" (tune and refit) respectively. Column 5 has the X ranges over which the error is evaluated. MAX/MIN [ $\cdot, \cdot$ ] takes the maximum or minimum of the two enclosed values.

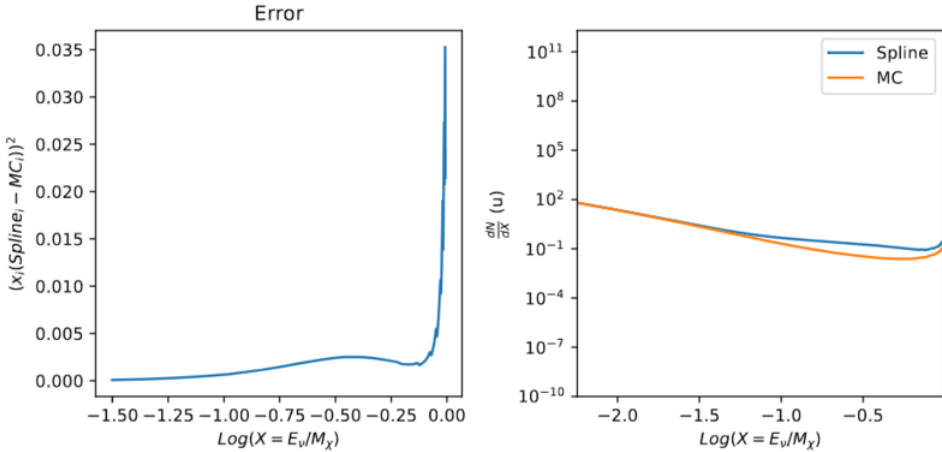


Figure 6.4 Example spline that failed the fit. Failed splines are corrected on a case by case basis unless the SM channel has a systematic problem fitting the splines. In this case, I made a bookkeeping error and loaded the incorrect spectral model

2078 the kernel mask as the upper limit of evaluation. Table 6.1 summarizes the tolerances for the DM  
 2079 annihilation channels used for this analysis.

2080 The errors are then assesed in two ways. First, FAIL and OK are directly plotted with  $e_i$  as a  
 2081 function of  $x$  with the full spline and MC. An example of a single failure is provided in Fig. 6.4.  
 2082 Second, a summary plot of all the splines is plotted and colors coded. Figure C.1 are the spline  
 2083 summaries as of writing this thesis. The goal broadly is to eliminate all red and inspect yellow  
 2084 statuses.

2085 The  $\nu_e$  spectra at Earth are not considered in this analysis, so no work was done to refine the

2086 spline fits for this flavor. Finally, I perform a visual inspection of the splines to verify that the spline  
 2087 fitting did not introduce spurious features that would corrupt the likelihood fitting.

### 2088 6.3.1.3 Composite Neutrino Spectra

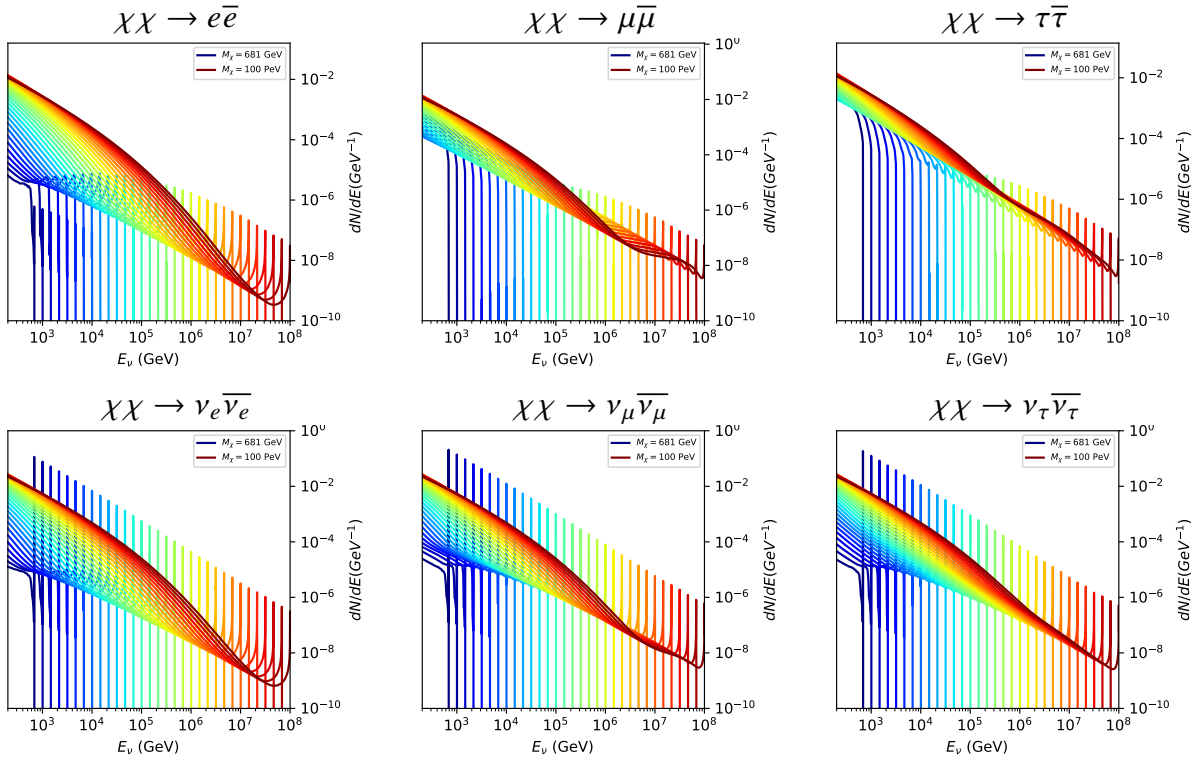


Figure 6.5 Summary of input spectral models that were smoothed with Gaussian kernels. Spectral models are for  $\chi\chi \rightarrow e\bar{e}$ ,  $\mu\bar{\mu}$ ,  $\tau\bar{\tau}$ ,  $\nu_e\bar{\nu}_e$ ,  $\nu_\mu\bar{\nu}_\mu$ , and  $\nu_\tau\bar{\nu}_\tau$ . These spectra are the composite ( $\nu_\mu + \nu_\tau$ ) of neutrino flavors. Every spectral model used for this analysis is featured as a colored solid line. Bluer lines are for low  $m_\chi$  models.  $m_\chi$  ranges from 681 GeV to 100 PeV. HDM [79],  $\chi$ arov [95], and Photospline [99] are used to generate these spectra. Energy (x-axis) was chosen to roughly represent the energy sensitivity of NST.

2089 With all the previously mentioned pieces, we are ready to fully assemble a comprehensive  
 2090 description of the particle physics term  $dN/dE$  in Eq. (6.1).

$$\frac{dN_\nu}{dE_\nu \oplus} = \left( \frac{dN_{\nu_e}}{dE_{\nu_e}} + \frac{dN_{\nu_\mu}}{dE_{\nu_\mu}} + \frac{dN_{\nu_\tau}}{dE_{\nu_\tau}} \right)_{\text{src}} \cdot \mathbf{P}(\nu_\alpha \rightarrow \nu_\beta) \quad (6.5)$$

2091 Figure 6.5 shows the spectral models that required Gaussian smoothing, the leptonic annihilation  
 2092 channels. The remaining models where the only processing were spline fitting and neutrino  
 2093 oscillation are documented in Section C.3. Notice that the different neutrino flavors are unique,

2094 especially in their low energy tails. Therefore, this analysis will be sensitive to DM annihilating to  
2095 the distinct neutrino flavors.

2096 **6.3.2 *J*- Astrophysical Component**

2097 For this analysis, we re-adopt the  $\mathcal{GS}$  model [59] used in Sec. 3 for dSphs. These models  
2098 are based on a modified Navarro-Frenk-White (NFW) profile where the indices of the NFW  
2099 (traditionally 1,3,1) are allowed to float. The angular width of these sources is much smaller than  
2100 the angular resolution of IceCube NST [98]. We therefore treat these sources as point sources  
2101 in this analysis, and forgo generating maps. These sources and the  $\mathcal{GS}$  model have already been  
2102 discussed at length in Section 3.3.2 and is not repeated here. IceCube uses identical sources to  
2103 Tab. 3.1 except we analyze source with declinations above  $0.0^\circ$ .

2104 **6.3.3 Source Selection and Annihilation Channels**

2105 We use all the dSphs presented in IceCube’s previous dSph DM search [93] and expand beyond  
2106 it. IceCube’s sources for this analysis studies include Boötes I, Canes Venatici I, Canes Venatici II,  
2107 Coma Berenices, Draco, Hercules, Leo I, Leo II, Leo V, Leo T, Segue 1, Segue 2, Ursa Major I,  
2108 Ursa Major II, and Ursa Minor. A full description of all sources used is in Table 3.1. Sources with  
2109 declinations less than  $0.0$  are excluded from this analysis.

2110 This analysis improves on the previous IceCube dSph paper [93] in the following ways. Previ-  
2111 ously, the IceCube detector was not yet completed to the 86 string configuration. Many more dSphs  
2112 will be observed, from 4 to 15. Previously, the particle physics model used for neutrino spectra  
2113 from DM annihilation did not have EW corrections where they are now included [79]. The spectral  
2114 models also predict substantial differences between the neutrino flavors, so this analysis will be the  
2115 first DM dwarf analysis to discriminate between primary neutrino flavors. The study performed  
2116 here studies 10.4 years of data.

2117 The SM annihilation channels probed for this study include  $\chi\chi \rightarrow$

2118  $b\bar{b}, t\bar{t}, u\bar{u}, d\bar{d}, e\bar{e}, \mu\bar{\mu}, \tau\bar{\tau}, ZZ, W^+W^-, \nu_e\bar{\nu}_e, \nu_\mu\bar{\nu}_\mu$ , and  $\nu_\tau\bar{\nu}_\tau$

2119 **6.4 Likelihood Methods**

2120 I use the Point-Source search likelihood which is widely used in IceCube analyses. The  
2121 likelihood function is defined as the following:

$$L(n_s) = \prod_{i=1}^N \left[ \frac{n_s}{N} S_i + \left(1 - \frac{n_s}{N}\right) B_i \right] \quad (6.6)$$

2122 where  $i$  is an event index,  $S$  and  $B$  are the signal PDF and background PDF respectively. For a joint  
2123 analysis where the sources are stacked the likelihood is expanded in the simplified way:

$$L(n_s) = \prod_{i=1}^{N_{\text{sources}}} L_i(n_s) \quad (6.7)$$

2124 Where  $L_i$  is the likelihood from the  $i$ -th source in the stacked analysis. The Test Statistic (TS)  
2125 definition remains the same as Eq. (3.7)

2126 **6.5 Background Simulation**

2127 Before we look at data, we must first analyze background and signal injection to validate our  
2128 analysis. We set out to characterize the TS distributions for each source, annihilation channel,  
2129 and  $m_\chi$ . Previous IceCube DM searches [97, 101] showed TS distributions that did not behave  
2130 according to a  $\chi^2$  distribution with 1 degree of freedom. TS distributions can also vary significantly  
2131 between DM mass and annihilation models. Therefore, Wilk's theorem may not be applicable to  
2132 the analysis. Instead, a critical value is defined from many background trials. We study the TS  
2133 distributions first for each source, then for the stacked analysis. The following sections show the  
2134 results of the likelihood fitting for a suite of background trials.

2135 I assume that TS values are physical:  $TS \geq 0$ .  $\epsilon[x]$  indicate the fraction of events where  $TS < x$ .  
2136 For TS plots shown here, the decimal values of  $x$  are 1.0e-2 and 1.0e-3. Each subplot represents  
2137 a simulation of 100,000 data-scrambled background trials. Section 6.5.1 show the background TS  
2138 distributions obtained from Segue 1, a source with little Earth attenuation and large  $J$ -factor, and  
2139 Ursa Major II, which has similarly large  $J$ -factor but significantly more Earth attenuation, assuming  
2140 DM annihilation into  $b\bar{b}$ ,  $\tau\bar{\tau}$ , and  $\nu_\mu\bar{\nu}_\mu$ . I show the TS distributions of a stacked study of 15 sources  
2141 for all DM annihilation channels.

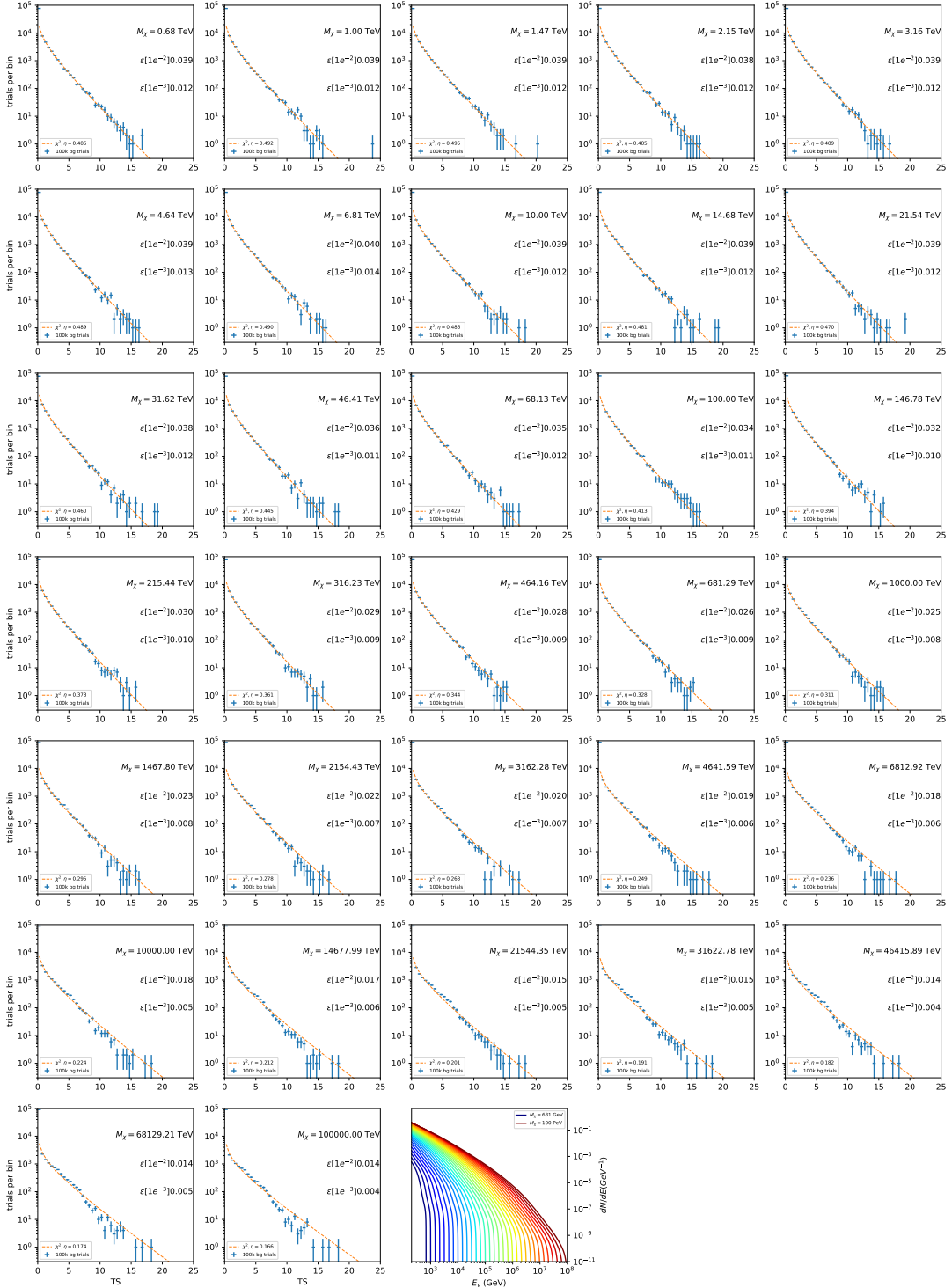


Figure 6.6 Test statistic (TS) distributions for Segue 1 and  $\chi\chi \rightarrow b\bar{b}$ . Each subplot, except the final, is the TS distribution for a specific DM mass listed in the subplot. Orange dashed lines are the traces for a  $\chi^2$  distribution with 1 degree of freedom.  $\epsilon[\cdot]$  is the fraction of trials smaller than the bracketed value. The final subplot features the all DM spectral models, similar to Fig. 6.5, used as input for the TS distributions.

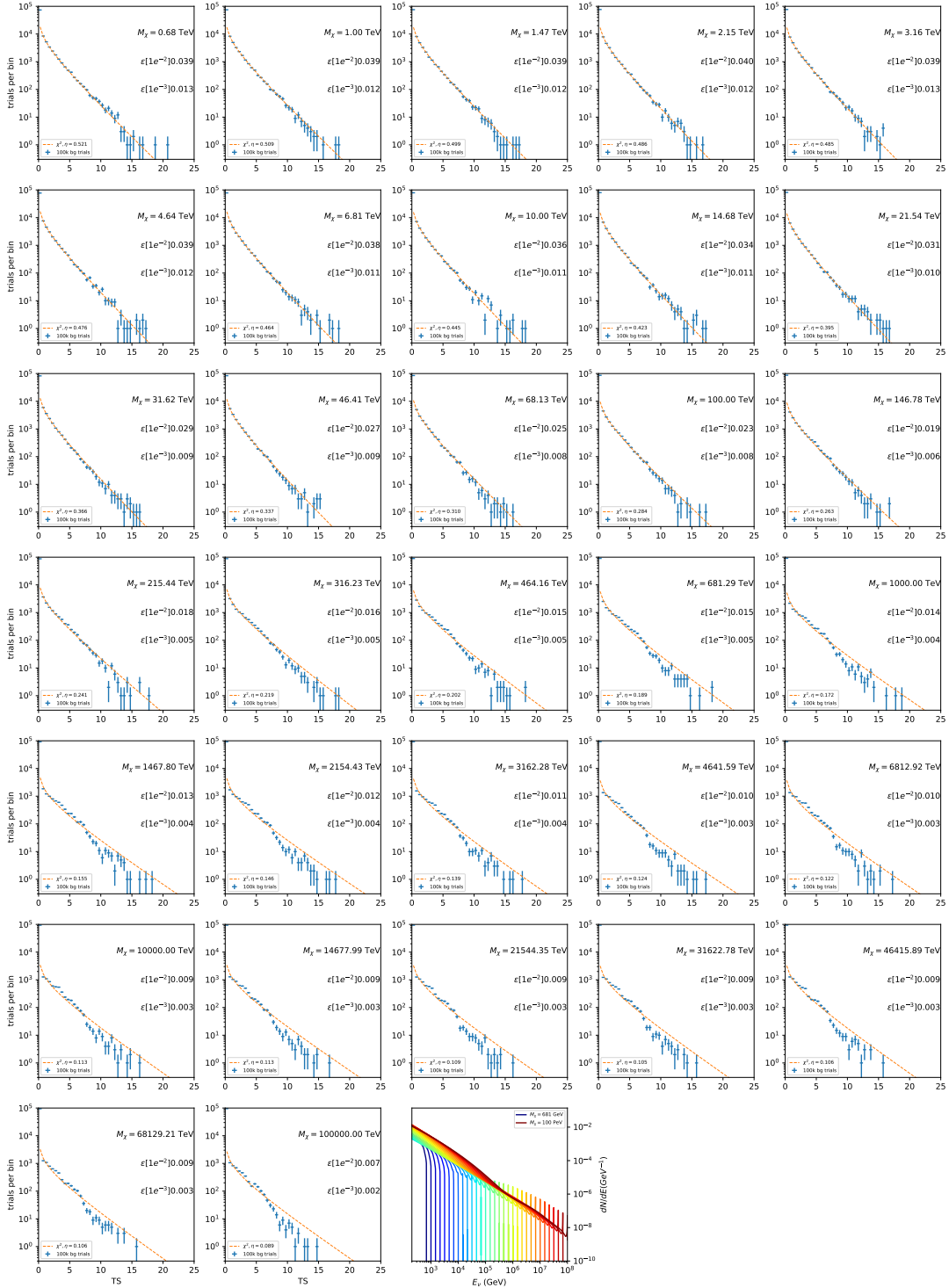


Figure 6.7 Same as Fig. 6.6 for Segue 1  $\chi\chi \rightarrow \tau\bar{\tau}$ .

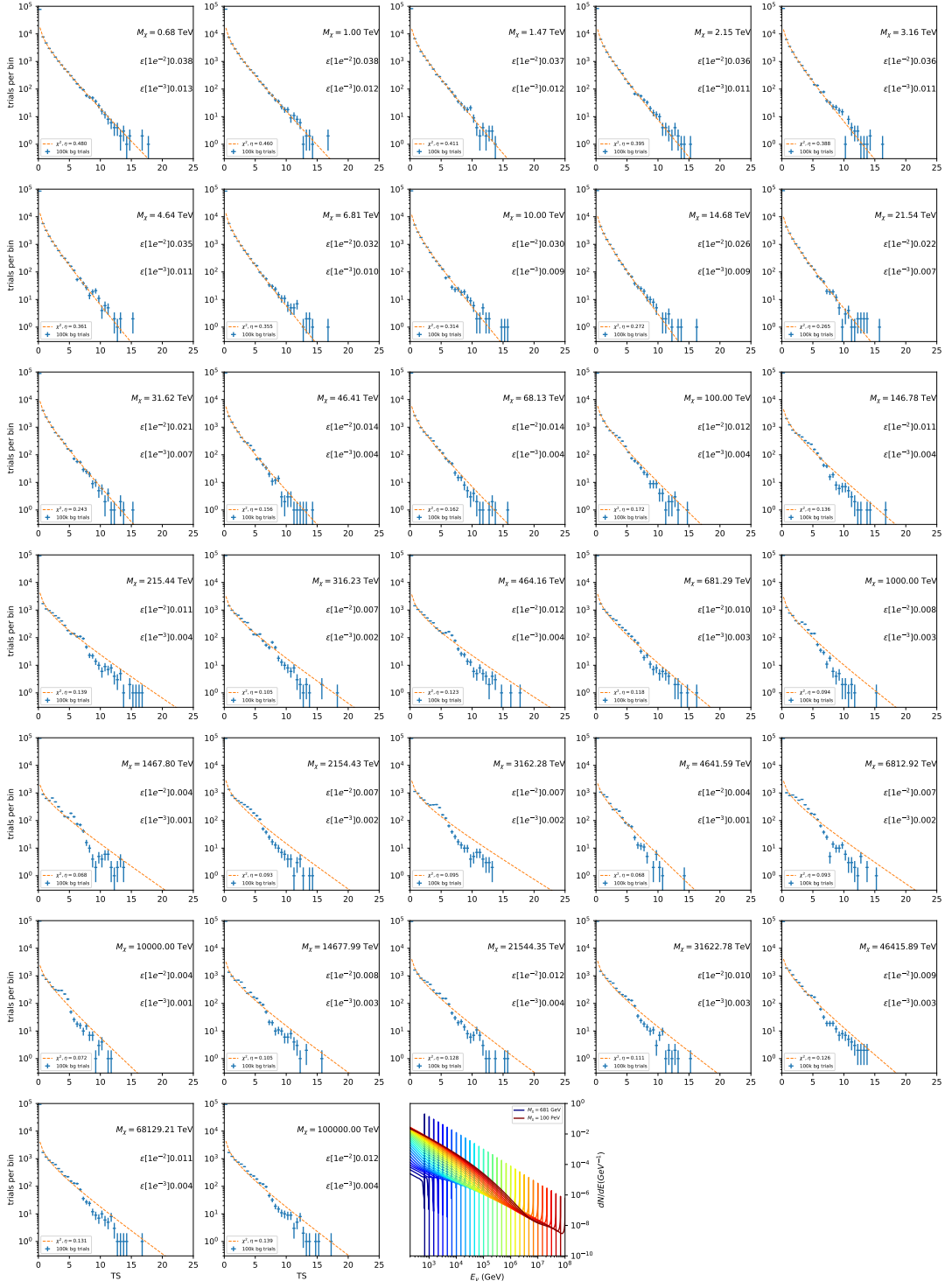


Figure 6.8 Same as Fig. 6.6 for Segue 1  $\chi\chi \rightarrow \nu_\mu\bar{\nu}_\mu$ .

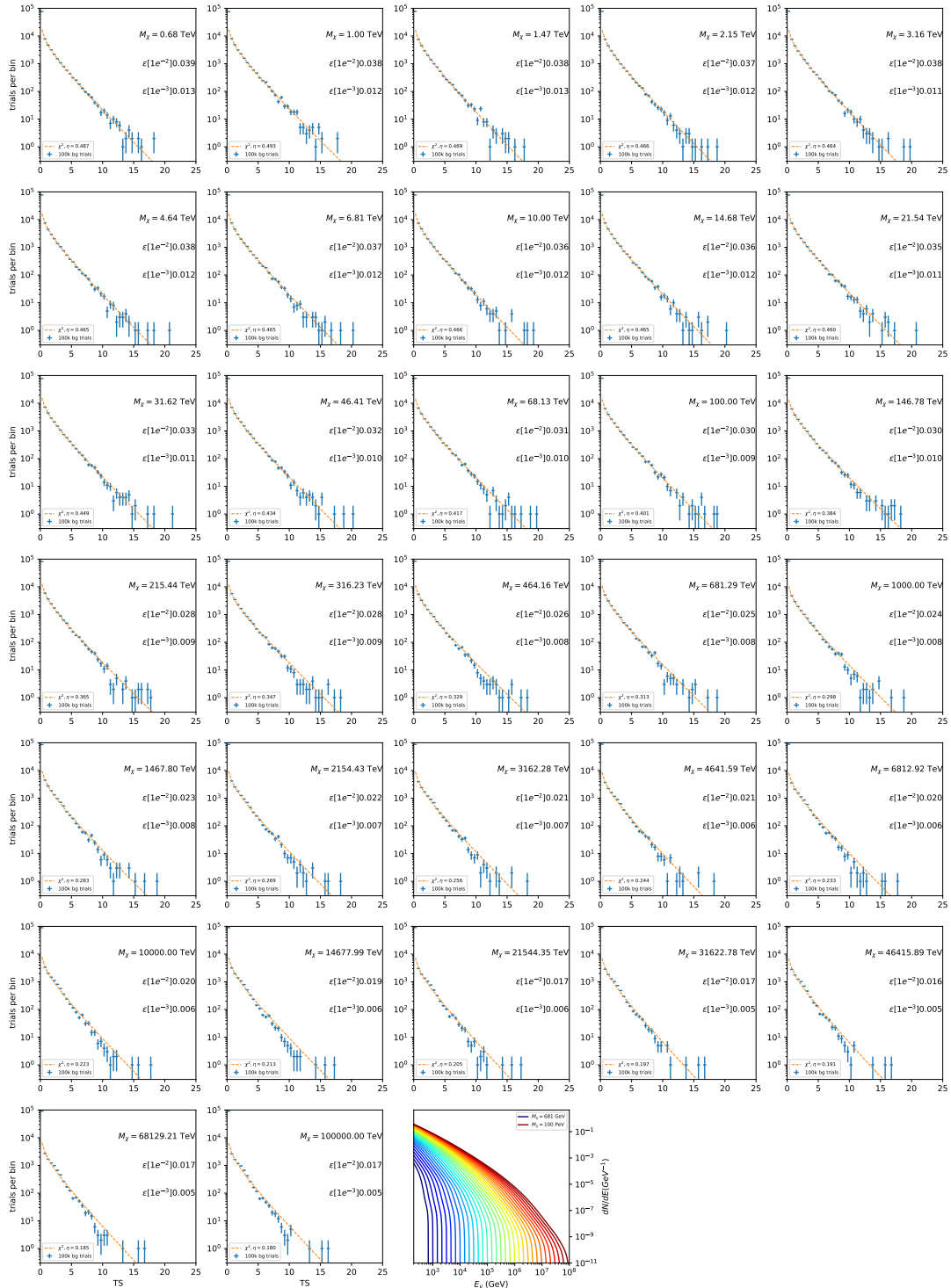


Figure 6.9 Same as Fig. 6.6 for Ursa Major II 1  $\chi\chi \rightarrow b\bar{b}$ .

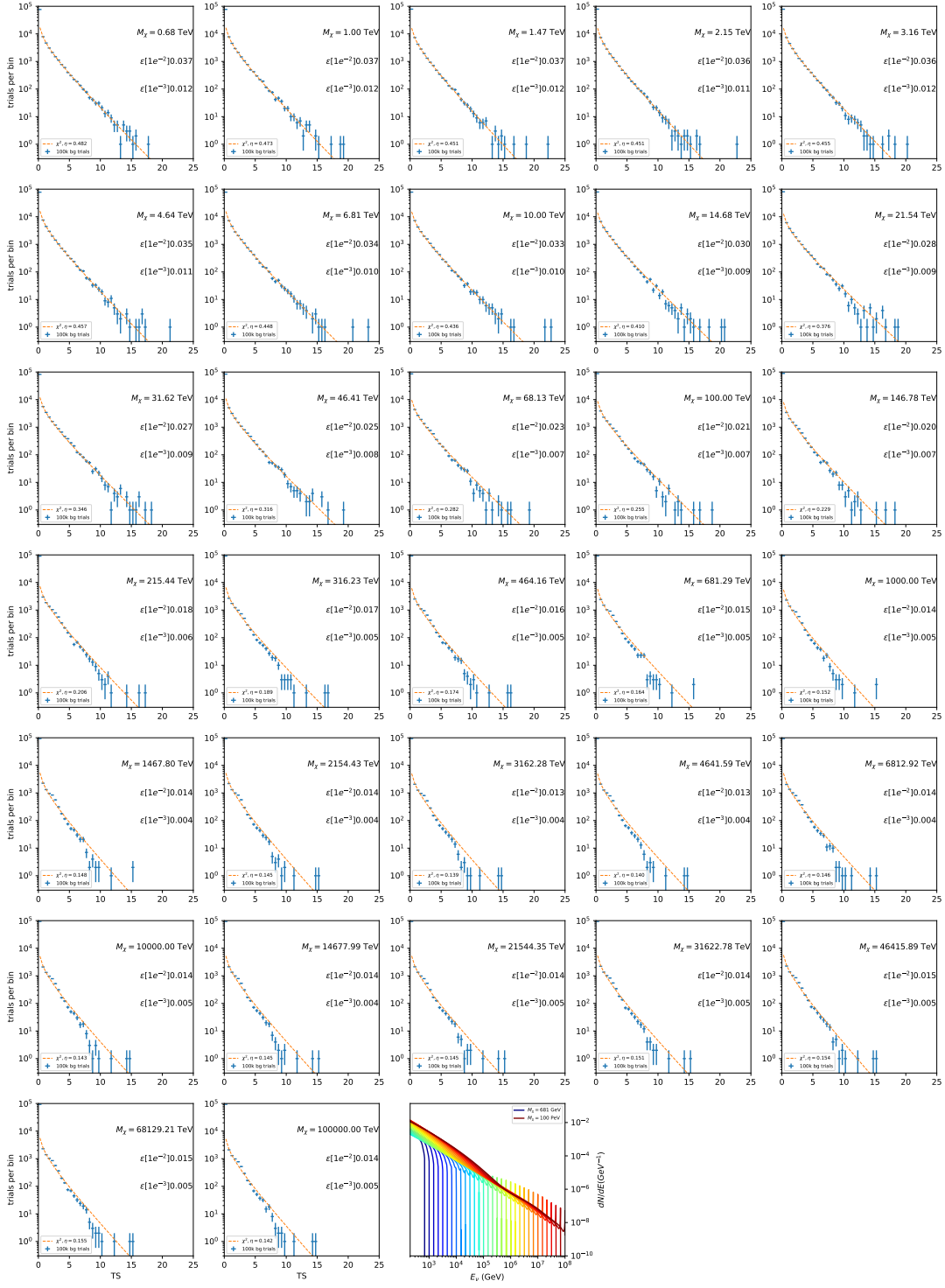


Figure 6.10 Same as Fig. 6.6 for Ursa Major II 1  $\chi\chi \rightarrow \tau\bar{\tau}$ .

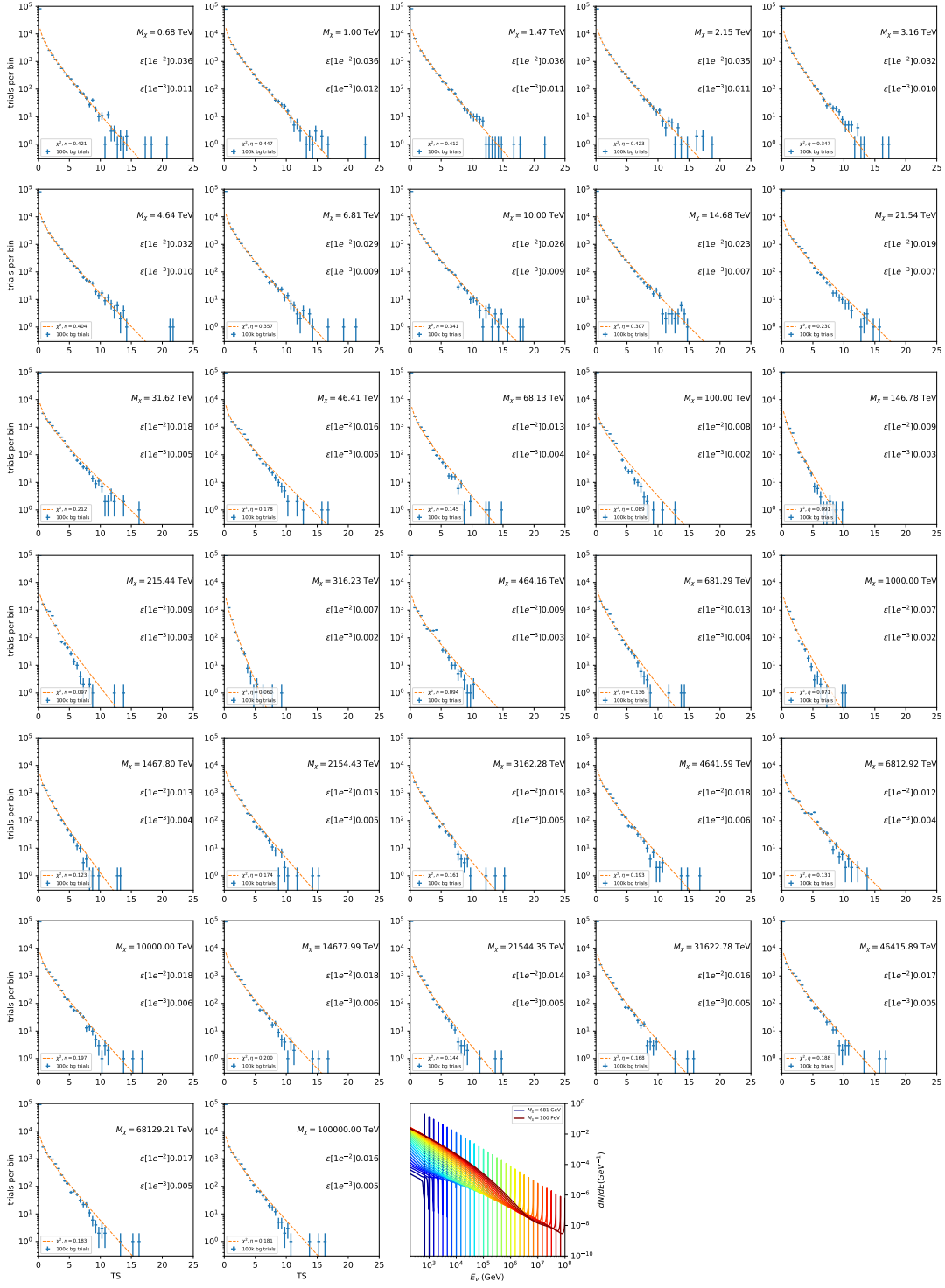


Figure 6.11 Same as Fig. 6.6 for Ursa Major II 1  $\chi\chi \rightarrow \nu_\mu\bar{\nu}_\mu$ .

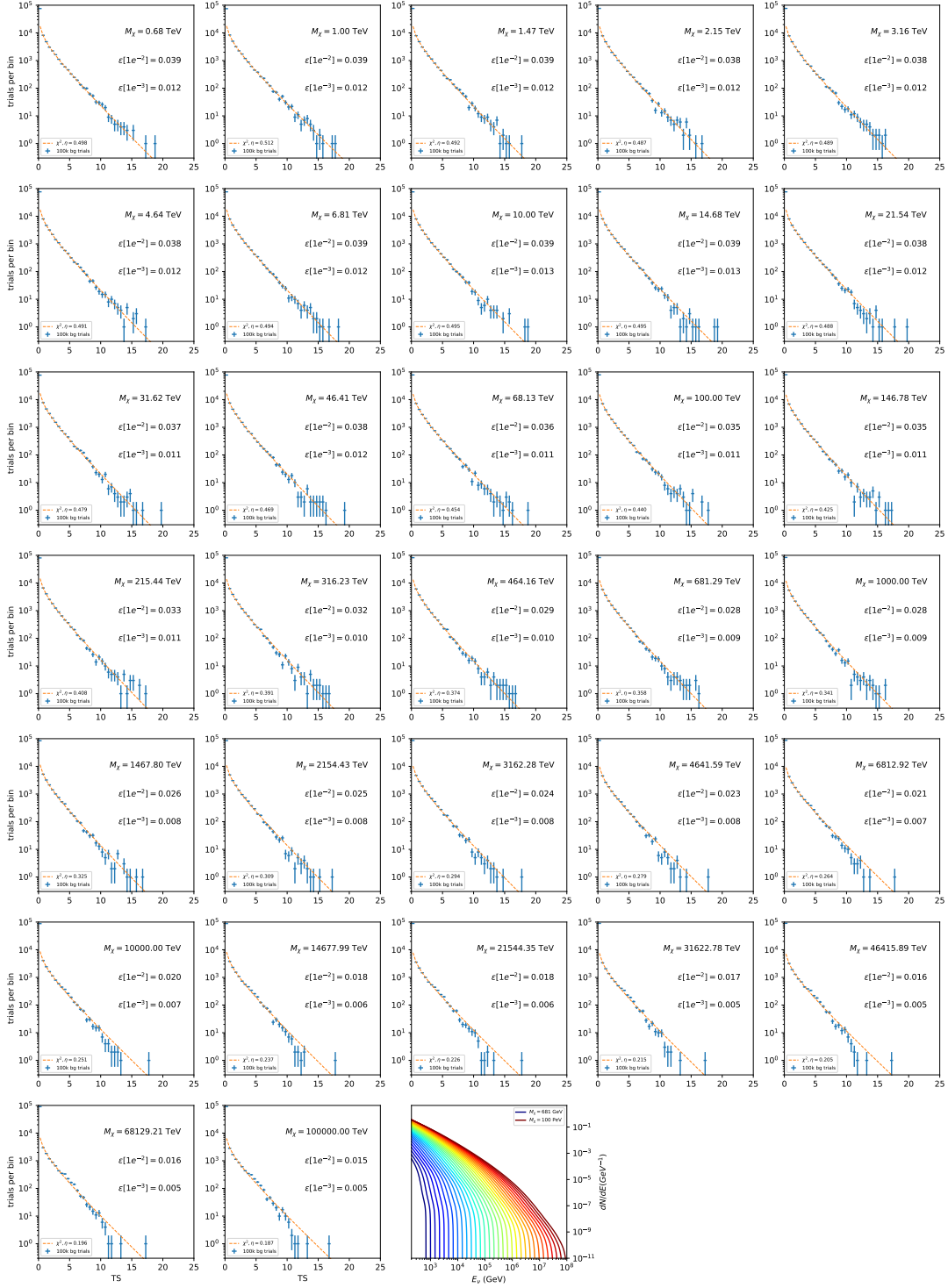


Figure 6.12 Same as Fig. 6.6 for 15,  $\mathcal{GS}$   $J$ -factor, stacked sources and  $\chi\chi \rightarrow b\bar{b}$ .

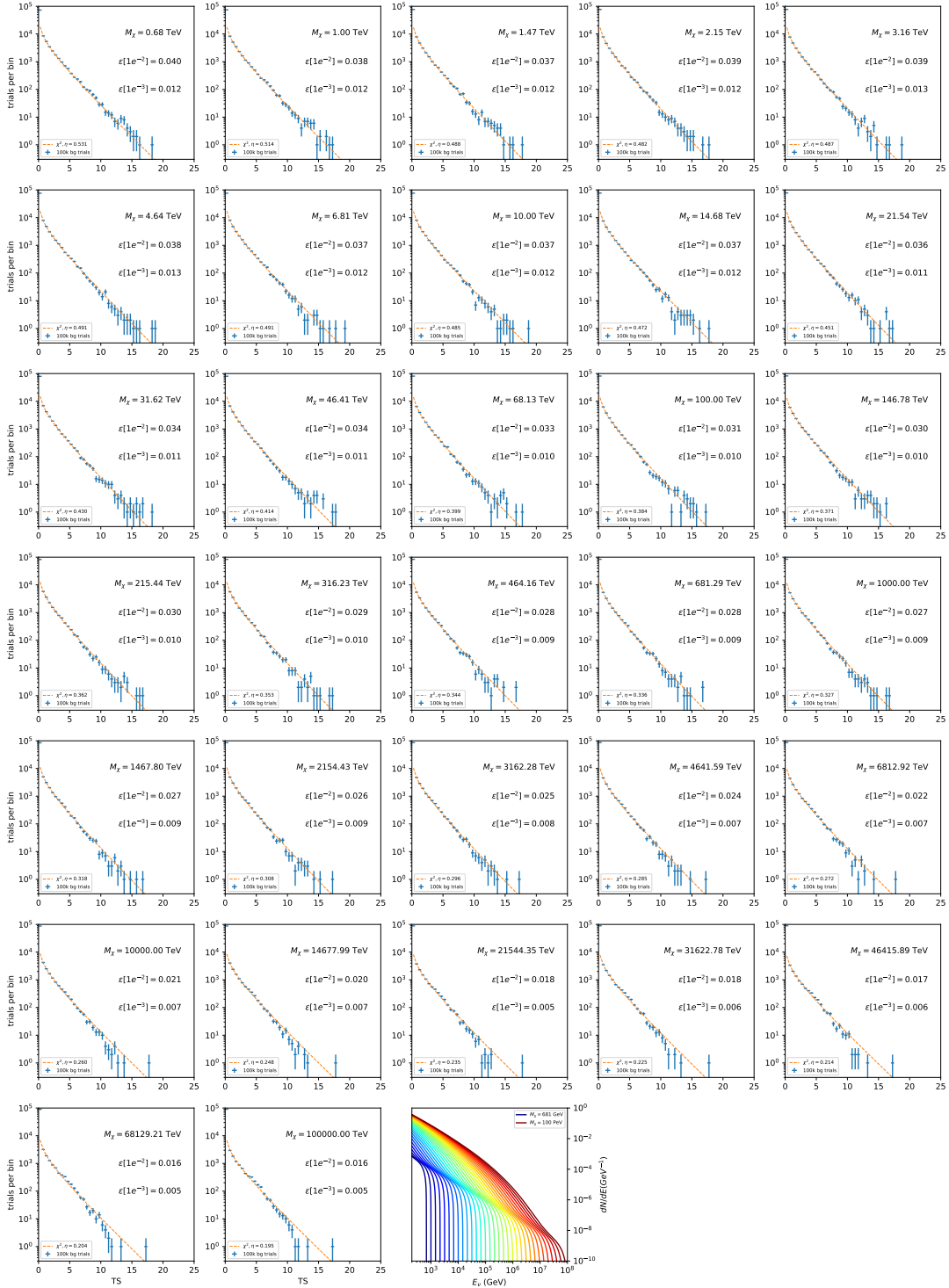


Figure 6.13 Same as Fig. 6.6 for 15, GS J-factor, stacked sources and  $\chi\chi \rightarrow t\bar{t}$ .

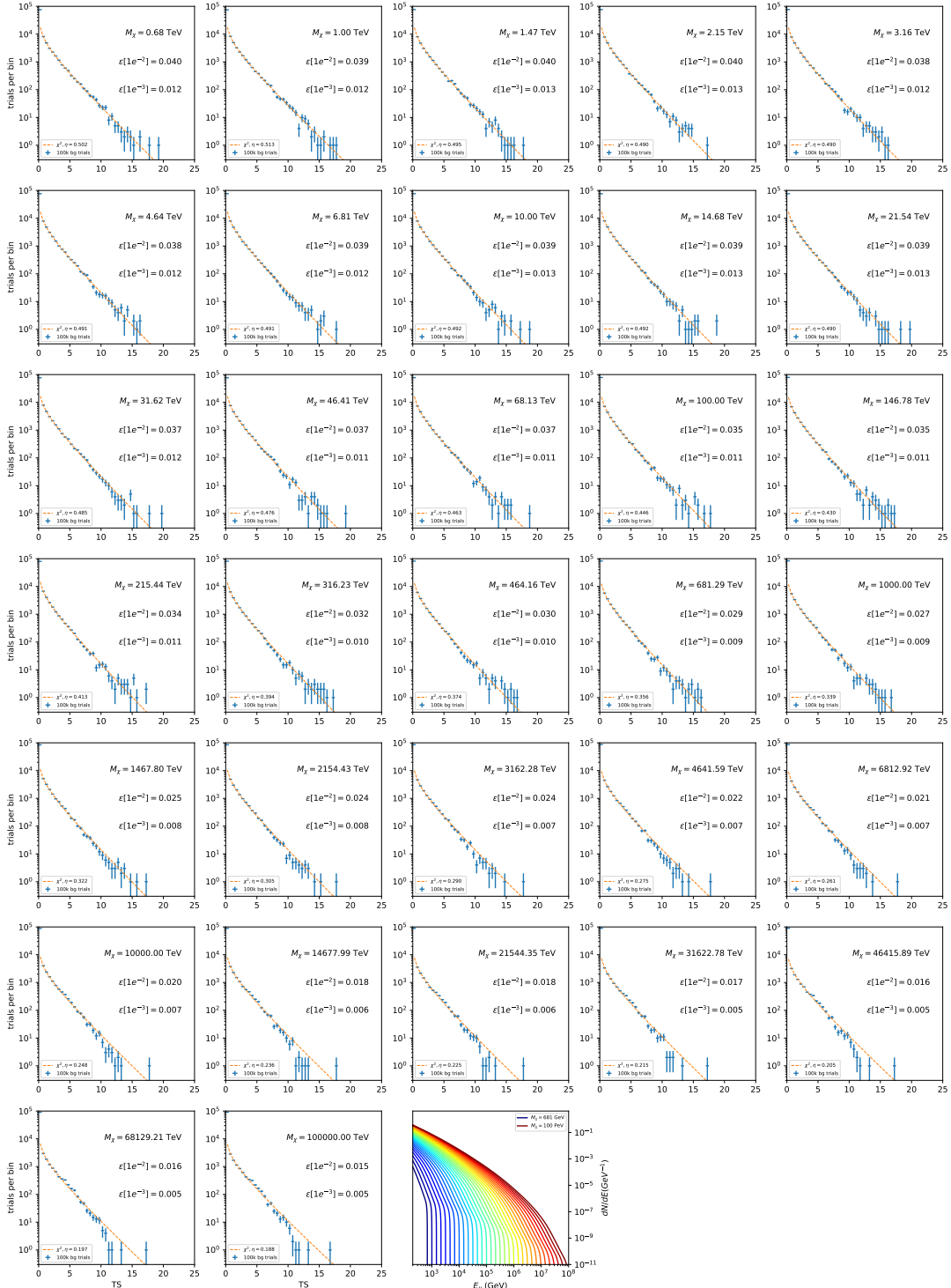


Figure 6.14 Same as Fig. 6.6 for 15,  $\mathcal{GS}$   $J$ -factor, stacked sources and  $\chi\chi \rightarrow u\bar{u}$ .

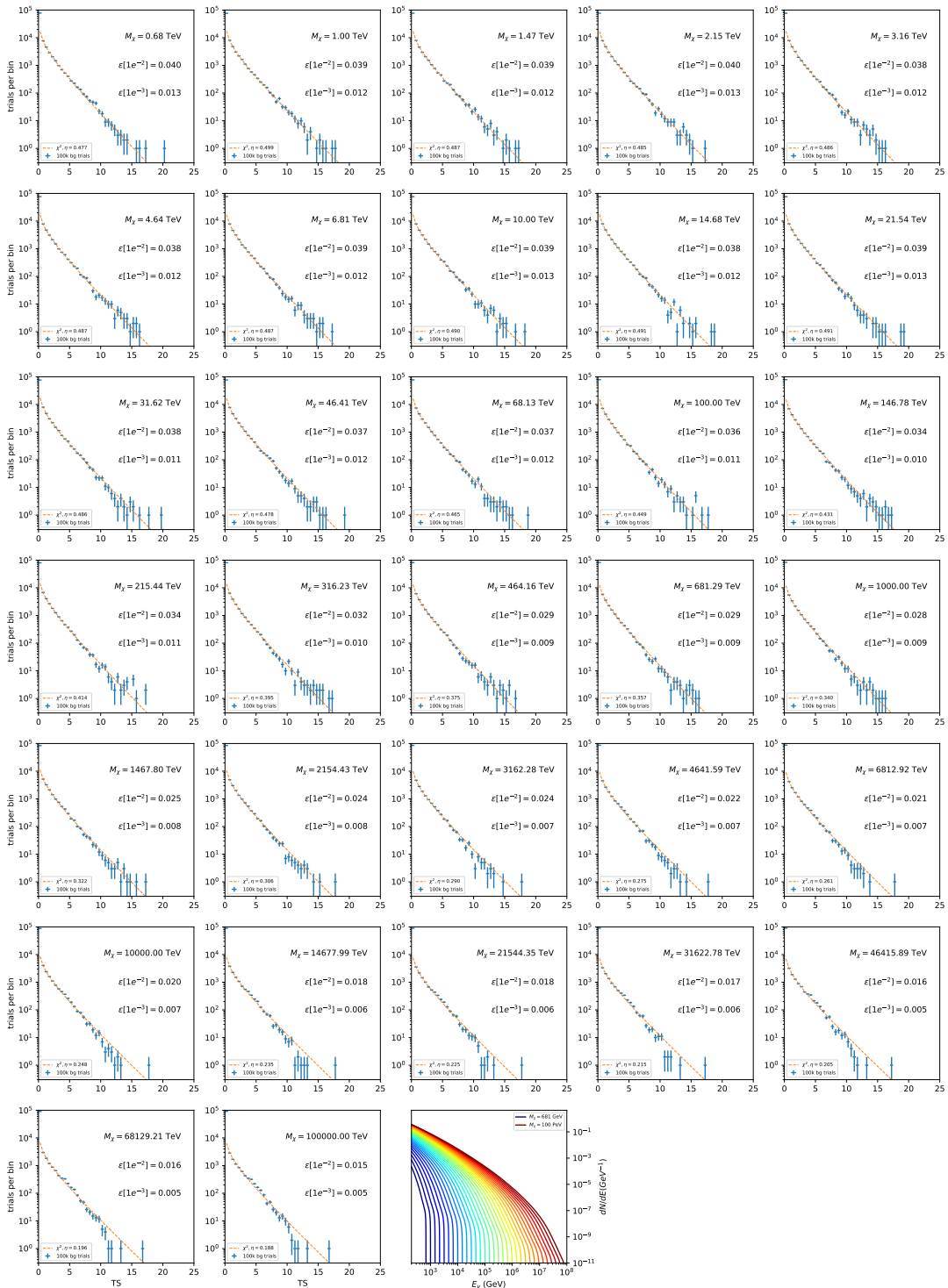


Figure 6.15 Same as Fig. 6.6 for 15,  $\mathcal{GS}$  J-factor, stacked sources and  $\chi\chi \rightarrow d\bar{d}$ .

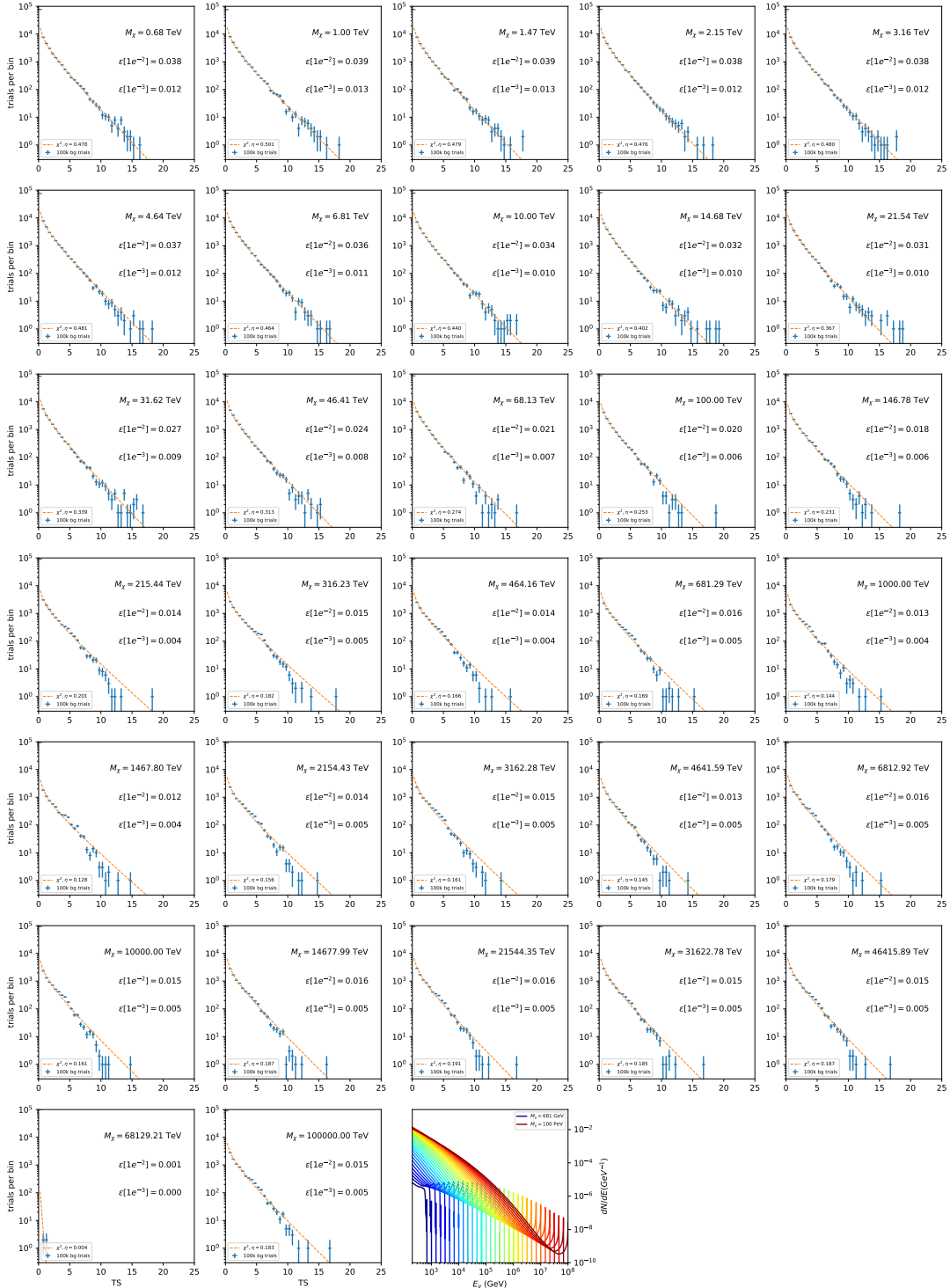


Figure 6.16 Same as Fig. 6.6 for 15,  $\mathcal{GS}$  J-factor, stacked sources and  $\chi\chi \rightarrow e\bar{e}$ .

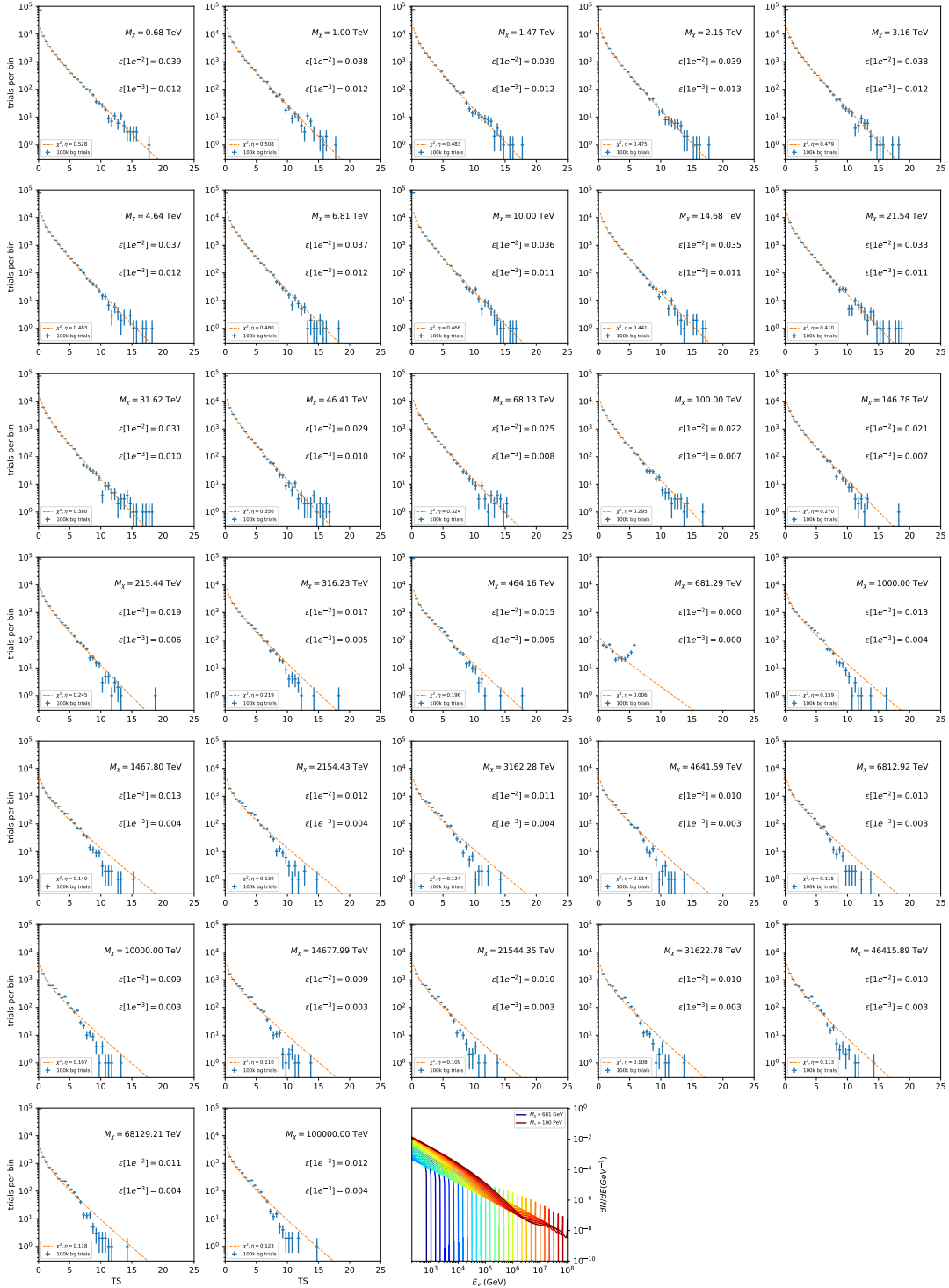


Figure 6.17 Same as Fig. 6.6 for 15,  $\mathcal{G}\mathcal{S}$   $J$ -factor, stacked sources and  $\chi\chi \rightarrow \mu\bar{\mu}$ .

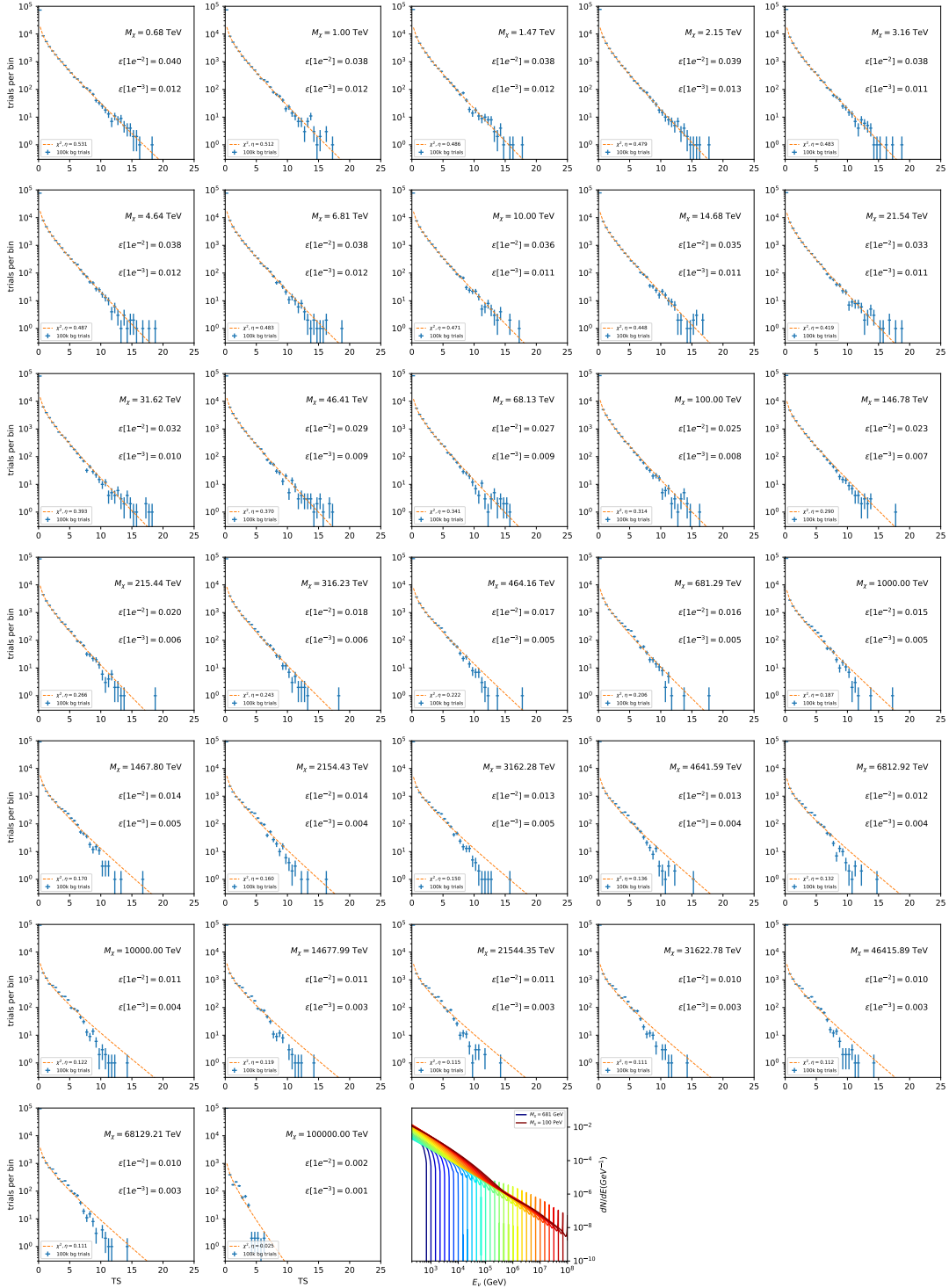


Figure 6.18 Same as Fig. 6.6 for 15,  $\mathcal{GS}$   $J$ -factor, stacked sources and  $\chi\chi \rightarrow \tau\bar{\tau}$ .

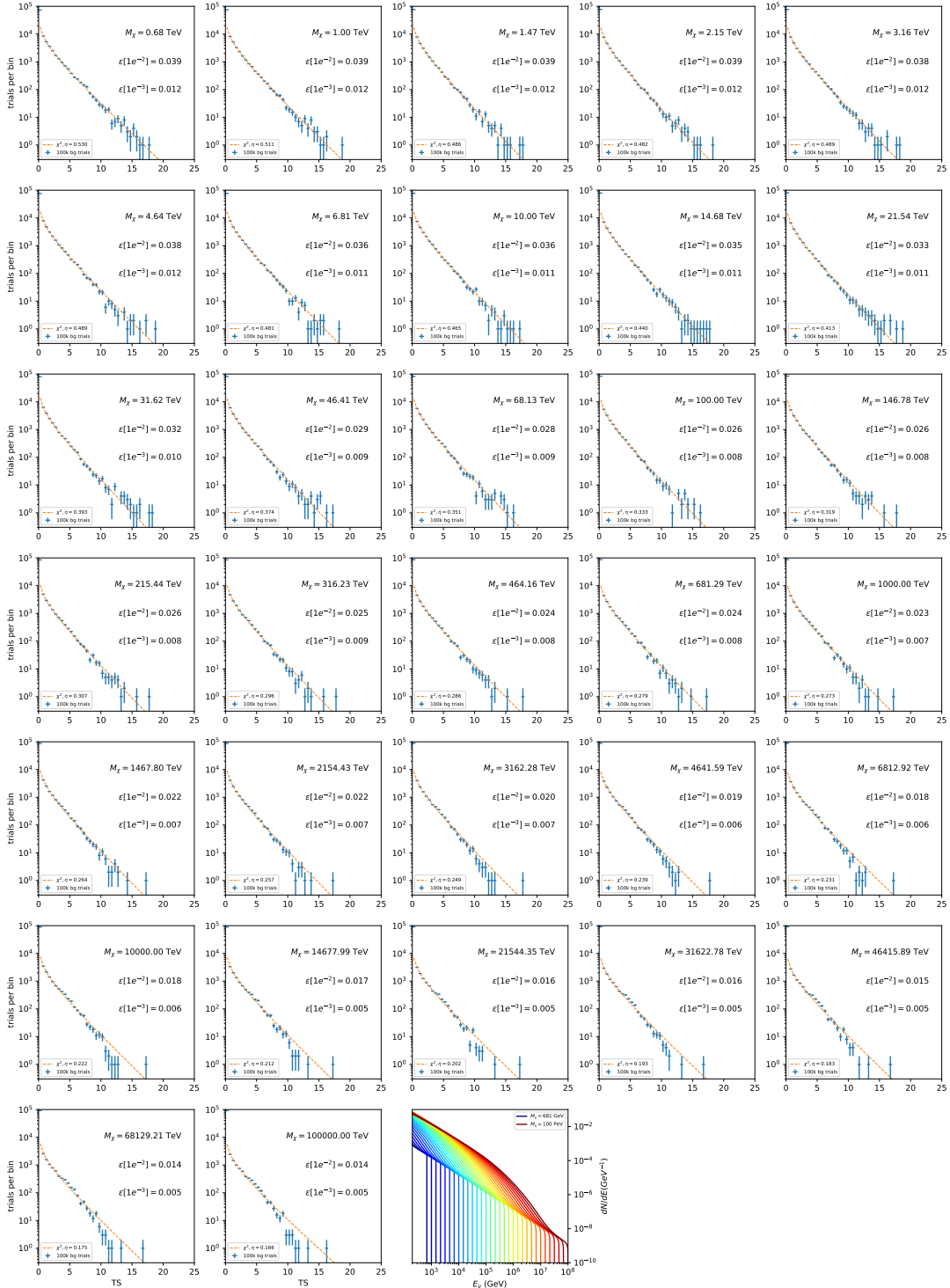


Figure 6.19 Same as Fig. 6.6 for 15,  $\mathcal{GS}$  J-factor, stacked sources and  $\chi\chi \rightarrow W^+W^-$ .

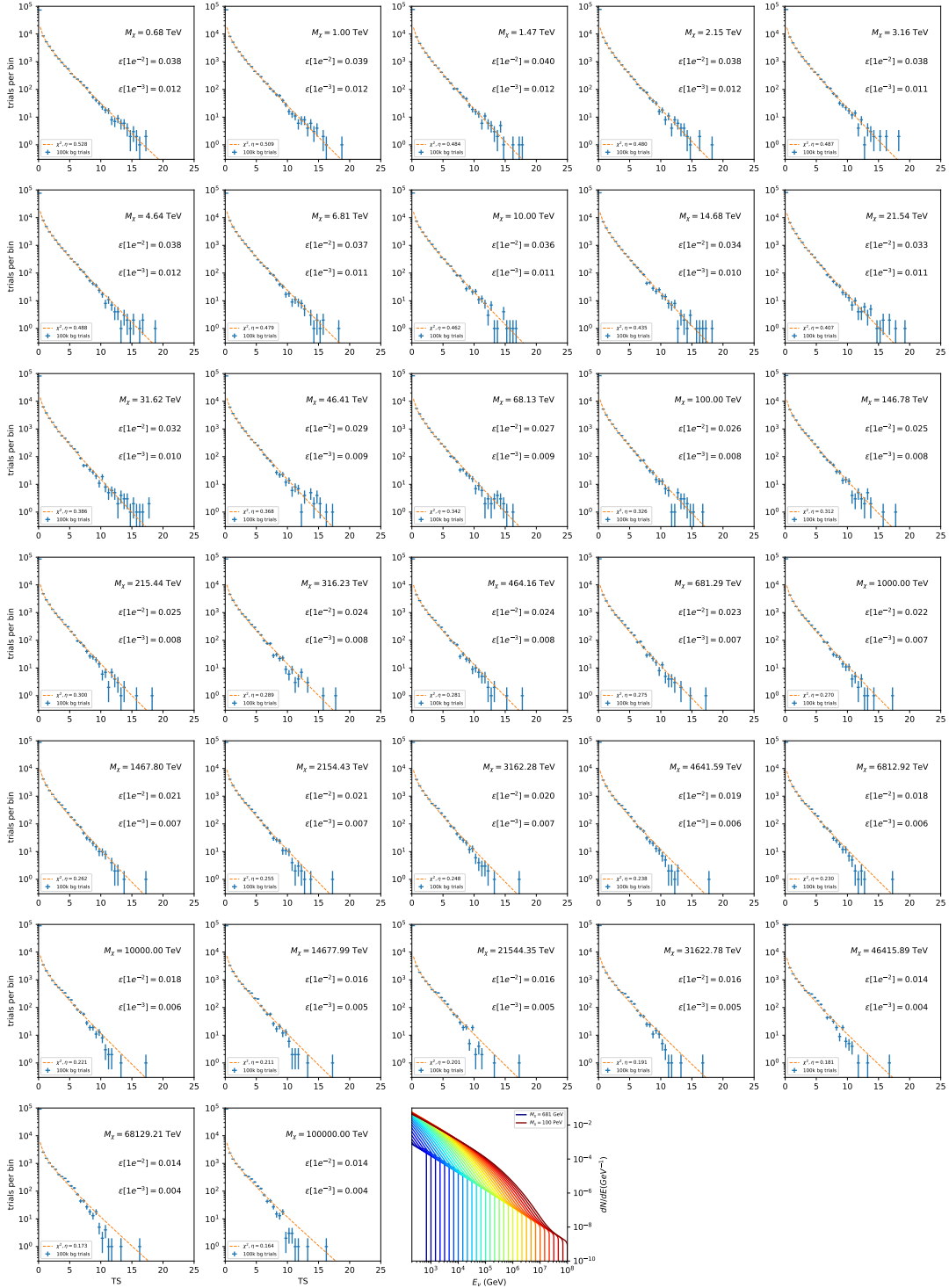


Figure 6.20 Same as Fig. 6.6 for 15,  $\mathcal{GS}$   $J$ -factor, stacked sources and  $\chi\chi \rightarrow ZZ$ .

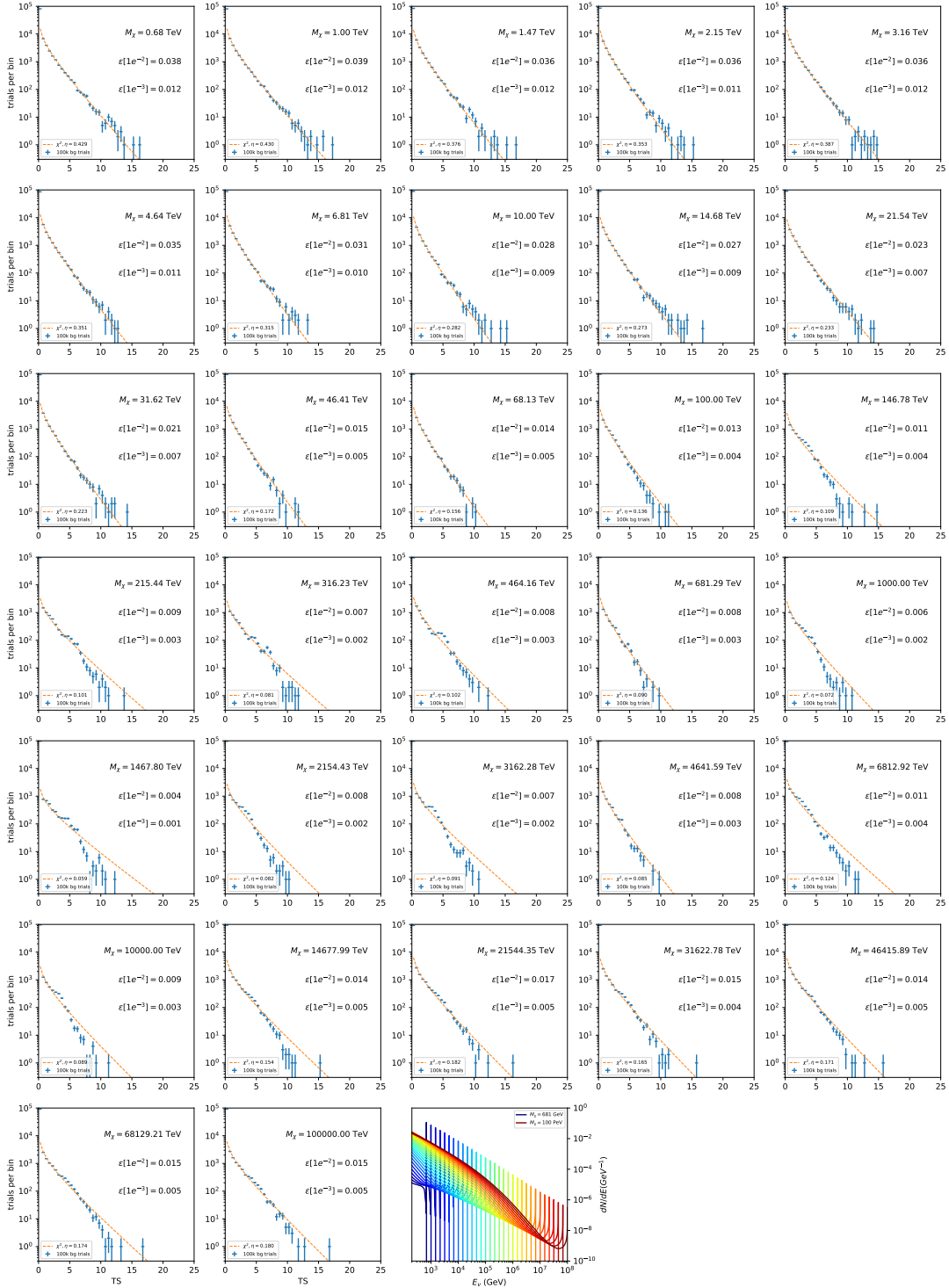


Figure 6.21 Same as Fig. 6.6 for 15,  $\mathcal{GS}$   $J$ -factor, stacked sources and  $\chi\chi \rightarrow \nu_e \bar{\nu}_e$ .

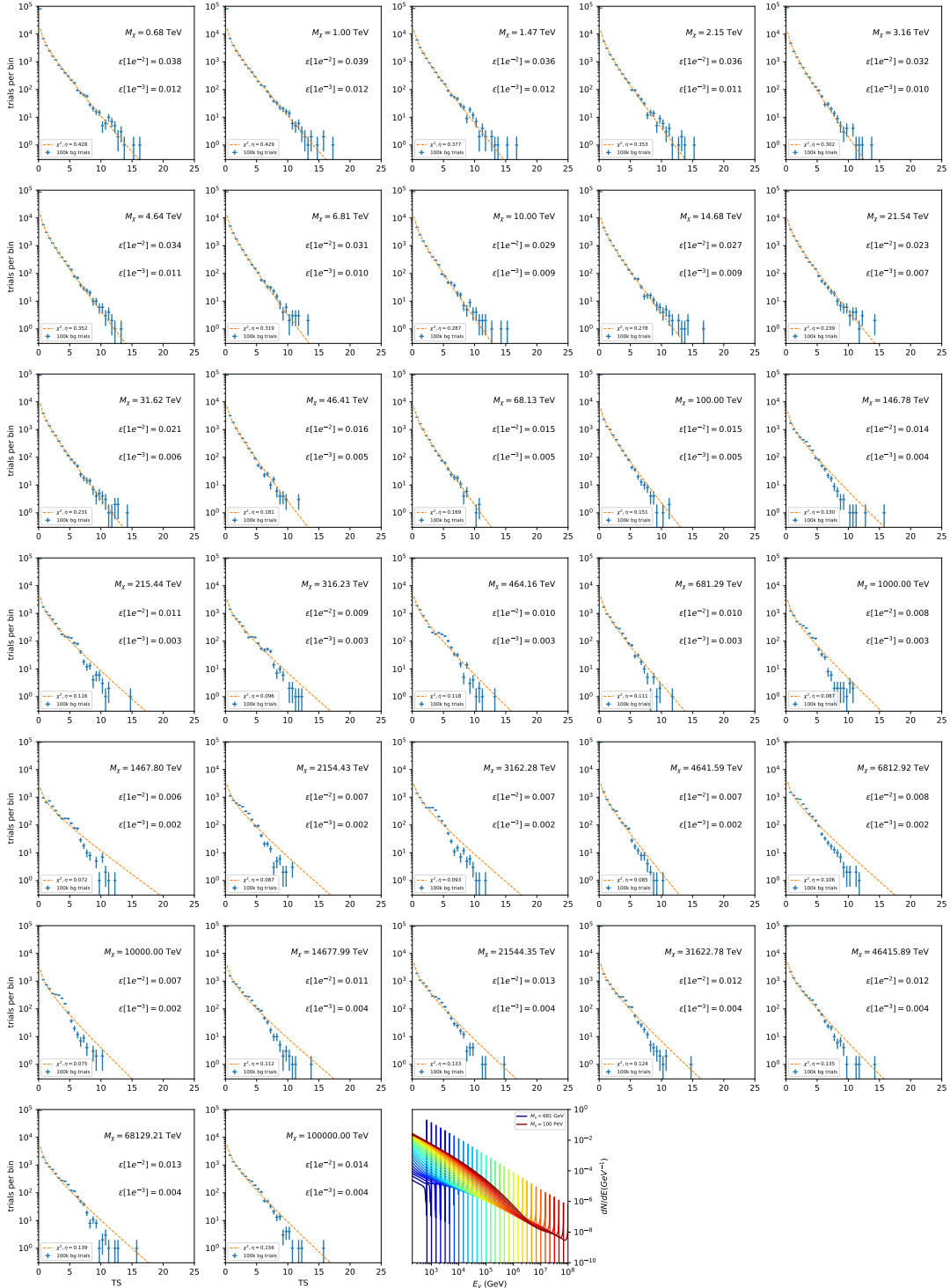


Figure 6.22 Same as Fig. 6.6 for 15,  $\mathcal{GS}$   $J$ -factor, stacked sources and  $\chi\chi \rightarrow \nu_\mu \bar{\nu}_\mu$ .

2142 **6.5.1 TS per Source**

2143 Figure 6.6 to Figure 6.11 present the TS distributions for Segue 1 and Ursa Major II for 100,000  
2144 trials. More studies for all annihilation channels and remaining 13 sources were also performed  
2145 and are documented in IceCube’s internal wiki.

2146 Almost every distribution produced follows a  $\chi^2$  distribution with 1 degree of freedom. This is  
2147 more true for low  $m_\chi$  than high  $m_\chi$  models. These observations are important for future assumptions  
2148 made in Sec. 7 and may justify statistical calculations assuming our test statistics follow a  $\chi^2$  with  
2149 1 degree of freedom.

2150 **6.5.2 Stacked TS**

2151 Figure 6.12 to Figure 6.22 present the TS distributions for a stacked study of 15 sources with  
2152  $\mathcal{GS}$   $J$ -factors on 100,000 trials. The presentation of these plots are identical to the single source  
2153 distributions in Section 6.5.1. We see similar behaviour in the stacked TS distributions compared  
2154 to the single source studies.

2155 **6.6 Signal Recovery**

2156 We also wish to understand how well the analysis is able to reconstruct signal neutrinos. In  
2157 order to test this, we inject neutrinos from our spectral models randomly then attempt to discern  
2158 the number of signal neutrinos in the simulated data. Figure 6.23 and Figure 6.24 show this study  
2159 for  $\chi\chi \rightarrow b\bar{b}$ ,  $t\bar{t}$ , and  $\nu_\mu\bar{\nu}_\mu$  for a stacked analysis of 15 sources. Figure C.3 to Figure C.8 show  
2160 identical studies for Segue 1 and Ursa Major II. We see that the analysis is conservative at smaller  
2161  $m_\chi$ , yet improves at larger  $m_\chi$ . We also see that the uncertainty is small for the neutrino annihilation  
2162 spectra, and the uncertainty is larger for softer channels like  $b\bar{b}$ .

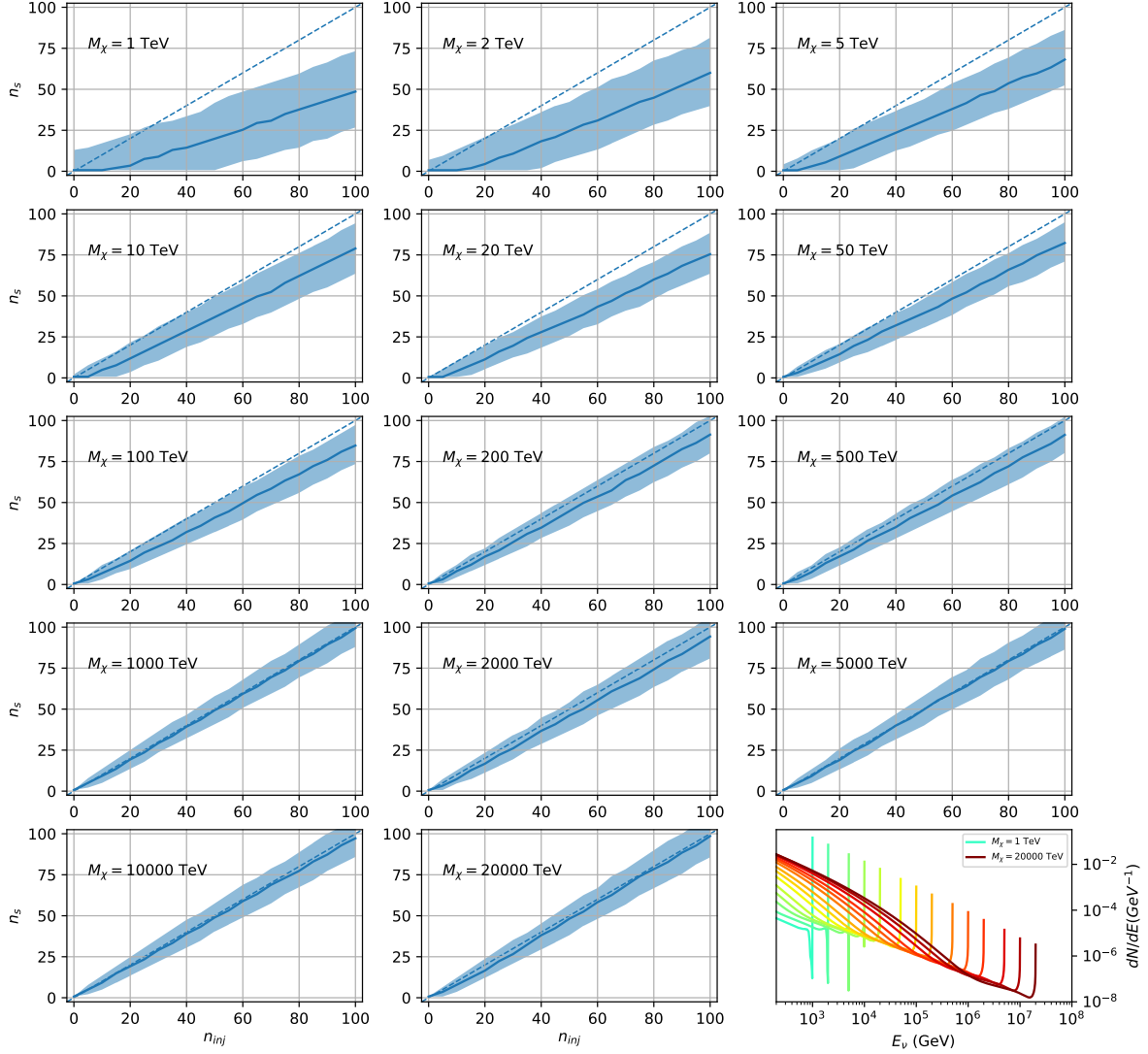


Figure 6.23 Signal Recovery study for an analysis with 15 stacked sources using the  $\mathcal{GS}$   $J$ -factors [59]. Above shows 14 studies for DM mass ranging between 1 TeV and 20 PeV for  $\chi\chi \rightarrow \mu_\mu\bar{\mu}_\mu$ . The bottom right subplot features every spectral model used as input for the remaining subplots. The remaining subplots show  $n_{inj}$  as the number of signal events injected into background simulation. Whereas,  $n_s$  is the number of signal events recovered from analyzing the injected simulation. Blue line represents the median values of 100 simulations. Light blue bands show the  $1\sigma$  statistical uncertainty around the median.

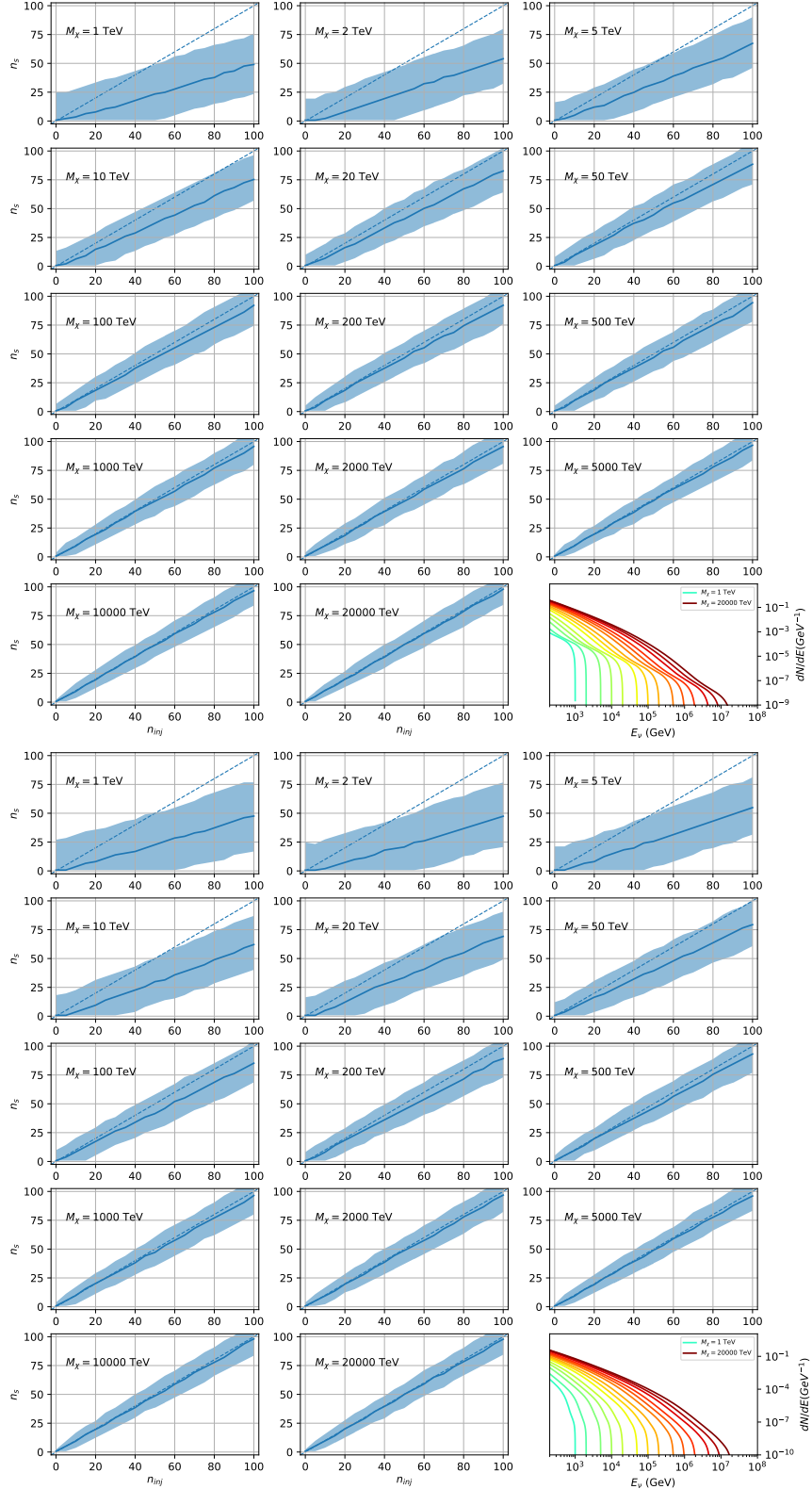


Figure 6.24 Same as Fig. 6.23 but for  $\chi\chi \rightarrow t\bar{t}$  (top) and  $b\bar{b}$  (bottom).

2163 **6.6.1 Sensitivities**

2164 In IceCube, we usually define the 90% confidence level (CL), as the minimum number of signal  
2165 events ( $n_s$ ) required to have a Type I error rate smaller than 0.5 and Type II error rate of 0.1. We  
2166 compute  $n_s$  from the following equation

$$n_s = T_{\text{live}} \int_0^{\Delta\Omega} d\Omega \int_{E_{\min}}^{E_{\max}} dE_\nu A_{\text{eff}}(\hat{n}, E_\nu) \frac{d\Phi_\nu}{d\Omega dE_\nu}(\hat{n}, E_\nu), \quad (6.8)$$

2167 to extract the sensitivity on the dark matter velocity-weighted annihilation cross-section,  $\langle\sigma v\rangle$ .  $T_{\text{live}}$   
2168 is the detector live time,  $A_{\text{eff}}$  is the effective area of the detector, and  $E_{\min}$ ,  $E_{\max}$  are the minimum,  
2169 maximum energies of the expected neutrinos, respectively.

2170 Sensitivities are calculated for each source individually as if they were the only source and as a  
2171 stack over 1000 trials. From Eq. (6.8) and Eq. (6.1) we can compute the  $\langle\sigma v\rangle$  at a 90% confidence  
2172 level. Figure 6.26 and Fig. 6.25 show the sensitivities for some DM annihilation channels. Not  
2173 all channels computed successfully in time for the writing of this dissertation. Among channels  
2174 missing include the charged leptons:  $e$  and  $\tau$ .

2175 **6.7 Systematics**

2176 The current analysis plan is to compare these sensitivities to another  $J$ -factor catalog such as  
2177  $\mathcal{LS}$  [80] although this was not completed in time for this dissertation. Additionally, we set out to  
2178 perform a standard suite of IceCube systematic studies which include: DOM efficiency, Hole ice,  
2179 ice absorption, and photon scattering. We do study Earth attenuation, and Section 6.7.1 enumerates  
2180 the impact of the Earth on our hardest neutrino spectra.

2181 **6.7.1 Earth Effects**

2182 We look to quantify the impact of the Earth on our sensitivity to  $\chi\chi \rightarrow \nu_\mu \bar{\nu}_\mu$ . This channel is  
2183 expected to be among the significantly impacted annihilation channels because it has a significant  
2184 contribution at PeV energies for  $m_\chi \geq 1\text{PeV}$ . The Earth is expected to attenuate these higher energy  
2185 neutrinos. However, these neutrino spectra have significant low energy contributions, so we do not  
2186 expect to entirely lose our sensitivity. This motivated a study examining our  $\langle\sigma v\rangle$  sensitivity over  
2187 all DM masses sampled for a selection of declinations.

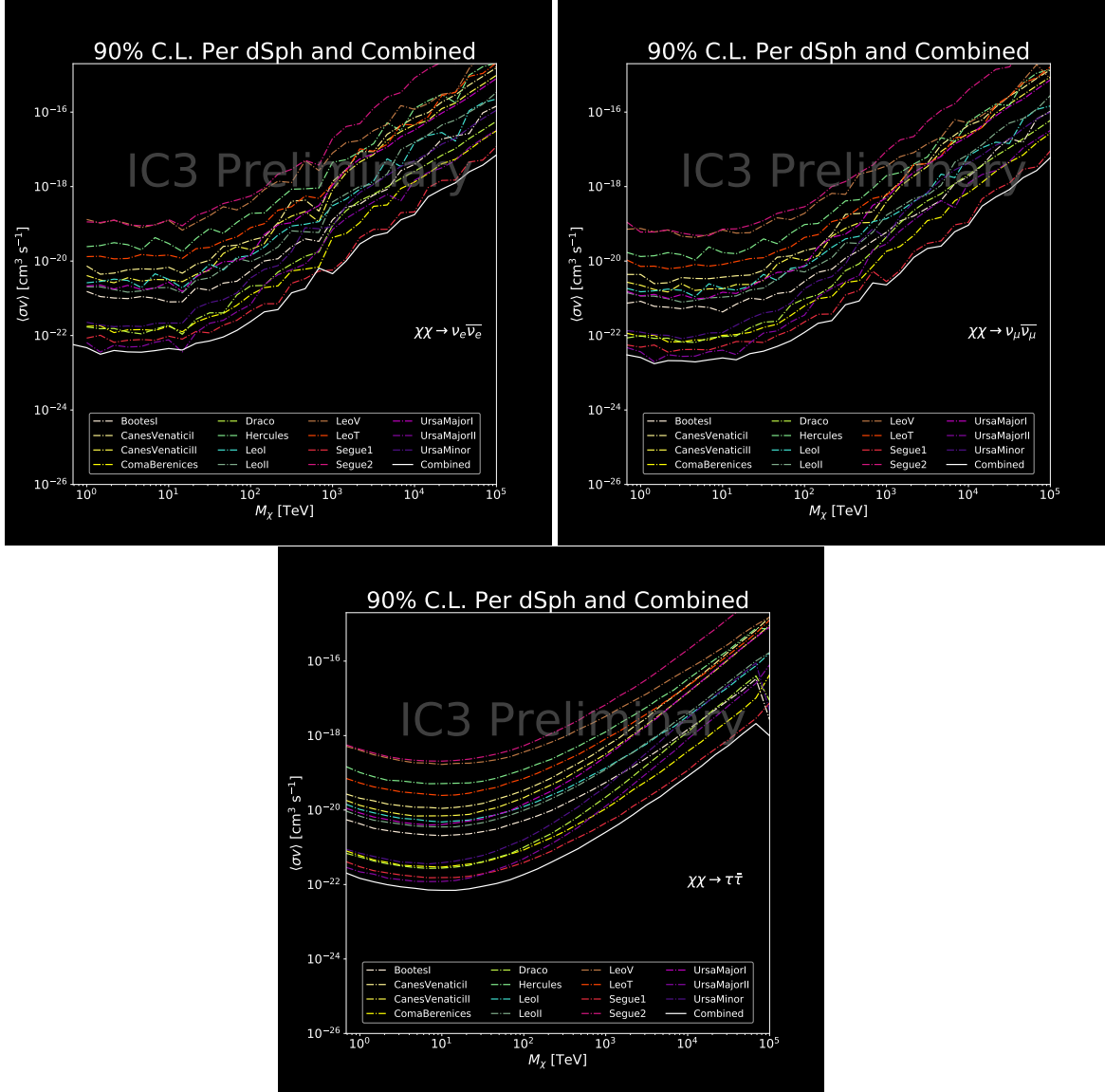


Figure 6.25 IceCube North Sky Track Sensitivities. Each panel shows sensitivity curves for various DM annihilation channels. Sensitivities are for the velocity-weighted cross-section  $\langle\sigma v\rangle$  versus  $m_\chi$ . Dotted, colored lines are sensitivities for individual sources. Solid white lines are for the combined sensitivity of all 15  $\mathcal{GS}$  sources used in this study.

For this systematic study, I sample 6 DM masses per decade from 681 GeV to 100 PeV. I select

declinations that are shared with sources in the  $\mathcal{GS}$  catalog: Boötes I, Canes Venatici II, Leo V,

Ursa Major I, and Ursa Minor. I study a fake source who's  $J$ -factor is shared with Ursa Major II,

but who's coordinates belong to the aforementioned list. The sensitivity studies performed for each

source (Fig. 6.25 and Section C.5) provided  $n_s$  for 1000 trials which we extracted from Eq. (6.8).

We derive  $\langle\sigma v\rangle$  using  $\log_{10} J = 19.42 \log_{10}(\text{GeV}^2 \text{cm}^{-5})$ . Figure 6.28 shows the results.

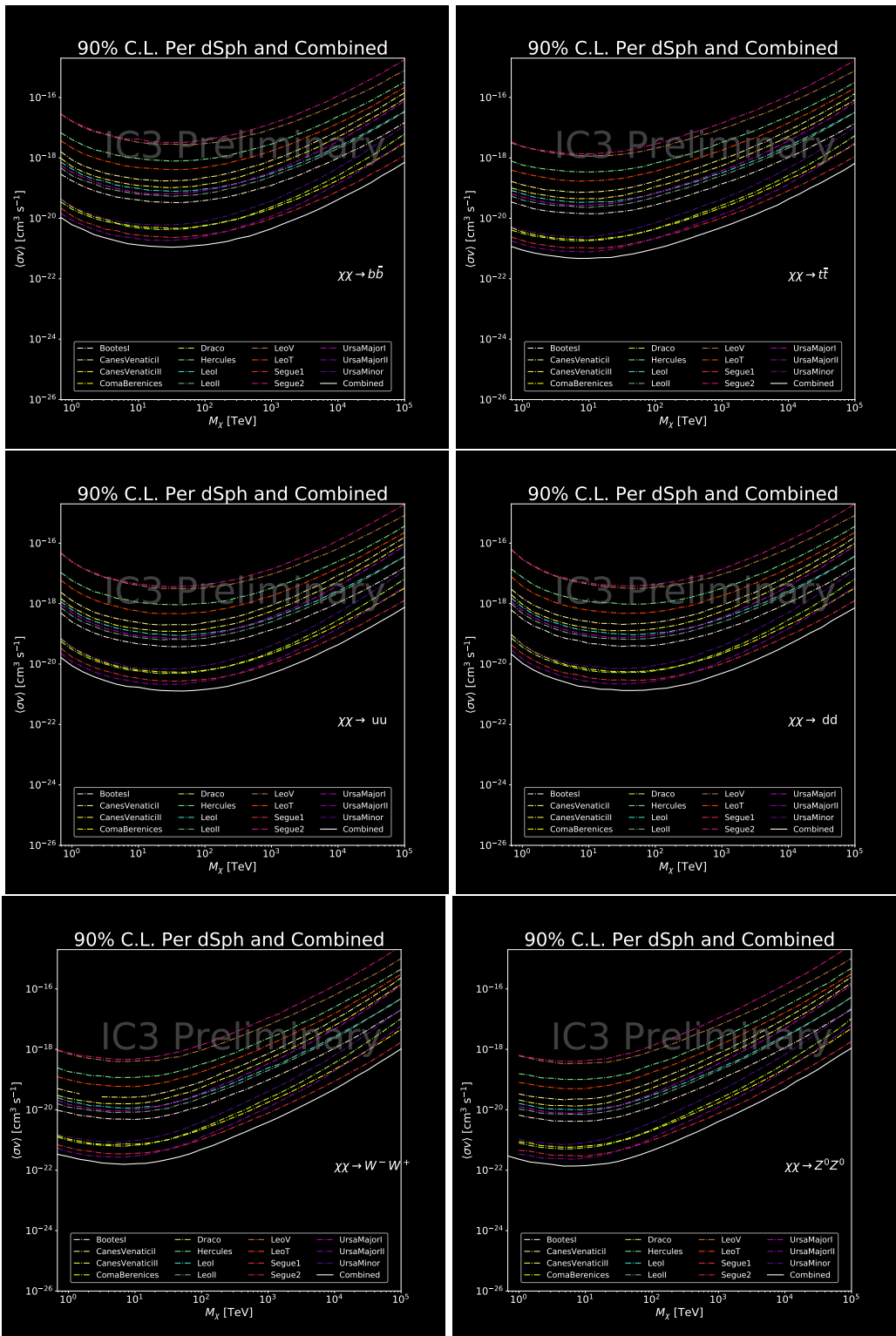


Figure 6.26 Same as Fig. 6.25 for three additional DM annihilation channels.

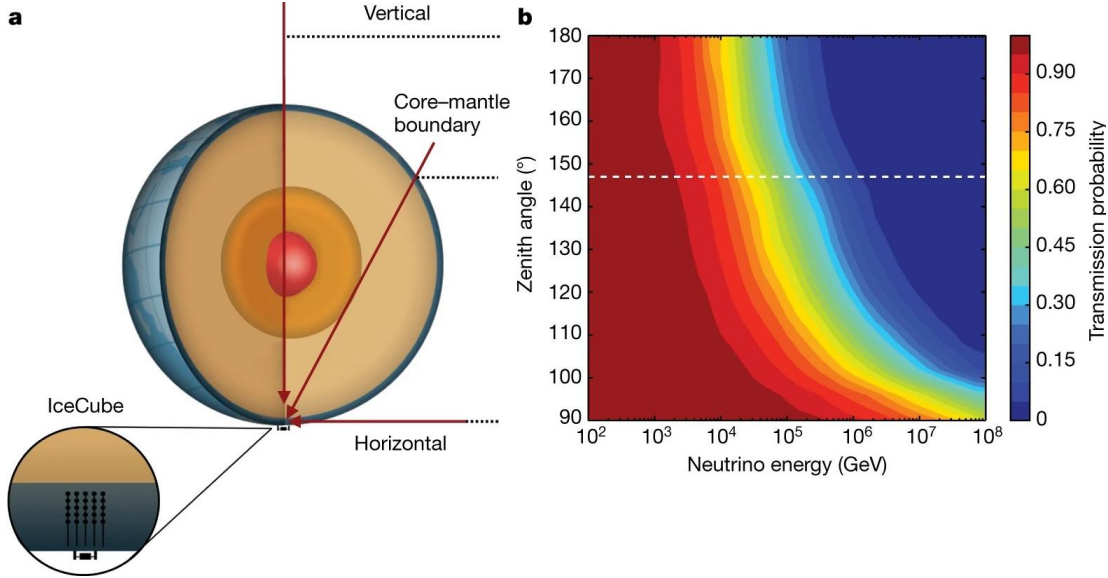


Figure 6.27 Panel A: Neutrino's from the Northern sky and incident on the IceCube detector will travel through the Earth. How much of the Earth these neutrinos travels is a function of zenith from the vertical axis. Panel B: SM prediction of neutrino transmission probabilities for neutrinos arriving at  $90^\circ - 180^\circ$  zenith and with 100 GeV to 100 PeV energies. High-energy neutrinos traversing the whole Earth are completely absorbed, whereas low-energy neutrinos pass through unimpeded. Neutrinos coming from above the horizon will arrive unimpeded for all neutrino energies. Figure pulled from [102].

2194     Figure 6.28 shows that we have significant but diminishing sensitivity to sources at high  
 2195     declination. We see in the worse case, the sensitivity at high declination is up to an order of  
 2196     magnitude worse than at low declination. However, for  $m_\chi < 1$  PeV, the sensitivities are very  
 2197     similar. The comparable sensitivities imply that a stacking analysis with IceCube is most powerful  
 2198     in the 500 GeV to 1 PeV region. Above 1 PeV, our limits and sensitivities are dominated by sources  
 2199     near the horizon. When we additionally consider the  $J$ -factors, we expect Segue 1 to dominate  
 2200     contributions to sensitivity and limits where  $m_\chi > 1$  PeV.

## 2201     6.8 Conclusions

2202     We utilized advanced computing techniques like parallel programming and spline fitting of  
 2203     particle physics Monte Carlo to greatly expand and refine IceCube's sensitivity to DM annihilation  
 2204     from dSphs. Furthermore, we imported updated astrophysical and particle physics models that  
 2205     better represent what we believe neutrino signals from DM annihilation should look like. We, for  
 2206     the first time, build an analysis that is sensitive to PeV DM annihilation.

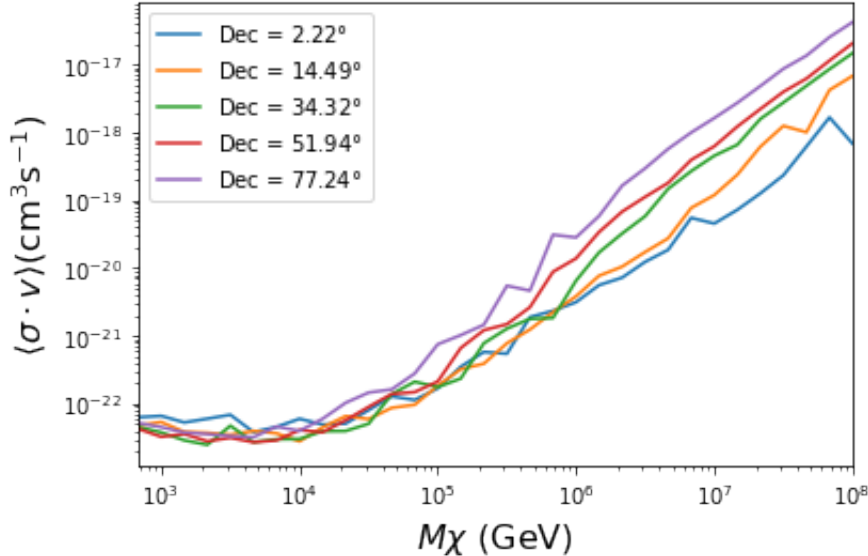


Figure 6.28  $\langle \sigma v \rangle$  sensitivities for 5 imaginary sources with  $\log_{10} J = 19.42$   $\log_{10}(\text{GeV}^2 \text{cm}^{-5})$ . Each imaginary source shares a declination with a source in Tab. 3.1

When we compare to previous IceCube publications of dSphs [93], we see an order of magnitude improvement to our sensitivity. This analysis has been working group approved within IceCube and is currently under collaboration review before unblinding. These processes did not complete in time for this dissertation. Therefore we do not show data for this thesis and is the clear next step.

The test statistic distributions in this analysis also demonstrate more characteristic behavior compared to previous DM analyses [97, 101]. With a 10-year dataset, we finally have enough statistics to almost trivially combine with other photon observatories, such as HAWC. The first groundwork for a multi-messenger DM search is provided with concluding remarks in chapter 7.

## CHAPTER 7

### NU DUCK: CONCLUSIONS AND FUTURE DIRECTIONS

#### 7.1 Conclusions

2216 **TODO: Chat GPT the shit of everything below** In this work, three analyses were performed  
2217 with data from the HAWC and IceCube observatories in order to explore some of the fundamental  
2218 questions in particle astrophysics. The goal was to contribute to the understanding of the sources of  
2219 cosmic rays, their acceleration mechanisms, and the nature of dark matter. The detection techniques  
2220 and reconstruction methods for both observatories were described, along with the properties that  
2221 make them ideal instruments to perform such searches.

2223 This dissertation used data from the HAWC detector to probe cutting-edge physics beyond  
2224 the Standard Model. The techniques by which HAWC is able to detect cosmic gamma rays were  
2225 demonstrated and the many advantages of HAWC in probing ultra-high energy gamma-ray physics  
2226 were detailed. It was shown how HAWC data can be used to explore unanswered questions such as  
2227 the nature of dark matter and the limits of Lorentz invariance. In particular, a search for evidence of  
2228 WIMP dark matter in the Milky Way Galactic Halo was performed. To accomplish this, simulations  
2229 of the dark matter density profile were combined with estimates of the HAWC sensitivity to dark  
2230 matter-like energy spectra. This allowed strong constraints on dark matter annihilation and decay  
2231 from the Galactic Halo to be derived that are insensitive to the large uncertainties arising from  
2232 systematics in the dark matter spatial distribution. Multi-hundred TeV photon spectra were also  
2233 significantly detected from HAWC sources within the Galactic Plane. These results lead to the  
2234 strongest constraints on Lorentz invariance violation to be published at the time of writing.

2235 The work of this dissertation was made possible by the ongoing development of new algorithms  
2236 and reconstruction techniques within the HAWC collaboration. Probing the Galactic Halo required  
2237 the creation of a novel background estimation technique that relied on HAWC's wide field of view  
2238 and strong ability to discriminate between gamma rays and cosmic rays. Meanwhile, the constraints  
2239 on Lorentz invariance violation were enabled by the improved energy resolution from a machine  
2240 learning technique. HAWC has recently completed a reprocessing of all archival data using an

updated set of algorithms that can lead to compelling follow-up work on these results. Combining the new background technique with the re-optimized energy estimators will allow for Galactic dark matter to be probed at even higher masses, as well as for analyses that require precise energy resolution such as gamma-ray line searches.

## 7.2 Future Directions: Multi-Messenger Dark Matter Search

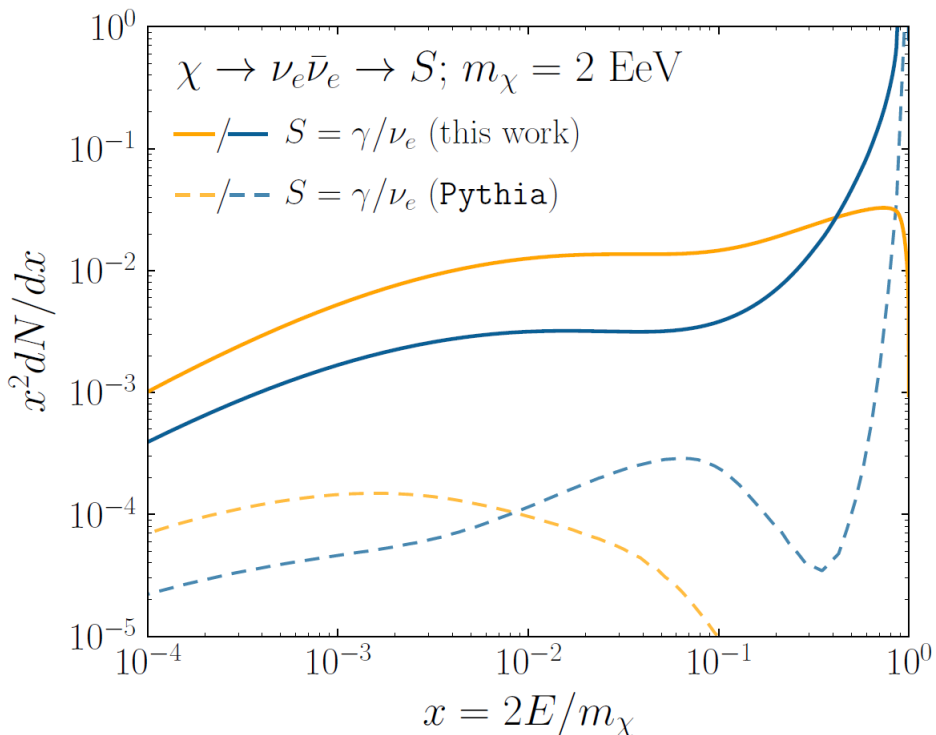


Figure 7.1 The prompt electron neutrino and photon spectrum resulting from the decay of a 2EeV DM particle to  $\nu_e \bar{\nu}_e$ , as currently being searched for at IceCube [5]. Solid curves represent the results of this work, and predict orders of magnitude more flux at certain energies than the dashed results of Pythia 8.2, one of the only existing methods to generate spectra at these masses. In both cases energy conservation is satisfied: there is a considerable contribution to a  $\delta$ -function at  $x = 1$ , associated with events where an initial W or Z was never emitted and thus no subsequent shower developed. Large disagreements are generically observed at these masses for electroweak dominated channels, while the agreement is better for colored initial SM states.

As I have shown previously in Sec. 3 and Sec. 4, we can build a fast and robust analysis that shares tools with the field. The hope being that IceCube can eventually combine data with gamma-ray observatories.



Figure 7.2 TODO: neutrino and bb plot with nu Sensitivities[NEEDS A SOURCE][FACT CHECK THIS]

## MULTI-EXPERIMENT SUPPLEMENTARY FIGURES

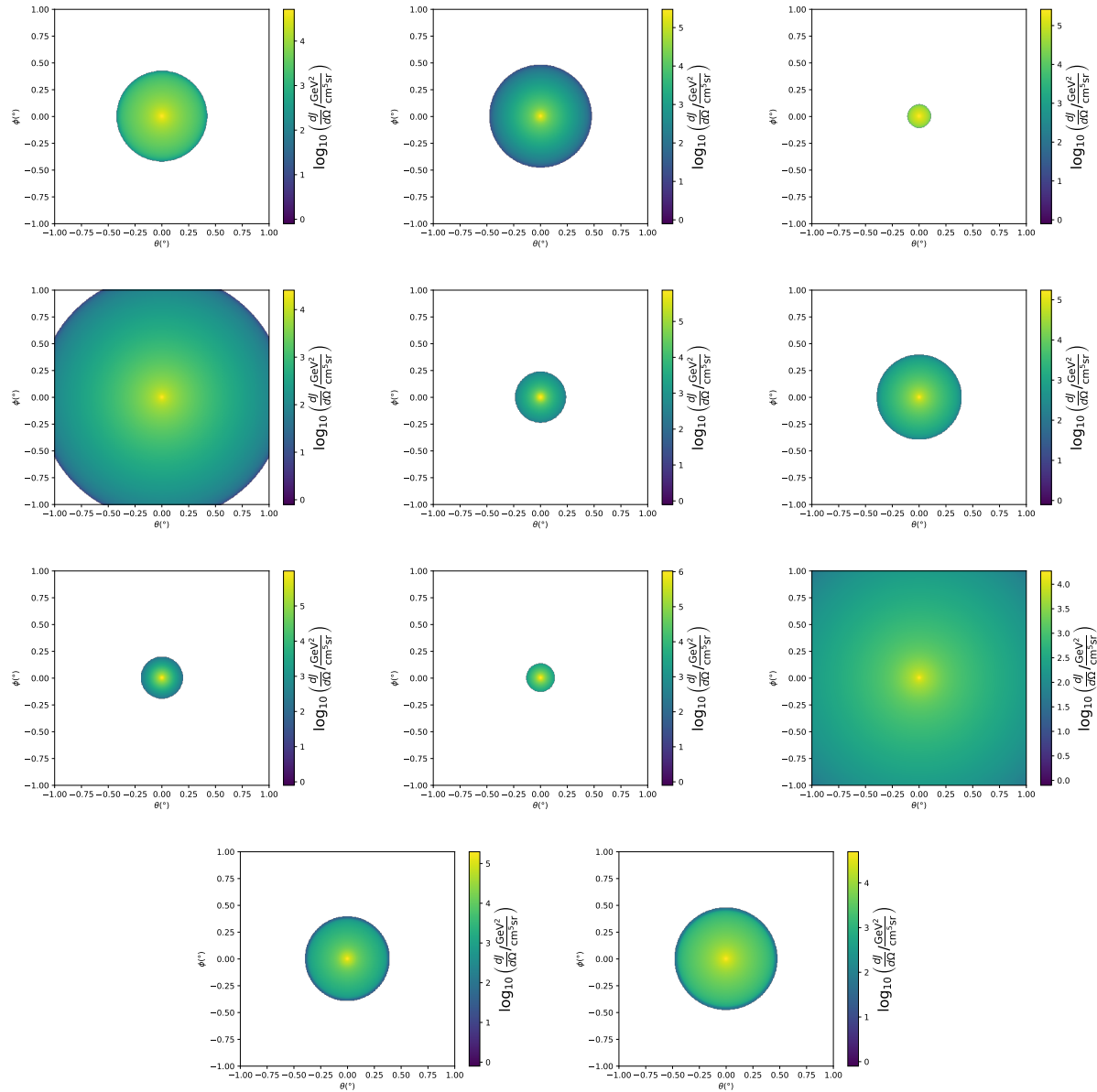


Figure A.1 Sister figure to Figure 3.3. Sources in the first row from left to right: Bootes I, Canes Venatici I, II. In second row: Draco, Hercules, Leo I. In the first row: Leo II, Leo IV, Sextans. In the final row: Ursa Major I, Ursa Major II.

## APPENDIX B

### 2250 MULTITHREADING DARK MATTER ANALYSES SUPPLEMENTARY MATERIAL

#### 2251 B.1 Remaining Spectral Models

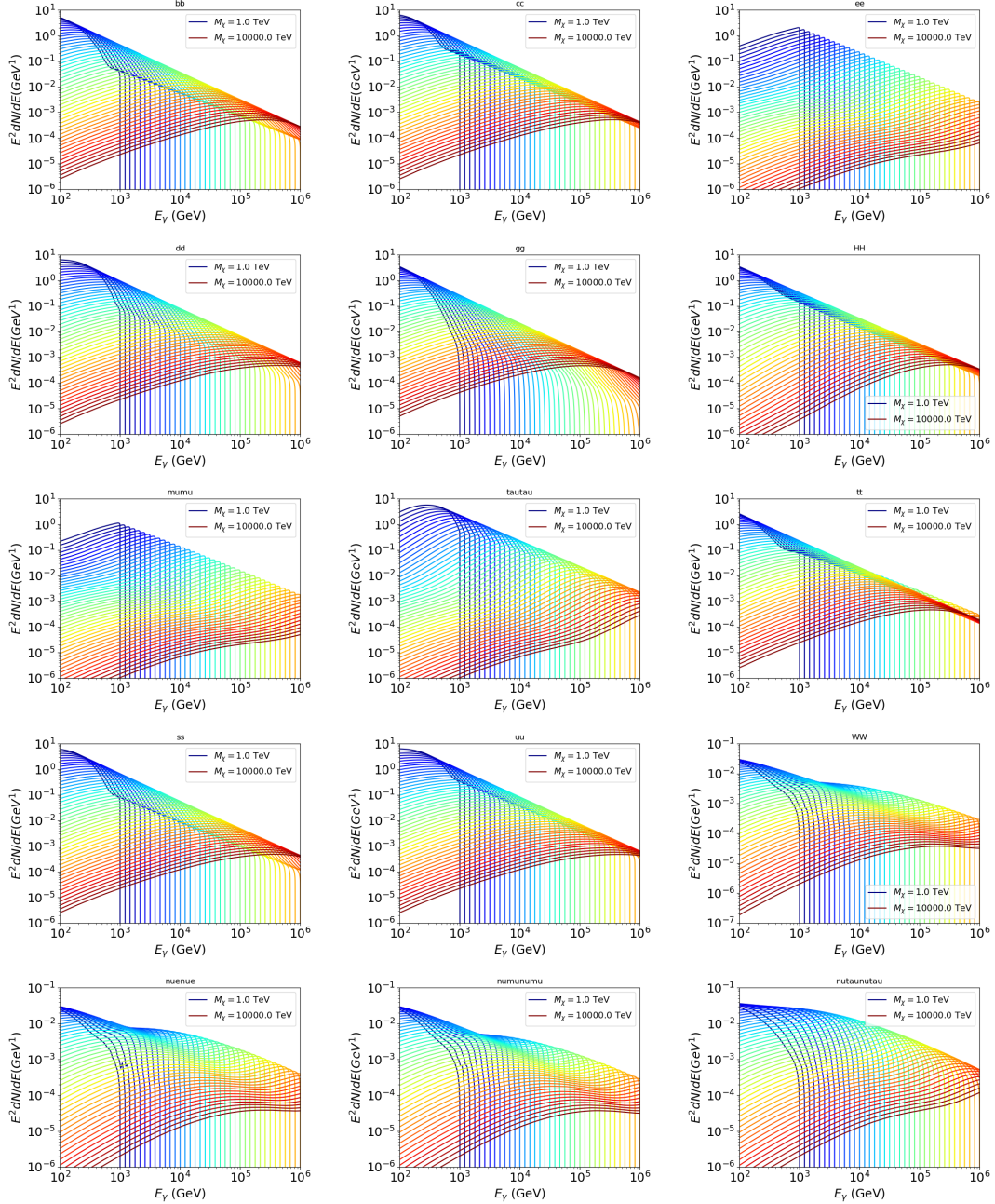


Figure B.1 Sister figure to Figure 4.2 for remaining SM primary annihilation channels studied for this thesis. These did not require any post generation smoothing and so are directly pulled from [79] with a binning scheme most helpful for a HAWC analysis.

## 2252 B.2 mpu\_analysis.py

```
2253 1 import warnings
2254 2 with warnings.catch_warnings():
2255 3     warnings.simplefilter("ignore")
2256 4 # Python base libraries
2257 5 import os
2258 6 import sys
2259 7 import time
2260 8 # Import general libraries with namespace
2261 9 import matplotlib
2262 10 # Necessary for computing on cluster
2263 11 matplotlib.use("agg")
2264 12 import numpy as np
2265 13 import multiprocessing as mp
2266 14 # Import HAWC software
2267 15 sys.path.insert(1, os.path.join(os.environ['HOME'], 'hawc_software', 'threeML-
2268 16     analysis-scripts', 'fitModel'))
2269 17 from analysis_modules import *
2270 18 from threeML import *
2271 19 from hawc_hal import HAL, HealpixConeROI
2272 20 from threeML.minimizer.minimization import FitFailed
2273 21 # Import Dark Matter HAWC Libraries
2274 22 import analysis_utils as au
2275 23 import spectra as spec
2276 24 import sources as srcs
2277 25
2278 26 #* READ ONLY PATHS This block will change eventually
2279 27 MASS_LIST = './plotting/studies/nd/masses.txt'
2280 28 CHAN_LIST = './plotting/studies/nd/chans.txt'
2281 29
2282 30 #* WRITE PATHS, default location is to scratch
2283 31 OUT_PATH = os.path.join(os.environ["SCRATCH"], os.environ["USER"], 'New_duck')
```

```

22841 print('Our out path is going to be {}'.format(OUT_PATH))
22852
22863 # Define parallel Function. Can also be run serially
22874 def some_mass_fit(sigVs, datalist, shape, dSph, jfactor, mass_chan,
22885                 progress=None, log_file='', queue=None, i_job=0):
22896
22907     if progress is None:
22918         progress = [0]
22929     else: # Create log files for each thread
22930         log_file = log_file.replace('.log', '_ThreadNo_')
22941         log_file = log_file + str(i_job) + ".log"
22952         sys.stdout = open(log_file, "w")
22963
22974     fits = []
22985
22996     try:
23007         for m_c in mass_chan:
23018             print(f'Mass chan tuple: {m_c}')
23029             mass = int(m_c[0])
23030             ch = m_c[1]
23041             # Build path to output files
23052             outPath = os.path.join(OUT_PATH, ch, dSph)
23063             au.ut.ensure_dir(outPath)
23074
23085             if progress[i_job] < 0:
23096                 # If the master gets a Keyboard interrupt, commit suicide.
23107                 break
23118
23129                 ### Start Model Building for DM mass and SM channel #####
23130                 spectrum = spec.DM_models.HDMSpectra()
23141                 spectrum.set_channel(ch)
23152
23163                 myDwarf = ExtendedSource(dSph, spatial_shape=shape,

```

```

23174                     spectral_shape=spectrum)

23185

23196     spectrum.J = jfactor * u.GeV**2 / u.cm**5
23207     spectrum.sigmav = 1e-24 * u.cm**3 / u.s
23218     spectrum.set_dm_mass(mass * u.GeV)

23229

23230     spectrum.sigmav.bounds = (1e-30, 1e-12)
23241     model = Model(myDwarf)
23252     ##### End model Building #####
23263
23274     jl = JointLikelihood(model, datalist, verbose=False)
23285
23296     try:
23307         result, lhdf = jl.fit(compute_covariance=False)
23318         ts = -2.* (jl.minus_log_like_profile(1e-30) - jl.
2332 _current_minimum)
23339         # Also profile the LLH vs sv
23340         ll = jl.get_contours(spectrum.sigmav, sigVs[0],
23351                         sigVs[-1], len(sigVs),
23362                         progress=False, log=['False'])
23373
23384         sigv_ll = au.ut.calc_95_from_profile(ll[0], ll[2])
23395         # Write results to file
23406         outFileLL = outPath+f"/LL_{dSph}_{ch}_mass{int(mass)}_GD.txt"
23417         np.savetxt(outFileLL, (sigVs, ll[2]),
23428                         delimiter='\t', header='sigV\tLL\n')
23439
23440         with open(outPath+f"/results_{dSph}_{ch}_mass{int(mass)}_GD.
2345 txt", "w") as results_file:
23461             results_file.write("mDM [GeV]\tsigV_95\tsigV_B.F.\n")
23472
23483             results_file.write("%i\t%.5E\t%.5E\t%.5E"%(mass, sigv_ll,
23494                                         ts, result.value[0]))

```

```

23505         # End write to file
23516     except FitFailed: # Don't kill all threads if a fit fails
23527         print("Fit failed. Go back and calculate this spectral model
2353 later")
23548         fits.append((ch, mass, -1, -1))
23559         with open(log_file+'.fail', 'w') as f_file:
23560             f_file.write(f'{ch}, {mass}\n')
23571
23582         progress[i_job] += 1
23593         matplotlib.pyplot.close() # Prevent leaky memory
23604
23615         fits.append((ch, mass, result.value[0], ts))
23626         progress[i_job] += 1
23637         matplotlib.pyplot.close()
23648     except KeyboardInterrupt:
23659         progress[i_job] = -1
23660
23671     fits = np.array(fits)
23682     if queue is None:
23693         return fits
23704     else:
23715         queue.put((i_job, fits))
23726
23737 def main(args):
23748     masses = np.loadtxt(MASS_LIST, dtype=int)
23759     chans = np.loadtxt(CHAN_LIST, delimiter=',', dtype=str)
23760     mass_chan = au.ut.permute_lists(chans, masses)
23771
23782     print(f"DM masses for this study are: {masses}")
23793     print(f"SM Channels for this study are XX -> {chans}")
23804     print(mass_chan)
23815
23826 # extract information from input argument

```

```

23837 dSph = args.dSph
23848 data_mngr = au.ut.Data_Selector('P5_NN_2D')
23859 dm_profile = srcts.Spatial_DM(args.catalog, dSph, args.sigma, args.decay)
23860
23871     ### Extract Source Information ####
23882 if dm_profile.get_dec() < -22.0 or dm_profile.get_dec() > 62.0:
23893     raise ValueError("HAWC can't see this source D: Exitting now...")
23904
23915 print(f'{dSph} information')
23926 print(f'jfac: {dm_profile.get_factor()}\tRA: {dm_profile.get_ra()}\tDec: {dm_profile.get_dec()}\n')
23947
23958 shape = SpatialTemplate_2D(fits_file=dm_profile.get_src_fits())
23969     ### Finish Extract Source Information ####
23970
23981     ### LOAD HAWC DATA ####
23992 roi = HealpixConeROI(data_radius=2.0, model_radius=8.0,
24003                         ra=dm_profile.get_ra(), dec=dm_profile.get_dec())
24014 bins = choose_bins.analysis_bins(args, dec=dm_profile.get_dec())
24025
24036 hawc = HAL(dSph, data_mngr.get_datmap(), data_mngr.get_detres(), roi)
24047 hawc.set_active_measurements(bin_list=bins)
24058 datalist = DataList(hawc)
24069     ### FINISH LOAD HAWC DATA ####
24070
24081 # set up SigV sampling. This sample is somewhat standardized
24092 sigVs = np.logspace(-28,-18, 1001, endpoint=True) # NOTE This will change
2410 with HDM
24113
24124 if args.n_threads == 1:
24135     # No need to start || programming just iterate over the masses
24146     kw_arg = dict(sigVs=sigVs, datalist=datalist, shape=shape, dSph=dSph,
24157                     jfactor=dm_profile.get_factor(), mass_chan=mass_chan,

```

```

24168                 log_file=args.log)
24169             some_mass_fit(**kw_arg)
24180         else:
24191             # I Really want to suppress TQMD output
24202             from tqdm import tqdm
24213             from functools import partialmethod
24224             tqdm.__init__ = partialmethod(tqdm.__init__, disable=True)
24235
24246             x = np.array_split(mass_chan, args.n_threads)
24257             n_jobs = len(x)
24268
24279             print("Thread jobs summary by mass and SM channel")
24280             for xi in x:
24291                 print(f'{xi}')
24302
24313             queue = mp.Queue()
24324             progress = mp.Array('i', np.zeros(n_jobs, dtype=int))
24335
24346             # Define task pool that will be split amongsts threads
24357             kw_args = [dict(sigVs=sigVs, datalist=datalist, shape=shape,
24368                             dSph=dSph, jfactor=dm_profile.get_factor(),
24379                             mass_chan=mass_chan, progress=progress,
24380                             queue=queue, i_job=i, log_file=args.log)
24391                 for i, mass_chan in enumerate(x)]
24402
24413             # Define each process
24424             procs = [mp.Process(target=some_mass_fit, kwargs=kw_args[i]) \
24435                 for i in range(n_jobs)]
24446
24457             ### Start MASTER Thread only code block ###
24468             # Begin running all child threads
24479             for proc in procs: proc.start()
24480

```

```

24491     try:
24502         # In this case, the master does nothing except monitor progress of
2451         the threads
24523         # In an ideal world, the master thread also does some computation.
24534         n_complete = np.sum(progress)
24545         while_count = 0
24556
24567         while n_complete < len(mass_chan):
24578
24589             if np.any(np.asarray(progress) < 0):
24590                 # This was no threads are stranded when killing the script
24601                 raise KeyboardInterrupt()
24612             if while_count%1000 == 0:
24623                 print(f"{np.sum(progress)} of {len(mass_chan)} finished")
24634
24645             n_complete = np.sum(progress)
24656             time.sleep(.25)
24667             while_count += 1
24678
24689         except KeyboardInterrupt:
24690             # signal to jobs that it's time to stop
24701                 for i in range(n_jobs):
24712                     progress[i] = -2
24723                     print('\nKeyboardInterrupt: terminating early.')
24734             ### End MASTER Thread only code block ###
24745
24756             fitss = [queue.get() for proc in procs]
24767             print(fitss)
24778             print(f'Thread statuses: {progress[:]}')
24789
24790             # putting results in a file
24801
24812             print("QUACK! All Done!")

```

```

24823
24834
24845 if __name__ == '__main__':
24856     import argparse
24867
24878     p = argparse.ArgumentParser(description="Run a DM annihilation analysis on
2488         a dwarf spheroidal for a specific SM channel for DM masses [1 TeV to 10
2489         PeV]")
24909
24910     # Dwarf spatial modeling arguements
24921     p.add_argument("-ds", "--dSph", type=str,
24932                     help="dwarf spheroidal galaxy to be studied", required=
2494     True)
24953     p.add_argument("-cat", "--catalog", type=str, choices=['GS15', 'LS20'],
24964                     default='LS20', help="source catalog used")
24975     p.add_argument("-sig", "--sigma", type=int, choices=[-1, 0, 1], default=0,
24986                     help="Spatial model uncertainty. 0 corresponds to the
2499 median. +/-1 correspond to the +/-1sigma uncertainty respectively.")
25007
25018     # Arguements for the energy estimators
25029     p.add_argument("-e", "--estimator", type=str,
25030                     choices=['P5_NHIT', 'P5_NN_2D'],
25041                     default="P5_NN_2D", required=False,
25052                     help="The energy estimator choice. Options are: P5_NHIT,
2506 P5_NN_2D. GP not supported (yet).")
25073     p.add_argument("--use-bins", default=None, nargs="*",
25084                     help="Bins to use for the analysis", dest="use_bins")
25095     p.add_argument('--select_bins_by_energy', default=None, nargs="*",
25106                     help="Does nothing. May fill in later once better
2511 understood")
25127     p.add_argument('--select_bins_by_fhit', default=None, nargs="*",
25138                     help="Also does nothing see above")
25149     p.add_argument( '-ex', '--exclude', default=None, nargs="*",

```

```

25150         help="Exclude Bins", dest="exclude")

25161

25172 # Computing and logging arguements.

25183 p.add_argument('-nt', '--n_threads', type=int, default=1,
25194                 help='Maximum number of threads spawned by script. Default
2520      is 4')

25215 p.add_argument('-log', '--log', type=str, required=True,
25226                 help='Name for log files. Especially needed for threads')

25237

25248 p.add_argument('--decay', action="store_true",
25259                 help='Set spectral DM hypothesis to decay')

25260

25271 args = p.parse_args()

25282 print(args.decay)

25293 if args.exclude is None: # default exclude bins 0 and 1
25304     args.exclude = ['B0C0Ea', 'B0C0Eb', 'B0C0Ec', 'B0C0Ed', 'B0C0Ee']

25315

25326 if args.decay: OUT_PATH += '_dec'
25337 else: OUT_PATH += '_ann'

25348

25359 OUT_PATH = OUT_PATH + '_' + args.catalog
25360 if args.sigma != 0: OUT_PATH += f'_{args.sigma}sig'

25371

25382 main(args)

```

2539 B.3 Comparison with Glory Duck

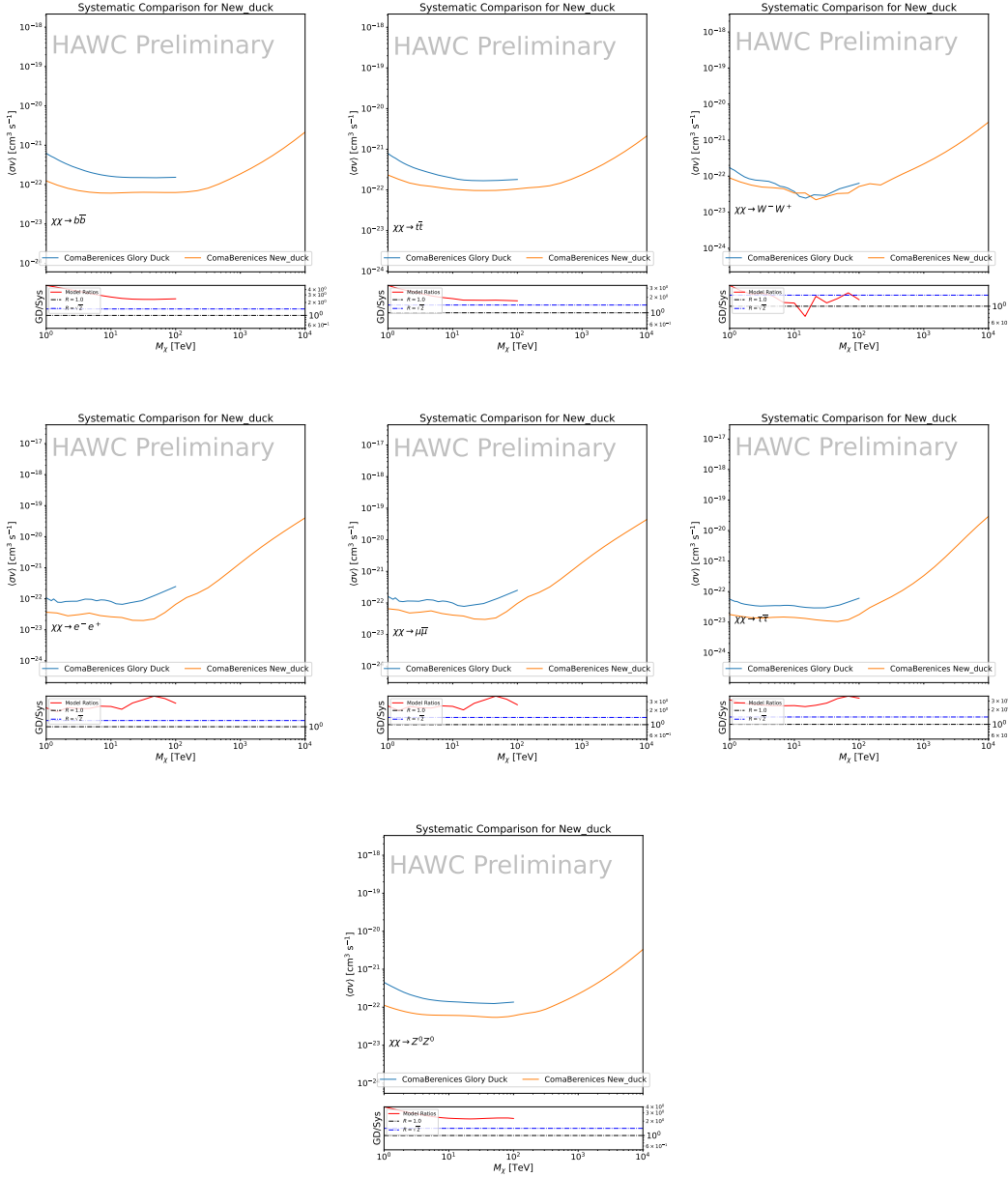


Figure B.2 Comparison of HAWC limits from this analysis to Glory Duck (Fig. 3.5) for Coma Berenices and 7 DM annihilation channels.

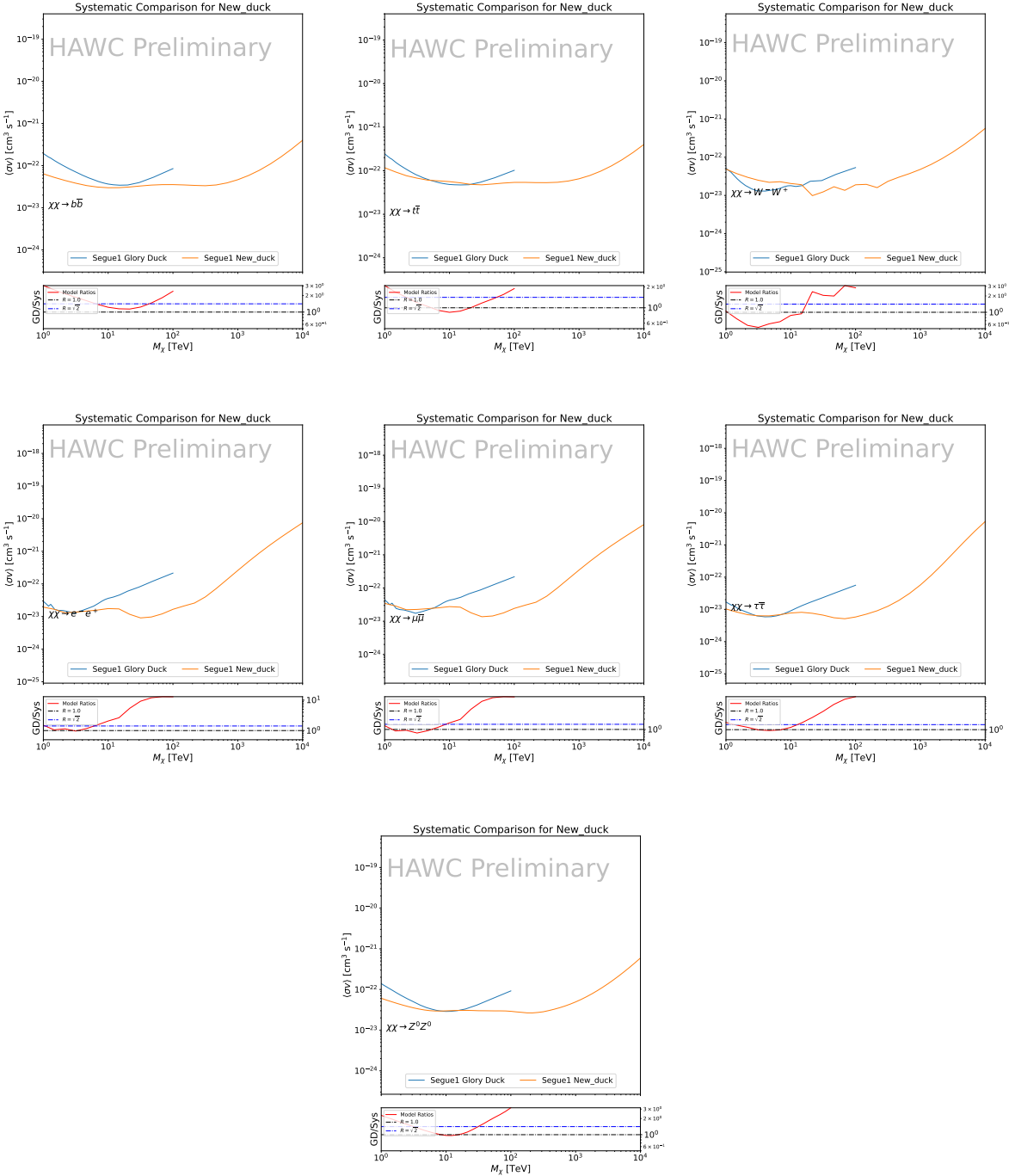


Figure B.3 Same as Fig. B.2 but for Segue 1.

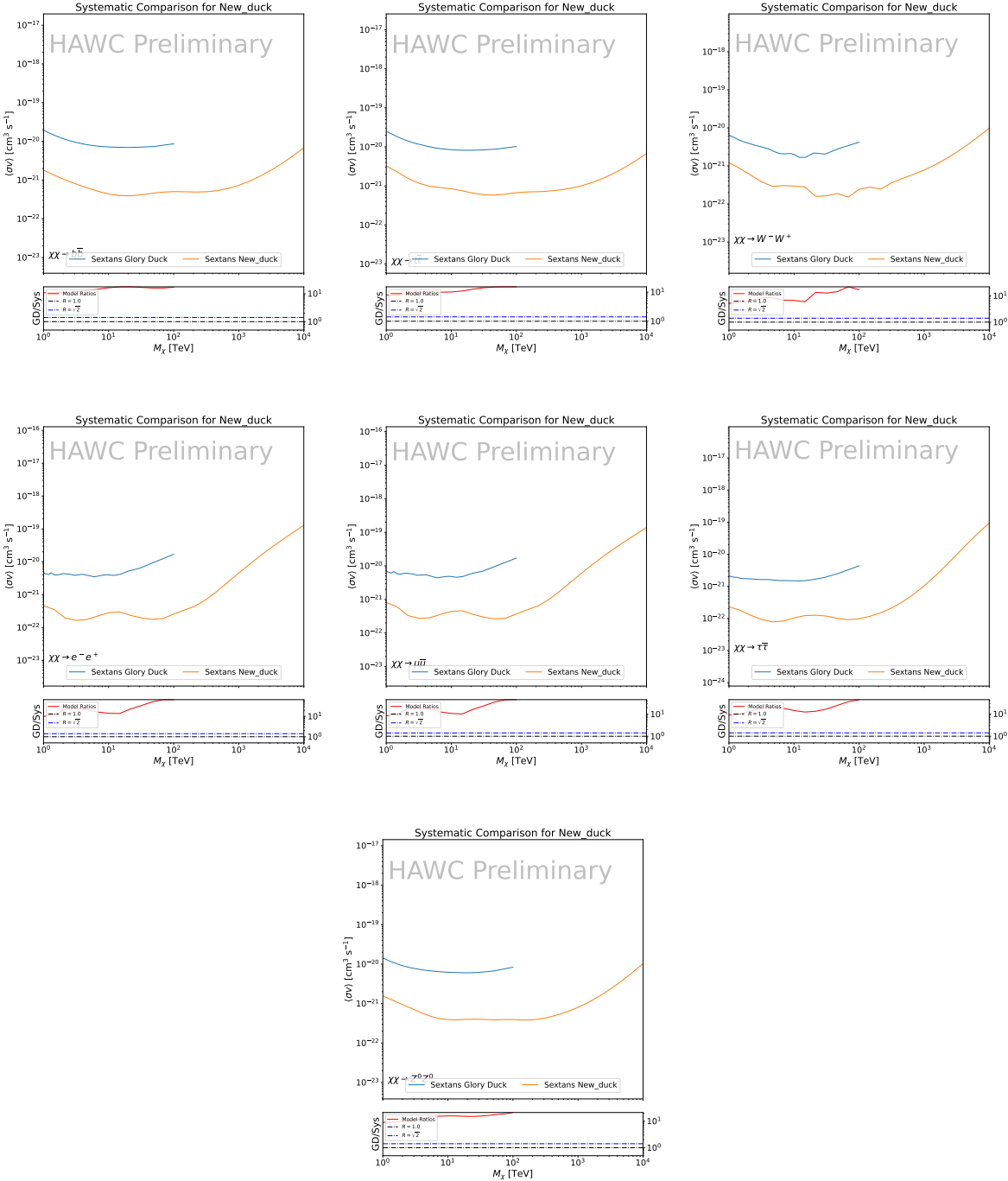


Figure B.4 Same as Fig. B.2 but for Sextans.

## APPENDIX C

### 2540 ICECUBE HEAVY DARK MATTER ANALYSIS SUPPLEMENTARY MATERIAL

#### 2541 C.1 Docker Image for Oscillating Neutrino Spectra

```
25421 FROM ubuntu:18.04
25432
25443 # Execute commands to install software packages
25454 RUN apt -y update
25465
25476     # Install utility programs
25487 RUN apt -y install vim wget git cmake
25498
25509 ARG DEBIAN_FRONTEND=noninteractive
25510
25521     # Install python
25532 RUN apt -y install python python-dev python-pip libjpeg-dev zlib1g-dev
25543
25554     # We need Python2 for installing Charon.
25565 RUN apt -y install python-numpy python-sympy python-matplotlib \
25576             python-sympy python-h5py python-astropy python-ipython
25587
25598     # Install dependencies of Charon : SQuIDS, NuSQuIDS
25609 RUN apt -y install libgsl-dev libgslcblas0 libgsl23 gsl-bin pkg-config
25610     # Install SQuIDS
25621 RUN mkdir /home/SQuIDS /home/SQuIDS_install
25632 WORKDIR /home/SQuIDS
25643 RUN git clone https://github.com/jsalvado/SQuIDS.git
25654 WORKDIR /home/SQuIDS/SQuIDS
25665 RUN git checkout 7ad9ba7c6ad06d1f0fa8418f937ebf1a403fef90
25676     # Before executing "make install" an environmental variable has to be set.
25687 ENV PKG_CONFIG_PATH=/home/SQuIDS/SQuIDS/lib
25698 RUN ./configure --prefix=../SQuIDS_install \
```

```

25709    && make
25710 RUN make install
25721
25732 # Set up an environmental variable that is required to install nuSQuIDS..
25743 ENV SQuIDS=/home/SQuIDS/SQuIDS
25754 ENV LD_LIBRARY_PATH=$SQuIDS/lib:$LD_LIBRARY_PATH
25765
25776 # Install NuSQuIDS
25787 RUN mkdir /home/nuSQuIDS
25798 WORKDIR /home/nuSQuIDS
25809 RUN git clone https://github.com/qrliu/nuSQuIDS.git
25810 WORKDIR /home/nuSQuIDS/nuSQuIDS
25821 RUN git checkout 072d8ef740e2fc7330f1fabaea94f0f4540c46f9
25832 RUN apt -y install libhdf5-dev hdf5-tools
25843 RUN apt -y install libboost1.65-all-dev
25854 RUN ./configure --with-squids=$SQuIDS --with-python-bindings --prefix=../
2586     nuSQuIDS_install \
2587     && make \
25886     && make install
25897
25908 # Set up an environmental variable for nuSQuIDS.
25919 ENV nuSQuIDS=/home/nuSQuIDS/nuSQuIDS
25920 ENV LD_LIBRARY_PATH=$nuSQuIDS/lib:$LD_LIBRARY_PATH
25931
25942 # Build the python bindings
25953 WORKDIR /home/nuSQuIDS/nuSQuIDS/resources/python/src
25964 RUN make
25975
25986 # Set up an environmental variable for the python bindings.
25997 ENV PYTHONPATH=$nuSQuIDS/resources/python/bindings/:$PYTHONPATH
26008
26019 # Install Charon in the /home/Charon/charon directory.
26020 RUN mkdir /home/Charon

```

```
26031 WORKDIR /home/Charon
26042 RUN git clone https://github.com/icecube/charon.git \
26053   && apt -y install unzip python-scipy
26064 WORKDIR charon
26075 RUN git checkout c531efe4e01dc364a60d1c83f950f04526ccd771
26086 RUN unzip ./charon/xsec/xsec.zip -d charon/xsec/ \
26097
26108 # Download neutrino spectra tables in the /home/Charon/charon/data directory
26111 .
26129   && mkdir ./charon/data
26130 WORKDIR ./charon/data
26141 RUN wget --no-check-certificate https://icecube.wisc.edu/~qliu/charon/
2615     SpectraEW.hdf5 \
26162   && wget --no-check-certificate https://icecube.wisc.edu/~qliu/charon/
2617     Spectra_PYTHIA.hdf5 \
26183   && wget --no-check-certificate https://icecube.wisc.edu/~qliu/charon/
2619     Spectra_noEW.hdf5
26204
26215 WORKDIR ../..
26226 RUN python setup.py install
26237 WORKDIR /home
```

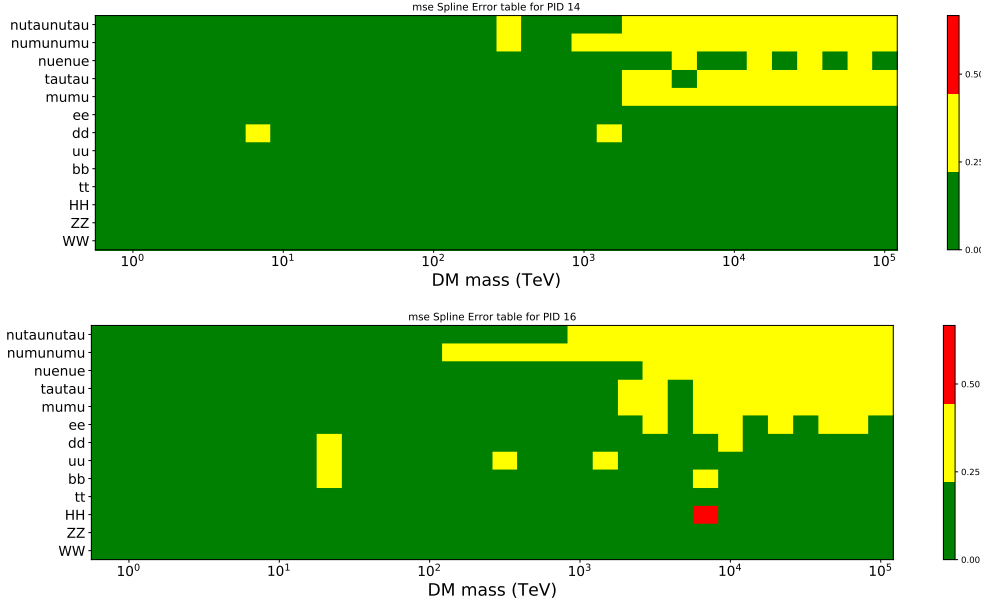


Figure C.1 Current status of spline tables according to constraints defined by Tab. 6.1. Green splines are splines that passed under the GOOD tolerance. Yellow are splines that are OK. Red are splines that FAIL. All yellow splines were inspected individually before running the analysis. Splines were made for the  $\mu$  (PID 14; top panel) flavor and  $\tau$  (PID 16; bottom panel) neutrino flavors.

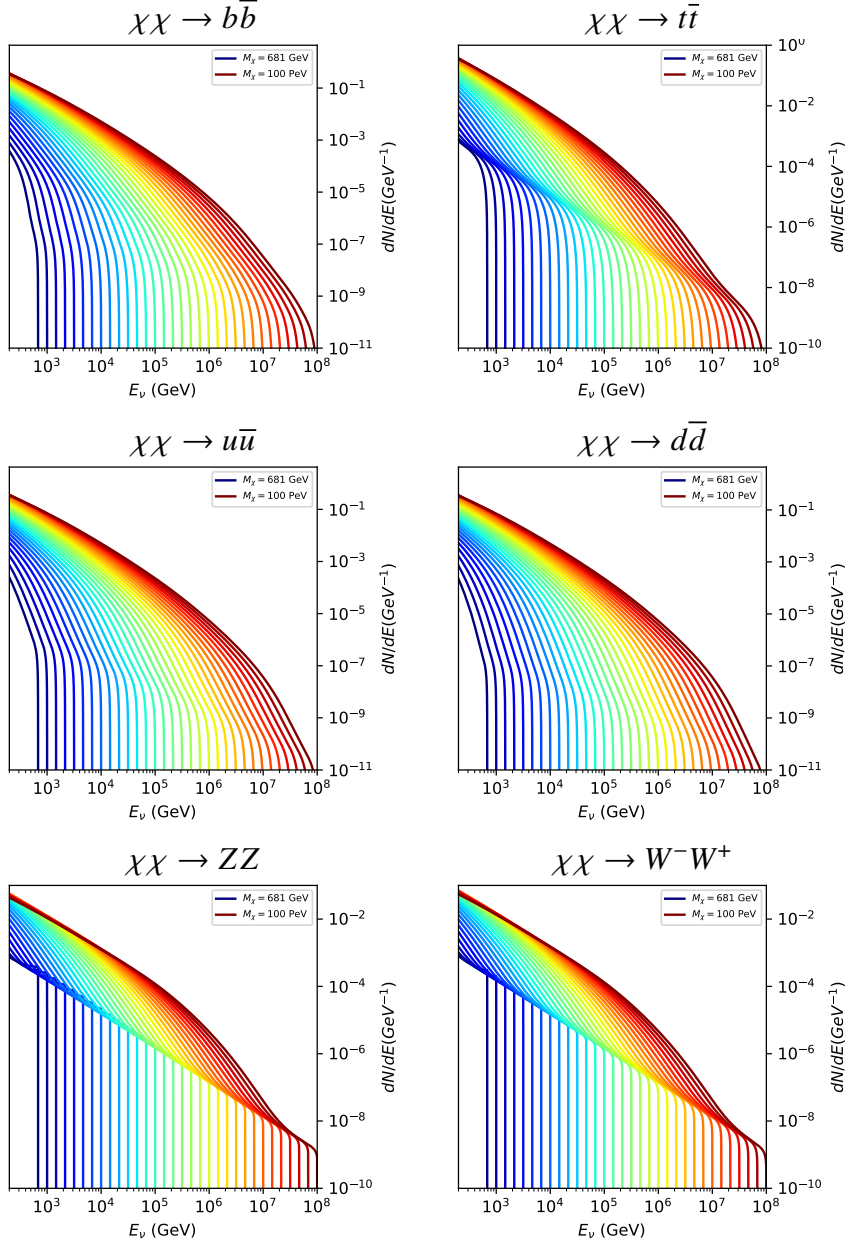


Figure C.2 Sister figure to Fig. 6.5 for annihilation channels that did not require kernel smoothing. These spectra are the composite ( $\nu_\mu + \nu_\tau$ ) of neutrino flavors. Every spectral model used for this analysis is featured as a colored solid line. Bluer lines are for lower DM mass spectral models. DM masses range from 681 GeV to 100 PeV.

2626 C.4 Segue 1 And Ursa Major II Signal Recovery

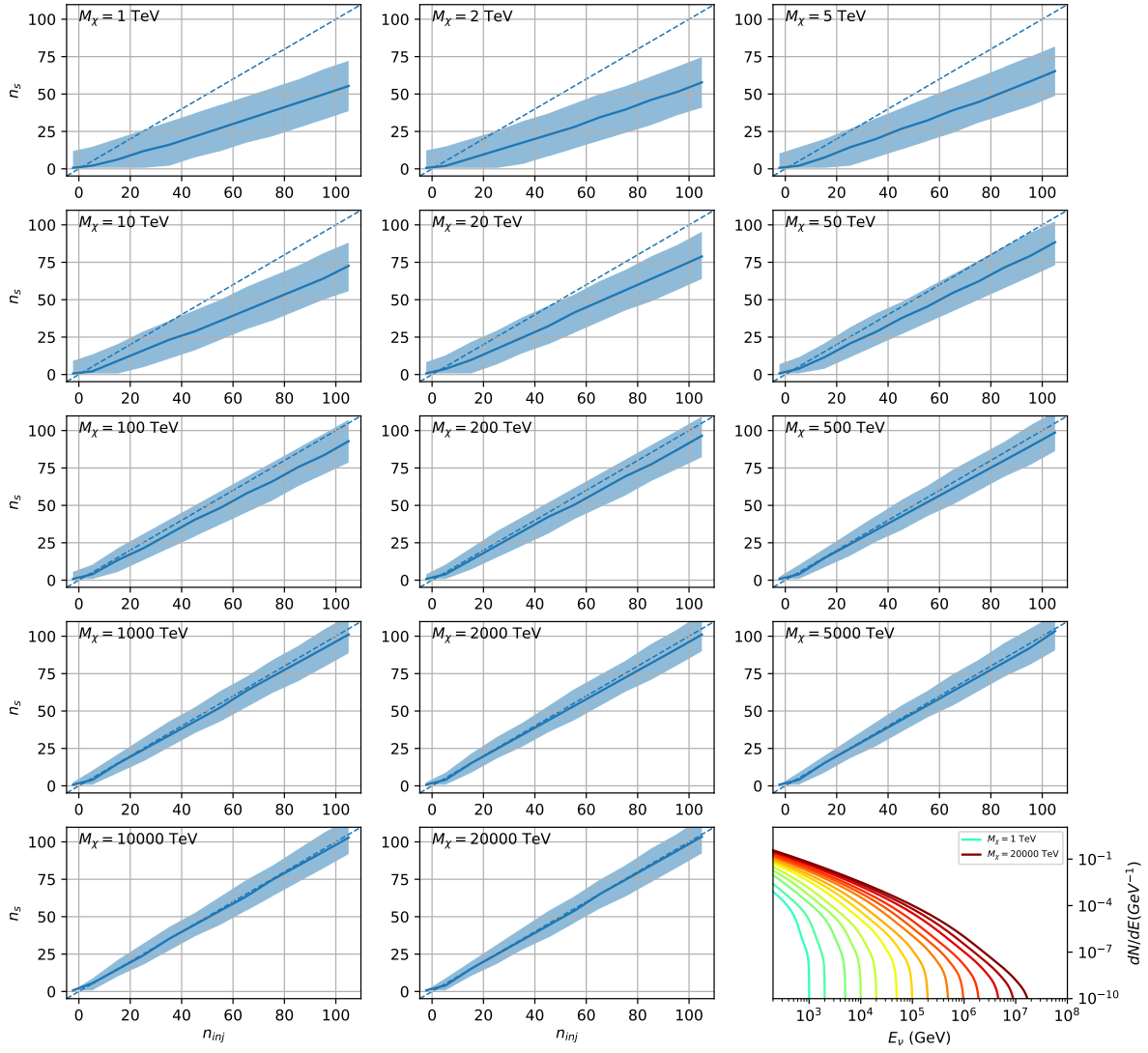


Figure C.3 Same as Fig. 6.23 but for Segue 1 and  $\chi\chi \rightarrow b\bar{b}$ .

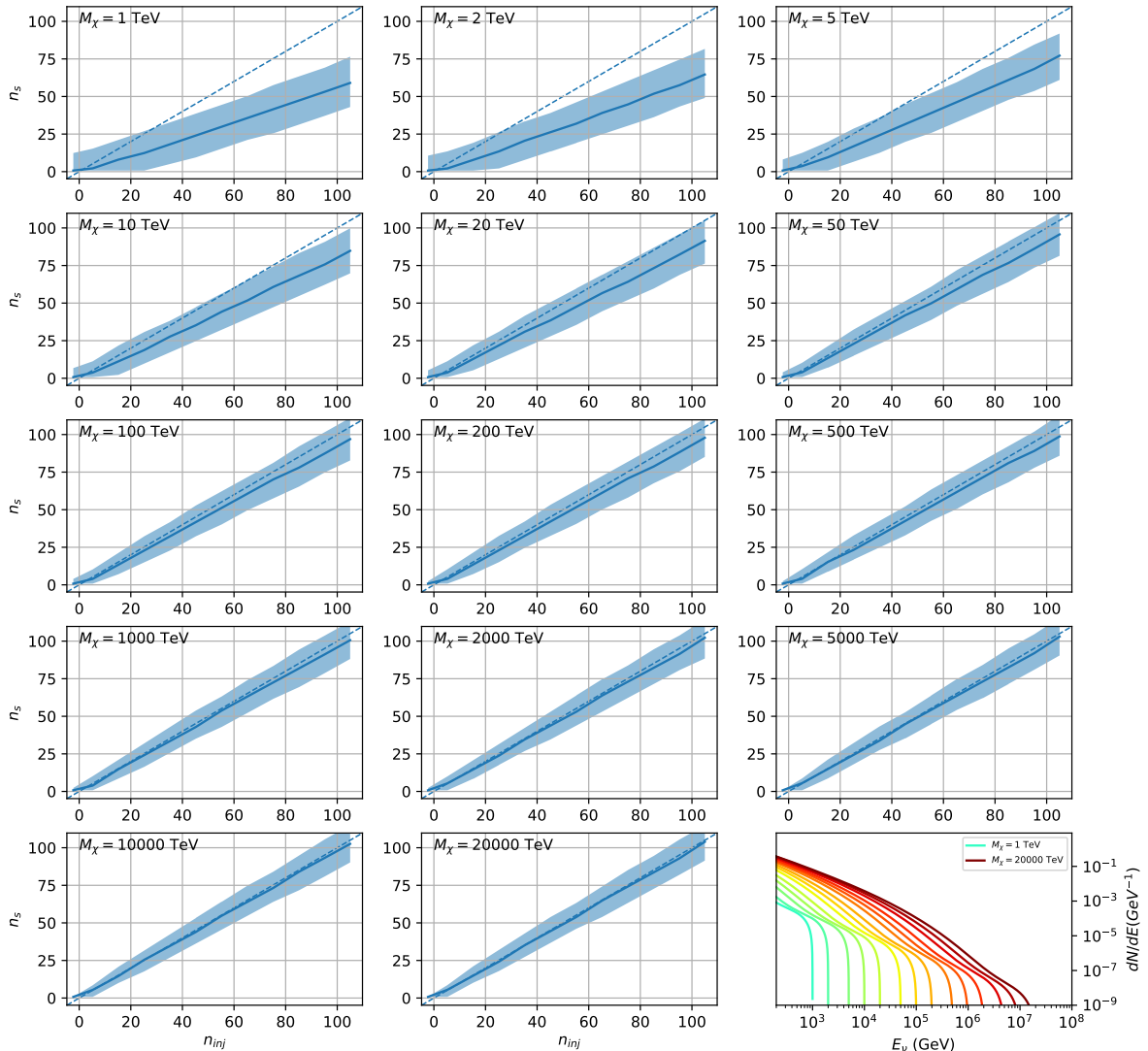


Figure C.4 Same as Fig. 6.23 but for Segue 1 and  $\chi\chi \rightarrow t\bar{t}$ .

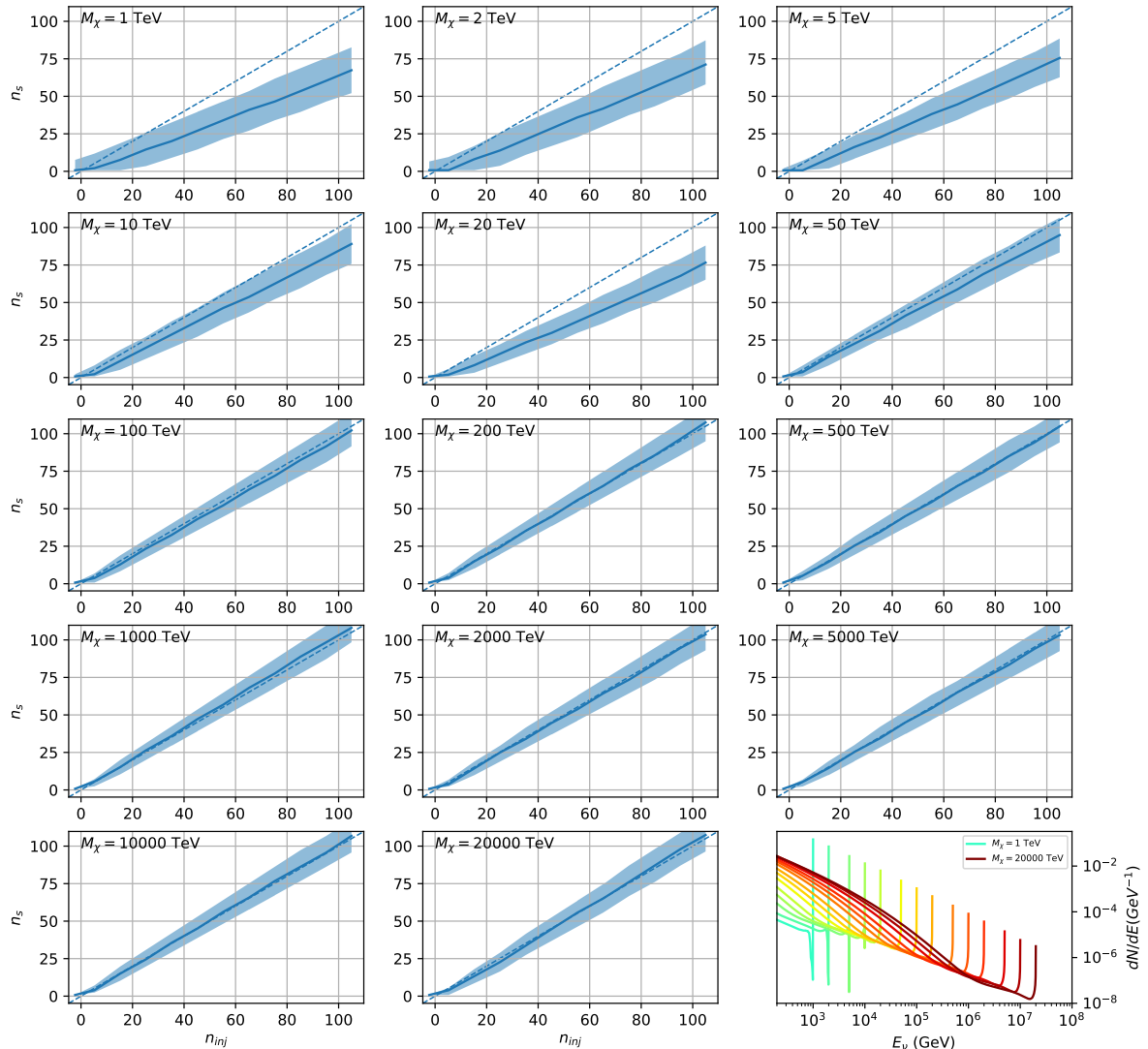


Figure C.5 Same as Fig. 6.23 but for Segue 1 and  $\chi\chi \rightarrow \nu_\mu \bar{\nu}_\mu$ .

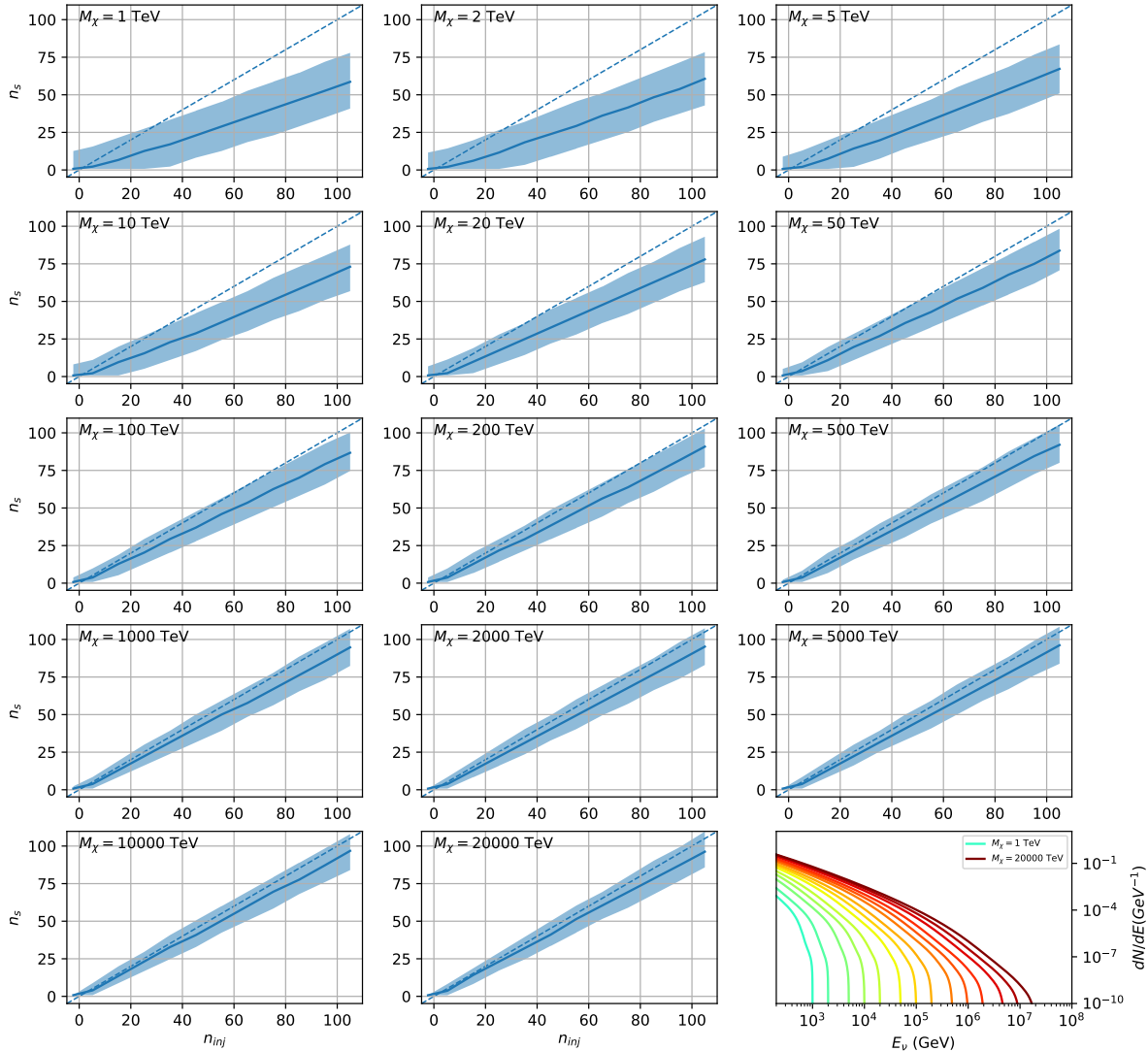


Figure C.6 Same as Fig. 6.23 but for Ursa Major II and  $\chi\chi \rightarrow b\bar{b}$ .

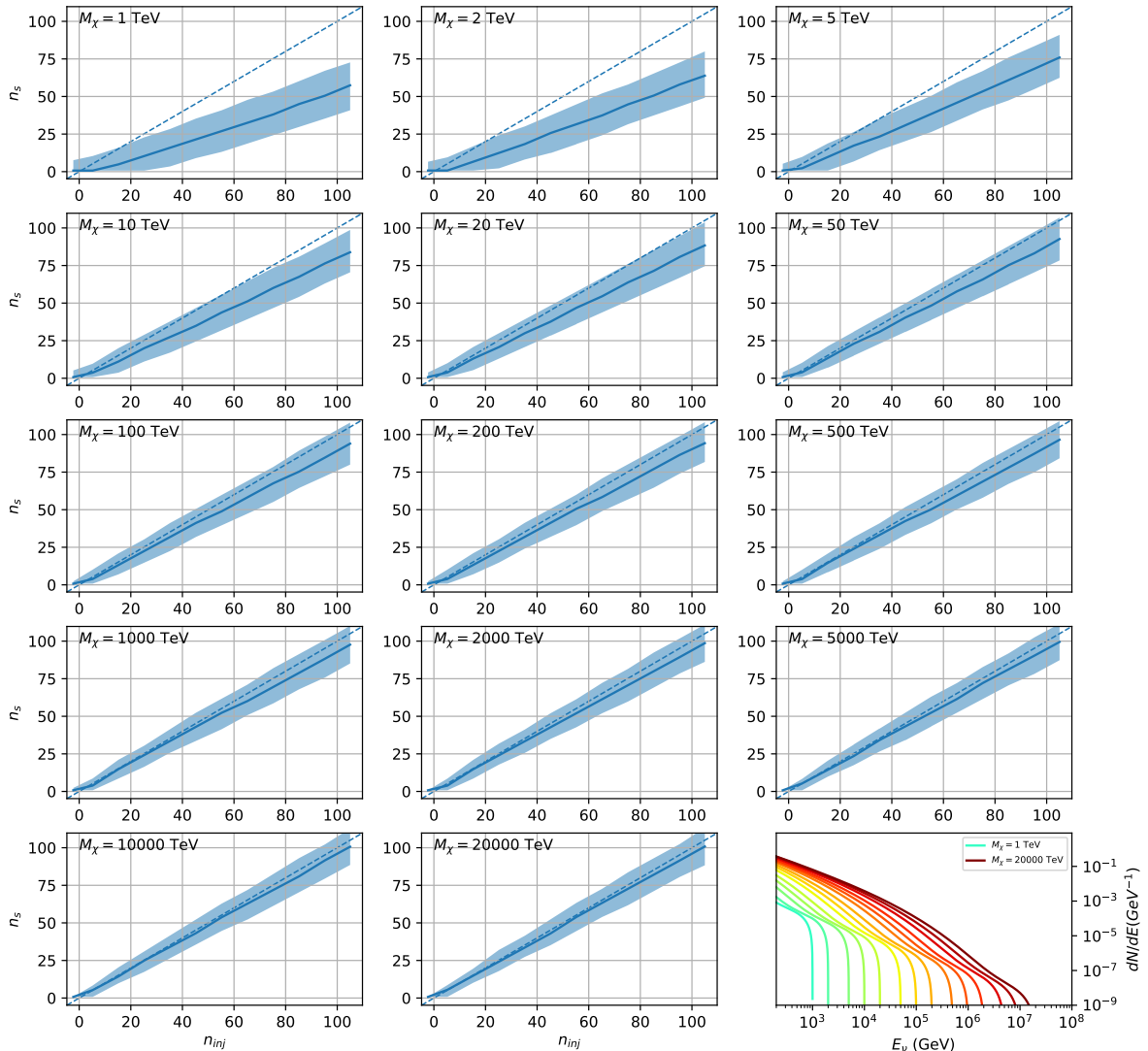


Figure C.7 Same as Fig. 6.23 but for Ursa Major II and  $\chi\chi \rightarrow t\bar{t}$ .

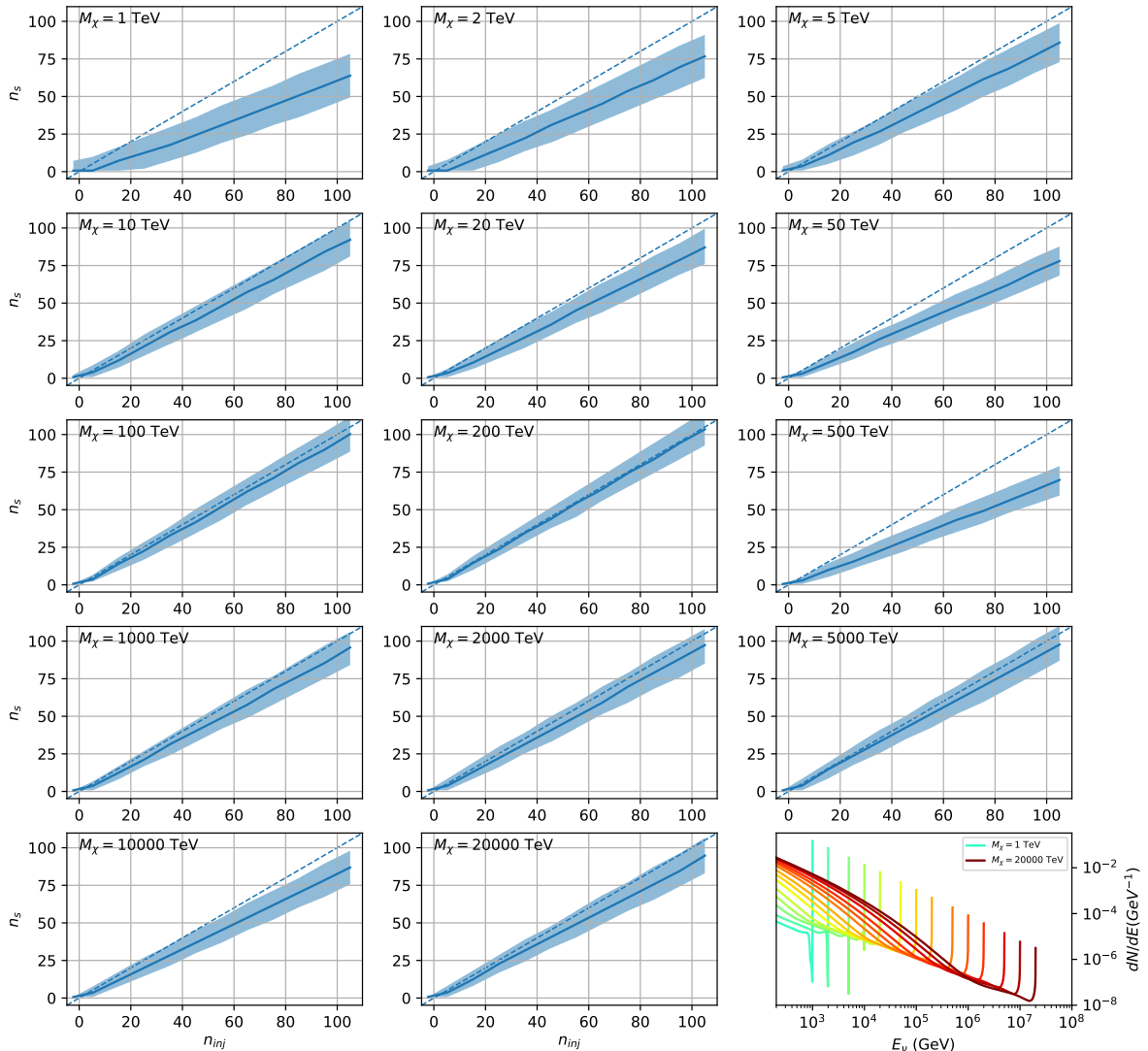


Figure C.8 Same as Fig. 6.23 but for Ursa Major II and  $\chi\chi \rightarrow \nu_\mu \bar{\nu}_\mu$ .

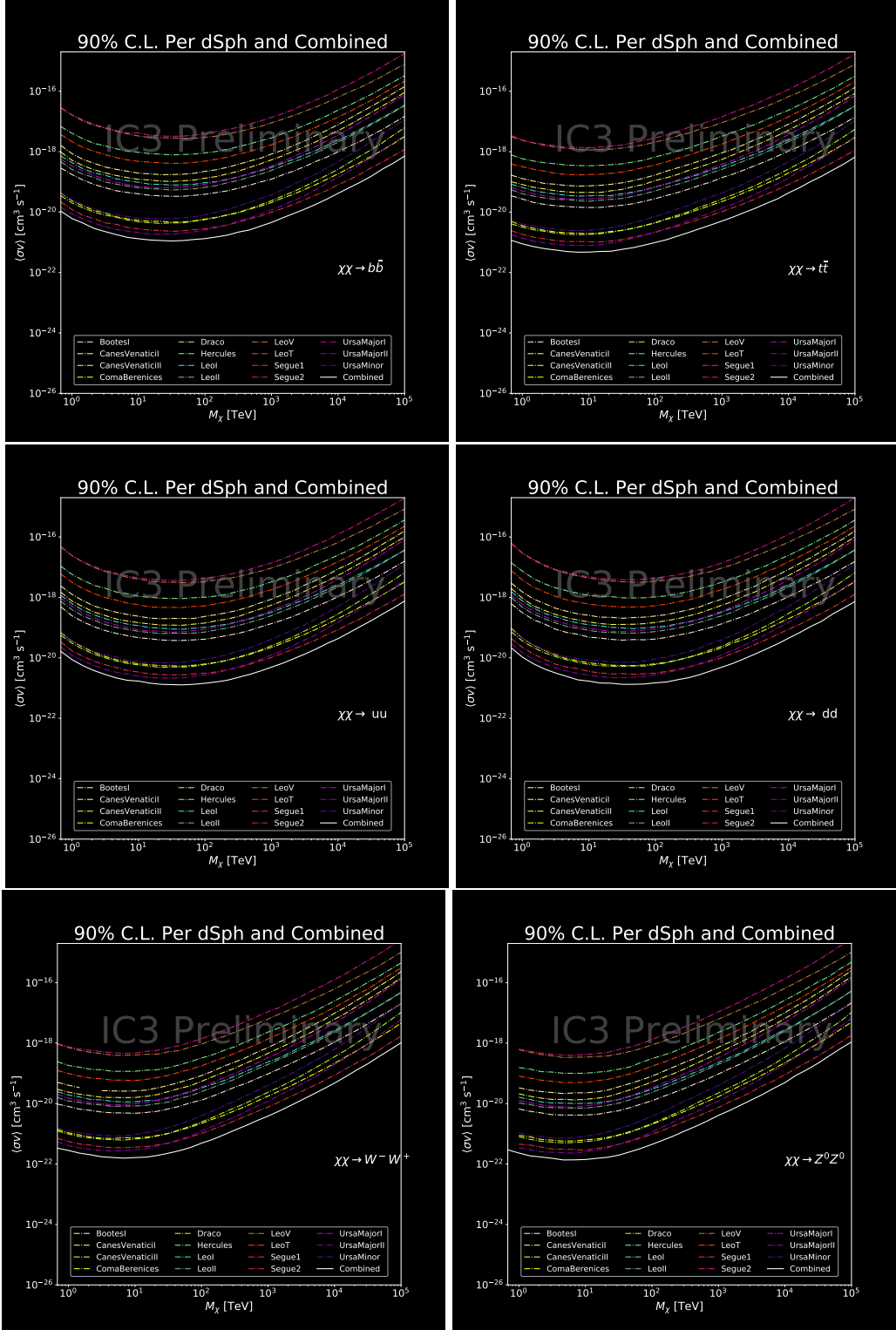


Figure C.9 IceCube North Sky Track Sensitivities for  $n_s/\langle N \rangle$ .  $n_s$  values are the counts fed into Eq. (6.8) to produce Fig. 6.26 and Fig. 6.25.

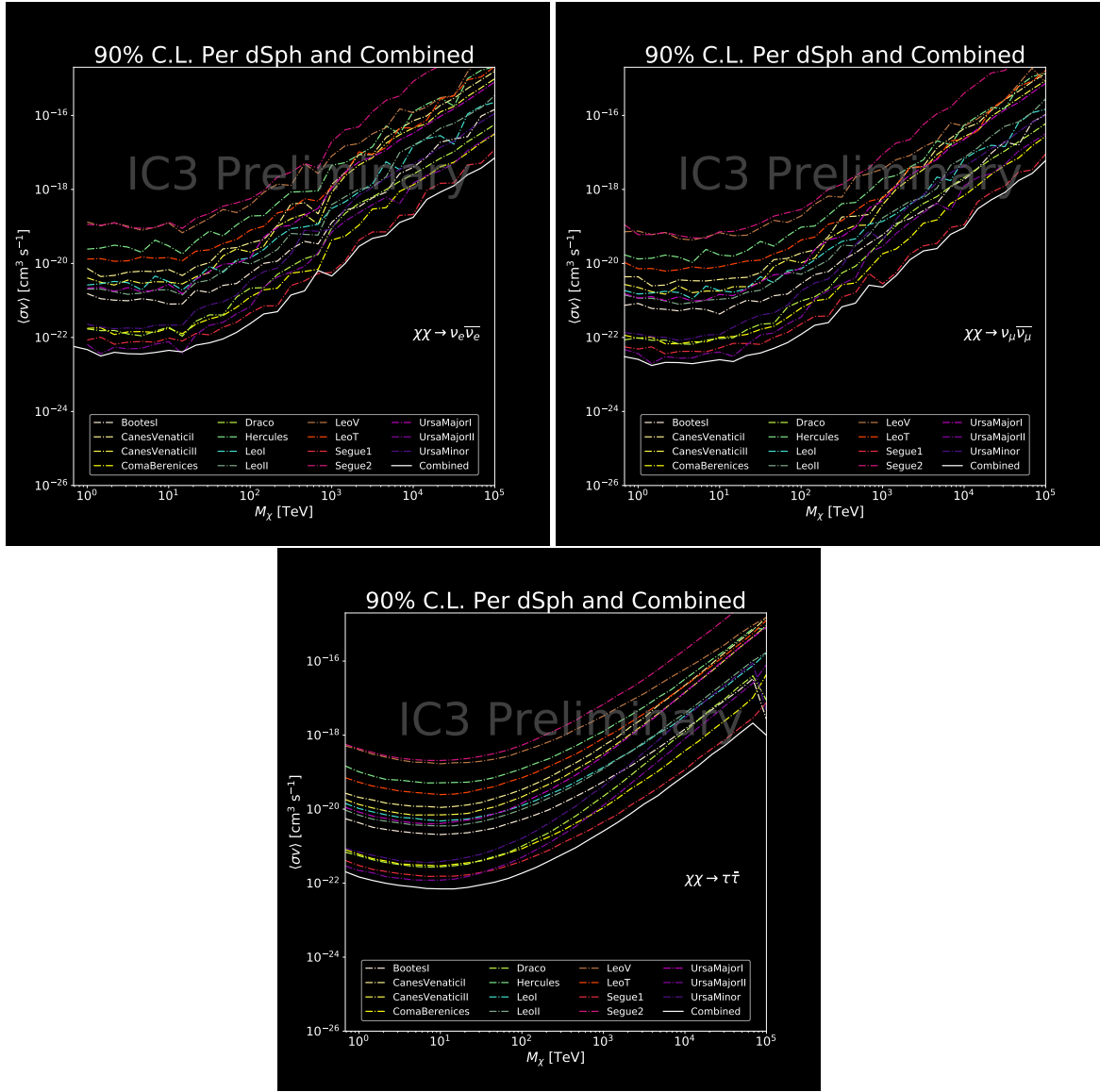


Figure C.10 Same as Fig. C.9 for three additional DM annihilation channels.

## BIBLIOGRAPHY

- [1] Anne M. Green. “Dark matter in astrophysics/cosmology”. In: *SciPost Phys. Lect. Notes* (2022), p. 37. doi: [10.21468/SciPostPhysLectNotes.37](https://doi.org/10.21468/SciPostPhysLectNotes.37). URL: <https://scipost.org/10.21468/SciPostPhysLectNotes.37>.
- [2] Bing-Lin Young. “A survey of dark matter and related topics in cosmology”. In: *Frontiers of Physics* 12 (Oct. 2016). doi: <https://doi.org/10.1007/s11467-016-0583-4>. URL: <https://doi.org/10.1007/s11467-016-0583-4>.
- [3] Gianfranco Bertone, Dan Hooper, and Joseph Silk. “Particle dark matter: evidence, candidates and constraints”. In: *Physics Reports* 405.5 (2005), pp. 279–390. ISSN: 0370-1573. doi: <https://doi.org/10.1016/j.physrep.2004.08.031>. URL: <https://www.sciencedirect.com/science/article/pii/S0370157304003515>.
- [4] Gianfranco Bertone and Dan Hooper. “History of dark matter”. In: *Rev. Mod. Phys.* 90 (4 Aug. 2018), p. 045002. doi: [10.1103/RevModPhys.90.045002](https://doi.org/10.1103/RevModPhys.90.045002). URL: <https://link.aps.org/doi/10.1103/RevModPhys.90.045002>.
- [5] Fritz Zwicky. “The Redshift of Extragalactic Nebulae”. In: *Helvetica Physica Acta* 6. (1933), pp. 110–127. doi: [10.5169/seals-110267](https://doi.org/10.5169/seals-110267).
- [6] Vera C. Rubin and Jr. Ford W. Kent. “Rotation of the Andromeda Nebula from a Spectroscopic Survey of Emission Regions”. In: *ApJ* 159 (Feb. 1970), p. 379. doi: [10.1086/150317](https://doi.org/10.1086/150317).
- [7] K. G. Begeman, A. H. Broeils, and R. H. Sanders. “Extended rotation curves of spiral galaxies: dark haloes and modified dynamics”. In: *Monthly Notices of the Royal Astronomical Society* 249.3 (Apr. 1991), pp. 523–537. ISSN: 0035-8711. doi: [10.1093/mnras/249.3.523](https://doi.org/10.1093/mnras/249.3.523). eprint: <https://academic.oup.com/mnras/article-pdf/249/3/523/18160929/mnras249-0523.pdf>. URL: <https://doi.org/10.1093/mnras/249.3.523>.
- [8] *Different types of gravitational lenses*. website. Feb. 2004. URL: <https://esahubble.org/images/heic0404b/>.
- [9] Douglas Clowe et al. “A Direct Empirical Proof of the Existence of Dark Matter”. In: *apjl* 648.2 (Sept. 2006), pp. L109–L113. doi: [10.1086/508162](https://doi.org/10.1086/508162). arXiv: [astro-ph/0608407 \[astro-ph\]](https://arxiv.org/abs/astro-ph/0608407).
- [10] Planck Collaboration and N. et. al. Aghanim. “Planck 2018 results I. Overview and the cosmological legacy of Planck”. In: *A&A* 641 (2020). doi: [10.1051/0004-6361/201833880](https://doi.org/10.1051/0004-6361/201833880). URL: <https://doi.org/10.1051/0004-6361/201833880>.
- [11] Wayne Hu. *Matter Density Animation*. web. 2024. URL: <http://background.uchicago.edu/~hu/density.html>

- 2662        [o.edu/~whu/animbut/anim2.html](http://o.edu/~whu/animbut/anim2.html).
- 2663 [12] Wenlong Yuan et al. “A First Look at Cepheids in a Type Ia Supernova Host with JWST”. In: *The Astrophysical Journal Letters* 940.1 (Nov. 2022). doi: [10.3847/2041-8213/ac9b27](https://doi.org/10.3847/2041-8213/ac9b27). URL: <https://dx.doi.org/10.3847/2041-8213/ac9b27>.
- 2666 [13] Wendy L. Freedman. “Measurements of the Hubble Constant: Tensions in Perspective”. In: *The Astrophysical Journal* 919.1 (Sept. 2021), p. 16. doi: [10.3847/1538-4357/ac0e95](https://doi.org/10.3847/1538-4357/ac0e95). URL: <https://dx.doi.org/10.3847/1538-4357/ac0e95>.
- 2669 [14] Jodi Cooley. “Dark Matter direct detection of classical WIMPs”. In: *SciPost Phys. Lect. Notes* (2022), p. 55. doi: [10.21468/SciPostPhysLectNotes.55](https://doi.org/10.21468/SciPostPhysLectNotes.55). URL: <https://scipost.org/10.21468/SciPostPhysLectNotes.55>.
- 2672 [15] “Search for new phenomena in events with an energetic jet and missing transverse momentum in  $pp$  collisions at  $\sqrt{s} = 13$  TeV with the ATLAS detector”. In: *Phys. Rev. D* 103 (11 July 2021), p. 112006. doi: [10.1103/PhysRevD.103.112006](https://doi.org/10.1103/PhysRevD.103.112006). URL: <https://link.aps.org/doi/10.1103/PhysRevD.103.112006>.
- 2676 [16] *Jetting into the dark side: a precision search for dark matter*. website. July 2020. URL: <https://atlas.cern/updates/briefing/precision-search-dark-matter>.
- 2678 [17] Celine Armand et. al. “Combined dark matter searches towards dwarf spheroidal galaxies with Fermi-LAT, HAWC, H.E.S.S., MAGIC, and VERITAS”. in: *Proceedings of Science*. Vol. 395. Mar. 2022. doi: <https://doi.org/10.22323/1.395.0528>.
- 2681 [18] Tracy R. Slatyer. “Les Houches Lectures on Indirect Detection of Dark Matter”. In: *SciPost Phys. Lect. Notes* (2022), p. 53. doi: [10.21468/SciPostPhysLectNotes.53](https://doi.org/10.21468/SciPostPhysLectNotes.53). URL: <https://scipost.org/10.21468/SciPostPhysLectNotes.53>.
- 2684 [19] Christian W Bauer, Nicholas L. Rodd, and Bryan R. Webber. “Dark matter spectra from the electroweak to the Planck scale”. In: *Journal of High Energy Physics* 2021.1029-8479 (June 2021). doi: [https://doi.org/10.1007/JHEP06\(2021\)121](https://doi.org/10.1007/JHEP06(2021)121).
- 2687 [20] Riccardo Catena and Piero Ullio. “A novel determination of the local dark matter density”. In: *Journal of Cosmology and Astroparticle Physics* 2010.08 (Aug. 2010), p. 004. doi: [10.1088/1475-7516/2010/08/004](https://doi.org/10.1088/1475-7516/2010/08/004). URL: <https://dx.doi.org/10.1088/1475-7516/2010/08/004>.
- 2691 [21] B. P. Abbott et al. “Observation of Gravitational Waves from a Binary Black Hole Merger”. In: *Phys. Rev. Lett.* 116 (6 Feb. 2016), p. 061102. doi: [10.1103/PhysRevLett.116.061102](https://doi.org/10.1103/PhysRevLett.116.061102). URL: <https://link.aps.org/doi/10.1103/PhysRevLett.116.061102>.
- 2694 [22] R. Abbasi et. al. “Observation of high-energy neutrinos from the Galactic plane”. In: *Science* 380.6652 (June 2023), pp. 1338–1343.

- 2696 [23] NASA Goddard Space Flight Center. *Fermi's 12-year view of the gamma-ray sky*. website.  
2697 2022. URL: <https://svs.gsfc.nasa.gov/14090>.
- 2698 [24] Marco Cirelli et al. "PPPC 4 DM ID: a poor particle physicist cookbook for dark matter  
2699 indirect detection". In: *Journal of Cosmology and Astroparticle Physics* 2011.03 (Mar.  
2700 2011), p. 051. doi: [10.1088/1475-7516/2011/03/051](https://doi.org/10.1088/1475-7516/2011/03/051). URL: <https://dx.doi.org/10.1088/1475-7516/2011/03/051>.
- 2702 [25] The HAWC Collaboration. "The High-Altitude Water Cherenkov (HAWC) observatory in  
2703 México: The primary detector". In: *Nuclear Instruments and Methods in Physics Research*  
2704 *Section A: Accelerators, Spectrometers, Detectors and Associated Equipment* 1052 (2023),  
2705 p. 168253. ISSN: 0168-9002. doi: <https://doi.org/10.1016/j.nima.2023.168253>.  
2706 URL: <https://www.sciencedirect.com/science/article/pii/S0168900223002437>.
- 2708 [26] Alicia Lopez Oramas. "Multi-year Campaign of the Gamma-Ray Binary LS I +61° 303  
2709 and Search for VHE Emission from Gamma-Ray Binary Candidates with the MAGIC  
2710 Telescopes". PhD thesis. Instituto de Astrofísica de Canarias, 2014. doi: <http://dx.doi.org/10.13140/RG.2.1.4140.4969>.
- 2712 [27] A.U. Abeysekara et. al. "The High-Altitude Water Cherenkov (HAWC) observatory in  
2713 México: The primary detector". In: *Nuclear Instruments and Methods in Physics Research*  
2714 *Section A: Accelerators, Spectrometers, Detectors and Associated Equipment* 1052 (2023),  
2715 p. 168253. ISSN: 0168-9002. doi: <https://doi.org/10.1016/j.nima.2023.168253>.  
2716 URL: <https://www.sciencedirect.com/science/article/pii/S0168900223002437>.
- 2718 [28] Hamamatsu Photonics KK. *Large Photocathode Area Photomultiplier Tubes*. 2019. URL:  
2719 [https://www.hamamatsu.com/content/dam/hamamatsu-photonics/sites/documents/99\\_SALES\\_LIBRARY/etd/LARGE\\_AREA\\_PMT TPMH1376E.pdf](https://www.hamamatsu.com/content/dam/hamamatsu-photonics/sites/documents/99_SALES_LIBRARY/etd/LARGE_AREA_PMT TPMH1376E.pdf).
- 2721 [29] The HAWC Collaboration. "Data acquisition architecture and online processing system  
2722 for the HAWC gamma-ray observatory". In: *Nuclear Instruments and Methods in Physics*  
2723 *Research Section A: Accelerators, Spectrometers, Detectors and Associated Equipment* 888  
2724 (2018), pp. 138–146. ISSN: 0168-9002. doi: <https://doi.org/10.1016/j.nima.2018.01.051>. URL: <https://www.sciencedirect.com/science/article/pii/S0168900218300688>.
- 2727 [30] The Milagro Collaboratio. "Milagrito, a TeV air-shower array". In: *Nuclear Instruments*  
2728 *and Methods in Physics Research Section A: Accelerators, Spectrometers, Detectors and*  
2729 *Associated Equipment* 449.3 (2000), pp. 478–499. ISSN: 0168-9002. doi: [https://doi.org/10.1016/S0168-9002\(00\)00146-7](https://doi.org/10.1016/S0168-9002(00)00146-7). URL: <https://www.sciencedirect.com/science/article/pii/S0168900200001467>.
- 2732 [31] Ian Gabriel Wisher. "Real-time Transient Monitoring With the HAWC Detector: Design

- 2733 and Performance”. PhD thesis. The University of Wisconsin - Madison, 2016.
- 2734 [32] The ZeroMQ authors. “ZeroMQ An open-source universal messaging library”. In: (2021).  
2735 URL: <https://zeromq.org>.
- 2736 [33] Zigfried Hampel-Archisman. “Cosmic Ray Observations at the TeV Scale with the HAWC  
2737 Observatory”. PhD thesis. University of Wisconsin-Madison, 2017.
- 2738 [34] A. U. Abeysekara et al. “Observation of the Crab Nebula with the HAWC Gamma-Ray  
2739 Observatory”. In: *The Astrophysical Journal* 843.1 (June 2017), p. 39. doi: [10.3847/1538-4357/aa7555](https://doi.org/10.3847/1538-4357/aa7555). URL: <https://doi.org/10.3847/1538-4357/aa7555>.
- 2741 [35] Kenneth Greisen. “Cosmic Ray Showers”. In: *ANNUAL REVIEW OF NUCLEAR AND  
2742 PARTICLE SCIENCE* 10 (1960), pp. 63–108.
- 2743 [36] The HAWC Collabortion. “Sensitivity of the high altitude water Cherenkov detector to  
2744 sources of multi-TeV gamma rays”. In: *Astroparticle Physics* 50-52 (2013), pp. 26–32.  
2745 ISSN: 0927-6505. doi: <https://doi.org/10.1016/j.astropartphys.2013.08.002>. URL: <https://www.sciencedirect.com/science/article/pii/S0927650513001230>.
- 2748 [37] The HAWC Collaboration. “Measurement of the Crab Nebula Spectrum Past 100 TeV with  
2749 HAWC”. in: *The Astrophysical Journal* 881.2 (Aug. 2019), p. 134. doi: [10.3847/1538-4357/ab2f7d](https://doi.org/10.3847/1538-4357/ab2f7d). URL: <https://dx.doi.org/10.3847/1538-4357/ab2f7d>.
- 2751 [38] Samuel Miranelli. “CONSTRAINTS ON LORENTZ-INVARIANCE VIOLATION WITH  
2752 THE HAWC OBSERVATORY”. PhD thesis. Michigan State University, 2019.
- 2753 [39] A. A. Abdo et al. “OBSERVATION AND SPECTRAL MEASUREMENTS OF THE  
2754 CRAB NEBULA WITH MILAGRO”. in: *The Astrophysical Journal* 750.1 (Apr. 2012),  
2755 p. 63. doi: [10.1088/0004-637X/750/1/63](https://doi.org/10.1088/0004-637X/750/1/63). URL: <https://dx.doi.org/10.1088/0004-637X/750/1/63>.
- 2757 [40] Javier Rico. “Gamma-Ray Dark Matter Searches in Milky Way Satellites—A Comparative  
2758 Review of Data Analysis Methods and Current Results”. In: *Galaxies* 8.1 (Mar. 2020),  
2759 p. 25. doi: [10.3390/galaxies8010025](https://doi.org/10.3390/galaxies8010025). arXiv: [2003.13482 \[astro-ph.HE\]](https://arxiv.org/abs/2003.13482).
- 2760 [41] W. B. Atwood et al. “The Large Area Telescope on the Fermi Gamma-Ray Space Telescope  
2761 Mission”. In: *apj* 697.2 (June 2009), pp. 1071–1102. doi: [10.1088/0004-637X/697/2/1071](https://doi.org/10.1088/0004-637X/697/2/1071). arXiv: [0902.1089 \[astro-ph.IM\]](https://arxiv.org/abs/0902.1089).
- 2763 [42] M. Ackermann et al. “Searching for Dark Matter Annihilation from Milky Way Dwarf  
2764 Spheroidal Galaxies with Six Years of Fermi Large Area Telescope Data”. In: *prl* 115.23,  
2765 231301 (Dec. 2015), p. 231301. doi: [10.1103/PhysRevLett.115.231301](https://doi.org/10.1103/PhysRevLett.115.231301). arXiv:  
2766 [1503.02641 \[astro-ph.HE\]](https://arxiv.org/abs/1503.02641).

- 2767 [43] Mattia Di Mauro, Martin Stref, and Francesca Calore. “Investigating the effect of Milky  
2768 Way dwarf spheroidal galaxies extension on dark matter searches with Fermi-LAT data”.  
2769 In: *Phys. Rev. D* 106 (12 Dec. 2022), p. 123032. doi: [10.1103/PhysRevD.106.123032](https://doi.org/10.1103/PhysRevD.106.123032).  
2770 URL: <https://link.aps.org/doi/10.1103/PhysRevD.106.123032>.
- 2771 [44] F. et al. Aharonian. “Observations of the Crab Nebula with H.E.S.S.”. In: *Astron.  
2772 Astrophys.* 457 (2006), pp. 899–915. doi: [10.1051/0004-6361:20065351](https://doi.org/10.1051/0004-6361:20065351). arXiv:  
2773 [astro-ph/0607333](https://arxiv.org/abs/astro-ph/0607333).
- 2774 [45] J. Albert et al. “VHE  $\gamma$ -Ray Observation of the Crab Nebula and its Pulsar with the  
2775 MAGIC Telescope”. In: *The Astrophysical Journal* 674.2 (Feb. 2008), p. 1037. doi:  
2776 [10.1086/525270](https://doi.org/10.1086/525270). URL: <https://dx.doi.org/10.1086/525270>.
- 2777 [46] N. Park. “Performance of the VERITAS experiment”. In: *Proceedings, 34th International  
2778 Cosmic Ray Conference (ICRC2015): The Hague, The Netherlands, July, 30th July - 6th  
2779 August.* Vol. 34. 2015, p. 771. arXiv: [1508.07070 \[astro-ph.IM\]](https://arxiv.org/abs/1508.07070).
- 2780 [47] A. Abramowski et al. “H.E.S.S. constraints on Dark Matter annihilations towards the  
2781 Sculptor and Carina Dwarf Galaxies”. In: *Astropart. Phys.* 34 (2011), pp. 608–616. doi:  
2782 [10.1016/j.astropartphys.2010.12.006](https://doi.org/10.1016/j.astropartphys.2010.12.006). arXiv: [1012.5602 \[astro-ph.HE\]](https://arxiv.org/abs/1012.5602).
- 2783 [48] A. Abramowski et al. “Search for dark matter annihilation signatures in H.E.S.S. obser-  
2784 vations of Dwarf Spheroidal Galaxies”. In: *Phys. Rev. D* 90 (2014), p. 112012. doi:  
2785 [10.1103/PhysRevD.90.112012](https://doi.org/10.1103/PhysRevD.90.112012). arXiv: [1410.2589 \[astro-ph.HE\]](https://arxiv.org/abs/1410.2589).
- 2786 [49] H. Abdalla et al. “Searches for gamma-ray lines and ‘pure WIMP’ spectra from Dark  
2787 Matter annihilations in dwarf galaxies with H.E.S.S”. in: *JCAP* 11 (2018), p. 037. doi:  
2788 [10.1088/1475-7516/2018/11/037](https://doi.org/10.1088/1475-7516/2018/11/037). arXiv: [1810.00995 \[astro-ph.HE\]](https://arxiv.org/abs/1810.00995).
- 2789 [50] J. Aleksić et al. “Optimized dark matter searches in deep observations of Segue 1 with  
2790 MAGIC”. in: *JCAP* 1402 (2014), p. 008. doi: [10.1088/1475-7516/2014/02/008](https://doi.org/10.1088/1475-7516/2014/02/008).  
2791 arXiv: [1312.1535 \[hep-ph\]](https://arxiv.org/abs/1312.1535).
- 2792 [51] V.A. Acciari et al. “Combined searches for dark matter in dwarf spheroidal galaxies observed  
2793 with the MAGIC telescopes, including new data from Coma Berenices and Draco”. In: *Physics of the Dark Universe* (2021), p. 100912. ISSN: 2212-6864. doi: <https://doi.org/10.1016/j.dark.2021.100912>. URL: <https://www.sciencedirect.com/science/article/pii/S2212686421001370>.
- 2797 [52] M. L. Ahnen et al. “Indirect dark matter searches in the dwarf satellite galaxy Ursa Major  
2798 II with the MAGIC Telescopes”. In: *JCAP* 1803.03 (2018), p. 009. doi: [10.1088/1475-7516/2018/03/009](https://doi.org/10.1088/1475-7516/2018/03/009). arXiv: [1712.03095 \[astro-ph.HE\]](https://arxiv.org/abs/1712.03095).
- 2800 [53] S. et al. Archambault. “Dark matter constraints from a joint analysis of dwarf Spheroidal  
2801 galaxy observations with VERITAS”. in: *prd* 95.8 (Apr. 2017). doi: [10.1103/PhysRevD.95.083008](https://doi.org/10.1103/PhysRevD.95.083008).

- 2802 . 95.082001. arXiv: 1703.04937 [astro-ph.HE].
- 2803 [54] Louise Oakes et al. “Combined Dark Matter searches towards dwarf spheroidal galaxies  
2804 with Fermi-LAT, HAWC, HESS, MAGIC and VERITAS”. in: *Proceedings of Science*.  
2805 2019.
- 2806 [55] Celine Armand et al. on behalf of the Fermi-LAT, HAWC, HESS, MAGIC, VERITAS.  
2807 “Combined Dark Matter searches towards dwarf spheroidal galaxies with Fermi-LAT,  
2808 HAWC, HESS, MAGIC and VERITAS”. in: *Proceedings of Science*. 2021.
- 2809 [56] Daniel Kerszberg et al. on behalf of the Fermi-LAT, HAWC, HESS, MAGIC, and VER-  
2810 TIAS collaborations. “Search for dark matter annihilation with a combined analysis of  
2811 dwarf spheroidal galaxies from Fermi-LAT, HAWC, H.E.S.S., MAGIC and VERITAS”. in:  
2812 *Proceedings of Science*. 2023.
- 2813 [57] Giacomo Vianello et al. *The Multi-Mission Maximum Likelihood framework (3ML)*. 2015.  
2814 arXiv: 1507.08343 [astro-ph.HE].
- 2815 [58] Marco Cirelli et al. “PPPC 4 DM ID: a poor particle physicist cookbook for dark matter  
2816 indirect detection”. In: *Journal of Cosmology and Astroparticle Physics* 2011.03 (Mar.  
2817 2011). ISSN: 1475-7516. doi: 10.1088/1475-7516/2011/03/051. URL: <http://dx.doi.org/10.1088/1475-7516/2011/03/051>.
- 2819 [59] Alex Geringer-Sameth, Savvas M. Koushiappas, and Matthew Walker. “DWARF  
2820 GALAXY ANNIHILATION AND DECAY EMISSION PROFILES FOR DARK MAT-  
2821 TER EXPERIMENTS”. in: *The Astrophysical Journal* 801.2 (Mar. 2015), p. 74. ISSN:  
2822 1538-4357. doi: 10.1088/0004-637x/801/2/74. URL: <http://dx.doi.org/10.1088/0004-637x/801/2/74>.
- 2824 [60] A. Albert et al. “Dark Matter Limits from Dwarf Spheroidal Galaxies with the HAWC  
2825 Gamma-Ray Observatory”. In: *The Astrophysical Journal* 853.2 (Feb. 2018), p. 154. ISSN:  
2826 1538-4357. doi: 10.3847/1538-4357/aaa6d8. URL: <http://dx.doi.org/10.3847/1538-4357/aaa6d8>.
- 2828 [61] HongSheng Zhao. “Analytical models for galactic nuclei”. In: *Mon. Not. Roy. Astron.*  
2829 *Soc.* 278 (1996), pp. 488–496. doi: 10.1093/mnras/278.2.488. arXiv: astro-ph/95  
2830 09122 [astro-ph].
- 2831 [62] Julio F. Navarro, Carlos S. Frenk, and Simon D. M. White. “The Structure of Cold Dark  
2832 Matter Halos”. In: *ApJ* 462 (May 1996), p. 563. doi: 10.1086/177173. eprint:  
2833 astro-ph/9508025 (astro-ph).
- 2834 [63] V. Bonnivard et al. “Spherical Jeans analysis for dark matter indirect detection in dwarf  
2835 spheroidal galaxies - Impact of physical parameters and triaxiality”. In: *Mon. Not. Roy.*  
2836 *Astron. Soc.* 446 (2015), pp. 3002–3021. doi: 10.1093/mnras/stu2296. arXiv:

- 2837        1407.7822 [astro-ph.HE].
- 2838 [64] M. Ackermann et al. “Searching for Dark Matter Annihilation from Milky Way Dwarf  
2839 Spheroidal Galaxies with Six Years of Fermi Large Area Telescope Data”. In: *prl* 115.23,  
2840 231301 (Dec. 2015), p. 231301. doi: [10.1103/PhysRevLett.115.231301](https://doi.org/10.1103/PhysRevLett.115.231301). arXiv:  
2841 [1503.02641](https://arxiv.org/abs/1503.02641) [astro-ph.HE].
- 2842 [65] M. L. Ahnen et al. “Limits to Dark Matter Annihilation Cross-Section from a Combined  
2843 Analysis of MAGIC and Fermi-LAT Observations of Dwarf Satellite Galaxies”. In: *JCAP*  
2844 1602.02 (2016), p. 039. doi: [10.1088/1475-7516/2016/02/039](https://doi.org/10.1088/1475-7516/2016/02/039). arXiv: [1601.06590](https://arxiv.org/abs/1601.06590)  
2845 [astro-ph.HE].
- 2846 [66] Javier Rico et al. *gLike: numerical maximization of heterogeneous joint  
2847 likelihood functions of a common free parameter plus nuisance parameters.*  
2848 <https://doi.org/10.5281/zenodo.4601451>. Version v00.09.03. Mar. 2021. doi:  
2849 [10.5281/zenodo.4601451](https://doi.org/10.5281/zenodo.4601451). URL: <https://doi.org/10.5281/zenodo.4601451>.
- 2850 [67] Tjark Miener and Daniel Nieto. *LklCom: Combining likelihoods from different ex-  
2851 periments.* <https://doi.org/10.5281/zenodo.4597500>. Version v0.5.3. Mar. 2021. doi:  
2852 [10.5281/zenodo.4597500](https://doi.org/10.5281/zenodo.4597500). URL: <https://doi.org/10.5281/zenodo.4597500>.
- 2853 [68] T. Miener et al. “Open-source Analysis Tools for Multi-instrument Dark Matter Searches”.  
2854 In: *arXiv e-prints*, arXiv:2112.01818 (Dec. 2021), arXiv:2112.01818. arXiv: [2112.01818](https://arxiv.org/abs/2112.01818)  
2855 [astro-ph.IM].
- 2856 [69] Alex Geringer-Sameth and Matthew Koushiappas Savvas M. and Walker. “Dwarf galaxy  
2857 annihilation and decay emission profiles for dark matter experiments”. In: *Astrophys.  
2858 J.* 801.2 (2015), p. 74. doi: [10.1088/0004-637X/801/2/74](https://doi.org/10.1088/0004-637X/801/2/74). arXiv: [1408.0002](https://arxiv.org/abs/1408.0002)  
2859 [astro-ph.CO].
- 2860 [70] Gianfranco Bertone, Dan Hooper, and Joseph Silk. “Particle dark matter: evidence,  
2861 candidates and constraints”. In: *Physics Reports* 405.5-6 (Jan. 2005), pp. 279–390. ISSN:  
2862 0370-1573. doi: [10.1016/j.physrep.2004.08.031](https://doi.org/10.1016/j.physrep.2004.08.031). URL: <http://dx.doi.org/10.1016/j.physrep.2004.08.031>.
- 2864 [71] V. Bonnivard et al. “Dark matter annihilation and decay in dwarf spheroidal galaxies: The  
2865 classical and ultrafaint dSphs”. In: *Mon. Not. Roy. Astron. Soc.* 453.1 (2015), pp. 849–  
2866 867. doi: [10.1093/mnras/stv1601](https://doi.org/10.1093/mnras/stv1601). arXiv: [1504.02048](https://arxiv.org/abs/1504.02048) [astro-ph.HE].
- 2867 [72] A. et al. Albert. “Searching for Dark Matter Annihilation in Recently Discovered Milky  
2868 Way Satellites with Fermi-LAT”. in: *Astrophys. J.* 834.2 (2017), p. 110. doi: [10.3847/1538-4357/834/2/110](https://doi.org/10.3847/1538-4357/834/2/110). arXiv: [1611.03184](https://arxiv.org/abs/1611.03184) [astro-ph.HE].
- 2870 [73] Mattia Di Mauro and Martin Wolfgang Winkler. “Multimessenger constraints on the dark  
2871 matter interpretation of the Fermi-LAT Galactic Center excess”. In: *prd* 103.12, 123005

- 2872 (June 2021), p. 123005. doi: [10.1103/PhysRevD.103.123005](https://doi.org/10.1103/PhysRevD.103.123005). arXiv: [2101.11027](https://arxiv.org/abs/2101.11027) [astro-ph.HE].
- 2873
- 2874 [74] H. C. Plummer. “On the Problem of Distribution in Globular Star Clusters: (Plate 8.)”  
2875 In: *Monthly Notices of the Royal Astronomical Society* 71.5 (Mar. 1911), pp. 460–470.  
2876 ISSN: 0035-8711. doi: [10.1093/mnras/71.5.460](https://doi.org/10.1093/mnras/71.5.460). eprint: <https://academic.oup.com/mnras/article-pdf/71/5/460/2937497/mnras71-0460.pdf>. URL:  
2877 <https://doi.org/10.1093/mnras/71.5.460>.
- 2878
- 2879 [75] Daniel R. Hunter. “Derivation of the anisotropy profile, constraints on the local velocity  
2880 dispersion, and implications for direct detection”. In: *JCAP* 02 (2014), p. 023. doi:  
2881 [10.1088/1475-7516/2014/02/023](https://doi.org/10.1088/1475-7516/2014/02/023). arXiv: [1311.0256](https://arxiv.org/abs/1311.0256) [astro-ph.CO].
- 2882
- 2883 [76] Barun Kumar Dhar and Liliya L. R. Williams. “Surface mass density of the Einasto family  
2884 of dark matter haloes: are they Sersic-like?” In: *Mon. Not. Roy. Astron. Soc.* (2010). doi:  
[10.1111/j.1365-2966.2010.16446.x](https://doi.org/10.1111/j.1365-2966.2010.16446.x).
- 2885
- 2886 [77] M. Baes and E. Van Hese. “Dynamical models with a general anisotropy profile”. In:  
2887 *Astron. Astrophys.* 471 (2007), p. 419. doi: [10.1051/0004-6361:20077672](https://doi.org/10.1051/0004-6361:20077672). arXiv:  
[0705.4109](https://arxiv.org/abs/0705.4109) [astro-ph].
- 2888
- 2889 [78] Matthew G. Walker, Edward W. Olszewski, and Mario Mateo. “Bayesian analysis of  
2890 resolved stellar spectra: application to MMT/Hectochelle observations of the Draco dwarf  
2891 spheroidal”. In: *mnras* 448.3 (Apr. 2015), pp. 2717–2732. doi: [10.1093/mnras/stv099](https://doi.org/10.1093/mnras/stv099).  
arXiv: [1503.02589](https://arxiv.org/abs/1503.02589) [astro-ph.GA].
- 2892
- 2893 [79] Nicholas L. Rodd et al. “Dark matter spectra from the electroweak to the Planck scale”.  
In: *J. High Energy Physics* 121.10.1007 (June 2021).
- 2894
- 2895 [80] Pace, Andrew B and Strigari, Louis E. “Scaling relations for dark matter annihilation and  
2896 decay profiles in dwarf spheroidal galaxies”. In: *Monthly Notices of the Royal Astronomical  
2897 Society* 482.3 (Oct. 2018), pp. 3480–3496. ISSN: 0035-8711. doi: [10.1093/mnras/sty2839](https://doi.org/10.1093/mnras/sty2839).
- 2898
- 2899 [81] Albert, A. et al. “Search for gamma-ray spectral lines from dark matter annihilation in  
2900 dwarf galaxies with the High-Altitude Water Cherenkov observatory”. In: *Phys. Rev. D* 101 (10 May 2020), p. 103001. doi: [10.1103/PhysRevD.101.103001](https://doi.org/10.1103/PhysRevD.101.103001). URL:  
<https://link.aps.org/doi/10.1103/PhysRevD.101.103001>.
- 2901
- 2902 [82] Victor Eijkhout and Edmund Show and Robert van de Geijn. *The Science of Computing.  
2903 The Art of High Performance Computing*. Vol. 3. Open Copy published under CC-BY 4.0  
2904 license, 2023, pp. 63–66.
- 2905
- 2906 [83] IceCube Gallery. 2019. URL: [https://gallery.icecube.wisc.edu/internal/v/SPIImages/weekly/winteroverweeklyphotos2019/icl.JPG.html?g2\\_imageView](https://gallery.icecube.wisc.edu/internal/v/SPIImages/weekly/winteroverweeklyphotos2019/icl.JPG.html?g2_imageView)

- 2907        **sIndex=1.**
- 2908 [84] The IceCube Collaboration. “The IceCube Neutrino Observatory: instrumentation and  
2909 online systems”. In: *Journal of Instrumentation* 12.03 (Mar. 2017), P03012. doi: [10.1088/1748-0221/12/03/P03012](https://doi.org/10.1088/1748-0221/12/03/P03012). URL: <https://dx.doi.org/10.1088/1748-0221/12/03/P03012>.
- 2912 [85] Ahlers, Markus and Helbing, Klaus and Pérez de los Heros, Carlos. “Probing particle  
2913 physics with IceCube”. In: *The European Physical Journal C* 78.11 (Nov. 2018). ISSN:  
2914 1434-6052. doi: [10.1140/epjc/s10052-018-6369-9](https://doi.org/10.1140/epjc/s10052-018-6369-9). URL: <http://dx.doi.org/10.1140/epjc/s10052-018-6369-9>.
- 2916 [86] Rene Reimann. “Search for the Sources of the Astrophysical High-Energy Muon-Neutrino  
2917 Flux with the IceCube Neutrino Observatory”. PhD thesis. Aachen University in Erlan-  
2918 gung, 2019.
- 2919 [87] IceCube Collaboration. *Detecting Neutrinos*. Web. 2024.
- 2920 [88] IceCube Collaboration. “Energy reconstruction methods in the IceCube neutrino tele-  
2921 scope”. In: *Journal of Instrumentation* 9.03 (Mar. 2014), P03009. doi: [10.1088/1748-0221/9/03/P03009](https://doi.org/10.1088/1748-0221/9/03/P03009). URL: <https://dx.doi.org/10.1088/1748-0221/9/03/P03009>.
- 2924 [89] The IceCube Collaboration. “Detection of astrophysical tau neutrino candidates in Ice-  
2925 Cube”. In: *The European Physical Journal C* 82.11 (Nov. 2022). ISSN: 1434-6052. doi:  
2926 [10.1140/epjc/s10052-022-10795-y](https://doi.org/10.1140/epjc/s10052-022-10795-y). URL: <http://dx.doi.org/10.1140/epjc/s10052-022-10795-y>.
- 2928 [90] J. Ahrens et al. “Muon track reconstruction and data selection techniques in AMANDA”.  
2929 in: *Nuclear Instruments and Methods in Physics Research Section A: Accelerators,  
2930 Spectrometers, Detectors and Associated Equipment* 524.1 (2004), pp. 169–194. ISSN:  
2931 0168-9002. doi: <https://doi.org/10.1016/j.nima.2004.01.065>. URL:  
2932 <https://www.sciencedirect.com/science/article/pii/S0168900204001871>.
- 2933 [91] Peter J. Huber. “Robust Estimation of a Location Parameter”. In: *The Annals of Math-  
2934 ematical Statistics* 35.1 (1964), pp. 73–101. doi: [10.1214/aoms/1177703732](https://doi.org/10.1214/aoms/1177703732). URL:  
2935 <https://doi.org/10.1214/aoms/1177703732>.
- 2936 [92] IceCube Collaboration. “Calibration and characterization of the IceCube photomultiplier  
2937 tube”. In: *Nuclear Instruments and Methods in Physics Research Section A: Accelerators,  
2938 Spectrometers, Detectors and Associated Equipment* 618.1 (2010), pp. 139–152. ISSN:  
2939 0168-9002. doi: <https://doi.org/10.1016/j.nima.2010.03.102>. URL: <https://www.sciencedirect.com/science/article/pii/S0168900210006662>.
- 2941 [93] Aartsen, M. et al. “IceCube search for dark matter annihilation in nearby galaxies and galaxy

- 2942        clusters". In: *Phys. Rev. D* 88 (12 Dec. 2013), p. 122001. doi: [10.1103/PhysRevD.88.122001](https://doi.org/10.1103/PhysRevD.88.122001). URL: <https://link.aps.org/doi/10.1103/PhysRevD.88.122001>.
- 2943
- 2944 [94] Pearl Sandick et al. "Sensitivity of the IceCube neutrino detector to dark matter annihilating  
2945        in dwarf galaxies". In: *Phys. Rev. D* 81 (8 Apr. 2010), p. 083506. doi: [10.1103/PhysRevD.81.083506](https://doi.org/10.1103/PhysRevD.81.083506). URL: <https://link.aps.org/doi/10.1103/PhysRevD.81.083506>.
- 2946
- 2947
- 2948 [95] Qinrui Liu and Jeffrey Lazar and Carlos A. Argüelles and Ali Kheirandish. " $\chi$ aro: a tool  
2949        for neutrino flux generation from WIMPs". In: *Journal of Cosmology and Astroparticle  
2950        Physics* 2020.10 (Oct. 2020), p. 043. doi: [10.1088/1475-7516/2020/10/043](https://doi.org/10.1088/1475-7516/2020/10/043). URL:  
2951 <https://dx.doi.org/10.1088/1475-7516/2020/10/043>.
- 2952
- 2953 [96] Tessa Cerver. "Time Integrated searches for Astrophysical Neutrino Sources using the  
2954        IceCube Detector and Gender in Physics studies for the Genera Project". PhD thesis.  
UNIVERSITE DE GEN ´ EVE, 2019, pp. 57–64.
- 2955
- 2956 [97] Minjin Jeong on behalf of the IceCube Collaboration. "Search for Dark Matter Decay in  
2957        Nearby Galaxy Clusters and Galaxies with IceCube". In: *Proceedings of Science* 444.38  
(2023).
- 2958
- 2959 [98] IceCube Collaboration. "Evidence for neutrino emission from the nearby active galaxy  
NGC 1068". In: *Science* 378.6619 (2022).
- 2960
- [99] Nathan Whitehorn and Jakob van Santen. *Photospline*. IceCube: GitHub.
- 2961
- 2962 [100] Paul H. C. Eilers and Brian D. Marx. "Flexible smoothing with B-splines and penalties".  
In: *Statistical Science* 11.2 (1996), pp. 89–121. doi: [10.1214/ss/1038425655](https://doi.org/10.1214/ss/1038425655). URL:  
<https://doi.org/10.1214/ss/1038425655>.
- 2963
- 2964 [101] The IceCube Collaboration. *Search for neutrino lines from dark matter annihilation and  
2965        decay with IceCube*. 2023. arXiv: [2303.13663](https://arxiv.org/abs/2303.13663) [astro-ph.HE].
- 2966
- 2967 [102] The IceCube Collaboration. "Measurement of the multi-TeV neutrino interaction cross-  
section with IceCube using Earth absorption". In: *Nature* 551 (2017).